Technische Universität
Kaiserslautern

Fachbereich
Physik

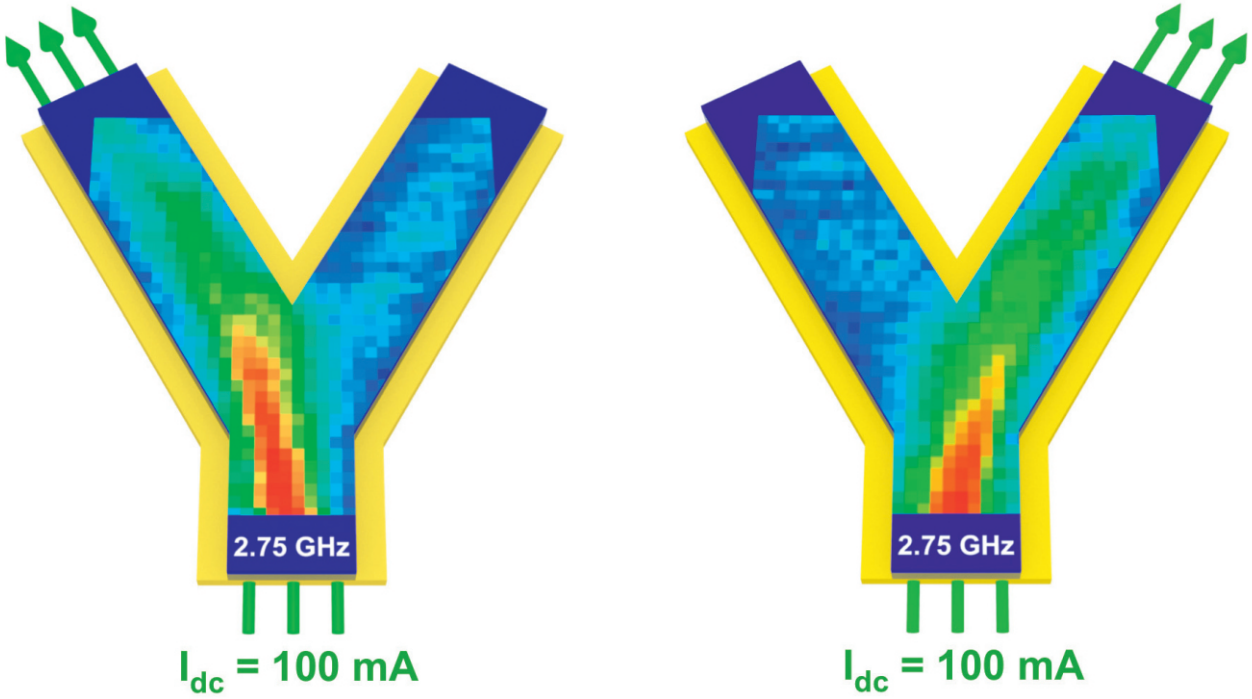

AG Magnetismus
Annual Report 2013

OPTIMAS

AG MAGNETISMUS
TU KAISERSLAUTERN

Front page: Illustration of a spin-wave multiplexer with measured spin-wave intensity for both transmission directions. The data was recorded via Brillouin light scattering microscopy. In this device, the spin-wave propagation in the $Ni_{81}Fe_{19}$-stripes on top of the structure (blue) is controlled via a direct current in the underlying gold layer (yellow). The Oersted field created by this direct current causes an alignment of the magnetization perpendicular to the propagation direction in one of the arms of the Y-structure, whereas the magnetization in the other arm is aligned along the waveguide due to the shape anisotropy. The spin-wave dispersion for in-plane magnetized samples is anisotropic with respect to the magnetization direction. As a result, the group velocity is much higher for perpendicular alignment of magnetization and propagation direction than for parallel alignment. Therefore, the spatial decay is much lower for the perpendicular alignment in the arm where the direct current is flowing and the propagation is suppressed in the other arm. By applying the electric current to the left or to the right arm spin-wave propagation can be switched between the arms. For more details about this phenomenon see Section 4.9 of the Report.

Annual Report 2013

Address:	Prof. Dr. Burkard Hillebrands Fachbereich Physik Landesforschungszentrum OPTIMAS Technische Universität Kaiserslautern Erwin-Schrödinger-Straße 56 67663 Kaiserslautern, Germany Tel.: +49-(0)631-205-4228 Fax.: +49-(0)631-205-4095
Postal address:	Postfach 3049 67653 Kaiserslautern, Germany
Internet:	http://www.physik.uni-kl.de/hillebrands/
E-Mail:	hilleb@physik.uni-kl.de

This Annual Report can be downloaded from:
http://www.physik.uni-kl.de/hillebrands/publications/annual-reports/

Our Group

From left to right:

Philipp Pirro, Dr. Andrés Conca Parra, Thomas Brächer, Donata Passarello, Dr. Andrii Chumak, Prof. Dr. Burkard Hillebrands, Thomas Langner, Roland Neb, Dr. Björn Obry, Dr. Vitaliy Vasyuchka, Milan Agrawal, Dr. Britta Leven, Peter Clausen, Thomas Meyer, Dr. Benjamin Jungfleisch, Dr. Thomas Sebastian, Akihiro Kirihara, Dr. Evangelos Papaioannou, Frank Heussner, Viktor Lauer, Ana Ruiz Calaforra, Dr. Florin Ciubotaru

Not on the picture: Dr. Alexander Serga, Dr. Katrin Schultheiß, Dmytro Bozhko, Dr. Isabel Sattler, Sibylle Müller, Dieter Weller

Contents

Chapter 1: Preface

Dear Colleagues and Friends,

we present our Annual Report 2013 covering the period November 2012 to October 2013.

Again, we are happy to report several new research highlights: The field of magnon gases is strongly advancing. We were able to demonstrate the condensation of magnon-phonon quasi-particles at a virtual energy minimum, whose frequency position is determined by magnon-phonon interaction. It is remarkable that these quasi-particles have a very high group velocity, and, thus, are very sensitive to the spatial configuration of the pumping field. In the field of magnonic crystals we have shown, that excellent performance can be achieved using ion implantation for the preparation of the periodic structures. We succeeded in improving the inverse spin Hall effect efficiency by designing the interfaces in Yttrium-Iron-Garnet/Platinum and Iron/Platinum bilayers. A novel non-reciprocal spin-wave mode localized at the rim of perpendicularly magnetized 2D structures has been found by numerical simulation. We also demonstrated the first YIG-based insulating micro-scaled spin-wave waveguide of 100 nm thickness and 5 µm width. We showed that the life time of the spin waves in this waveguide is more than an order of magnitude higher than in usually used microstructured metallic systems like Permalloy. Time resolved investigations of the longitudinal spin Seebeck effect revealed that this effect is caused by thermally driven magnons and depends on thermal magnon diffusion in a magnetic material. We also confirmed, that volume waves are elastically scattered at the end of a waveguide whereas magnetostatic surface waves undergo a chiral reflection in combination with the formation of both width and thickness standing modes.

Our German-Japanese collaboration “Advanced Spintronic Materials and Transport Phenomena (ASPIMATT)” was evaluated positively and we are receiving funding for a second funding period by the Deutsche Forschungsgemeinschaft (DFG) and the Japanese Science and Technology Foundation (JST).

Again, there have been several changes in our group. We are happy to welcome (in alphabetical order) Dmytro Bozhko, Viktor Lauer, and Donata Passarello for PhD work (Donata is working in the lab of Stuart Parkin and is a member of the Graduate School of Excellence “Materials Science in Mainz”). We also welcome Akihiro Kirihara from NEC Corporation, as a guest scientist for a full year. He is involved in our projects in the framework of the DFG-funded Priority Program “Spincaloric Transport (SpinCaT)”. Dr. Tomohiro Koyama has left us after a successful year as a A.v.Humboldt fellow for a permanent position at Tokyo University. Several group members finished their Ph.D. and left us, or will leave us soon: Benjamin Jungfleisch, Björn Obry, Katrin Schultheiß (née Vogt) and Thomas Sebastian. Philipp Fuhrmann and Viktor Lauer finished their Diploma in Physics, and Stefan Weirich his Master of Education.

Our work would not have been possible without valuable collaborations with people all over the world. They are too many to list them here all. In particular we would like to thank, in alphabetical order, Johan Åkerman, Toshu An, Yasuo Ando, Christian Back, Gerrit Bauer, Arne Brataas, Frederick Casper, Russell Cowburn, Sergei Demokritov, Bernard Dieny, Marco Doms, Carsten Dubs, Ursula Ebels, Hajo Elmers, Jürgen Fassbender, Gerhard Fecher, Claudia Felser, Albert Fert, Yasuhiro Fukuma, Sebastian Goennenwein, John Gregg, Hubert Grimm, Dirk Grundler, Gianluca Gubbiotti, Konstantin Gusliyenko, Jaroslav Hamrle, Uwe Hartmann, Michel Hehn, Jos Heremans, Axel Hoffmann, Koichiro Innomata, Gerhard Jakob, Xiaofeng Jin, Martin Jourdan, Gleb Kakazei, Boris Kalinikos, Alexy Karenowska, Sang-Koog Kim, Olivier Klein, Mathias Kläui, Peter Kopietz, Mikhail Kostylev, Volodymyr Kruglyak, Takahide Kubota, Bert Lägel, Ronald Lehndorff,

Luis Lopez Diaz, Jörg Lösch, Wolfram Maaß, Sadamichi Maekawa, Stéphane Mangin, Gennadiy Melkov, Claudia and Tim Mewes, Shuichi Murakami, Hiroshi Naganuma, Ulrich Nowak, Jean-Pierre Nozières, Kevin O'Grady, Mikihiko Oogane, Yoshichika Otani, Stuart Parkin, Johannes Paul, Marco Rahm, Günter Reiss, Sergio Rezende, Bernhard Reuscher, Caroline Ross, Manfred Rührig, Eiji Saitoh, John R. Sandercock, Rudi Schäfer, Gerd Schönhense, Hussein Shanak, Andrei Slavin, Rolf Slatter, Bob Stamps, Yoshishige Suzuki, Koki Takanashi, Vasyl Tiberkevich, Simon Trudel, Yaroslav Tserkovnyak, Ken-ichi Uchida, Alexey Ustinov, Ben Van de Wiele, Bart van Wees, Arne Vansteenkiste, and Mingzhong Wu for their interactions with us and their strong input to our work.

Collaborations within the Fachbereich Physik at the University of Kaiserslautern (in particular Martin Aeschlimann, James Anglin, Sebastian Eggert, Michael Fleischhauer, Georg von Freymann, Herwig Ott, Hans-Christian Schneider, Volker Schünemann, and Arthur Widera and their groups), Michael Kopnarski and his team from the Institut für Oberflächen- und Schichtanalytik, as well as Sandra Wolff and her team from the Nano Structuring Center have again been very stimulating. We are very grateful to be a member of the State Research Center for Optics and Material Sciences (OPTIMAS).

I would also like to thank all our sponsors, which are the Deutsche Forschungsgemeinschaft (DFG), the Bundesministerium für Bildung und Forschung (BMBF), the Deutscher Akademischer Austauschdienst (DAAD), the European Community (EFRE, INTAS, INTERREG), the Carl Zeiss Foundation, the State of Rhineland Palatinate and the University of Kaiserslautern. Concerning our projects in applied research, I would like to express my gratitude to Sensitec GmbH and Singulus Technologies AG as our strong partners in R&D on spintronic sensors.

My special thanks go to Thomas Langner, Benjamin Jungfleisch, and Sibylle Müller for their help in preparing this report, Dieter Weller for preparing the impressions of our group life on the last page, and to Hubert Gerber from Photo-Repro-Druck, TU Kaiserslautern.

It is my special pleasure to greet all former group members. May this report help to stay in touch. If you are interested in our work I would be happy to hear from you. If you have any questions, comments or suggestions please contact us.

With all my best wishes for Christmas, and a Happy New Year,

Burkard Hillebrands

Kaiserslautern, November 2013

Vorwort

Liebe Kolleginnen und Kollegen und Freunde unserer Arbeitsgruppe,

wir freuen uns, Ihnen unseren Jahresbericht 2013 zu präsentieren, welcher den Zeitraum von November 2012 bis Oktober 2013 abdeckt.

Einige Höhepunkte unserer Forschung in diesem Zeitfenster: Das Forschungsfeld "Magnonengase" schreitet stark voran. Wir konnten zeigen, dass Magnon-Phonon-Quasiteilchen in einem virtuellen Energieminimum kondensieren, dessen Frequenzposition durch die Magnon-Phonon-Wechselwirkung bestimmt ist. Bemerkenswert ist, dass diese Quasiteilchen eine sehr hohe Gruppengeschwindigkeit haben und folglich sehr empfindlich auf die räumliche Konfiguration des Pumpfeldes reagieren. Im Bereich magnonischer Kristalle haben wir gezeigt, dass periodische Strukturen, die mittels Ionenimplantation hergestellt wurden, eine exzellente Funktionalität aufweisen. Darüber hinaus haben wir eine deutliche Verbesserung der Effizienz des inversen Spin-Hall-Effekts erreicht, indem wir das Design der Yttrium-Eisen-Granat/Platin-Grenzfläche und der Eisen/Platin-Bilagenschichten optimiert haben. Wir konnten numerisch die Existenz einer nichtreziproken Spinwellenmode nachweisen, die am Rand einer senkrecht magnetisierten zweidimensionalen Struktur lokalisiert ist. Ein weiteres Highlight ist, dass wir den ersten YIG-basierten isolierenden mikrostrukturierten Spinwellen-Wellenleiter mit einer Dicke von 100 nm und einer Breite von 5 µm demonstriert haben. Wir konnten zeigen, dass die Lebenszeit von Spinwellen in diesem Wellenleiter mehr als eine Größenordnung größer ist als in vergleichbaren metallischen Systemen wie z.B. Permalloy. Auf dem Gebiet der Spinkalorik gelang es uns mit Hilfe zeitaufgelöster Messungen nachzuweisen, dass der longitudinale Spin-Seebeck-Effekt durch thermische Magnonen getrieben wird und stark von der thermischen Diffusion der Magnonen im magnetischen Material abhängt. Wir konnten außerdem zeigen, dass Volumenwellen am Ende eines Wellenleiters elastisch reflektiert werden, wohingegen magnetostatische Oberflächenwellen hier eine chirale Reflexion in Kombination mit der Erzeugung stehender Breiten- und Schichtdickenmoden erleiden.

Unser Deutsch-Japanisches Kooperationsprojekt "Advanced Spintronic Materials and Transport Phenomena (ASPIMATT)" wurde positiv begutachtet. Die Förderung für einen zweiten Förderabschnitt wurde von der Deutschen Forschungsgemeinschaft (DFG) und der Japanese Science and Technology Foundation (JST) genehmigt.

Erneut gab es einige Veränderungen in unserer Gruppe. Wir freuen uns, (in alphabetischer Reihenfolge) Dmytro Bozhko, Viktor Lauer und Donata Passarello für Forschungstätigkeiten im Rahmen einer Doktorarbeit in unserer Gruppe zu begrüßen (Donata forscht im Labor von Stuart Parkin und wird von der Graduiertenschule "Materials Science in Mainz" gefördert). Wir heißen Akihiro Kirihara von der NEC Corporation willkommen, der in unserer Gruppe für ein Jahr als Gastwissenschaftler das Team im Rahmen des von der DFG geförderten Schwerpunktprogramms "Spincaloric Transport (SpinCaT)" verstärkt. Tomohiro Koyama hat uns nach einem erfolgreichen Jahr als A.v.Humboldt-Forschungsstipendiat verlassen. Er hat eine Professur an der Universität Tokyo angenommen. Einige Gruppenmitglieder haben ihre Doktorarbeit abgeschlossen und haben uns oder werden uns in naher Zukunft verlassen: Benjamin Jungfleisch, Björn Obry, Katrin Schultheiß (geborene Vogt) und Thomas Sebastian. Philipp Fuhrmann und Viktor Lauer haben Ihr Diplom und Stefan Weirich seinen Master of Education (Abschluss für das Lehramt an weiterführenden Schulen) erfolgreich abgeschlossen.

Unsere Arbeit wäre nicht ohne wertvolle Kooperationen mit Partnern aus der ganzen Welt möglich

gewesen. Es sind zu viele um sie alle an dieser Stelle aufzulisten. Insbesondere möchten wir, in alphabetischer Reihenfolge, Johan Åkerman, Toshu An, Yasuo Ando, Christian Back, Gerrit Bauer, Arne Brataas, Frederick Casper, Russell Cowburn, Sergei Demokritov, Bernard Dieny, Marco Doms, Carsten Dubs, Ursula Ebels, Hajo Elmers, Jürgen Fassbender, Gerhard Fecher, Claudia Felser, Albert Fert, Yasuhiro Fukuma, Sebastian Goennenwein, John Gregg, Hubert Grimm, Dirk Grundler, Gianluca Gubbiotti, Konstantin Gusliyenko, Jaroslav Hamrle, Uwe Hartmann, Michel Hehn, Jos Heremans, Axel Hoffmann, Koichiro Innomata, Gerhard Jakob, Xiaofeng Jin, Martin Jourdan, Gleb Kakazei, Boris Kalinikos, Alexy Karenowska, Sang-Koog Kim, Olivier Klein, Mathias Kläui, Peter Kopietz, Mikhail Kostylev, Volodymyr Kruglyak, Takahide Kubota, Bert Lägel, Ronald Lehndorff, Luis Lopez Diaz, Jörg Lösch, Wolfram Maaß, Sadamichi Maekawa, Stéphane Mangin, Gennadiy Melkov, Claudia and Tim Mewes, Shuichi Murakami, Hiroshi Naganuma, Ulrich Nowak, Jean-Pierre Nozières, Kevin O'Grady, Mikihiko Oogane, Yoshichika Otani, Stuart Parkin, Johannes Paul, Marco Rahm, Günter Reiss, Sergio Rezende, Bernhard Reuscher, Caroline Ross, Manfred Rührig, Eiji Saitoh, John R. Sandercock, Rudi Schäfer, Gerd Schönhense, Hussein Shanak, Andrei Slavin, Rolf Slatter, Bob Stamps, Yoshishige Suzuki, Koki Takanashi, Vasyl Tiberkevich, Simon Trudel, Yaroslav Tserkovnyak, Ken-ichi Uchida, Alexey Ustinov, Ben Van de Wiele, Bart van Wees, Arne Vansteenkiste, und Mingzhong Wu für eine gute Zusammenarbeit und ihren großen Beitrag zu unserer Arbeit danken.

Die Zusammenarbeit mit dem Fachbereich Physik der Technischen Universität Kaiserslautern (insbesondere mit Martin Aeschlimann, James Anglin, Sebastian Eggert, Michael Fleischhauer, Georg von Freymann, Herwig Ott, Hans-Christian Schneider, Volker Schünemann und Arthur Widera und ihren Arbeitsgruppen), Michael Kopnarski und seinem Team des Instituts für Oberflächen- und Schichtanalytik und Sandra Wolff und ihrem Team des Nano Structuring Centers waren sehr stimulierend. Wir sind sehr dankbar, Mitglied des Landesforschungszentrums für Optik und Materialwissenschaften (OPTIMAS) zu sein.

Ich möchte außerdem unseren Geldgebern danken: Der Deutschen Forschungsgemeinschaft (DFG), dem Bundesministerium für Bildung und Forschung (BMBF), dem Deutschen Akademischen Austauschdienst (DAAD), der Europäischen Gemeinschaft (EFRE, INTAS, INTERREG), der Carl Zeiss Stiftung, dem Land Rheinland-Pfalz und der Technischen Universität Kaiserslautern. In Bezug auf unsere Projekte in der angewandten Forschung möchte ich meine Dankbarkeit gegenüber der Sensitec GmbH und der Singulus Technologies AG, unseren starken Partnern in R&D von spintronischen Sensoren, zum Ausdruck bringen.

Mein besonderer Dank geht an Thomas Langner, Benjamin Jungfleisch und Sibylle Müller für ihre Hilfe beim Erstellen dieses Berichtes, Dieter Weller für die Bereitstellung der Impressionen aus unserem Gruppenalltag, und an Hubert Gerber von Photo-Repro-Druck, TU Kaiserslautern.

Es ist mir eine besondere Freude, hiermit auch allen ehemaligen Gruppenmitgliedern einen Gruß zu senden. Möge dieser Bericht uns helfen, im Kontakt zu bleiben. Wenn Sie an unserer Arbeit interessiert sind, würde ich mich freuen, von Ihnen zu hören. Wenn Sie irgendwelche Fragen, Kommentare oder Anregungen haben, kontaktieren Sie uns bitte.

Mit den besten Wünschen für ein frohes Weihnachtsfest und ein gutes Neues Jahr

Burkard Hillebrands

Kaiserslautern, im November 2013

Chapter 2: Personnel

2.1 Members of the group

Group leader:

Prof. Dr. Burkard Hillebrands

Senior scientists:

Dr. Andrii Chumak
Dr. Andrés Conca Parra
Dr. Britta Leven, Akad. Oberrätin
Dr. Evangelos Papaioannou
Dr. habil. Alexander Serga
Dr. Vitaliy Vasyuchka

Postdocs and long-term guest scientists:

Dr. Florin Ciubotaru	
Dr. Benjamin Jungfleisch	since 10/13
Akihiro Kirihara	since 04/13
Dr. Tomohiro Koyama	until 03/13
Dr. Björn Obry	since 10/13
Dr. Helmut Schultheiß	04/13 - 05/13
Dr. Katrin Schultheiß	since 09/13
Dr. Thomas Sebastian	since 10/13

Ph.D. students:

Dipl.-Phys. Milan Agrawal	
Dipl.-Phys. Dmytro Bozhko	since 09/13
Dipl.-Phys. Thomas Brächer	
Dipl.-Phys. Peter Clausen	
Dipl.-Phys. Benjamin Jungfleisch	until 10/13
Dipl.-Phys. Thomas Langner	
Dipl.-Phys. Viktor Lauer	since 08/13
Dipl.-Phys. Thomas Meyer	
Dipl.-Phys. Roland Neb	
Dipl.-Phys. Björn Obry	until 10/13
Dipl.-Phys. Donata Passarello (IBM Research lab)	since 10/12
Dipl.-Phys. Philipp Pirro	
Dipl.-Phys. Ana Ruiz Calaforra	
Dipl.-Phys. Thomas Sebastian	until 10/13
Dipl.-Phys. Katrin Schultheiß (née Vogt)	until 09/13

Diploma and Master Students:

Philipp Fuhrmann	until 09/13
Viktor Lauer	until 12/12
Stefan Weirich	12/12 - 03/13

Student Assistants:

Tanita Eichert	
Tobias Fischer	
Moritz Geilen	since 05/13
Jochen Greser	
Björn Heinz	since 06/13
Frank Heussner	
Philipp Jaeger	since 08/13
Stefan Klingler	
Susanne Schander	until 06/13
Matthias Schweizer	since 06/13
Linda Thesing	until 12/12

Engineers and Technicians

Dipl.-Ing. (FH) Dieter Weller

Administration:

Sibylle Müller
Dr. Isabel Sattler

2.2 Visiting scientists, postdoctoral fellows and exchange students

(sorted by date of first arrival in our group)

Manuel Langer, Helmholtz-Zentrum Dresden-Rossendorf, Germany — 21.01. - 23.01.2013

Manuel Langer is a PhD Student from the group of Dr. Kilian Lenz. His research focus lies on nanomagnetism and tailoring of the properties of magnetic materials. In his diploma thesis, he investigated antiferromagnetically coupled CoFe/Ru/CoFe trilayers, patterned by focused ion beam irradiation. During his visit, we discussed results and possible applications of ion-beam patterning for several magnetic systems, including patterned storage media and spin wave guides.

Dmytro Bozhko, National Taras Shevchenko University of Kyiv, Ukraine — 01.03. - 26.04.2013

Dmytro Bozhko was a graduate student working in the magnetism group of Prof. G. A. Melkov at the National University of Kyiv. After his visits in 2011 and 2012 he visited us this year for 2 months to investigate the temporal dynamics of parametrically controlled magnon gases and condensates. Dmytro significantly improved the adjustment procedure of the wavevector resolved BLS setup and obtained new interesting results on the density distribution of dipolar-exchange magnons in the low-energy spectral area. In September this year he has joined our group as a PhD student.

Dr. Andrey Nikitin, Electrotechnical University St. Petersburg, Russia — 25.03. - 05.05.2013

Dr. Andrey Nikitin is a member of the group of Prof. B. Kalinikos with whom we have a long and productive cooperation record. This time Dr. Nikitin experimentally investigated magnetically controlled magnonic crystals. The stay of Dr. Nikitin was supported in the framework of our German-Russian project "Coherent nonlinear spin-wave states in ferromagnetic films and ferromagnetic/ferroelectronic layered structures" (DFG RUS 113/644/0).

Akihiro Kirihara, NEC Corporation, Tsukuba, Japan — 05.04.2013 -

Akihiro Kirihara is a visiting researcher, belonging to Smart Energy Research Laboratories of NEC Corporation. In NEC, he works on the development of thermoelectric devices using the spin-Seebeck effect (SSE). He now stays in our group, and joins experimental projects related to the SSE and spin pumping. He is going to stay here till the end of March 2014.

Prof. Olle Eriksson, Uppsala Universitet, Sweden — 26.06. - 28.06.2013

Prof. Olle Eriksson together with 5 members of his group (Jonathan Chico, Manuel Pereiro López, Raghuveer Chimata, Corina Etz, Angela Burlamaki) visited us for a one day mini-workshop. During the workshop both groups presented their work, and exchange ideas how to meet spin-dynamics simulations with our magnon research. The foundations for future collaboration between our group and Prof. Olle Eriksson's group have been established.

Prof. Gennadii A. Melkov, National Taras Shevchenko University of Kyiv, Ukraine — 01.07. - 26.08.2013

This year the regular visit of Prof. Melkov to our group was supported by the Deutsche Forschungsgemeinschaft in the frame of the SFB/Transregio 49 "Condensed Matter Systems with Variable Many-Body Interactions". During his stay Prof. Melkov was mainly working on different aspects of phonon-magnon interactions in parametrically and thermally driven magnetic insulators. The recent results of our joint work have been presented on the Magnonics Conference in Varberg, Sweden, the JEMS in Rhodes, Greece, and the EASTMAG Conference in Vladivostok, Russia.

Dr. Alexy Karenowska, University of Oxford, United Kingdom — 15.08. - 16.08.2013

Alexy Karenowska is Junior Research Fellow in Clarendon Laboratory of University of Oxford and our long-term collaborator. During her visit in Kaiserslautern we have spent a very useful day discussing the perspectives, trends and problems of the field of magnonic crystals and magnon spintronics in general. The cross-sections of the research interest which might result in future joint projects have been defined.

2.3 Guest seminars

Manuel Langer 22.01.2013	Helmholtz-Zentrum Dresden-Rossendorf, Germany *Fabrication and characterization of magnetic meta-structures* Special seminar
Dr. Andrey Nikitin 22.04.2013	Electrotechnical University St. Petersburg, Russia *Ferrite-ferroelectric structures. Physics and applications* Special group seminar
Johannes Paul 24.06.2013	Sensitec GmbH, Mainz, Germany *MR-Sensorics at Sensitec* Special group seminar
Prof. Koki Takanashi 08.07.2013	Tohoku University, Sendai, Japan *Advanced spintronic materials for generation and control of spin current* Special seminar
Prof. Shuichi Murakami 16.07.2013	Department of Applied Physics, University of Tokyo, Hongo, Bunkyo-ku, Tokyo, Japan *Topological phenomena in magnetostatic spin waves* Special seminar
Dr. Tom Silva 01.08.2013	NIST, Boulder, Colorado, USA *New directions in spin current research at NIST, Boulder* OPTIMAS seminar
Prof. Takuya Satoh 25.10.2013	Institute of Industrial Science, University of Tokyo, Japan *Generation and directional control of spin wave by spatially-shaped light pulses* Special seminar

2.4 Visits of group members at other laboratories

Katrin Vogt	Materials Science Division, Argonne National Laboratory, Argonne, Illinois, USA 26.10.2012 - 05.04.2013 Host: Dr. Axel Hoffmann
Evangelos Papaioannou	Department of Physics, Uppsala Universitet, Sweden 02.04.2013 - 04.04.2013 Host: Prof. Björgvin Hjörvarsson
Stefan Klingler	Center for Materials for Information Technology (MINT), University of Alabama, Tuscaloosa, USA 03.06. - 02.08.2013 Host: Prof. Dr. Tim Mewes
Tobias Fischer	Department of Chemistry, University of Galgary, Alberta, Canada 03.09.2013 - Host: Dr. Simon Trudel

2.5 Group member photo gallery

Milan Agrawal
Ph.D. student

Dmytro Bozhko
Ph.D. student

Thomas Brächer
Ph.D. student

Dr. Andrii Chumak
Senior scientist

Dr. Florin Ciubotaru
Postdoc

Peter Clausen
Ph.D. student

Dr. Andrés Conca Parra
Senior scientist

Tanita Eichert
Student assistant

Tobias Fischer
Student assistant

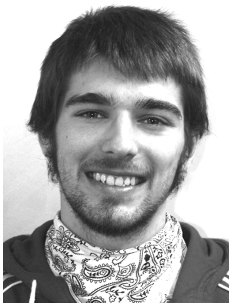

Philipp Fuhrmann
Diploma student

Moritz Geilen
Student assistant

Jochen Greser
Student assistant

Björn Heinz
Student assistant

Frank Heussner
Student assistant

Prof. Dr. Burkard Hillebrands
Group leader

Philipp Jaeger
Student assistant

Dr. Benjamin Jungfleisch
Ph.D. student

Akihiro Kirihara
Guest scientist

Stefan Klingler
Student assistant

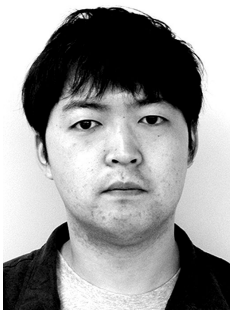

Dr. Tomohiro Koyama
Postdoc

Thomas Langner
Ph.D. student

Viktor Lauer
Ph.D. student

Dr. Britta Leven
Senior scientist

Thomas Meyer
Ph.D. student

Sibylle Müller
Secretary

Roland Neb
Ph.D. student

Dr. Björn Obry
Ph.D. student

Dr. Evangelos Papaioannou
Senior scientist

Donata Passarello
Ph.D. student

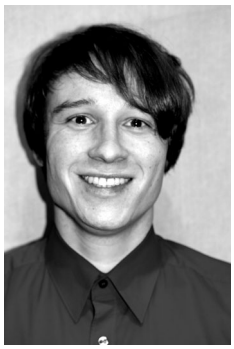

Philipp Pirro
Ph.D. student

Ana Ruiz Calaforra
Ph.D. student

Dr. Isabel Sattler
Administration

Susanne Schander
Student assistant

Dr. Helmut Schultheiß
Postdoc

Dr. Katrin Schultheiß (née Vogt)
Ph.D. student

Matthias Schweizer
Student assistant

Dr. Thomas Sebastian
Ph.D. student

Dr. Alexander Serga
Senior scientist

Linda Thesing
Student assistant

Dr. Vitaliy Vasyuchka
Senior scientist

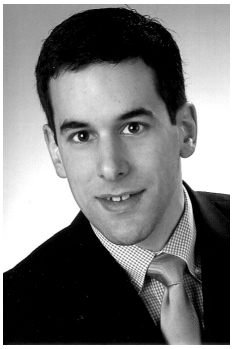

Stefan Weirich
Master student

Dieter Weller
Mechanical engineer

Chapter 3: Methods

3.1 Brillouin light scattering spectroscopy (BLS)

Brillouin light scattering (BLS) spectroscopy is one of the key techniques in our laboratory to investigate the dynamic properties of magnetic materials and devices. It is based on the interaction of photons with the fundamental excitations of a solid such as magnons, the quanta of magnetic excitations. The interaction can be understood as an inelastic scattering process of the incident photons with magnons, taking into account energy and momentum conservation as indicated in Fig. 1.

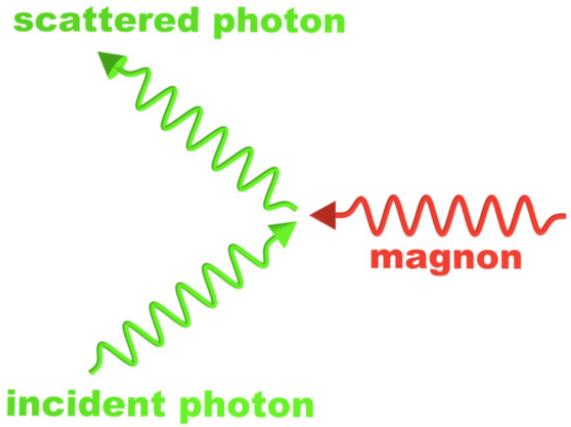

Fig. 1: Scheme of inelastic scattering of an incident photon by a magnon.

The detection of the inelastically scattered photons, i.e. the separation from the elastically scattered photons and the determination of the transferred energy, requires an interferometry technique with extremely high contrast and sensitivity. In our laboratory we implemented the (3+3) Tandem-Fabry-Perot-Interferometer, designed by John R. Sandercock and schematically shown in Fig. 2. It consists of two Fabry-Perot interferometers (FPI), each one passed three times by the inelastically scattered light. This approach results in a contrast better than 10^{10} for the separation of the elastically and inelastically scattered photons in a frequency range from 500 MHz up to 1 THz.

In the last decade we made significant progress in the improvement of BLS spectroscopy. The spatial resolution was pushed to the fundamental limit of classical optics by constructing a BLS-microscope (Fig. 3) with sophisticated active stabilization methods. Spin-wave transport phenom-

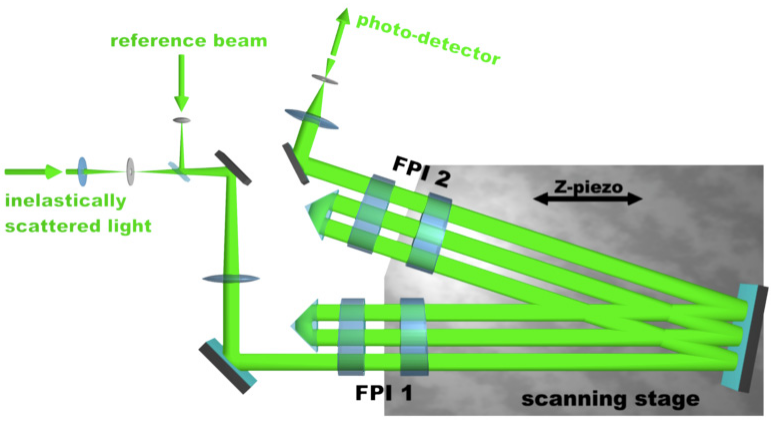

Fig. 2: Scheme of a (3+3) tandem Fabry-Perot interferometer, designed and build by John R. Sandercock (JRS Scientific Instruments, Zürich)

ena can be investigated by time, phase- and wave-vector resolution. The following list gives an overview of the different BLS setups available in our group:

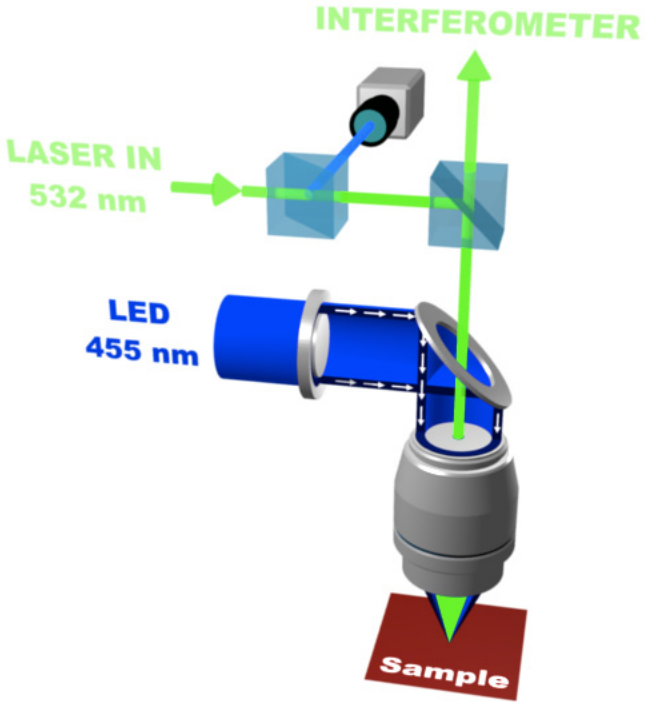

Fig. 3: Schematic setup of a BLS-microscope. The LED light is used to monitor the position of the laser focus on the sample by a CCD camera and to apply active position control to the sample stage.

BLS1: High-field electromagnet (1.2 T), standard BLS spectroscopy equipment. Time resolution, phase resolution, space resolution (50 µm), wave-vector resolution.

BLS2: High-field electromagnet (1.2 T), standard BLS spectroscopy equipment. Microscope stage with 200 nm spatial resolution and build-in time and phase resolution.

BLS3: High-field electromagnet (1.2 T), standard BLS spectroscopy equipment. Microscope stage with 200 nm spatial resolution and build-in time and phase resolution.

BLS4: Electromagnet (0.1 T), standard BLS spectroscopy equipment. Microscope stage with 200 nm spatial resolution and build-in time and phase resolution.

3.2 Microwave techniques

Brillouin Light Scattering (BLS) spectroscopy described in the previous section is indeed a powerful tool for the detection of spin waves and measurement of their characteristics. Nevertheless, it allows no spin-wave excitation. Thus, in many of our experiments BLS spectroscopy is combined with microwave techniques which ensures high-efficient generation of spin waves in magnetic structures. Spin waves are emitted by nano- and micro-sized microstip antennas placed on the surface of magnetic thin films and is driven by a microwave signal in the GHz frequency range [1]. Microwave sources in our laboratories generate the signals up to 67 GHz providing access to spin-waves in a very wide range of frequencies and wavenumbers. Furthermore, large powers (up to 100 W) provided by microwave amplifiers allow the study of strongly nonlinear spin-wave dynamics as well as quantum effects in parametrically-driven magnon gases. The microwave technique allows the excitation of both, continuous spin waves as well as short spin-wave packets. Among the

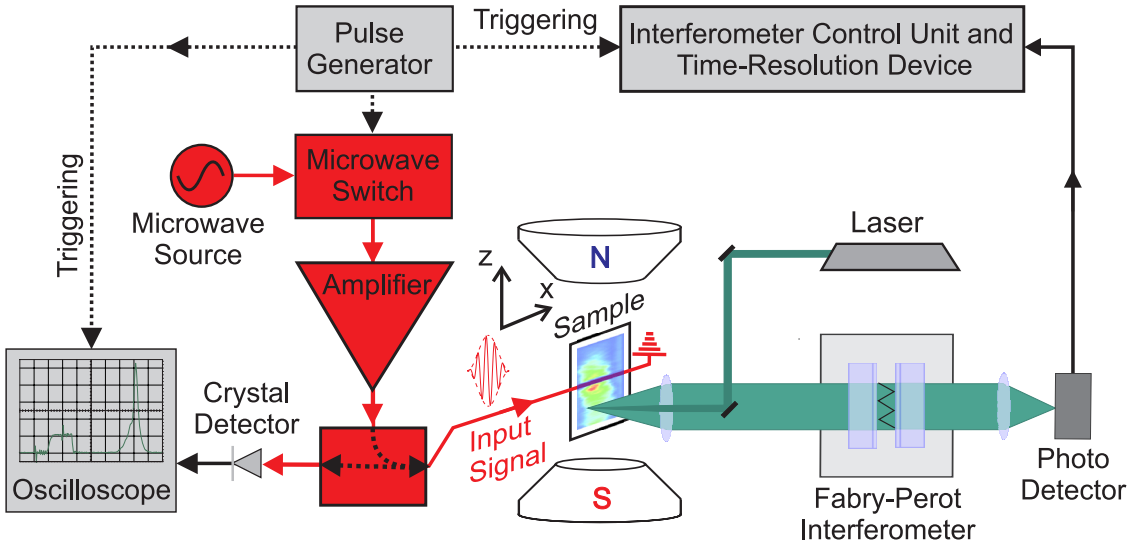

Fig. 1: Scheme of the microwave-assisted time- and space-resolved BLS setup

others advantages, the pulsed technique allows the realization of time resolved (resolution down to 250 ps) BLS spectroscopy [2] shown in Fig. 1. The continuous microwave excitation, by-turn, allows realization of phase-resolved BLS spectroscopy [3, 4].

Besides the excitation of spin waves, the microwave technique is intensively used for high-sensitive (10^{-13} W) detection. Using the same antennas the magnetization precession is converted into microwave currents. These currents are amplified by low-noise amplifiers and analyzed using wide-band oscilloscopes, vector network analyzers or a spectrum analyzer [1]. A vector network analyzer is also used for the ferromagnetic resonance (FMR) measurements allowing determination of such characteristics of the magnetic thin films as magnetization saturation, exchange constant, and damping. Recently we amended these techniques by detection of spin waves using the inverse spin Hall effect [5].

References

[1] A.A. Serga, A.V. Chumak, B. Hillebrands, *YIG magnonics*, J. Phys. D **43**, 264002 (2010).

[2] O. Büttner, M. Bauer, S.O. Demokritov, B. Hillebrands, Yu.S. Kivshar, V. Grimalsky, Yu. Rapoport, A.N. Slavin, *Linear and nonlinear diffraction of dipolar spin waves in yttrium iron garnet films observed by space- and time-resolved Brillouin light scattering*, Phys. Rev. B **61**, 11576 (2000).

[3] A.A. Serga, T. Schneider, B. Hillebrands, S.O. Demokritov, M.P. Kostylev, *Phase-sensitive Brillouin light scattering spectroscopy from spin-wave packets*, Appl. Phys. Lett. **89**, 063506 (2006).

[4] K. Vogt, H. Schultheiss , S.J. Hermsdoerfer, P. Pirro , A.A. Serga, B. Hillebrands, *All-optical detection of phase fronts of propagating spin waves in a $Ni_{81}Fe_{19}$ microstripe*, Appl. Phys. Lett. **95**, 182508 (2009).

[5] A.V. Chumak, A.A. Serga, M.B. Jungeisch, R. Neb, D.A. Bozhko, V.S. Tiberkevich, B. Hillebrands, *Direct detection of magnon spin transport by the inverse spin Hall effect*, Appl. Phys. Lett. **100**, 082405 (2012).

3.3 Magneto-optic Kerr effect magnetometry and microscopy (MOKE)

The magneto-optical Kerr effect (MOKE) is a well established technique to study magnetization properties. The effect is based on the fact, that the plane of polarization of light is rotated when the light is reflected from a magnetic material [1]. The physical origin of MOKE is the magnetic

circular dichroism effect: exchange and spin-orbit coupling in a magnetic material lead to different absorption spectra for left- and right-circularly polarized light. Measuring the change of the polarization of the reflected beam (often referred to as Kerr angle Θ_{Kerr}) gives access to the magnetization state of the sample.

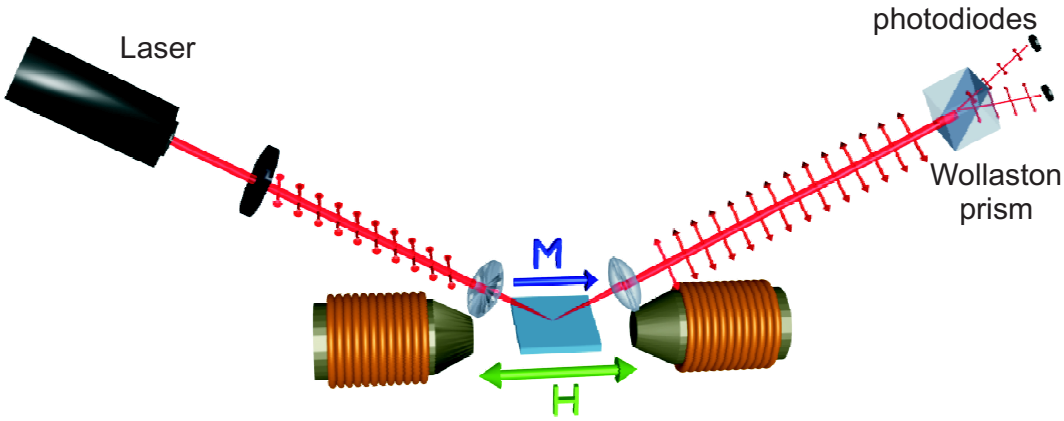

Fig. 1: Schematic setup of a longitudinal Kerr magnetometer.

With MOKE it is possible to study quasi-static magnetization reversal properties and magnetic anisotropies. When using a pulsed laser system it is also possible to study the time dependence of the magnetization under the influence of, e.g., a pulsed magnetic field or a microwave field. Since it is an optical technique it is non invasive, and the spatial resolution is only limited by the optical resolution. Thus, we are able to study the static and dynamic properties of magnetic thin films and magnetic structures with lateral dimension down to 1 µm.

Our group uses four different MOKE setups, all of them using the same principle. The light of a laser source is s-polarized through a thin-film polarizer. The beam is focused onto the sample. The polarization of the reflected light is analyzed by a detector unit that was developed and is built in our laboratory. A Wollaston prism divides the beam into two orthogonally polarized beams, which are monitored by a pair of photodiodes. The detector works as an opto-electrical bridge circuit to increase the signal-to-noise ratio. The obtained normalized differential signal $(I_1 - I_2)/(I_1 + I_2)$ is directly proportional to the Kerr angle Θ_{Kerr}.

Four experimental setups are available to investigate different scientific aspects:

Longitudinal Kerr magnetometer: Longitudinal MOKE geometry to probe quasi-static properties of magnetic thin films. Optical resolution $\sim 100\,\mu\mathrm{m}$, magnetic field up to 2 T, automated sample positioning and rotation.

Microfocus Kerr microscope with rotation unit: Longitudinal MOKE geometry to probe quasi-static properties of micro-structured magnetic elements. Optical resolution $< 1\,\mu\mathrm{m}$, magnetic field up to 0.6 T, automated sample positioning, rotation and stabilization.

Dual MOKE magnetometer: Two combined MOKE magnetometers working in parallel, one in longitudinal and one in polar geometry to study the quadratic MOKE effects on magnetic thin films. Optical resolution $\sim 100\,\mu\mathrm{m}$, two orthogonal pairs of magnet coils to provide any in-plane field direction up to 0.25 T, automated sample positioning and rotation.

Time resolved scanning Kerr microscope: Longitudinal or polar MOKE geometry to study dynamic magnetization reversal properties of micro-structured elements. Optical resolution $<$ 500 nm, time resolution $\sim 60\,\mathrm{ps}$, magnetic field up to 150 mT, automated sample positioning and stabilization.

References

[1] J. Kerr, *On rotation of the plane of polarization by reflection from the pole of a magnet*, Phil. Mag. **4**(5), 321 (1877).

3.4 Molecular beam epitaxy (MBE)

The Molecular Beam Epitaxy (MBE) technique involves highly controlled evaporation of materials in an ultra-high vacuum chamber (pressure in the low 10^{-11} mbar region). This deposition from the vapor phase can lead to single crystal film growth. For this reason MBE possesses a dominant role in the world of nanotechnology regarding fabrication of materials for high performance applications.

Our group operates two MBE clusters. One of them is displayed in Fig. 1. Both systems are equipped with tools for cleaning the substrates, for controlling the evaporation from the sources and the film deposition, for *in-situ* structural and chemical characterization, as well as sample storage.

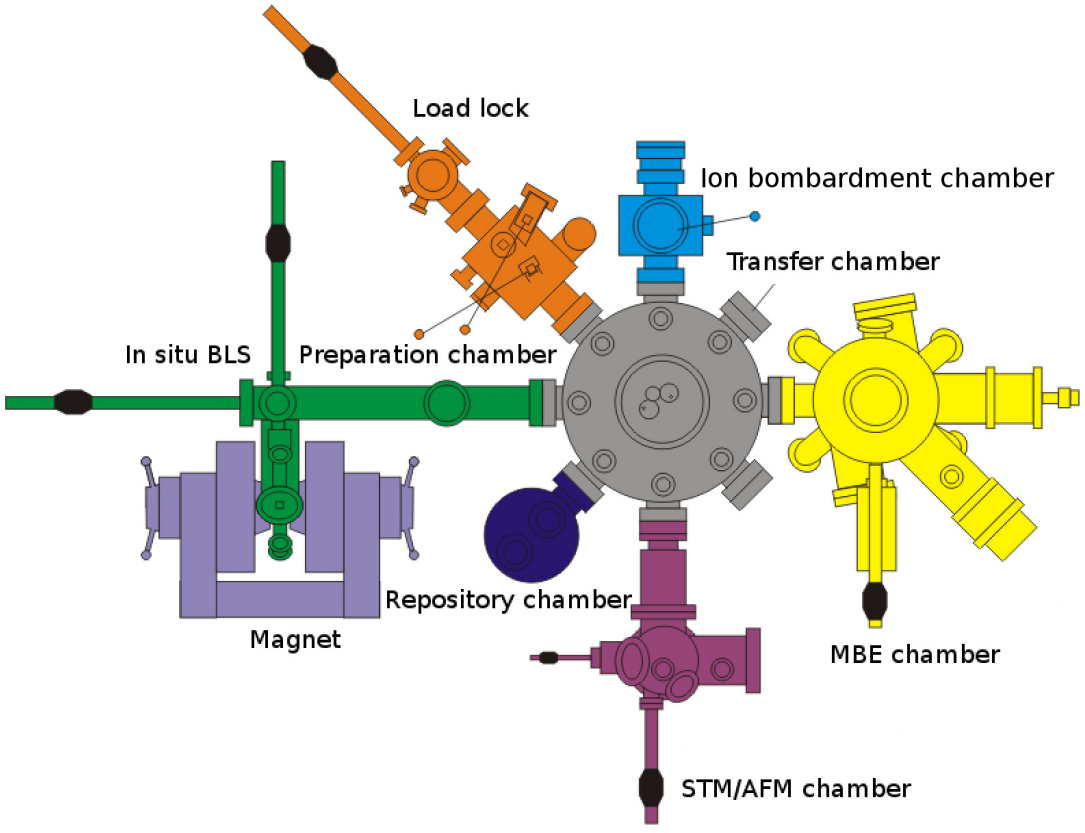

Fig. 1: Schematic diagram of the MBE growth cluster.

In more details, the heart of the cluster shown in Fig. 1 constitutes an ultra-high vacuum (UHV) Molecular Beam Epitaxy (MBE) growth chamber. It contains two Knudsen cells, and one electron gun with 4 crucibles that are used to heat and evaporate the materials. The growth procedure is controlled *in-situ* by a quartz crystal. One of the great advantages of our MBE system is the capability to control the *in-situ* growth by means of Reflection of High-Energy Electron Diffraction

(RHEED) and of Low-Energy Electron Diffraction (LEED) and Auger analytics. The characteristics of the RHEED technique is not to interfere with the deposition. This renders it as a unique tool for real-time structural characterization of the sample during the growth process.

In addition to the aforementioned techniques and linked to the MBE, an scanning tunneling microscope (STM) set-up is used for *in-situ* atomic probing. This increases further the capabilities of our MBE chamber. In Fig. 2 *in-situ* STM images for 4 Fe films grown at different substrate temperatures are presented. The Fe surfaces show a clear evolution with the growth temperature. STM is a unique tool for surface investigation of the evaporated samples. The cluster includes furthermore a load chamber for inserting samples in vacuum and preparation chamber. The latter is used for cleaning the samples since there is the possibility to heat up to 800 °C the samples. Furthermore, there is an option for optical coatings. The ionization chamber is equipped with a fine-focus noble gas keV ion source. A transfer chamber connects all the parts of the growth cluster while a repository chamber is also available.

The MBE chamber of Fig. 1 has another unique feature: that of *in-situ* magnetic characterization with Brillouin light scattering (BLS) spectroscopy and Kerr effect magnetometry. The applied magnetic field can reach 1.2 T. There is an option for implementation of a cryostat.

The MBE evaporation technique offers unique advantages for the fabrication of patterned samples. The good control of the film growth and the directionality of the beam renders MBE suitable to grow materials on patterned masks. Patterned samples of extreme quality can be produced either with pre- or post treatment techniques.

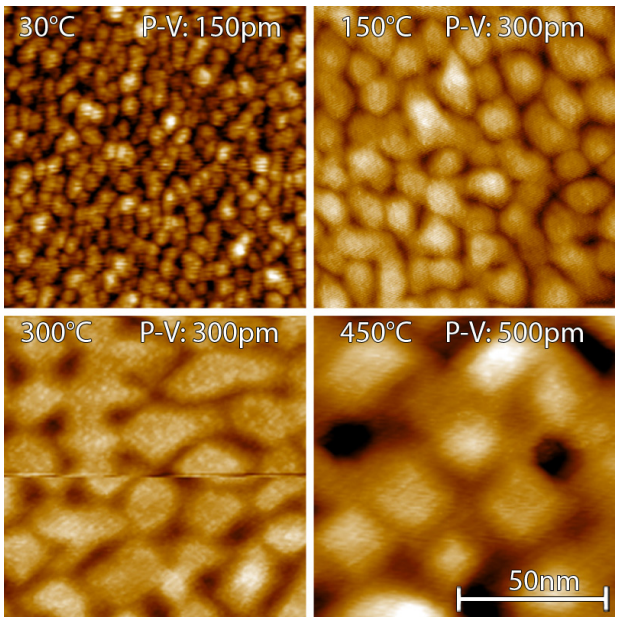

Fig. 2: Scanning tunneling microscopy surface images of four Fe films grown at different substrate temperatures. Samples were grown at RT, 150 °C, 300 °C and 450 °C. STM offers unique advantages in controlling the quality of the produced samples.

2013 was a very productive year for our growth chambers. Several samples like Fe/Pt, Fe/Cr, YIG/Py, YIG/Pt, Py/Au bilayers and multilayers and Py, Fe, Au films were produced. Furthermore, upgrades in the RHEED, STM systems and heating units were performed.

Chapter 4: Reports on Experimental Results

A. Magnon Gases and Condensates

In ferromagnetic materials atoms having unpaired electrons act as individual magnets. Their magnetism is mostly caused by the magnetic moments of the uncompensated electron spins. Since these atomic magnets tend to be oriented in the same direction due to quantum-mechanical exchange interaction, a macroscopic magnetic moment appears. As the atoms strongly interact, a reversal of a single atomic magnetic moment is not spatially localized but spreads through the solid as a wave of discrete magnetic momentum transfer. This wave is known as a spin wave, and in frame of the second quantization it is associated with a quasi-particle called magnon. Weakly interacting magnons can be considered as a gas of magnetic bosonic quasi-particles and, therefore, this is called a magnon gas.

Recently magnon gases have been recognized as an excellent model environment for the experimental investigation of collective classical and quantum macroscopic properties of bosonic systems. Its potential is due to the wide controllability of the magnon density as well as of the spectral properties influencing the magnon-magnon interaction. For example, the dispersion branch of a magnon gas can be frequency shifted or even drastically modified by change in the strength or orientation of a bias magnetic field. The magnon population density can be effectively controlled by means of electromagnetic parametric pumping (see Gurevich and Melkov, Magnetization Oscillation and Waves, CRC, Cleveland, 1996). In the simplest case one photon of the pumping electromagnetic field excites two magnons with half the energy/frequency that propagate in opposite directions. Such a mechanism creates a huge quantity of phase correlated magnons, which are called a condensate of photon-coupled magnon pairs. The behavior of parametrically created magnon condensates, of gaseous magnon phases, and of Bose-Einstein condensates (BEC), which can be formed at the lowest energy state of a magnon gas, constitutes a hot research topic. The main goal of our work is to study the phase transition processes resulting in the formation of quantum macroscopic states of a magnon gas and to understand the role of magnon-magnon and magnon-phonon interactions in the properties of these correlated states of matter in comparison with the dynamics of ultra-cold quantum gases and quantum spin systems. We investigate the dynamics of the magnon system in a low-damping magnetic insulator (yttrium-iron-garnet, YIG) using wavevector- and time-resolved Brillouin light scattering spectroscopy with special attention on the pump-free evolution of the magnetic medium after pumping.

We have already shown that the dynamics of the free-evolving magnon BEC can be properly understood in the frame of a model of a spectrally non-uniform magnon temperature. As a specific outcome a spectrally localized overheating of the condensed magnon gas up to 30'000 K was found. This year we present the experimental results which allow us to conclude that the chemical potential of a magnon gas is a spectrally dependent quantity as well.

In Report 4.1 "Bose-Einstein condensation of exchange magnons" the thermalization of a condensate of photon-coupled magnon pairs is studied in phase space and a dominant role of short-wavelength exchange magnons to the population of the lowest energy states of the magnon spectrum is experimentally demonstrated.

In Report 4.2 "Condensation of mixed magnon-phonon states below the bottom of the magnon spectrum" we show the condensation of magnon-phonon quasi-particles at a virtual energy minimum whose frequency position is determined by weakening of magnon-phonon interaction. It is

remarkable that these quasi-particles have an extremely high group velocity, and, thus, are very sensitive to the spatial configuration of the pumping field.

In Report 4.3 “Localized parametric generation of spin waves in a longitudinally $Ni_{81}Fe_{19}$ waveguide” and in Report 4.4 “Localized parametric spin-wave generation in the Damon-Eshbach geometry by geometric variation of a microstrip antenna” we study the technique and physics of the parametric pumping of thin-film magnetic structures with a sparse magnon spectrum.

A. Magnonengase und -kondensate

In ferromagnetischen Materialien treten Atome, die ungepaarte Elektronen haben, als einzelne Magnete auf. Ihr Magnetismus wird in der Regel durch die magnetischen Momente des nicht kompensierten Elektronenspins verursacht. Diese atomaren Magnete richten sich häufig aufgrund der quantenmechanischen Austauschwechselwirkung in einem Ferromagneten parallel zueinander aus. Daher beobachtet man ein makroskopisches magnetisches Moment. Da die Atome stark miteinander wechselwirken, wird das Umklappen eines einzelnen atomaren magnetischen Moments nicht räumlich lokalisiert sein, sondern breitet sich als Welle mit einem diskreten magnetischen Moment über den gesamten Festkörper aus. Diese Welle wird als Spinwelle bezeichnet und ist im Rahmen der zweiten Quantisierung mit einem Quasiteilchen, dem so genannten Magnon, verbunden. Schwach miteinander wechselwirkende Magnonen können als Gas von magnetischen bosonischen Quasiteilchen angesehen werden. Daher werden sie auch als Magnonengas bezeichnet.

Magnonengase sind unlängst als hervorragendes Modellsystem erkannt worden und dienen zur Untersuchung von korrelierten bosonischen Systemen mit sowohl klassischen Eigenschaften als auch mit makroskopischen Quanteneigenschaften. Ihr Potenzial liegt dabei in der guten Kontrollierbarkeit der Magnonendichte und den Eigenschaften des Spektrums, welche die Magnon-Magnon-Wechselwirkung beeinflusst. Zum Beispiel kann durch die Änderung der Richtung oder der Stärke eines externen Magnetfelds das Spektrum des Magnonengases leicht in der Frequenz verschoben oder auch stark verändert werden. Der wirkungsvollste Mechanismus, die Dichte eines Magnonengases zu erhöhen, ist parametrisches Pumpen mittels Mikrowellen (s. Gurevich and Melkov, Magnetization Oscillation and Waves, CRC, Cleveland, 1996). Im einfachsten Fall erzeugt ein Photon des elektromagnetischen Pumpfeldes zwei Magnonen mit je der Hälfte der Energie des Photons, die sich in entgegengesetzte Richtungen ausbreiten. Dieser Mechanismus erzeugt eine große Anzahl von phasenkorrelierten Magnonen, ein Kondensat von photonengekoppelten Magnonenpaaren. Die Verhaltensweisen parametrisch erzeugter Magnonenkondensate, gasförmiger Magnonenzustände, und von magnonischen Bose-Einstein-Kondensaten (BEC), welche im Zustand niedrigster Energie des Magnonengases erzeugt werden können, bilden ein heisses Forschungsthema. Das Hauptziel der aktuellen Forschung ist die Untersuchung der Phasenübergänge, die zu der Bildung von Zuständen mit makroskopischen Quanteneigenschaften in Magnonengasen führen, und das Verständnis der Funktion der Viel-Magnonen-Wechselwirkungen in diesen korrelierten Zuständen der Materie im Vergleich mit der Dynamik von ultrakalten Quantengasen und Quanten-Spinsystemen. Wir untersuchen die Dynamik des Magnonensystems in einem Isolator mit niedriger Dämpfung (Yttrium-Eisen-Granat, YIG) mit Hilfe von wellenvektor- und zeitaufgelöster Brillouin- Lichtstreuspektroskopie mit besonderem Augenmerk auf die pumpfreie Entwicklung des magnetischen Mediums nach dem Pumpprozess.

Wir haben bereits gezeigt, dass die Dynamik eines sich frei entwickelnden Magnon-BECs sehr gut anhand eines Modells einer spektral nichteinheitlichen Magnontemperatur verstanden werden

kann. Ein besonders zu erwähnendes Ergebnis ist ein spektral lokalisiertes Überhitzen des kondensierten Magnonengases bis zu einer Temperatur von 30.000 K. Dieses Jahr präsentieren wir experimentelle Ergebnisse die es uns erlauben anzunehmen, dass das chemische Potential eines Magnonengases auch eine spektral abhängige Größe ist.

In Bericht 4.1 “Bose-Einstein condensation of exchange magnons” wird die Thermalisierung des Kondensates von photonengekoppelten Magnonenpaaren im Phasenraum untersucht und es wird eine dominierende Rolle der kurzwelligen Austauschmagnonen auf die Bevölkerung des niedrigsten Energiezustandes des Magnonenspektrums experimentell nachgewiesen.

In Bericht 4.2 “Condensation of mixed magnon-phonon states below the bottom of the magnon spectrum” zeigen wir die Kondensation von Magnon-Phonon-Quasiteilchen an einem virtuellen Energieminimum dessen Frequenzposition anhand der Abschwächung der Magnon-Phonon Wechselwirkung bestimmt wird. Es ist anzumerken, dass diese Quasiteilchen eine extrem hohe Gruppengeschwindigkeit besitzen und deshalb sehr empfindlich auf die räumliche Beschaffenheit des Pumpfeldes reagieren.

In den Berichten 4.3 “Localized parametric generation of spin waves in a longitudinally $Ni_{81}Fe_{19}$ waveguide” und 4.4 “Localized parametric spin-wave generation in the Damon-Eshbach geometry by geometric variation of a microstrip antenna” wird die Technik und die Physik des parametrischen Pumpens in magnetischen dünnen Filmstrukturen mit einem schmalen Magnonenspektrum untersucht.

4.1 Bose-Einstein condensation of exchange magnons

P. Clausen, D. A. Bozhko, V. I. Vasyuchka, A. A. Serga, and B. Hillebrands

In collaboration with G. A. Melkov, Faculty of Radiophysics, Taras Shevchenko National University of Kyiv, 01601 Kyiv, Ukraine.

The technique of parallel parametric pumping [1, 2] is widely used to inject magnons in ferri- and ferromagnetic films [3–5]. However, the physics of the evolution of a parametrically pumped magnon gas is still under investigation. In this Report, we provide experimental insight into this evolution by four-magnon scattering of a non-equilibrium magnon gas in time and wavevector space.

The measurements were performed using a combined microwave and Brillouin light scattering (BLS) setup. The magnon system is parametrically pumped by the microwave part and the response of the magnon system is analyzed by wavevector and time-resolved BLS spectroscopy. The experiments were carried out using an yttrium iron garnet (YIG) film of 6.7 µm thickness and lateral dimensions of 2 mm × 10 mm placed on top of a microstrip resonator as illustrated in Fig. 1. The 50 µm wide resonator, deposited on an aluminum nitride substrate, was used as a pumping exciter. A bias magnetic field of $\mu_0 H_0 = 165\,\mathrm{mT}$ was applied in the plane and along the long axis of the YIG film and perpendicular to the microstrip resonator. The bias magnetic field was chosen in such a way that the parametrically injected magnons pairs are located slightly above the ferromagnetic resonance (FMR) frequency. In this case, the direct scattering of the parametric magnons to the bottom of spin-wave spectrum is prohibited by conservation laws. Thus, the conditions for multistage magnon scattering, and consequently for the effective thermalization of the magnon gas are ensured.

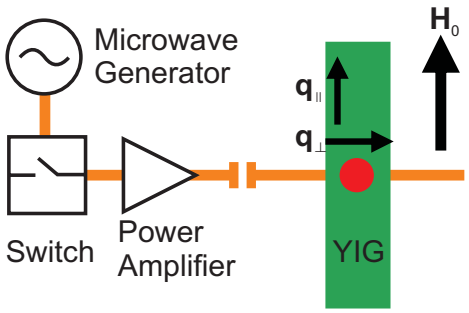

Fig. 1: Schematic illustration of the experimental setup. The 6.7 µm thick YIG film is 10 mm long and 2 mm wide. A microstrip resonator is fabricated below the YIG film and tuned to the pumping frequency of $\omega_p/2\pi = 13.562\,\mathrm{GHz}$. The microstrip resonator is driven by a microwave circuit consisting of a microwave source, switch and amplifier. The red dot illustrates the focus position of the BLS laser and hence the area of interest. The directions of the applied external bias magnetic field $\mathbf{H}_0$ and the wave vectors $\mathbf{q}_\parallel$ and $\mathbf{q}_\perp$ of the corresponding spin-wave modes are indicated by arrows.

The microwave pumping pulse with the frequency of $\omega_p/2\pi = 13.562\,\mathrm{GHz}$ and duration of $t_p = 45\,\mathrm{ns}$ was generated every $t_{rep} = 5\,\mu\mathrm{s}$ and applied to the microstrip resonator. Therefore, sample-heating effects were significantly suppressed. For the same reason, a metalized aluminum nitride substrate was chosen due to its high thermal conductivity. The pumping power was controlled by an amplifier and attenuator up to the maximum value of $P_p = 40\,\mathrm{W}$. For further insight into the wavevector resolved BLS setup, please refer to Report 4.2 and [6].

Figure 2a shows the color-coded BLS intensity map in the frequency range from 6.5 GHz to 7.5 GHz in time and wavevector space for $\mathbf{q} \perp \mathbf{H}$. These correspond to the parametrically injected magnons at $\omega_p/2$. The two dashed lines indicate the 45 ns long microwave pumping pulse. It is clearly visible that parametrically injected magnons appear with a short delay of about 10 ns

relative to the front of the pumping pulse at wavenumbers of about $8 \cdot 10^4\,\mathrm{rad/cm}$. This delay corresponds to the time, which is necessary in order to increase the density of the parametrically generated magnons to a detectable level. Surprisingly, the BLS signal from the parametric magnons vanishes while the pumping is still on.

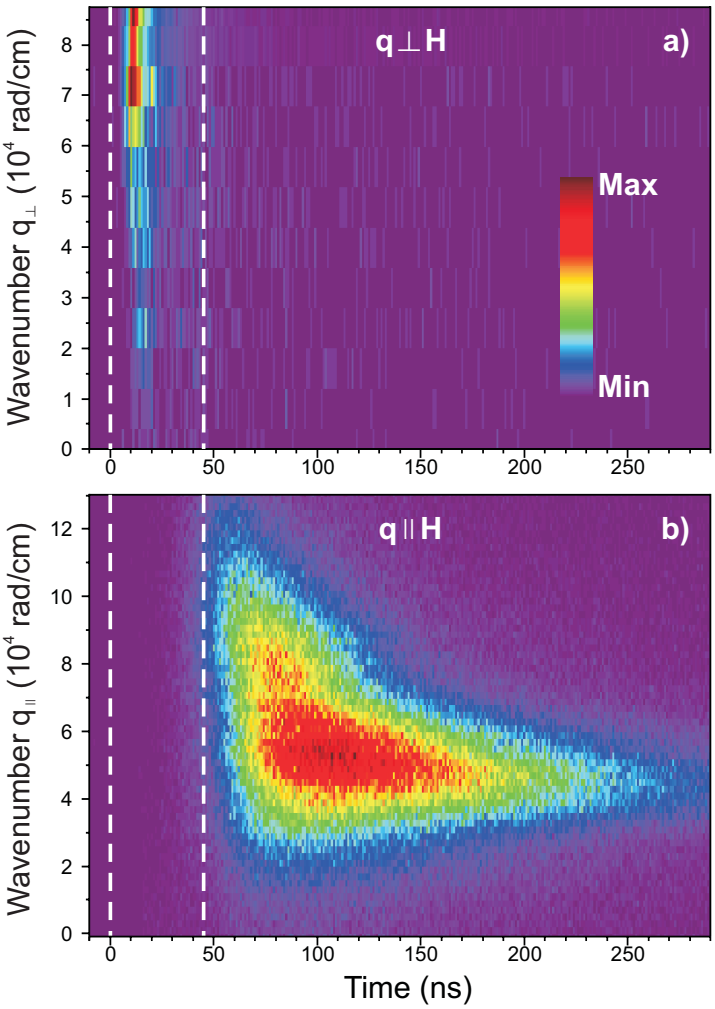

Fig. 2: Color-coded BLS intensity maps of a) parametrically injected magnons ($\mathbf{q} \parallel \mathbf{H}$) with $\omega_\mathrm{p}/2$ and b) the BLS intensity from the magnon gas ($\mathbf{q} \perp \mathbf{H}$) at the bottom of the dispersion relation at about 5 GHz. The BLS intensity is shown in time and wave vector space.

Figure 2b shows the color-coded BLS intensity map of magnons with a frequency ranging from 4.7 GHz to 5.7 GHz in time and wavevector space for $\mathbf{q} \parallel \mathbf{H}$. They correspond to the magnons at the bottom of the dispersion relation. The magnons first appear with high wave numbers and after the pumping is switched off. These magnons thermalize to states with lower wave numbers. Near the global energy minimum at $4 \cdot 10^4\,\mathrm{rad/cm}$ they form a sharp-peaked Bose-Einstein condensate and finally decay.

It is remarkable, that no strong magnon signal is visible from 25 ns to 50 ns. Our model, for calculations following [7] see Fig. 3a, show that this gap in the BLS signal can be explained solely by multi-stage four-magnon scattering mainly outside of the wavevector detection window of $0 - 12 \cdot 10^4\,\mathrm{rad/cm}$ from the experimental setup. The magnons from the transverse branch of a backward volume magnetostatic spin wave (BVMSW) mode ($\mathbf{q} \perp \mathbf{H}$) , which have the strongest coupling with the pumping electromagnetic field [8], are generated first. When the number of the parametrically injected magnons exceeds the threshold of the second order parametric instability they scatter in pairs to the longitudinal BVMSW branch ($\mathbf{q} \parallel \mathbf{H}$). Just this branch has the lowest

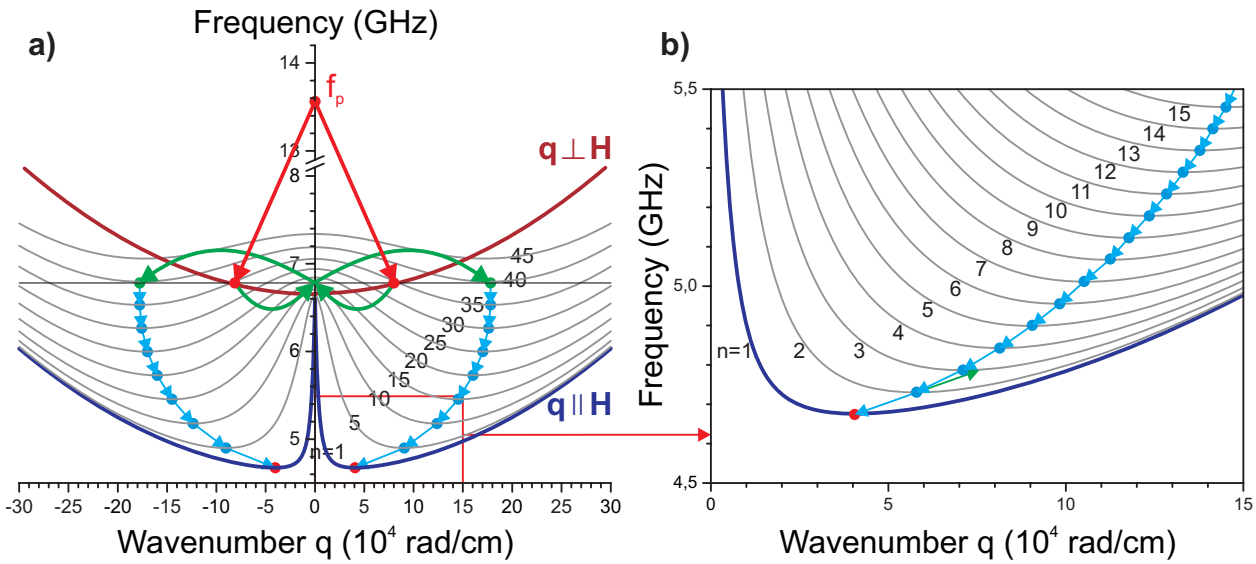

Fig. 3: a) Spin-wave dispersion relation, calculated following [7], for the first transverse ($\mathbf{q} \perp \mathbf{H}$) mode and several BVMSW thickness modes ($\mathbf{q} \parallel \mathbf{H}$). For clarity, only every fifth BVMSW thickness mode is shown. In b) all thickness modes up to $n = 15$ are shown. Parametrically pumped magnons populate the first transverse mode at $\pm 8 \cdot 10^4\,\mathrm{rad/cm}$. These magnons then scatter by four-magnon scattering to the minima of a high ($n \approx 40$) BVMSW thickness mode ($\mathbf{q} \parallel \mathbf{H}$). Our calculations show, that a step-by-step thermalization by four-magnon scattering from the energy minima of thickness mode $n = m$ to $n = m - 1$ is possible while conserving energy and momentum. Thus magnons thermalize from $n = 40$ down to the first mode $n = 1$.

threshold of the perpendicular parametric pumping, which occurs here [9]. Moreover, the magnons scatters to the energy minimum of a high (in our case $n = 40$) BVMSW thickness mode. In this spectral point, the scattered magnons have a zero group velocity, and thus suffer no additional damping caused by magnon efflux from the pumping area. Magnons from the minima of the 40th mode can scatter by four-magnon scattering to the energy minima of the 39th mode independently of each other while conserving energy and momentum. Our evaluation shows, that a step-by-step thermalization by four-magnon scattering from the energy minima of thickness mode $n = m$ to $n = m - 1$ is possible down to the first mode $n = 1$.

Our basic calculation only considers scattering between neighboring modes. Allowing scattering to not-neighboring modes will increase the number of channels for thermalization and allow faster thermalization but will not change the fundamental principle of scattering from minimum to minimum. In the interest of clarity, the energy and momentum conservation is only displayed in Fig. 3b solely for the scattering from the mode $n = 2$ to $n = 1$. In the global energy minimum of the first BVMSW thickness mode at $4 \cdot 10^4\,\mathrm{rad/cm}$ the magnons then form the observed magnon condensate.

The scattering from minimum to minimum is essential for this experiment. In the energy minima, the group velocity is close to zero. Therefore the magnons stay within the excitation area, see also Fig. 1. Magnons with a non-zero group velocity will propagate out of the detection region and do not contribute to the formation of the observed magnon condensate.

In conclusion, our experimental findings show two distinctly different phases of the thermalization process of a parametrically driven magnon gas: The energy degenerated magnon transfer from the transverse to the longitudinal branch of the spin-wave spectrum is followed by a multistage magnon scattering between the local energy minima within the longitudinal branch. This mechanism evidences the spectrally local character of magnon thermalization process, and thus further

supports the theory of evaporative cooling presented in [10, 11].

Support by the Deutsche Forschungsgemeinschaft within the SFB/TR 49 is gratefully acknowledged.

References

[1] E. Schlömann, J.J. Green, U. Milano, *Recent developments in ferromagnetic resonance at high powerlevels*, J. Appl. Phys. **31**, 386S (1960).

[2] S.M. Rezende, F.M. de Aguiar, *Spin-wave instabilities, auto-oscillations, and chaos in yttrium-iron-garnet*, IEEE Proc. 78, **6** (1990).

[3] B.A. Kalinikos, M.P. Kostylev, *Parametric amplification of spin wave envelope solitons in ferromagnetic films by parallel pumping*, IEEE Trans. Magn. **33**, 3445 (1994).

[4] S.O. Demokritov, V.E. Demidov, O. Dzyapko, G.A. Melkov, A.A. Serga, B. Hillebrands, A.N. Slavin, *Bose-Einstein condensation of quasi-equilibrium magnons at room temperature under pumping*, Nature **443**, 430 (2006).

[5] T. Brächer, P. Pirro, B. Obry, B. Leven, A.A. Serga, B. Hillebrands, *Mode selective parametric excitation of spin waves in a $Ni_{81}Fe_{19}$ microstripe*, Appl. Phys. Lett. **99**, 162501 (2011).

[6] C.W. Sandweg, M.B. Jungfleisch, V.I. Vasyucka, A.A. Serga, P. Clausen, H. Schultheiss, B. Hillebrands, A. Kreisel, P. Kopietz, *Wide-range wavevector selectivity of magnon gases in Brillouin light scattering spectroscopy*, Rev. Sci. Instrum. **81**, 073902 (2010).

[7] B.A. Kalinikos, A.N. Slavin, *Theory of dipole-exchange spin wave spectrum for ferromagnetic films with mixed exchange boundary conditions*, J. Phys. C: Solid State Phys. **19**, 7013 (1986).

[8] A.A. Serga, C.W. Sandweg, V.I. Vasyuchka, M.B. Jungfleisch, B. Hillebrands, A. Kreisel, P. Kopietz, M.P. Kostylev, *Brillouin light scattering spectroscopy of parametrically excited dipole-exchange magnons*, Phys. Rev. B **86** (13), 134403 (2012).

[9] A.G. Gurevich, G.A. Melkov, *Magnetization Oscillations and Waves*, CRC Press, New York (1996).

[10] A.A. Serga, V.S. Tiberkevich, C.W. Sandweg, V.I. Vasyuchka, D.A. Bozhko, A.V. Chumak, T. Neumann, B. Obry, G.A. Melkov, A.N. Slavin, B. Hillebrands, *Bose-Einstein condensation in an ultra-hot gas of pumped magnons*, submitted.

[11] C.W. Sandweg, A.A. Serga, V.I. Vasyuchka, T. Neumann, A.V. Chumak, B. Obry, H. Schultheiss, B. Hillebrands, *Pumping-free dynamics of Bose-Einstein condensate of magnons*, Annual Report 2009: http://www.physik.uni-kl.de/hillebrands/publications/annual-reports/annual-report-2009.

4.2 Condensation of mixed magnon-phonon states below the bottom of the magnon spectrum

D. A. Bozhko, A. A. Serga, P. Clausen, V. I. Vasyuchka, A. V. Chumak, and B. Hillebrands

In collaboration with G. A. Melkov, Faculty of Radiophysics, Taras Shevchenko National University of Kyiv, 01601 Kyiv, Ukraine

The importance of the interplay between the magnon and phonon subsystems for a good understanding of the magnetic relaxation and the magnon temperature [1], thermoelectric magnetic phenomena [1,2], the non-equilibrium time evolution and thermalization of an overpopulated magnon gas [3], has already been widely recognized.

Here we report about our last results on the recently observed phenomenon of the overpopulation of a magneto-elastic magnon (MEM) mode in a parametrically driven magnon gas [4]. In general, this mode is formed in an in-plane magnetized magnetic film due to the hybridization of dipole-exchange magnon branches with a circularly right polarized acoustic wave (see Fig. 1). The position of the hybridization area in phase space can be adjusted by a change in the bias magnetic field. In a single-crystal yttrium iron garnet (YIG) film magnetized by a bias magnetic field $H_0 = 1710\,\mathrm{Oe}$ this mode is practically frequency degenerated with the minimum of the magnon spectrum but has approximately twice the wavenumber of the Bose-Einstein condensate (BEC) of magnons. Both the magnon BEC and the MEM mode can be observed by means of a time-, space-, and wavenumber-resolved Brillouin light scattering (BLS) spectroscopy [5].

The experiment was performed using the experimental setup shown schematically in Fig. 2. Both a sample holder and a magnetic system are mounted on a rotating stage in order to be able to change the angle $\theta_{B\|}$ between the YIG sample and the probing laser beam holding the magnetization conditions constant. By varying this angle, spin waves with different wavevectors parallel

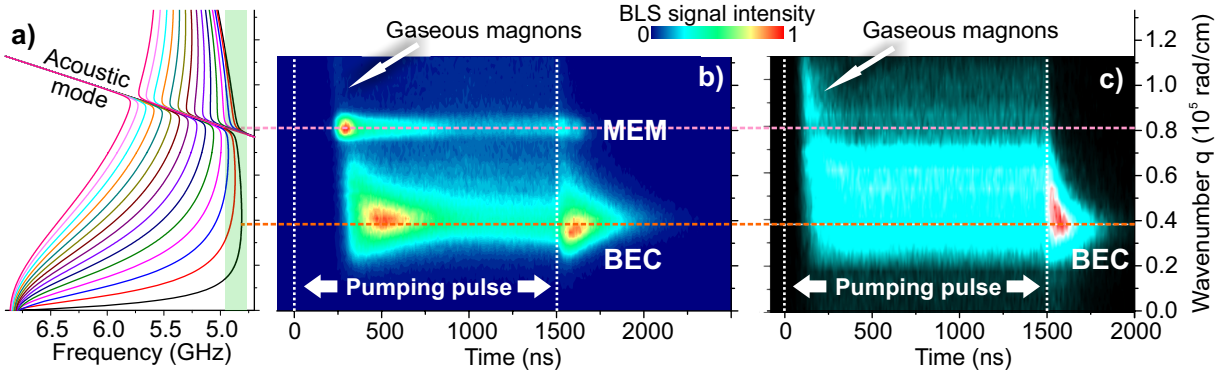

Fig. 1: Magnon spectrum and its population under different pumping conditions. a) Spin-wave dispersion branches hybridized with a transversal acoustic mode in an in-plane magnetized YIG film. The bias magnetic field is $H_0 = 1710\,\mathrm{Oe}$. The calculation is done for backward volume spin waves propagating along the magnetization direction. The first fifteen thickness spin-wave modes are shown. b) Temporal dynamics of the magnon gas density measured in the case of spatially uniform parametric pumping. Resonator width – 500 µm. The BLS data are collected in the frequency band of 150 MHz near the bottom of the magnon spectra (shadowed band in panel (a). c) The same dependence as in (b) but measured for a pumping area width of 50 µm.

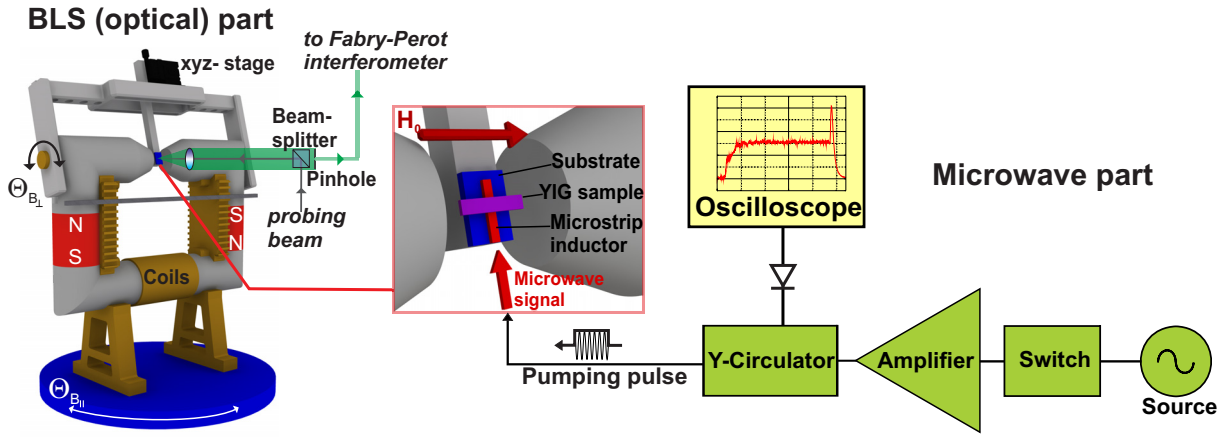

Fig. 2: Sketch of the experimental setup. The setup consists of permanent magnets which are mounted on top of a rotating plate. The tuning of the field between the two poles is realized by iron shunts mounted parallel to the poles and a small electromagnet. The YIG sample is placed on a microstrip resonator which is fabricated on top of an alumina substrate. A microwave source, a switch, a power amplifier and a Y-circulator are connected to the circuit in order to drive the spin-wave system.

to the external magnetic field $\mathbf{H_0}$ can be resolved. By changing $\theta_{B\perp}$ spin waves with an in-plane wavevector oriented perpendicular to the bias field can be investigated. A 3-dimensional pivotal lever utilizing a small xyz-moving stage allows for a precise positioning of the sample. The magnetic system comprises two NdFeB permanent magnets embedded in an iron yoke. The permanent magnets ensure long-term stability of the bias magnetic field in combination with a sufficiently large field strength. Iron shunts are used to tune the magnetic field strength inside the pole gap. For the automated fine control of the bias magnetic field a small electric coil in combination with a Hall sensor has been installed. As a result, the magnetic field strength can be adjusted in the range from 1200 to 2100 Oe with an accuracy better than 0.5 Oe. The probing light beam of 532 nm wavelength is generated by a single-mode solid-state laser. The incident light is redirected by a beam-splitter cube and focused by a precise aspherical objective onto the sample. The diameter of the focal point is about 25 µm. The same objective collects the inelastically scattered light. A pinhole placed behind the objective and the beam-splitter cube assure that only the light coming directly through the middle of the objective can pass to the interferometer. It increases the sensitivity of the optical setup to the small declinations of the scattered light, and consequently improves its wavevector resolution. For a proper focusing and spatial stabilization the setup is equipped with a CCD camera and a white light source (not shown in Fig. 2) installed behind the beam-splitter cube and enabling direct observation of the sample. The described setup allows us to detect dipole-exchange magnons having wavenumbers up to $q = 2.36 \cdot 10^5$ rad/cm with a resolution of $4.1 \cdot 10^3$ rad/cm. In the reported experiment, time and frequency resolutions of the BLS setup are of 250 ps and 150 MHz, respectively.

The YIG film sample of 6.7 µm thickness is placed on top of a microstrip resonator (see Fig. 2). Two resonators of different width (500 µm and 50 µm) are used to realize the regimes of quasi-uniform and spatially localized parametric pumping. Both resonators are fabricated on top of an alumina substrate, which was used due to its low dielectric losses and good thermal conductivity to avoid spurious heating effects which could be potentially caused by high microwave powers. A pumping circuit consisting of a microwave source, a switch, and a power amplifier feeds the resonator with 1.5 µs long microwave pulses at 13.62 GHz carrier frequency. A Y-circulator redirects the microwave power reflected from the resonator to a crystal detector and thus permits to

monitor the efficiency of the parametric excitation process by an oscilloscope. The microstrip resonators induce a pumping Oersted field along the bias field $\mathbf{H_0}$. Thus, the geometry of parallel parametric pumping, when one pumping photon splits into two magnons at half of the pumping frequency [6], is realized. In all measurements the bias magnetic field is tuned to $H_0 = 1710\,\mathrm{Oe}$ to excite the magnons just above the ferromagnetic resonance (FMR) frequency. In this case direct scattering of the parametrically injected magnons to the bottom of the spin-wave spectrum is prohibited by conservation laws. As a result, the conditions for multistage four-magnon scattering process, necessary for the effective thermalization of a magnon gas, are satisfied.

From Fig. 1b-c one can see that the parametrically injected magnons populate the lowest energy states of the spin-wave spectrum with some delay relative to the application of the pumping pulse. The delay decreases with the increase of the pumping power. It is due to the enhancement of four-magnon scattering processes with increasing magnon gas density, which are responsible for the thermalization of the magnon gas. More detailed overview of the thermalization processes is presented in Report 4.1. For the narrow resonator (50 µm) and a microwave power of 4 W this delay is typically 125 ns. For the 500 µm resonator and the same microwave power the delay increases to 200 ns because of the smaller density of the microwave current in the wide metal strip.

During further time evolution, the magnons occupy the states around the global energy minimum $q = 0.4 \cdot 10^5\,\mathrm{rad/cm}$ and tend to form there a Bose-Einstein condensate (BEC). However, the BEC formation is significantly suppressed by an increasing effective temperature of the parametrically pumped quasi-particle gas. This suppression is clearly visible in Fig. 1b. In the case of stronger pumping presented in Fig. 1b no BEC exists at all. The cooling of the magnon gas, after the pumping is switched off, allows for the BEC formation and leads to the appearance of the pronounced BEC peak just after the pump pulse [4]. The described process, which is common for any quasi-particle gas, is shown in Fig. 1 for both the quasi-uniform and spatially localized pumping regimes.

At the same time, the thermalization dynamics at wavenumbers near $q = 0.8 \cdot 10^5\,\mathrm{rad/cm}$ is strictly different for these two regimes. In the case of the wide resonator (Fig. 1b) there is a strong peak of magnon density, which corresponds to the MEM mode. In the case of the narrow resonator (Fig. 1c) there is no such peak. Moreover, the population of this spectral region is even lower than the population of its vicinity.

In order to understand this large difference, one needs to look closer at the intersection of the magnon spectrum with the transversal acoustic wave. The magnon-phonon interplay is described by a system of linearized equations for the coupled magnon-phonon states [6]:

$$\begin{array}{rcl} i\omega m_x + \omega_{BV} m_y - i\gamma q B_2 u_y &=& 0 \\ i\omega m_y - \omega_{BV} m_x + i\gamma q B_2 u_x &=& 0 \\ \left(\omega^2\rho - q^2 c_{44}\right) u_x - iq\frac{B_2}{M_0} m_x &=& 0 \\ \left(\omega^2\rho - q^2 c_{44}\right) u_y - iq\frac{B_2}{M_0} m_y &=& 0 \end{array} \quad , \tag{1}$$

where ω_{BV} is the dispersion of the lowest BVMSW mode [7] in the region of the hybridization, $m_{x,y}$ and $u_{x,y}$ represent projections of the amplitudes of oscillation, B_2 is the magnetoelastic constant, c_{44} is the component of the fourth-rank tensor of elastic stiffness constants, ρ is the mass density and q is the wavenumber. Numerical solution of this system gives us the hybridized magnon-phonon dispersions shown in Fig. 3b.

Substitution of $m_\pm = m_x \pm i m_y$ and $u_\pm = u_x \pm i u_y$ into Eq. (1) yields equations for the amplitudes

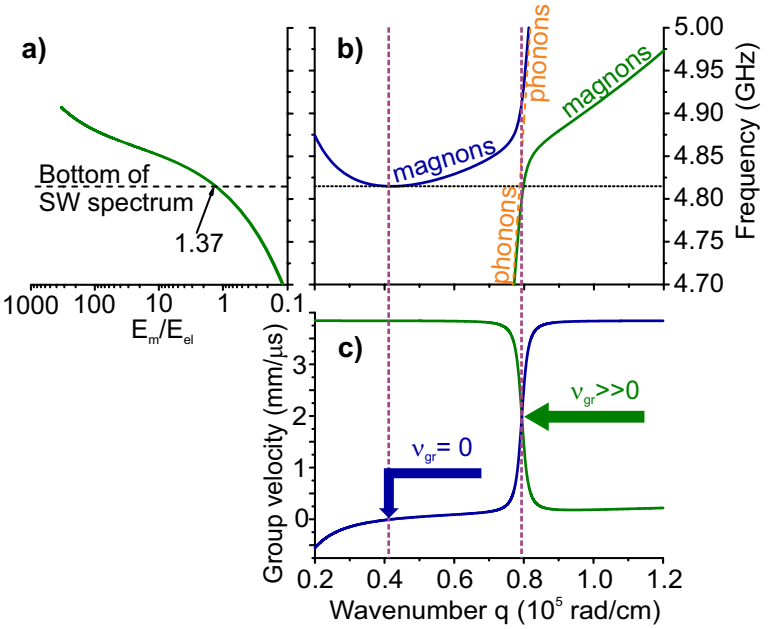

Fig. 3: a) Ratio of magnetic and elastic energies E_m/E_{el} in the lowest right-polarized magnon-phonon mode; b) Calculated magnon-phonon spectrum near the hybridization region; c) Calculated group velocities for the two branches of the magnon-phonon spectrum. All calculations were performed with the following parameters: $4\pi M_0 = 1750\,\mathrm{Oe}$, $H_0 = 1710\,\mathrm{Oe}$, $B_2 = 6.96\cdot 10^6$, $\gamma = 2\pi\cdot 2.8\cdot 10^6\,\mathrm{MHz/Oe}$, $c_{44} = 7.64\cdot 10^{11}$, $\rho = 5.17\,\mathrm{g/cm^3}$, $\upsilon_\perp = 3.843\cdot 10^5\,\mathrm{cm/s}$, YIG film thickness $L = 6.7\,\mu\mathrm{m}$

of right polarized spin and acoustic waves:

$$\begin{aligned} \omega^2\rho u_+ - q^2 c_{44} u_+ - iq\tfrac{B_2}{M_0} m_+ &= 0 \\ i\omega m_+ - i\omega_{BV} m_+ - \gamma q B_2 u_+ &= 0 \end{aligned} \quad . \tag{2}$$

The ratio of these amplitudes is given by

$$\frac{m_+}{u_+} = \frac{\gamma q B_2}{i(\omega - \omega_{BV})} \quad . \tag{3}$$

The magnetic and elastic energies of the MEM mode can be written as

$$\begin{aligned} E_m &= \alpha_m |m_+|^2 \\ E_{el} &= \alpha_{el} |u_+|^2 \end{aligned} \quad . \tag{4}$$

where α_m and α_{el} are certain coefficients. It is known that these energies are equal at the cross-point of the pure magnon and phonon dispersion branches $\omega_{BV}(q_0) = \omega_{el}(q_0)$ [6]. By substitution of q_0 into m_+/u_+ one can find

$$\frac{\alpha_m}{\alpha_{el}} = \left| \frac{\omega(q_0) - \omega_{BV}(q_0)}{\gamma B_2 q_0} \right|^2 \quad , \tag{5}$$

and thus calculate the E_m/E_{el} ratio.

The frequency dependence of E_m/E_{el} is shown in Fig. 3a. It is notable, that E_m/E_{el} significantly exceeds 1 at the lowest magnon frequency. It means that the magnon-phonon quasi-particles, which constitute the MEM mode, still possess magnetic properties below the energy minimum of the pure magnon spectrum (Fig. 3b). Consequently, they can effectively interact with the magnetic subsystem. Moreover, due to the high linearity of the magnon-phonon dispersion branch below the bottom of the spin-wave spectrum no direct transitions from the MEM area to the pure elastic states with lower energies is possible. As a result, the virtual energy minimum appears in the spectrum of magnon states below the bottom of the pure spin-wave spectrum.

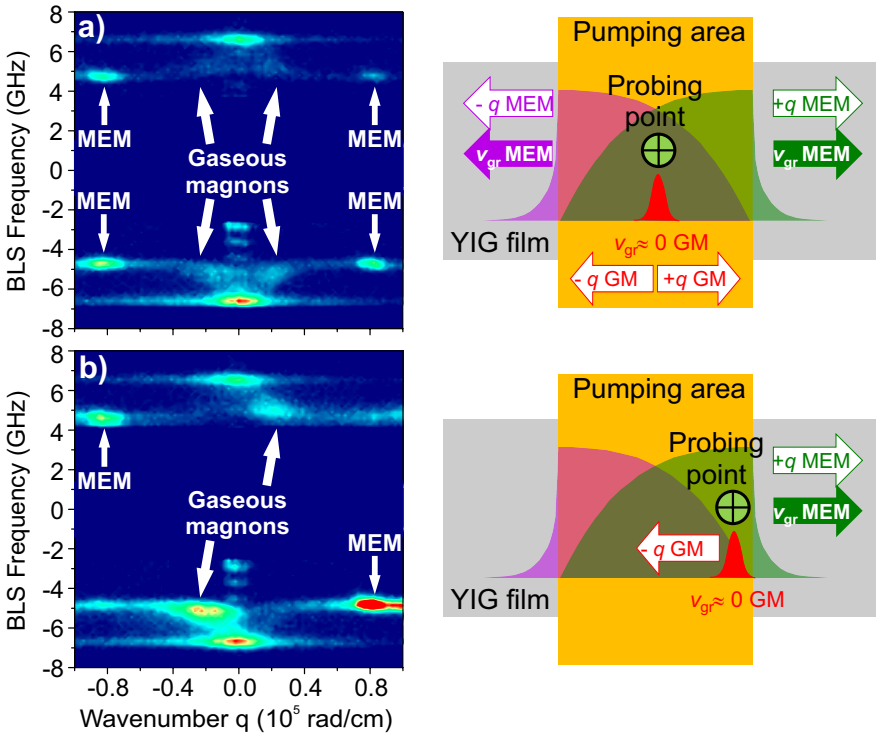

Fig. 4: BLS spectrum at different spatial probing points and sketch of the experiment. a) Probing beam is focused in the middle of the pumping area: The inelastically scattered light shows asymmetry population of the magnon spectrum; b) Probing beam near the resonator edge: The MEM peak and the hump of the gaseous magnons (GM) are observed at opposite wavenumbers due to the direction dependent magnon condensation.

The existence of this minimum drastically modifies the dynamics of the parametrically driven magnon gas. The injected magnons can spontaneously condense at this minimum and populate the MEM mode simultaneously with the BEC phase as it is shown in Fig. 1b. Furthermore, as opposed to the classical magnon BEC, this magnon-phonon phase has non-zero group velocity ($v_{gr}^{\mathrm{MEM}} = 2\,\mathrm{mm/\mu s}$) (see Fig. 3c). It leads to a strong flow of the condensed quasi-particles through the pumping region. In the case of uniform or quasi-uniform pumping (the middle area of the wide resonator in our experiment) this flow does not change the density of the MEM mode as at each point the magnon efflux and influx compensate each other. On the other hand, in the course of propagation through the pumping region the MEM mode collects the gaseous magnons (GM), and thus after some propagation distance its amplitude exceeds the noise level (see Fig. 1b). In the case of spatially localized pumping (the narrow resonator) the pumping area is too small to ensure significant amplification, and thus an observation of the travelling MEM mode is not possible. In addition, the condensed quasi-particles flow out from the pumping region, and thus the magnon gas density even decreases as it is shown in Fig. 1c.

In turn, the described mechanism leads to another effect that occurs near the edges of the wide pumping area. When the probing beam is pointing at the center of the microstrip resonator (see Fig. 4a) the distribution of the magnon density is symmetrical relative to the magnon propagation direction: The intensities of the Stokes and anti-Stokes BLS signals, produced by the gaseous magnon states and the MEM mode, are the same for negative and positive wavenumbers. However, when the laser spot is shifted to the edge of the resonator, a pronounced asymmetry of the magnon density is observed (see Fig. 4b). The explanation is straightforward: The MEM mode, which propagates to the probing point from the left side of the pumping area, is significantly amplified by the magnon condensation, and thus effectively collects the thermalized gaseous magnons having the same wavevector direction at the probing point. The gaseous magnons with the opposite wavenumbers can't scatter to this mode due to the momentum and energy conservation laws. At the same time the intensity of the MEM mode propagating to the probing point from the right

resonator edge is negligibly small (see Fig. 4b) and no visible suppression of gaseous states occurs.

Additional thermalized magnon states below the frequency of the bottom of the spin-wave spectrum were experimentally found. The accumulation of magnons in that region could be explained as trapping magnon-phonon quasi-particles in a semi-linear area of the spectrum, where transitions to the other energy states are prohibited. Nonsymmetrical behavior on the edges of pumping resonator occurs due to the non-zero group velocity of coupled excitation and suppression of the gaseous states by the travelling magnon-phonon mode.

Financial support by the Deutsche Forschungsgemeinschaft within the SFB/TRR 49 is gratefully acknowledged.

References

[1] M. Agrawal, V.I. Vasyuchka, A.D. Karenowska, A.A. Serga, G.A. Melkov, B. Hillebrands, *Direct measurement of magnon temperature: New insight into magnon-phonon coupling in magnetic insulators*, Phys. Rev. Lett. **111**, 1072 (2013).

[2] K. Uchida, H. Adachi, T. An, T. Ota, M. Toda, B. Hillebrands, S. Maekawa, E. Saitoh, *Long-range spin Seebeck effect and acoustic spin pumping*, Nature Materials **10**, 737 (2011).

[3] J. Hick, T. Kloss, P. Kopietz, *Thermalization of magnons in yttrium-iron garnet: nonequilibrium functional renormalization group approach*, Phys. Rev. B **86**, 184417 (2012).

[4] Annual Report 2012: http://www.physik.uni-kl.de/hillebrands/publications/annual-reports/annual-report-2012.

[5] C.W. Sandweg, M.B. Jungfleisch, V.I. Vasyuchka, A.A. Serga, P. Clausen, H. Schultheiss, B. Hillebrands, A. Kreisel, P. Kopietz, *Wide-range wavevector selectivity of magnon gases in Brillouin light scattering spectroscopy*, Rev. Sci. Instr. **81** 073902 (2010).

[6] A.G. Gurevich, G.A. Melkov, *Magnetization oscillations and waves* (CRC, New York, 1996).

[7] B.A. Kalinikos, *Excitation of propagating spin waves in ferromagnetic films*, IEE PROC, Vol. 127, Pt. H, No. 1, February 1980.

[8] F.A. Olson, *Study of magnetoelastic interactions by parallel pumping*, J. Appl. Phys. **34**, 1281 (1963).

4.3 Localized parametric generation of spin waves in a longitudinally magnetized $Ni_{81}Fe_{19}$ waveguide

T. Brächer, P. Pirro, A. A. Serga, and B. Hillebrands

The excitation of spin waves, or magnons, in ferromagnetic microstructures has been extensively studied in the past years [1–7]. This is due to the fact that, for instance, the utilization of magnonic currents, i.e., the angular momentum which is transported by propagating spin waves, offers a viable alternative to electric currents [8–10]. These currents are predicted to be able to interact with topological objects such as domain walls [2,11]. This offers promising potential for the realization of logic devices based on domain wall motion [12, 13]. For this purpose, the efficient excitation of spin waves in a longitudinally magnetized magnonic waveguide is of great importance as the large fields that are needed to transversally magnetize a waveguide in general lead to the absence of domain walls. However, in a longitudinally magnetized microstructured magnonic waveguide the excitation of spin waves needs to be further explored, since the excitation by the direct torque of a microwave current flowing through a microstrip antenna is inefficient and non-local in this geometry [1, 7, 14].

In this Report [15] we demonstrate localized parallel parametric generation of backward volume spin waves, i.e., the parallel parametric amplification of thermal spin waves [4, 16–18], in a longitudinally magnetized $Ni_{81}Fe_{19}$ waveguide (see geometry in Fig. 1a). The in-plane component of the Oersted field created by a microwave current flowing through the microstrip antenna placed across the waveguide exerts no torque on the static magnetization. Still, it can be used to parametrically generate spin waves at half the frequency of the applied microwave current [16]. By

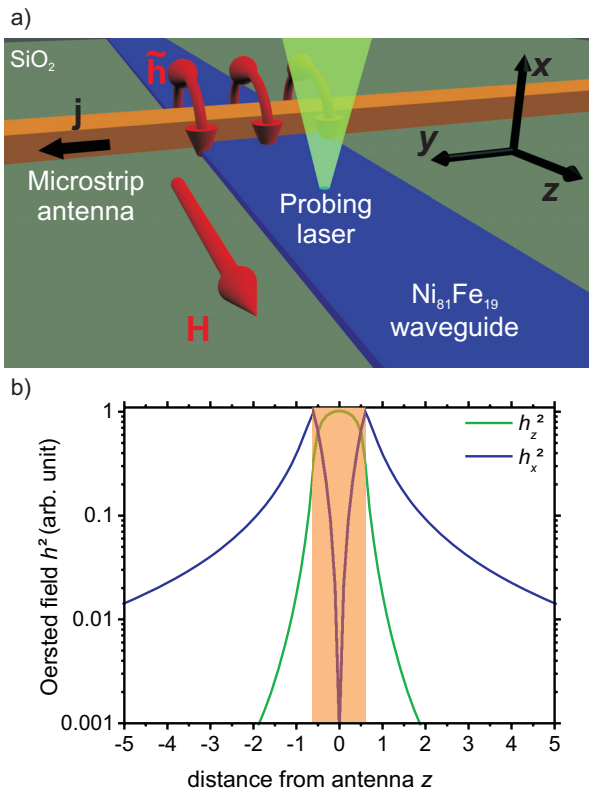

Fig. 1: a) Schematic view of the investigated sample and setup: A Cu microstrip (width $w_a = 1.2\,\mu m$, thickness $t_a = 400\,nm$) has been patterned across a $Ni_{81}Fe_{19}$ waveguide (width $w_s = 2.2\,\mu m$, thickness $t_s = 20\,nm$) and is connected to a microwave generator. A magnetic bias field is applied along the long axis of the $Ni_{81}Fe_{19}$ waveguide. b) Spatial distribution of the square of the in-plane (h_z) and out-of-plane (h_x) Oersted field along the waveguide which is created by a microwave current flowing through the Cu microstrip. The shaded area represents the extent of the microstrip antenna.

employing microfocus Brillouin light scattering (BLS) spectroscopy [19], we analyze the spatial intensity distribution of the created spin waves, showing that odd as well as even waveguide modes can be generated. To prove that the excitation takes place underneath the microstrip antenna we analyze the propagation characteristics along the waveguide. The observed exponential spin-wave decay length of $\delta = 0.63\,\mu\text{m}$ is in good agreement with the value expected from the theory of spin waves in thin ferromagnetic films [20].

The investigated magnetic structure is a $w_s = 2.2\,\mu\text{m}$ wide and $t_s = 20\,\text{nm}$ thick magnonic waveguide made from $Ni_{81}Fe_{19}$ (Permalloy). On top of this waveguide, a $w_a = 1.2\,\mu\text{m}$ wide and $t_a = 400\,\text{nm}$ thick Cu microstrip has been patterned. A schematic view of the investigated sample and the Oersted field components along the long axis of the waveguide created by the microwave current are shown in Fig. 1. The latter have been calculated assuming a rectangular current distribution inside the Cu microstrip.

The microstrip can be considered as an antenna which emits spin waves by the direct torque of the created Oersted field on the magnetization [1, 5]. This concept has proven to be very successful in transversely magnetized magnonic waveguides, where the in-plane component, which is strongly localized underneath the microstrip antenna (cf. Fig. 1b), is oriented perpendicular to the static magnetization and, thus, can excite spin waves efficiently. In a longitudinally magnetized waveguide, the in-plane field component is oriented parallel to the static magnetization. Hence, only the out-of-plane field component can exert a direct torque. However, the spin-wave excitation by the latter is inefficient, as it only couples to the out-of-plane component of the dynamic magnetization which is small in thin films due to the strong shape anisotropy [20].

In a longitudinally magnetized waveguide an additional problem arises, since the group velocity is small and, thus, the propagation distance of spin waves in this geometry is rather short. In thin films, this can lead to the peculiar case that spin waves created in one point decay much faster in space than the out-of-plane component which excites them. As a consequence, this excitation can mask the propagational character of the excited spin waves.

The shape anisotropy mentioned above leads to the fact that the out-of-plane component of the dynamic magnetization in thin films is smaller than its in-plane component, resulting in a strongly elliptic precession. This gives rise to a longitudinal component of the dynamic magnetization which oscillates along the direction of the static magnetization with twice the frequency f_{SW} of the transverse magnetization precession [21]. If a dynamic Oersted field is applied parallel to the static magnetization at twice the precession frequency $f_p = 2f_{SW}$ it couples to this longitudinal component of the dynamic magnetization and, by the annihilation of microwave photons, pairs of magnons are created [16]. The in-plane component of the dynamic Oersted field h_z created by the current flowing through the microstrip antenna fulfills this geometric condition and, thus, can excite spin waves by means of parallel parametric generation. Still, this generation can only be achieved if such a longitudinal component of the dynamic magnetization already exists and the threshold for parametric amplification is exceeded [16, 17]. In this Report, the initial precessional motion is given by the thermally excited waveguide modes. The threshold is in general determined by the damping of the waveguide modes at $f_{SW} = 1/2f_p$ and by their coupling to the microwave field h_z [4, 17, 22]. The combination of this threshold with the fast decrease of h_z along the waveguide leads to a strong localization of the parametric excitation.

In Fig. 2 the color coded spin-wave intensity (logarithmic scale) is shown for an applied microwave frequency of $f_p = 12\,\text{GHz}$ as a function of the applied microwave power P and the external bias magnetic field $\mu_0 H_{ext}$ at a spin-wave frequency of $f_{SW} = f_p/2 = 6\,\text{GHz}$. The microwave current is applied in $T = 10\,\text{ns}$ long pulses every $\tau = 30\,\text{ns}$ to avoid sample heating. In a field range from

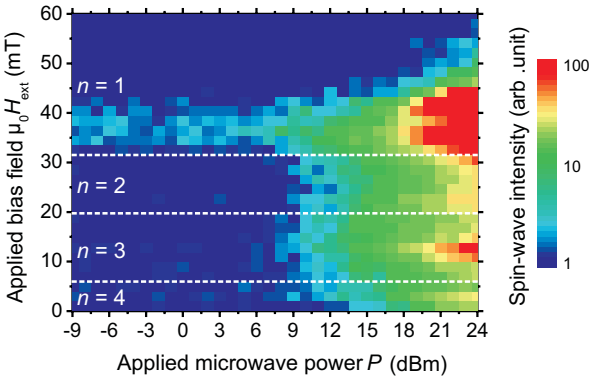

Fig. 2: Color coded spin-wave intensity (logarithmic scale) as a function of the applied magnetic bias field $\mu_0 H_{ext}$ and the applied microwave power P for a spin-wave frequency of $f_{SW} = 6\,\mathrm{GHz}$.

$\mu_0 H_{ext} = 0\,\mathrm{mT}$ to $\mu_0 H_{ext} = 42\,\mathrm{mT}$ the parametric generation of spin waves can be observed with threshold powers of around $P_{th} \approx 9\,\mathrm{dBm}$ while for fields larger than $\mu_0 H_{ext} = 42\,\mathrm{mT}$ the threshold drastically increases. For applied microwave powers below the threshold, the spin-wave intensity is given by the thermal excitations of the system. In particular, these thermal spin waves are clearly visible in the field range from $\mu_0 H_{ext} \approx 42\,\mathrm{mT}$ to $\mu_0 H_{ext} \approx 32\,\mathrm{mT}$ where their detection efficiency is the highest. To make sure that the observed intensity at $f_{SW} = 6\,\mathrm{GHz}$ above the threshold power P_{th} is indeed due to parallel parametric generation and not due to a perpendicular parametric instability [23] resulting from a strong direct excitation of spin waves at $f_{SW} = 12\,\mathrm{GHz}$, the spin-wave intensity at $f = 12\,\mathrm{GHz}$ has also been recorded (not shown). In general, this direct excitation is weak in the field range where the excitation at $f_{SW} = 6\,\mathrm{GHz}$ can be observed and shows no signs of a premature saturation [23]. Hence, a transverse parametric amplification by secondary processes from decaying magnons at $f_{SW} = 12\,\mathrm{GHz}$ can be excluded and we conclude that the spin waves at $f_{SW} = 6\,\mathrm{GHz}$ are indeed generated parametrically by the in-plane component of the antenna field.

To investigate which particular waveguide mode is amplified, the spin-wave intensity is recorded across the waveguide right in front of the microstrip antenna as a function of the magnetic field. The result of this measurement is shown in Fig. 2 by the mode numbers n - which represent the number of anti-nodes of the observed waveguide mode - and dashed lines which mark the fields where a transition between the modes occurs. In addition, Fig. 3a shows exemplary mode profiles, recorded at the points of maximal intensity in Fig. 2.

In order to understand these transitions between the amplified waveguide modes and the strong increase of the power needed to excite spin waves parametrically above $\mu_0 H_{ext} = 42\,\mathrm{mT}$, one should consider the spin-wave dispersion relation in the $Ni_{81}Fe_{19}$ waveguide. Since the waveguide is only 20 nm thick, standing spin-wave modes across the thickness of the film can be neglected in our discussion since their frequencies lie well above 12 GHz. Still, one has to consider a set of transversal waveguide modes due to the finite width of the waveguide [24]. Figure 3b shows the spin-wave wave vectors k_z as a function of the applied magnetic bias field for a fixed frequency of $f_{SW} = 6\,\mathrm{GHz}$ following Ref. [25], utilizing a calculated effective width [26] $w_{eff} = 2.3\,\mu\mathrm{m}$, a thickness $t_s = 20\,\mathrm{nm}$, a saturation magnetization $M_s = 800\,\mathrm{kA\,m^{-1}}$ and an exchange constant $A = 1.6 \cdot 10^{-11}\,\mathrm{J\,m^{-1}}$, for the first four waveguide modes n from 1 to 4. The lowest available waveguide mode $n = 1$ has the highest cut-off field of $\mu_0 H_{ext} \approx 42\,\mathrm{mT}$, above which no real wave vector k_z exists anymore. This explains the strong decrease of the spin-wave intensity above this field value. For smaller fields, more than one spin-wave wave vector for a given field can exist. Among these possible spin-wave modes the one with the smallest wave vector will have the lowest threshold. This is because of the decrease of the coupling efficiency of the waveguide modes

to the in-plane microwave field with increasing wave vector as the ellipticity of the precession decreases [4, 22]. Following this argument, the mode $n = 1$ is preferably generated at fields above $\mu_0 H_{\text{ext}} \approx 31\,\text{mT}$ since the mode $n = 2$ features a larger k_z and k_y. One would expect the most efficient excitation of the mode $n = 1$ for $\mu_0 H_{\text{ext}} \approx 31\,\text{mT}$ due to the highest possible coupling. However, spin waves with $k_z \approx 0\,\text{rad}\,\mu\text{m}^{-1}$ are confined under the antenna due to their very small group velocity. Hence, the position of the intensity maximum for the mode $n = 1$ in Fig. 2, which occurs at a field slightly larger than the fields where $k_z \approx 0\,\text{rad}\,\mu\text{m}^{-1}$, are determined by the competition between most efficient excitation and propagation out of the antenna region.

At fields lower than $\mu_0 H_{\text{ext}} \approx 31\,\text{mT}$ the mode $n = 1$ can only exist with very large wave vector component k_z. Since the difference between the possible wave vector components k_z of the modes $n = 1$ and $n = 2$ is much larger than the difference $\Delta k_y = \pi / w_{\text{eff}} \approx 1.4\,\text{rad}\,\mu\text{m}^{-1}$ between their wave vector components k_y, the total wave vector $\mathbf{k}$ of the mode $n = 2$ is much smaller. Therefore, it exhibits a higher coupling to the microwave field and, thus, at $\mu_0 H_{\text{ext}} \approx 31\,\text{mT}$ a transition from mode $n = 1$ to mode $n = 2$ occurs. For the same reasons, between $\mu_0 H_{\text{ext}} \approx 31\,\text{mT}$ and $\mu_0 H_{\text{ext}} \approx 19\,\text{mT}$ and, respectively, between $\mu_0 H_{\text{ext}} \approx 19\,\text{mT}$ and $\mu_0 H_{\text{ext}} \approx 7\,\text{mT}$ the modes $n = 2$ and $n = 3$ are preferably amplified while from $\mu_0 H_{\text{ext}} \leq 7\,\text{mT}$ to $\mu_0 H_{\text{ext}} = 0\,\text{mT}$ the mode $n = 4$ takes over.

It should be noted that, as the width of the waveguide determines the separation of the waveguide modes n, the accessible wave vector regime for a given mode can be chosen by the dimensions of the waveguide [26]. By changing the working frequency this allows for a selection of the amplified mode even at $\mu_0 H_{\text{ext}} = 0\,\text{mT}$.

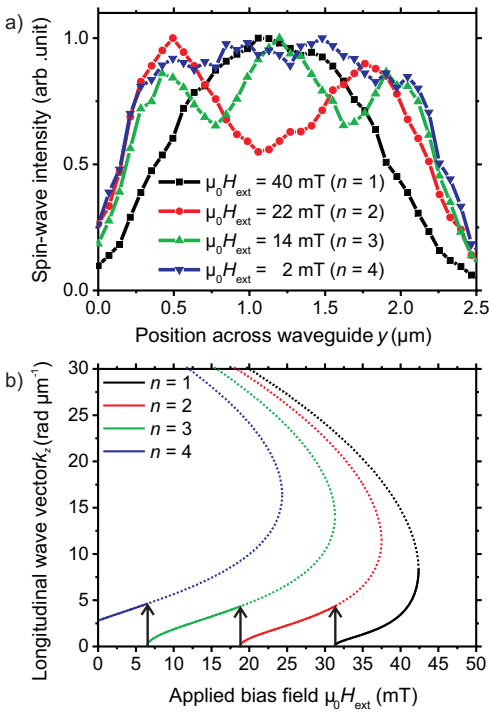

Fig. 3: a) Experimentally determined profiles of the generated waveguide modes at the bias fields where the maxima in Fig. 2 occur. The fact that the spin-wave intensity between the anti-nodes does not drop to zero is due to the convolution of the finite shape of the laser spot with the real profiles of the waveguide modes. b) Wave vectors k_z for the modes $n = 1$ to $n = 4$ as a function of the applied bias magnetic field for a fixed frequency of $f_{\text{SW}} = 6\,\text{GHz}$. The full lines highlight the mode with the highest coupling.

In order to analyze whether the parametrically generated spin waves propagate along the long axis of the waveguide with an exponential decay, as is expected by the theoretical predictions for spin waves in a thin film, [20] we study how these spin waves evolve in space. To do so, the spin-wave intensity along the waveguide is measured in the center of the waveguide. This

propagation characteristic is shown in Fig. 4a for a power of $P = 10\,\mathrm{dBm}$, which is slightly above the parametric generation threshold, and, for reference, at a much higher power of $P = 24\,\mathrm{dBm}$. An exponential fitting of the decay at $P = 10\,\mathrm{dBm}$, i.e. in the vicinity of the threshold power, yields a decay length of the spin-wave intensity of $\delta_{\mathrm{exp}} = 0.62 \pm 0.05\,\mu\mathrm{m}$. The dashed line in the figure represents the theoretical curve which is obtained following Ref. [20] assuming the material parameters stated above and a standard Gilbert damping for $Ni_{81}Fe_{19}$ of $\alpha = 0.01$. The calculation yields a theoretical decay length of $\delta = 0.63\,\mu\mathrm{m}$ and is in good agreement with the experimental findings. In addition, the components h_z^2 and h_x^2 of the antenna field are shown. It is clearly visible that the fields do not follow an exponential decay and that their spatial distribution is not connected to the decay of the spin-wave intensity. Especially the strong localization of the in-plane component of the antenna field in comparison to the spin-wave intensity is clearly visible.

If the same analysis is applied to the decay at $P = 24\,\mathrm{dBm}$, one obtains a significantly reduced decay length $\delta_{\mathrm{exp}} = 0.45 \pm 0.01\,\mu\mathrm{m}$. Hence, the propagation distance of the generated spin waves is reduced by the application of a large microwave power. If a large power is applied, a strong direct excitation of spin waves at $f_{\mathrm{SW}} = 12\,\mathrm{GHz}$ by the out-of-plane component of the antenna field might lead to a transverse parametric generation of spin waves at $f_{\mathrm{SW}} = 6\,\mathrm{GHz}$ [23]. To rule out the occurrence of such spin waves, Fig. 4b shows the distribution of the spin waves at $P = 24\,\mathrm{dBm}$ and $f_{\mathrm{SW}} = 12\,\mathrm{GHz}$ in comparison to the decay of the parametrically excited spin waves at $f_{\mathrm{SW}} = 6\,\mathrm{GHz}$ and the antenna field. It is obvious that the decay of the directly excited spin waves is following the square of the out-of-plane component of the antenna field which indicates that these spin waves are really created by the direct torque of this component, as assumed above. On the other hand, the exponential decay of the parametrically generated spin waves does not scale with the direct excitation. Hence, we deduce that the observed reduction of the decay length is not a result of the influence of the directly excited spin waves at $f_{\mathrm{SW}} = 12\,\mathrm{GHz}$. We assume that it is a consequence of a reduction of the static magnetization of the waveguide as the number of magnons is increased, since, at the considered point of the spin-wave dispersion relation, a decrease in the static magnetization by only 1% already causes a drop in the group velocity, v_{g}, by 30%. This can well explain the observed reduced decay length. Independently of the applied microwave power, the decay of the spin waves follows an exponential law and is very different from the antenna field distribution. These are strong indications that the spin waves are generated underneath the antenna and are indeed propagating out of the antenna region along the waveguide not interacting with the out-of-plane field of the antenna.

In conclusion, we have shown parallel parametric generation of traveling spin waves in a longitudinally magnetized waveguide by the in-plane component of the Oersted field of a microstrip antenna. This method shows several advantages over the conventional excitation by the direct torque of the out-of-plane component of the antenna field. For instance, it allows for the excitation of even and odd waveguide modes which propagate along the waveguide. We have demonstrated that this generation is localized underneath the antenna and that the spin-wave propagation can be described by the theoretical predictions for spin waves in thin ferromagnetic films. We emphasize that this efficient local generation also works without the application of an external bias magnetic field which opens up the way for experiments on the interaction of spin waves with domain walls and the creation of bias-free magnonic devices. Furthermore, we have shown that the application of large applied microwave powers leads to a reduction of the observed spin-wave decay length.

This work has been recently published in Applied Physics Letters [15].

The authors thank the Nano Structuring Center of the Technische Universität Kaiserslautern for their assistance in sample preparation. T. Brächer is supported by a fellowship of the Graduate

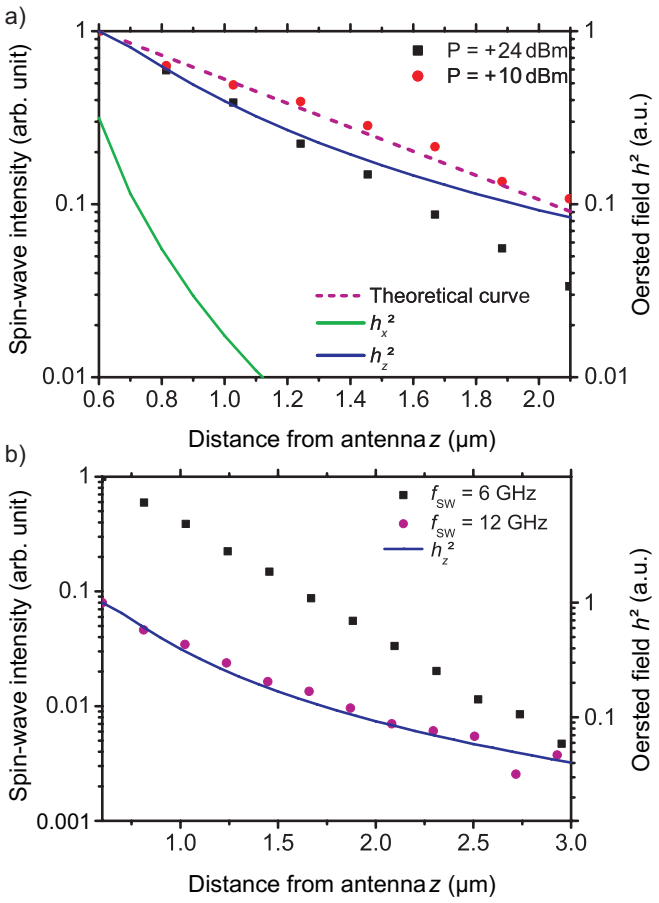

Fig. 4: a) Spin-wave intensity as a function of the distance from the center of the antenna for $f_{SW} = 6\,\text{GHz}$ at two different applied microwave powers ($P = 10\,\text{dBm}$, red dots and $P = 24\,\text{dBm}$, black squares) for an applied bias field $\mu_0 H_{ext} = 32\,\text{mT}$ in comparison to the square of the field created by the microstrip antenna. The dashed line represents the theoretical decay expected from thin film theory. b) Comparison of the spatial decay of the excited spin waves at $f_{SW} = 6\,\text{GHz}$ and $f_{SW} = 12\,\text{GHz}$ for an applied power of $P = 24\,\text{dBm}$.

School Materials Science in Mainz (MAINZ) through DFG-funding of the Excellence Initiative (GSC 266). Financial support by the DFG (TRR49) is greatly acknowledged.

References

[1] V.E. Demidov, M.P. Kostylev, K. Rott, P. Krzysteczko, G. Reiss, S.O. Demokritov, *Excitation of microwaveguide modes by a stripe antenna*, Appl. Phys. Lett. **95**, 112509 (2009).

[2] G. Duerr, R. Huber, D. Grundler, *Enhanced functionality in magnonics by domain walls and inhomogeneous spin configurations*, J. Phys.: Condens. Matter **24**, 024218 (2012).

[3] Y. Au, T. Davison, E. Ahmad, P.S. Keatley, R.J. Hicken, V.V. Kruglyak, *Excitation of propagating spin waves with global uniform microwave fields*, Appl. Phys. Lett. **98**, 122506 (2011).

[4] T. Brächer, P. Pirro, B. Obry, B. Leven, A.A. Serga, B. Hillebrands, *Mode selective parametric excitation of spin waves in a $Ni_{81}Fe_{19}$ microstripe*, Appl. Phys. Lett. **99**, 162501 (2011).

[5] P. Pirro, T. Brächer, K. Vogt, B. Obry, H. Schultheiss, B. Leven, B. Hillebrands, *Interference of coherent spin waves in micron-sized ferromagnetic waveguides*, Phys. Status Solidi B **248**, No. 10, 2404 (2011).

[6] H. Ulrichs, V.E. Demidov, S.O. Demokritov, S. Urazhdin, *Spin-torque nano-emitters for magnonic applications*, Appl. Phys. Lett. **100**, 162406 (2012).

[7] T. Brächer, P. Pirro, J. Westermann, T. Sebastian, B. Lägel, B. Van de Wiele, A. Vansteenkiste, B. Hillebrands, *Generation of propagating backward volume spin waves by phase-sensitive mode conversion in two-dimensional microstructures*, Appl. Phys. Lett. **102**, 132411 (2013).

[8] K.-S. Lee, S.-K. Kim, *Conceptual design of spin wave logic gates based on a Mach-Zehnder-type spin wave interferometer for universal logic functions*, J. Appl. Phys. **104**, 053909 (2008).

[9] A. Khitun, M. Bao, K.L. Wang, *Magnonic logic circuits*, J. Phys. D: Appl. Phys. **43**, 264005 (2010).

[10] Y. Kajiwara, K. Harii, S. Takahashi, J. Ohe, K. Uchida, M. Mizuguchi, H. Umezawa, H. Kawai, K. Ando, K. Takanashi, S. Maekawa, E. Saitoh, *Transmission of electrical signals by spin-wave interconversion in a magnetic insulator*, Nature **464**, 262-266 (2010).

[11] D.-S. Han, S.-K. Kim, J.-Y,. Lee, S.J. Hermsdoerfer, H. Schultheiss, B. Leven, B. Hillebrands, *Magnetic domain-wall motion by propagating spin waves*, Appl. Phys. Lett. **94**, 112502 (2009).
[12] D.A. Allwood, G. Xiong, C.C. Faulkner, D. Atkinson, D. Petit, R. P. Cowburn, *Magnetic domain-wall logic*, Science **309**, 1688-1692 (2005).
[13] S.S.P. Parkin, M. Hayashi, L. Thomas, *Magnetic domain-wall racetrack memory*, Science **320** (5873): 190-194 (2008).
[14] B. Lenk, H. Ulrichs, F. Garbs, M. Münzenberg, *The building blocks of magnonics*, Physics Reports **507**, 107 (2011).
[15] T. Brächer, P. Pirro, A.A. Serga, B. Hillebrands, *Localized parametric generation of spin waves in a longitudinally magnetized $Ni_{81}Fe_{19}$ waveguide* Appl. Phys. Lett. **103**, 142415 (2013).
[16] E. Schlömann, J.J. Green, U. Milano, *Recent developments in ferromagnetic resonance at high power levels*, J. Appl. Phys. **31**, p. 386S (1960).
[17] V.E. Zakharov, V.S. Lvov, S.S. Starobinets, *Stationary nonlinear theory of parametric excitation of waves*, Sov. Phys. JETP **32**, 656 (1971).
[18] H. Ulrichs, V.E. Demidov, S.O. Demokritov, S. Urazhdin, *Parametric excitation of eigenmodes in microscopic magnetic dots*, Phys. Rev. B **84**, 094401 (2011).
[19] V.E. Demidov, S.O. Demokritov, B. Hillebrands, M. Laufenberg, P.P. Freitas, *Radiation of spin waves by a single micrometer-sized magnetic element*, Appl. Phys. Lett. **85**, 2866 (2004).
[20] D.D. Stancil, A. Prabhakarl, *Spin waves - theory and applications*, Springer, New York, Berlin, Heidelberg (2009).
[21] A.G. Gurevich, G.A. Melkov, *Magnetization oscillations and waves* (CRC, New York, 1996).
[22] A.A. Serga, C.W. Sandweg, V.I. Vasyuchka, M.B. Jungfleisch, B. Hillebrands, A. Kreisel, P. Kopietz, M.P. Kostylev, *Brillouin light scattering spectroscopy of parametrically excited dipole-exchange magnons*, Phys. Rev. B **86**, 134403 (2012).
[23] H. Suhl, *The theory of ferromagnetic resonance at high signal powers*, J. Phys. Chem. Solids **1**, 209 (1957).
[24] J. Jorzick, C. Krämer, S.O. Demokritov, B. Hillebrands, B. Bartenlian, C. Chappert, D. Decanini, F. Rousseaux, E. Cambril, E. Sondergard, M. Bailleul, C. Fermon, A.N. Slavin, *Spin wave quantization in laterally confined magnetic structures*, J. Appl. Phys. **89**, 7091 (2001).
[25] B.A. Kalinikos, A.N. Slavin, *Theory of dipole-exchange spin wave spectrum for ferromagnetic films with mixed boundary conditions*, J. Phys. C **19**, 7013 (1986).
[26] K.Yu. Guslienko, S.O. Demokritov, B. Hillebrands, A.N. Slavin, *Effective dipolar boundary conditions for dynamic magnetization in thin magnetic stripes*, Phys. Rev. B **66**, 132402 (2002).

4.4 Localized parametric spin-wave generation in the Damon-Eshbach geometry by geometric variation of a microstrip antenna

T. Brächer, P. Pirro, F. Heussner, A. A. Serga, and B. Hillebrands

Parallel parametric amplification is a versatile tool to excite [1, 2], manipulate [3, 4] and restore [5, 6] spin waves, or their quanta, magnons, in a magnetic system. The implementation of this method into micro-structured magnetic systems is an important step towards a spin-wave based logic, as it enables signal processing steps like pulse cloning [3] or signal restoration [5] and the transport of information in form of spin waves over large distances [7]. Recently, the application of parallel parametric amplification to micro-structured systems has been explored. Spin-wave generation, i.e., the parametric amplification of thermal spin waves, in several geometries [1, 8, 9] and its control by pure spin currents [10] have been reported. While most of this studies have focused on a non-local generation of spin waves in micro-structured systems a localized parametric amplification offers interesting perspectives for the generation of propagating spin waves [1] and their manipulation [3, 5] on the micrometer scale. Still, while the localized generation in a longitudinally magnetized magnonic waveguide has already been reported [1], there is no experimental realization of a localized generation in a transversally magnetized magnonic waveguide. However, since in the latter case the spin-waves exhibit a larger group velocity, this geometry, known as the Damon Eshbach geometry, is of great importance for the field of magnonics [7].

Here, we report the localized parallel parametric generation of spin waves in a transversally magnetized $Ni_{81}Fe_{19}$ waveguide by a geometric variation of the current carrying microstrip which provides the generating field. By employing microfocussed Brillouin light scattering spectroscopy [11], we show how the spin-waves generated in a region with a higher current density evolve along the waveguide. Using COMSOL [12], we calculate the distribution of the microwave field created by the current flow through the antenna structure. We show that, due to the geometric variation, the microwave field falls below the threshold field of parametric generation outside of the central region. Furthermore, we derive a simple model to describe the expected spin-wave intensity distribution inside the waveguide and compare it to our results.

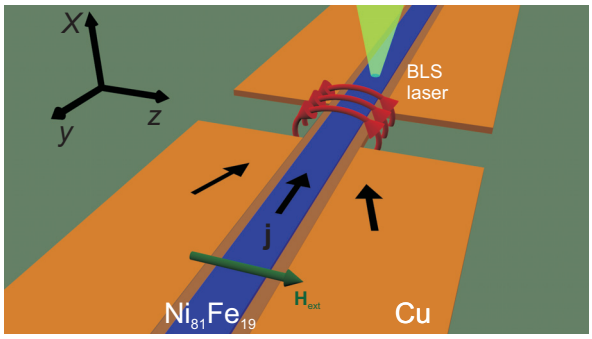

Fig. 1: Schematic view of the investigated sample (dimensions see text): A $Ni_{81}Fe_{19}$ waveguide has been patterned on top of a Cu microstrip. Under the central region of the $Ni_{81}Fe_{19}$ waveguide, the Cu microstrip has been narrowed to locally enhance the dynamic magnetic field created by the microwave current passing through the microstrip. The Cu and the $Ni_{81}Fe_{19}$ layers are separated by an insulating SiO_2 layer.

The investigated sample, as sketched in Fig. 1, consists of a $Ni_{81}Fe_{19}$ waveguide (length $L_s = 60\,\mu m$, width $w_s = 2.7\,\mu m$, thickness $d_s = 40\,nm$) which has been structured on top of a Cu microstrip and capped with a $d_c = 2\,nm$ thick Al_2O_3 layer. The Cu and the $Ni_{81}Fe_{19}$ layers are separated by a $d_i \approx 60\,nm$ thick SiO_2 insulation layer. The Cu microstrip is $d_a = 200\,nm$ thick and has a base width of $w_{a1} = 20\,\mu m$. Underneath the central region of the $Ni_{81}Fe_{19}$ waveguide

the Cu microstrip has a narrowed region with a length $L_g = 6\,\mu m$ and a width $w_{a2} = 4\,\mu m$. In the following, this region is addressed as "generation area".

A pulsed microwave current is sent through the Cu microstrip and the dynamic Oersted field created by this current is used for the parallel parametric amplification [13, 14] of thermal spin waves in the $Ni_{81}Fe_{19}$ waveguide. To realize the geometry of parallel parametric amplification [13], an external magnetic bias field $\mu_0 H_{ext}$ is applied along the short axis of the waveguide (z-axis). As a consequence, the $\tilde{h}_z$ component of the dynamic Oersted field interacts with the longitudinal component of the dynamic magnetization which arises from the ellipticity of the magnetization precession in a thin film [15]. The current density $\mathbf{j}$ inside the Cu waveguide and, thus, $\tilde{h}_z$ are inhomogeneous along the y-direction. Hence, it should be possible that the alternating Oersted field in the generation area exceeds the threshold of parametric generation [13, 15], while in the wider area the field is not sufficient to overcome this threshold.

The experimental observation of this parametric generation is carried out by means of microfocussed Brillouin light scattering (BLS), which offers a space and frequency resolved analysis of the generated spin waves. The microwave current is applied to the Cu microstrip in $t_p = 15\,ns$ long pulses every $\tau = 50\,ns$ to avoid sample heating and to minimize nonlinear saturation effects. The microwave current is applied with a frequency $f_p = 12\,GHz$, and with BLS the created magnons at $f_{SW} = 6\,GHz$ are analyzed.

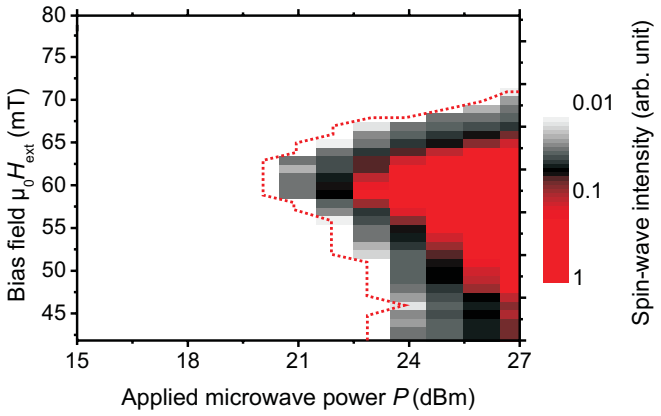

Fig. 2: Color coded spin-wave intensity in the center of the generation area at $f_{SW} = f_p/2 = 6\,GHz$ as a function of the applied microwave power P (x-axis) and external bias field $\mu_0 H_{ext}$ (y-axis). The dashed line marks the threshold powers P_{th}.

As a first characterization, the color-coded spin-wave intensity as a function of the applied microwave power P (x-axis) and external magnetic bias field $\mu_0 H_{ext}$ (y-axis) in the center of the generation area is shown in Fig. 2. The threshold power P_{th} of parametric generation is highlighted by the dashed line. Below this threshold, the spin-wave intensity for each magnetic field is given by thermal noise. If it is exceeded, a strong increase of the spin-wave signal can be observed, caused by the parametrically generated spin waves. As shown in Ref. [8], the strong increase of the threshold power P_{th} for fields larger than $\mu_0 H_{ext} = 72\,mT$ can be identified with the cut-off of the spin-wave dispersion in the waveguide [16, 17] while the increase of P_{th} for lower fields is attributed to the decrease of the coupling of the spin-wave modes to the amplification field. All further analysis is carried out at fields $\mu_0 H_{ext} < 55\,mT$, i.e., in the range where the first waveguide mode is preferably amplified [8]. From the position of the cut-off field and from thermal spectra (not shown) the saturation magnetization of the investigated $Ni_{81}Fe_{19}$ can be deduced to $M_s = (550 \pm 50)\,kA/m$. This comparably low value of M_s and the rather large error are attributed to the imperfect growth of the $Ni_{81}Fe_{19}$ on top of the rather rough Cu and SiO_2. This also leads to an enhanced Gilbert damping of $\alpha = 0.015$ which is significantly higher than the value $\alpha = 0.01$

achieved under good growth conditions [1].

In the following, the spatial distribution of the generated spin waves along the $Ni_{81}Fe_{19}$ waveguide is analyzed. The spin-wave intensity from an exemplary linescan at $\mu_0 H_{ext} = 52\,\mathrm{mT}$ is shown in Fig. 3a, where $y \approx 1\,\mu\mathrm{m}$ marks the center of the generation area. For this measurement, as for all other measured spatial distributions, a microwave power of $P = 27\,\mathrm{dBm}$ is applied. As can be seen from Fig. 3a, the largest spin-wave intensity is created in the center of the generation area. After some plateau ($y \approx 0 - 3.5\,\mu\mathrm{m}$), the spin-wave intensity drops rapidly ($y \approx 3.7 - 7.5\,\mu\mathrm{m}$) until it finally decays exponentially for $y > 7.5\,\mu\mathrm{m}$. At $\mu_0 H_{ext} = 52\,\mathrm{mT}$, the applied microwave power of $P = 27\,\mathrm{dBm}$ corresponds to $P \approx 5\,P_{th}$ in the center of the generation area. As the magnetic field $\tilde{h}_z$ scales with $\sqrt{P}$, this means that the field in the center of the generation area is equal to $\tilde{h}_z \approx 2.2\tilde{h}_{z,\mathrm{th}}$.

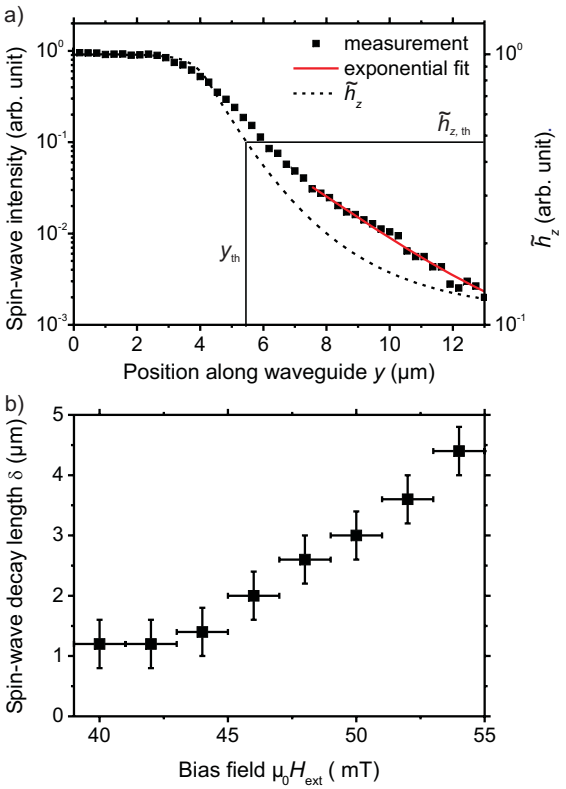

Fig. 3: a) Spin-wave intensity (squares) along the waveguide for an applied field of $\mu_0 H_{ext} = 42\,\mathrm{mT}$ in comparison with the distribution of $\tilde{h}_z$ (dashed line) calculated using COMSOL. The horizontal and the vertical line mark the threshold field $\tilde{h}_{z,\mathrm{th}}$ and the position y_{th} where the field falls below this threshold value, respectively. The fit represents an exponential fit to the data in the region where the spin-wave decay shows no further influence of the amplifying field. b) Spin-wave decay length δ as a function of the applied magnetic bias field.

In order to understand this spatial distribution, one has to compare the spin-wave intensity with the distribution of the microwave magnetic field inside the $Ni_{81}Fe_{19}$ waveguide. To do so, the current distribution inside the Cu microstrip and the resulting Oersted field $\tilde{h}_z$ have been calculated for $f = 12\,\mathrm{GHz}$ using the microwave package of the commercial software COMSOL. The resulting normalized field distribution of $\tilde{h}_z$ along the y-direction at $f = 12\,\mathrm{GHz}$ is shown in Fig. 4. The calculation is performed at a distance $x = 80\,\mathrm{nm}$ (i.e. in the middle of the waveguide) above the microstrip and averaged across the width of the waveguide. The inset shows the simulated structure. Here, the color code represents the current density. The increased current density in the generation area is clearly visible. It is obvious that the current density $\mathbf{j}$ and, thus, the field $\tilde{h}_z$ are larger not only in the geometrically defined generation area.

In the case of Figure 3 this implies that the the field $\tilde{h}_z$ drops below the threshold field $\tilde{h}_{z,\mathrm{th}}$ at a distance $y_{th} \approx 5.4\,\mu\mathrm{m}$. Thus, the spin-wave intensity at $y > y_{th}$ is caused by spin waves propagating

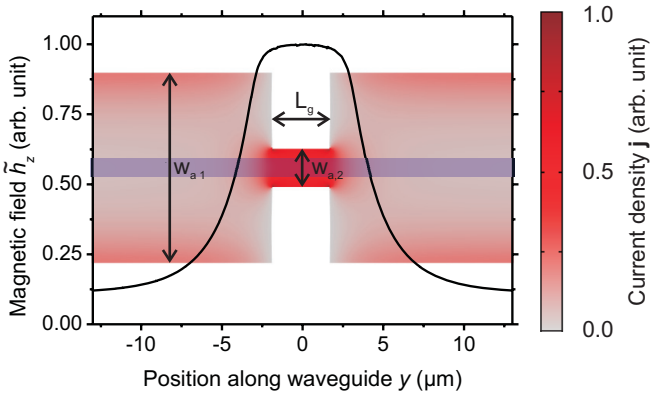

Fig. 4: COMSOL calculation of the field $\tilde{h}_z$ as a function of the position y along the waveguide (averaged across the waveguide width) for $f = 12\,\mathrm{GHz}$. The inset shows the simulated structure, where the color code represents the current distribution inside the Cu microstrip. The shaded bar represents the $Ni_{81}Fe_{19}$ waveguide.

out of the generation area. In this region, an exponential fit to the data, as shown in Fig. 3, yields the spin-wave decay length δ. This fit, which is performed at a slightly larger distance to reduce any further influence of the amplifying field, yields a spin-wave decay length of $\delta = (3.6 \pm 0.4)\,\mu\mathrm{m}$. This is in good agreement with the predictions of the theory for spin waves in thin magnetic films [18] using the material parameters stated above. Using this procedure, it is possible to determine the spin-wave decay length δ for each applied external magnetic field. The results are shown in Fig. 3b, revealing a strong decrease of the decay length at lower magnetic fields. This drop of the spin-wave decay length is denoted to a reduction of the spin-wave group velocity v_g.

In order to have a better understanding of the measured intensity distribution in space, we model the spin-wave intensity using the simulated field distribution. To do so, we make use of the following: If the threshold of parametric generation is overcome, one microwave photon splits into two magnons [13]. The density of these created magnons in the vicinity of the threshold of parametric generation at the point y_i can be described by [5, 14]

$$n(t, y_i) = n_0 \cdot \mathrm{e}^{-2(\Gamma - V \cdot \tilde{h}_z(y_i)) \cdot t} \quad , \tag{1}$$

with the starting population n_0, the relaxation frequency Γ and the coupling parameter V to the microwave field $\tilde{h}_z$. Due to its dependency on $\tilde{h}_z(y)$, $n(t, y)$ is a function of y as well. As the generated BLS intensity, which is proportional to the magnon density, is measured as an integral over time, it reaches a value of

$$\begin{aligned} I_i(t_p, y_i) &= \beta \cdot \left(\int_0^{t_p} \mathrm{e}^{-2(\Gamma - V \cdot \tilde{h}(y_i)) \cdot t} \mathrm{d}t - C \right) + \kappa \\ &= \beta \cdot \left(\frac{\mathrm{e}^{-2(\Gamma - V \cdot \tilde{h}(y_i)) \cdot t_p} - 1}{2(\Gamma - V \cdot \tilde{h}(y_i))} - C \right) + \kappa \end{aligned} \tag{2}$$

in the point y_i if an amplifying pulse with a duration of t_p is applied to the Cu microstrip. Here, β describes the proportionality factor of the BLS intensity to the magnon density, κ the thermal background noise, and C is an instrumental correction factor. The latter accounts for the insufficient statistics of the BLS spectra, as, in the vicinity of the generation threshold, the finite acquisition time is too short to detect a sufficient amount of scattering events. After being created in one point y_i we assume the magnons leave the point of their generation and propagate along the waveguide in the $\pm y$ direction with $\pm k_y$, respectively. The damping of the spin waves during this propagation leads to an exponential decay of the spin-wave intensity following [18]

$$I_\mathrm{p}(y,y_\mathrm{i}) = I_\mathrm{i}\cdot \mathrm{e}^{-2\frac{|y-y_\mathrm{i}|}{\delta}} \quad . \tag{3}$$

Therefore, the total measured BLS intensity originates from a sum of incoherent point sources i that emit spin waves in the $+y$- and $-y$-direction with a starting intensity $I_{\mathrm{p0,i}}$ and an exponential decay in space with a decay constant δ:

$$I(y) \approx \sum_\mathrm{i} \beta \cdot \left(\frac{(\mathrm{e}^{-2(\Gamma - V\cdot\tilde{h}(y_\mathrm{i}))\cdot t_\mathrm{p}} - 1)\cdot \mathrm{e}^{-2\frac{|y-y_\mathrm{i}|}{\delta}}}{2(\Gamma - V\cdot\tilde{h}(y_\mathrm{i}))} - C \right) + \kappa \quad . \tag{4}$$

It should be noted that this simple model does not take into account any peculiarities occurring from the localization of the parametric generation in space or an amplification of the generated spin waves inside the generation area.

Knowing δ and the ratio $\tilde{h}_z$ over $\tilde{h}_{z,\mathrm{th}}$, it is possible to use Eq. (4) to model the measured spin-wave intensity. For this, we make use of the assumption that the change in $\tilde{h}_{z,\mathrm{th}}$ with H_ext (see Fig. 2) is caused by a change of the coupling V to the microwave field, which is due to the change of the ellipticity of precession, and not by a significant change of the spin-wave damping [2, 8]. Therefore, we assume the same relaxation frequency $\Gamma \approx 0.16\,\mathrm{GHz}$ for all spin-wave modes which follows from the theory of spin waves in a magnetic thin film with $M_\mathrm{s} = 550\,\mathrm{kA/m}$, $\alpha = 0.015$, and $\gamma = 28\,\mathrm{GHz/T}$ for fields between $\mu_0 H_\mathrm{ext} = 40\,\mathrm{mT}$ and $\mu_0 H_\mathrm{ext} = 55\,\mathrm{mT}$ [18]. At the threshold of parametric generation, the energy inserted into the magnon system is just compensating the damping losses, i.e., $V\cdot\tilde{h}_{z,\mathrm{th}} = \Gamma$. Figure 5a shows the spin-wave intensity along the waveguide at an external magnetic bias field of $\mu_0 H_\mathrm{ext} = 42\,\mathrm{mT}$, i.e., for $\delta = 1.2\,\mu\mathrm{m}$ and $h_z/h_{z,\mathrm{th}} \approx 2$, in comparison with the reconstructed spin-wave intensity.

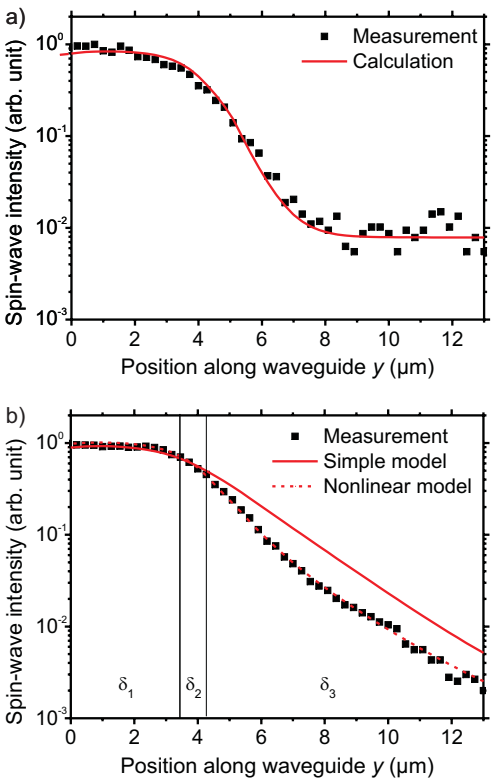

Fig. 5: a) Spin-wave intensity at $f_\mathrm{SW} = 6\,\mathrm{GHz}$ along the waveguide (squares) in comparison with modeled BLS intensity (line) for an applied bias field $\mu_0 H_\mathrm{ext} = 42\,\mathrm{mT}$ and $P \approx 4P_\mathrm{th}$. b) Spin-wave intensity at $f_\mathrm{SW} = 6\,\mathrm{GHz}$ along the waveguide (squares) in comparison with the modeled BLS intensity assuming a simple decay (line) or a nonlinear decay (dashed line) for an applied bias field $\mu_0 H_\mathrm{ext} = 52\,\mathrm{mT}$ and $P \approx 5P_\mathrm{th}$.

As can be seen from Fig. 5a, for this external field and in this regime of applied microwave power the model gives a good description of the experimental results. However, if the same model is applied to reconstruct the spin-wave intensity at an applied bias field of $\mu_0 H_{\mathrm{ext}} = 52\,\mathrm{mT}$, where a much higher spin-wave intensity is reached inside the generation area (see Fig. 2), a quite significant deviation of the calculations from the model can be observed, as shown in Fig. 5b. While the model gives a good description of the unperturbed decay for $y > 7.5\,\mu\mathrm{m}$, the steep decrease of the BLS intensity in the region of $y \approx 2.7 - 6.3\,\mu\mathrm{m}$ cannot be reproduced.

In order to understand the measured BLS intensity, a space dependent, reduced decay length needs to be introduced as a nonlinear parameter. This can either be caused by a drop of the saturation magnetization due to the large precession angle and, thus, a drop of the spin-wave group velocity, or by a nonlinear damping mechanism. As a first approximation, we consider Γ as a constant and assume δ as a function of space, assuming the reduction of δ is mainly caused by a local drop of the spin-wave group velocity v_{g}. The dashed line in Fig. 5 shows the modeled spin-wave intensity assuming three different decay lengths δ as a function of space[1] . This gives a very good agreement with the experimental data, where the small deviations around the center of the generation area are caused by saturation effects at large t where Eq. (1) is not strictly valid anymore.

To conclude, we have shown that it is possible to achieve a localized parametric generation of propagating spin waves in the Damon Eshbach geometry by modulating the width of the Cu microstrip used as antenna for the amplification field. We have compared the spatial distribution of the generated spin waves with the numerically calculated field distribution inside the microstrip antenna. Knowing the threshold power P_{th}, we conclude that the generation takes place in a confined area. The size of this area is slightly larger than the the geometrically defined generation area, as the microwave current is not strictly following the geometry of the microstrip. Therefore, the size of the active generation area depends on the applied microwave power, as this determines where the field falls below the threshold of parametric generation. Furthermore, we have compared the measured spin-wave intensity to a simple model of incoherent point sources emitting spin waves. While this gives a rather good agreement for small spin-wave intensities, a space dependent decay constant has had to be assumed to explain the measured BLS intensity if a large number of magnons are created.

The authors thank R. Neb and the Nano Structuring Center of the Technische Universität Kaiserslautern for their assistance in sample preparation. T. Brächer is supported by a fellowship of the Graduate School Materials Science in Mainz (MAINZ) through DFG-funding of the Excellence Initiative (GSC 266). A.A. Serga acknowledges financial support by the DFG (TRR49).

References

[1] T. Brächer, P. Pirro, A.A. Serga, B. Hillebrands, *Localized parametric generation of spin waves in a longitudinally magnetized $Ni_{81}Fe_{19}$ waveguide*, Appl. Phys. Lett. **103**, 142415 (2013).

[2] A.A. Serga, C.W. Sandweg, V.I. Vasyuchka, M.B. Jungfleisch, B. Hillebrands, A. Kreisel, P. Kopietz, M.P. Kostylev, *Brillouin light scattering spectroscopy of parametrically excited dipole-exchange magnons*, Phys. Rev. B **86**, 134403 (2012).

[3] K.R. Smith, V.I. Vasyuchka, M. Wu, G.A. Melkov, C.E. Patton, *Cloning and trapping of magnetostatic spin-wave pulses by parametric pumping*, Phys. Rev. B **76**, 054412 (2007).

[1] $\delta_1 = 1.6\,\mu\mathrm{m}$ for spin waves generated between $y = -1.5\,\mu\mathrm{m}$ and $y = 3.5\,\mu\mathrm{m}$, $\delta_2 = 2.2\,\mu\mathrm{m}$ between $y = -2.3\,\mu\mathrm{m}$ and $y < -1.5\,\mu\mathrm{m}$ and between $y > 3.5\,\mu\mathrm{m}$ and $y = 4.3\,\mu\mathrm{m}$, and $\delta_3 = 3.6\,\mu\mathrm{m}$ at $y < -2.3\,\mu\mathrm{m}$ and $y > 4.3\,\mu\mathrm{m}$, respectively.

[4] B.A. Kalinikos, M.P. Kostylev, *Parametric amplification of spin wave envelope solitons in ferromagnetic films by parallel pumping* , IEEE Trans. Magn. **33**, 3445 (1994).
[5] S. Schäfer, A.V. Chumak, A.A. Serga, G.A. Melkov, B. Hillebrands, *Microwave spectral analysis by means of non-resonant parametric recovery of spin-wave signals in a thin magnetic film*, Appl. Phys. Lett. **92**, 162514 (2008).
[6] A.V. Chumak, V.I. Vasyuchka, A.A. Serga, M.P. Kostylev, V.S. Tiberkevich, B. Hillebrands, *Storage-recovery phenomenon in magnonic crystal*, Phys. Rev. Lett. **108**, 257207 (2012).
[7] B. Lenk, H. Ulrichs, F. Garbs, M. Münzenberg, *The building blocks of magnonics*, Physics Reports **507**, 107 (2011).
[8] T. Brächer, P. Pirro, B. Obry, B. Leven, A.A. Serga, B. Hillebrands, *Mode selective parametric excitation of spin waves in a $Ni_{81}Fe_{19}$ microstripe*, Appl. Phys. Lett. **99**, 162501 (2011).
[9] H. Ulrichs, V.E. Demidov, S.O. Demokritov, S. Urazhdin, *Parametric excitation of eigenmodes in microscopic magnetic dots*, Phys. Rev. B **84**, 094401 (2011).
[10] E.R.J. Edwards, H. Ulrichs, V.E. Demidov, S.O. Demokritov, S. Urazhdin, *Parametric excitation of magnetization oscillations controlled by pure spin current*, Phys. Rev. B **86**, 134420 (2012).
[11] V.E. Demidov, S.O. Demokritov, B. Hillebrands, M. Laufenberg, P.P. Freitas, *Radiation of spin waves by a single micrometer-sized magnetic element*, Appl. Phys. Lett. **85**, 2866 (2004).
[12] COMSOL multiphysics, www.comsol.com.
[13] E. Schlömann, J.J. Green, U. Milano, *Recent developments in ferromagnetic resonance at high power levels*, J. Appl. Phys. **31**, 386S (1960).
[14] V.E. Zakharov, V.S. L'Vov, S.S. Starobinets, *Stationary nonlinear theory of parametric excitation of waves*, Sov. Phys. JETP **32**, 656 (1971).
[15] A.G. Gurevich, G.A. Melkov, *Magnetization oscillations and waves* (CRC, New York, 1996).
[16] B.A. Kalinikos, A.N. Slavin, *Theory of dipole-exchange spin wave spectrum for ferromagnetic films with mixed boundary conditions*, J. Phys. C **19**, 7013 (1986).
[17] K.Yu. Guslienko, S.O. Demokritov, B. Hillebrands, A.N. Slavin, *Effective dipolar boundary conditions for dynamic magnetization in thin magnetic stripes*, Phys. Rev. B **66**, 132402 (2002).
[18] D.D. Stancil, A. Prabhakar, *Spin waves - theory and applications*, Springer, New York, Berlin, Heidelberg (2009).

B. Magnon Spintronics

Spintronics is the field of spin-based data storage and processing. In conventional spintronics the electron is used as a carrier of spin. In particular, the manipulation of spin currents in nanostructures has potential applications in computing devices and magnetic memory. For the successful utilization of spin information, difficulties like the short distance over which an electron retains memory of its spin direction, the so-called spin diffusion length, have to be overcome. Here, a promising approach is the combination of standard spintronics with spin-wave dynamics resulting in *magnon spintronics*. A magnon, i.e. the quantum of a spin wave, carries an angular momentum or spin as well and can be used for storage, processing and transport of spin information, building on its outstanding properties such as long lifetime and potential for dissipationless transport. The field of magnon spintronics is currently emerging, and the main objects of studies are magnon conduits providing efficient transfer of spin information over macroscopic distances, new means of magnon currents manipulation, and magnon to charge current converters.

The first two Reports of the chapter (Reports 4.5 and 4.6) are devoted to the conversion of a magnon flow into a charge current. An effective method for detecting magnonic spin currents is the combination of spin pumping and the inverse spin Hall effect (ISHE). Spin pumping refers to the generation of spin-polarized electron currents in a normal metal from the magnetization precession in an attached magnetic material. These spin-polarized electron currents are transformed into conventional charge currents by the ISHE, which allows for a convenient electric detection of spin-wave spin currents. Report 4.5 deals with yttrium iron garnet (YIG)/ Platinum (Pt) bi-layers and addresses the question of the dependence of spin-pumping on the YIG thickness in the nanometer range. It is shown that the effective Gilbert damping parameter of the the YIG/Pt samples is enhanced for smaller YIG film thicknesses, which is attributed to an increase of the ratio between surface to volume. We observe a theoretically expected increase of the ISHE-voltage with increasing YIG film thickness tending to saturate above a certain thickness. In the second Report 4.6 we examine the influence of crystal growth on the spin-pumping induced inverse spin Hall effect in Fe/Pt bi-layers. The morphology of the Fe/Pt interface influences the effective spin mixing conductance. By increasing the growth temperature we have achieved epitaxy of Pt on Fe which led to an increase of ISHE current and ISHE efficiency. Moreover, the spin-pumping induced ISHE voltage showed two distinct ISHE-voltage peaks along the hard magnetization axis revealing its strong dependence on the magnetic anisotropies.

On of the strongest advantages of the spin system in comparison to other physical systems is its natural non-reciprocity. In Report 4.7 we use micro-magnetic simulations of perpendicularly magnetized permalloy nano-structures in order to demonstrate a non-reciprocal spin-wave mode which is localized at the sample edge and is allowed to propagate only in one direction. We show that this mode can propagate following a curved edge including 90° corners and, thus, propose an excellent solution for transfer of spin information in two-dimensional magnonic circuits. Further, it was found that due to an asymmetry with respect to the excitation antenna, asymmetric spin-wave emission in nano-structures can also be achieved for reciprocal volume waves. We demonstrate that the symmetric or asymmetric character of the spin-wave emission can be controlled by the excitation frequency.

In Report 4.8, we present experimental results about spin-wave excitation and propagation in a 100 nm thick and 5 µm wide YIG waveguide covered with Pt. YIG is one of the most commonly used materials in magnon spintronics since it has the smallest known damping and it is an insulator allowing for an electron-currentless data processing. Nevertheless, the generally used YIG

structures have lateral dimensions of millimeters and thicknesses of the order of microns what makes them inappropriate for competetive applications. Here we show that from high-quality liquid-phase epitaxy YIG micro-sized waveguides of nanometer thickness can be fabricated and successfully used for spin-wave propagation. Since the most practical interest is now concentrated on YIG/Pt bi-layers, we have covered the spin-wave waveguide with a 9 nm thick layer of Pt. As expected, the deposition of Pt leads to spin-pumping and thus to an enhanced Gilbert damping compared to the pure YIG case. However, we show that the life time of the spin waves in the YIG/Pt bilayer is still more than an order of magnitude higher than in the usually used microstructured metallic systems like Permalloy what leads to a high decay length of 31 µm. Further studies based on our results could make use of the spin Hall and spin transfer torque effect to directly reduce the damping by applying a DC current to the Pt film.

The last Report 4.9 addresses the fundamental issue of the control of the magnon flow direction which is required for a novel magnonic approach for information transport and processing. In this Report we demonstrate the implementation of a micro-structured spin-wave multiplexer. In our approach, we use a DC current to locally generate magnetic fields. In contrast to uniform external fields, the locally generated fields alter the magnetization direction solely in designated regions of the spin-wave multiplexer. This enables tailoring of the dispersion relation in different parts of the structure to our advantage. Thereby, we exploit the unique feature of the anisotropic dispersion relation of spin waves, and, thus, are able to switch spin-wave propagation directions. The presented multiplexer is an initial but crucial step toward the development of a viable spin-wave-based processor.

B. Magnon-Spintronik

Die Spintronik umfasst das Gebiet der Spin-basierten Informationsspeicherung und Verarbeitung. Bei der konventionellen Spintronik wird das Elektron als Träger des Spins verwendet. Ein besonderes Augenmerk im Hinblick auf potentielle Anwendungen in Computern oder magnetischen Speichern liegt auf der Manipulation von Spinströmen in Nanostrukturen. Für eine erfolgreiche Nutzung der Spininformationsübertragung ist es allerdings notwendig, Schwierigkeiten wie die vergleichbar kurze Länge der Erhaltung der Spinausrichtung in Materialien, der sogenannten Spindiffusionslänge, zu überwinden. Ein sehr erfolgreicher Ansatz ist hier die Kombination der Spintronik mit der Spinwellendynamik, die "Magnon-Spintronik". Ein Magnon, das Quant einer Spinwelle, trägt ebenfalls einen Drehimpuls oder Spin und kann analog zur konventionellen Spintronik für den Spin-basierten Datentransfer und die Datenverarbeitung genutzt werden, bietet aber zusätzlich herausragende Möglichkeiten wie z. B. lange Lebensdauern und das Potential eines verlustfreien Transports. Das Feld der Magnon-Spintronik befindet sich derzeit in der Entwicklungsphase. Dabei ist die Realisation von drei Hauptzielen von besonderem Interesse: (1) Magnonenleiter zur effizienten Spininformations-Übertragung über makroskopische Distanzen, (2) Konverter für die Umwandlung von Magnonen- in Ladungsströme und (3) Konverter für Ladungs- und Spinströme in Magnonen, was die Erzeugung und Verstärkung von Magnonen erlaubt.

Die ersten beiden Berichte des Kapitels (Berichte 4.5 und 4.6) sind der Konversion von Magnonenflüssen in Ladungsströme gewidmet. Eine effiziente Methode zur Detektion von Magnonenströmen ist die Kombination des Spinpumpens mit dem inversen Spin Hall Effekt (ISHE). Dabei bezeichnet das Spinpumpen die Generation eines spinpolarisierten Elektronenstroms in einem nichtmagnetischen Metall durch die Spinpräzession im angrenzenden magnetischen Material. Dieser

spinpolarisierte Elektronenstrom wird durch den ISHE in einen konventionellen Ladungsträgerstrom umgewandelt, was eine herkömmliche elektrische Detektion von Spinströmen auf Spinwellenbasis ermöglicht. Der Bericht 4.5 behandelt Doppelschichten bestehend aus Yttrium-Eisen-Granat (YIG) und Platin (Pt) und untersucht dabei die Abhängigkeit des Spinpumpens von der im Nanometer-Bereich liegenden Dicke des YIG Films. Hierbei wurde festgestellt, dass der effektive Gilbert Dämpfungsparameter der YIG/Pt Proben mit fallender YIG Schichtdicke wächst, was auf einen Anstieg des Verhältnisses von Oberfläche zu Volumen zurückgeführt wird. Wir beobachten, dass der theoretisch erwartete Zuwachs der ISHE-Spannung mit steigender YIG-Schichtdicke beim Überschreiten einer gewissen Dicke in Sättigung übergeht. Im zweiten Bericht 4.6 untersuchen wir den Einfluss des Kristallwachstums auf den durch das Spinpumpen hervorgerufen inversen Spin Hall Effekt in Doppelschichtsystemen aus Eisen (Fe) und Platin (Pt). Die Morphologie der Fe/Pt Grenzfläche beeinflusst die Spin-Mischungs-Leitfähigkeit. Durch eine erhöhte Wachstumstemperatur wurde ein epitaktisches Wachstum von Pt auf Fe erreicht, was zu einem Anstieg des ISHE-Stroms und der ISHE-Effizienz führte. Außerdem wies die ISHE-Spannung zwei ausgeprägte Maxima bei Variation des externen Magnetfeldes entlang der harten Achse auf, was den starken Einfluss der Anisotropie des Systems deutlich macht.

Einer der größten Vorteile des Spin-Systems im Vergleich zu anderen physikalischen Systemen sind seine intrinsischen, nicht-reziproken Eigenschaften. Im Bericht 4.7 benutzen wir mikromagnetische Simulationen von senkrecht zur Oberfläche magnetisierten Permalloy-Nanostrukturen um eine nicht-reziproke Spinwellenmode zu demonstrieren, die an den Kanten der Struktur lokalisiert ist und nur in eine Richtung propagieren kann. Wir zeigen, dass die Propagation dieser Mode gekrümmten Kanten inklusive einer 90° Kurve folgen kann und somit eine exzellente Möglichkeit für den Transport von Spin-Informationsströmen in zweidimensionalen Systemen darstellt. Außerdem wurde festgestellt, dass die Asymmetrie der Anregungsfelder einer Antenne eine asymmetrische Spinwellenemission in Nanostrukturen auch für reziproke Volumenwellen ermöglicht. Hierbei wurde auch gezeigt, dass der Symmetriecharakter der Spinwellen-Emission durch die Anregungsfrequenz kontrolliert werden kann.

Im Bericht 4.8 präsentieren wir experimentelle Ergebnisse zur Spinwellen-Anregung und -Propagation in einem 100 nm dicken, 5 µm breiten und mit Pt bedeckten YIG-Wellenleiter. YIG ist eines der meist genutzten Materialien in der Magnon-Spintronik, da es die kleinste bekannte Dämpfung aufweist und als elektrischer Isolator eine ladungsstromfreie Datenprozessierung ermöglicht. Die generell benutzten YIG Strukturen haben jedoch laterale Abmessungen im Millimeterbereich und Schichtdicken von Mikrometern, was sie für wirtschaftlich wettbewerbsfähige Anwendungen ungeeignet macht. Wir zeigen, dass aus qualitativ hochwertigem, mit Flüssigkeitsepitaxie hergestelltem YIG mikrostrukturierte Wellenleiter mit Schichtdicken im Nanometerbereich hergestellt werden und zur Spinwellenpropagation genutzt werden können. Da weitergehende Untersuchungen vor allem in Schichtsystemen von YIG/Pt interessant sind wurde der Wellenleiter mit einer 9 nm dicken Lage Pt bedeckt. Wie erwartet erhöht die Deposition von Pt die Gilbert Dämpfung im Vergleich zum reinen YIG-Film. Allerdings konnten wir zeigen, dass die Lebensdauer der Spinwellen in der YIG/Pt Doppelschicht immer noch um eine Größenordnung höher ist als in den gewöhnlich verwendeten mikrostrukturierten Systemen aus z. B. Permalloy. Dieser Umstand führt zu einer vergleichsweise hohen Abklinglänge von 31 µm. Weitere Untersuchungen basierend auf den hier gewonnen Erkenntnissen können den Spin-Hall und Spin-Transfer Effekt nutzen um die Spinwellendämpfung durch einen Gleichstrom im Pt zu erniedrigen.

Der letzte Bericht 4.9 behandelt die grundsätzliche Fragestellung, wie die Kontrolle der Richtung des Magnonenflusses realisiert werden kann. Eine solche Kontrolle ist die Voraussetzung für

neuartige Konzepte des Transports und der Verarbeitung von Informationen auf Basis von Spinwellen. Hier demonstrieren wir einen mikrostrukturierten Spinwellen-Multiplexer, bei dem lokal Magnetfelder mit Hilfe eines Gleichstroms in der Mikrostruktur erzeugt werden. Im Gegensatz zu uniformen externen Magnetfeldern ermöglichen die lokal generierten Felder die Beeinflussung der Magnetisierung exklusiv in den gewünschten Regionen des Spinwellen-Multiplexers. So konnte die Dispersionrelation in verschiedenen Teilen der Struktur in geeigneter Weise eingestellt und mit Hilfe ihrer Anisotropie die Spinwellen-Propagationsrichtung geschaltet werden. Der so realisierte Multiplexer stellt einen ersten, aber grundlegenden Schritt in der Entwicklung von Spinwellen-Prozessoren dar.

4.5 YIG thickness dependence of the spin-pumping effect in YIG/Pt heterostructures

V. Lauer, M. B. Jungfleisch, A. V. Chumak, and B. Hillebrands

In collaboration with: A. Kehlberger and M. Kläui, Institute of Physics, Johannes Gutenberg-Universität Mainz, Mainz, Germany, D. H. Kim, M. C. Onbasli, and C. A. Ross, Department of Materials Science and Engineering, MIT, Cambridge, USA.

The spin-pumping effect refers to the generation of a spin-polarized current in a non-magnetic metal induced by the magnetization precession in an attached magnetic layer [1]. Recently, spin pumping was discovered in heterostructures of the ferrimagnetic insulator $Y_3Fe_5O_{12}$ (yttrium iron garnet, YIG) and the non-magnetic metal platinum (Pt) [2]. Since no direct injection of electrons between YIG and Pt is possible, only the exchange interaction between localized electrons of the YIG film and conduction electrons of the attached Pt layer can contribute to spin pumping in such systems. This process decreases the angular momentum of the magnetization precession in the YIG film and, in turn, a spin-polarized electron current is generated in the Pt layer. Consequently, the spin current is transformed into a perpendicular charge current by means of the inverse spin Hall effect (ISHE) [3]. Since magnons (the quanta of spin waves) denote the collective precession of the magnetization in a magnetic material, the combination of spin pumping and ISHE is a promising candidate for the electrical detection of magnons. In the present work the spin-pumping driven ISHE voltage in YIG/Pt heterostructures is investigated as a function of the YIG thickness.

Because spin pumping is an interface effect, the magnitude of the transferred angular momentum is independent on the thickness of the ferromagnetic layer. Tashiro et al. experimentally demonstrated that the spin mixing conductance is independent of the YIG thickness in YIG/Pt structures [4]. On the other hand, with decreasing YIG film thickness the deprivation of angular momentum at the interface becomes notable with respect to the entire magnetization precession of the ferromagnetic layer. Castel et al. reported on the YIG thickness and frequency dependence of the spin-pumping process [5] for rather thick YIG films ($> 200\,\text{nm}$), which are much thicker than the exchange correlation length in YIG [6]. In contrast, the present work addresses the dependence of spin pumping on the YIG thickness in the nanometer range, from 20 nm up to 300 nm. The effective damping and the ISHE-current are determined as functions of the YIG thickness. Furthermore, the spin mixing conductance and the spin Hall angle are estimated.

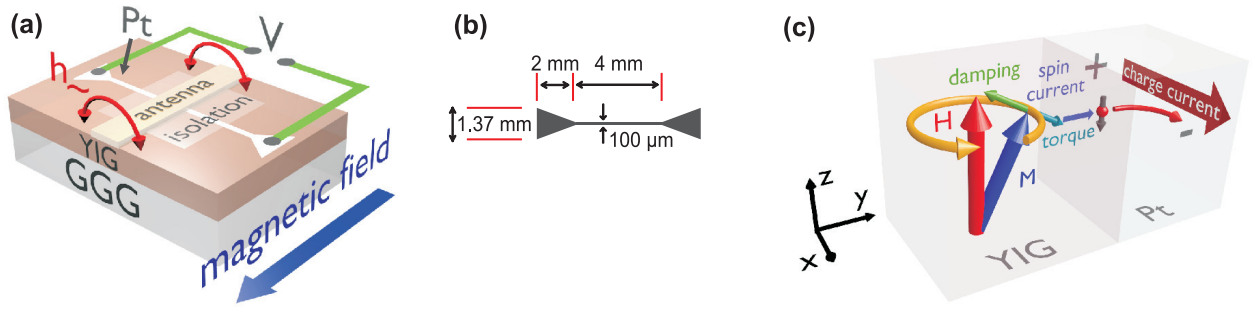

Fig. 1: [8] (a) Schematic illustration of the experimental setup. (b) Dimensions of the structured Pt layer on the YIG films. (c) Scheme of combined spin-pumping process and inverse spin Hall effect.

Figure 1a shows a sketch of the sample structure that was investigated in this work. Monocrystalline $Y_3Fe_5O_{12}$ films with thicknesses of $20, 70, 130$ and $300\,\text{nm}$ were fabricated by means of pulsed laser deposition (PLD) on a single crystalline substrate of $Gd_3Ga_5O_{12}$ (gadolinium gallium garnet, GGG) and annealed *ex-situ*. In order to deposit Pt onto the samples, they were transferred at atmosphere leading to possible surface adsorbates. Therefore, the YIG film surfaces were cleaned *in-situ* by a low power ion etching [7]. The subsequent deposition of $8.5\,\text{nm}$ Pt was performed for all samples simultaneously by means of DC sputtering at room temperature. The Pt layer was structured by photolithography and ion etching, its shape size is shown in Fig. 1b. Finally, a $300\,\text{nm}$ thick square of SU-8 photoresist was deposited on each sample for electrical isolation of the Pt structure from the microstrip antenna. All measurements in this work were performed at room temperature.

First, ferromagnetic resonance (FMR) measurements were performed, using a vector network analyzer (VNA). For this purpose, an external bias magnetic field $\mathbf{H}$ was applied. The magnetization dynamics was excited by an alternating microwave field $\mathbf{h}_\sim$ of a microstrip antenna oriented perpendicular to $\mathbf{H}$. In such a geometry $\mathbf{h}_\sim$ applies a torque on the magnetic moments of the YIG film, causing them to precess. At FMR the magnetic field $\mathbf{H}$ and the precession frequency f of the magnetization $\mathbf{M}$ fulfill the Kittel equation [9] $f_{\text{FMR}} = \frac{\mu_0\gamma}{2\pi}\sqrt{H_{\text{FMR}}(H_{\text{FMR}}+M_\text{s})}$, where μ_0 is the vacuum permeability, γ is the gyromagnetic ratio, H_{FMR} is the ferromagnetic resonance field corresponding to the frequency f_{FMR} and M_s is the saturation magnetization. The intrinsic Gilbert damping parameter α_0 can be estimated from the FMR linewidth ΔH (full width at half maximum) of pure YIG samples without Pt overlayer via the relation [10]

$$\mu_0 \Delta H = 4\pi f \alpha_0 / \gamma. \tag{1}$$

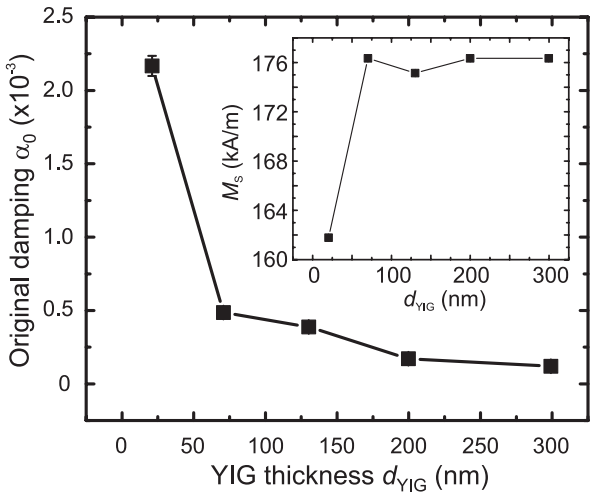

Fig. 2: [8] Gilbert damping parameter α_0 measured by VNA-FMR technique. The increased damping at low sample thickness is explained by an enhanced ratio between surface to volume, which results in an increased number of scattering centers and, thus, in an increased damping. The inset shows the saturation magnetization M_s as a function of the YIG film thickness d_{YIG}. The error bars are not visible in this scale.

The attached Pt structure of the investigated YIG films increases the damping due to the spin-pumping effect and, thus, the obtained linewidth. However, the area covered with Pt is small in comparison to the entire sample size and the main excitation power was confined to the bare YIG area. For this reasons, the overestimation of α_0 is negligible in our case. In Fig. 2 the values for α_0 and M_s are shown. The $20\,\text{nm}$ sample exhibits the largest damping of $\alpha_0^{20\text{nm}} = (2.169 \pm 0.069) \cdot 10^{-3}$. With increasing YIG thickness the damping decreases up to $\alpha_0^{300\text{nm}} = (0.093 \pm 0.007) \cdot 10^{-3}$ for the $300\,\text{nm}$ thick YIG film. The observed behavior might be explained by the increase of the surface to volume ratio for thinner films and, therefore, a more pronounced

two-magnon scattering process at the interface which causes additional damping [11]. Also it is possible, that the quality of thin films is worse due to the fabrication process by PLD. The observed M_s values as well as their general trend for film thickness dependence (see inset of Fig. 2) are in agreement with values reported for thin films [12]. The reason why they are larger than the bulk values for YIG might be related to a lower crystal quality after the annealing.

In order to measure the damping of Pt covered YIG parts of the samples, spin-pumping measurements were performed. The magnetization precession of the YIG film was excited by an alternating microwave field $\mathbf{h}_\sim$ of a microstrip antenna, in a geometry like it is shown in Fig. 1a. When the system is resonantly driven in the FMR condition, a spin-polarized electron current is injected from the magnetic material (YIG) into the normal metal (Pt). Due to spin relaxation in the normal metal (Pt) the injected spin current j_s decays along the Pt thickness (y-direction in Fig. 1c) as $j_s(y) = j_s^0 \cdot \sinh(\frac{d_{Pt}-y}{\lambda})/\sinh(\frac{d_{Pt}}{\lambda})$, where λ is the spin-diffusion length in the Pt layer [10,13]. From a phenomenological spin-pumping model one can deduce the spin-current density at the interface ($y = 0$) [13]:

$$j_s^0 = \frac{g_{eff}^{\uparrow\downarrow}\gamma^2(\mu_0 h_\sim)^2\hbar(\mu_0 M_s\gamma + \sqrt{(\mu_0 M_s\gamma)^2 + 16(\pi f)^2})}{8\pi\alpha_{eff}^2((\mu_0 M_s\gamma)^2 + 16(\pi f)^2)}, \tag{2}$$

where α_{eff} is the effective Gilbert damping parameter and $g_{eff}^{\uparrow\downarrow}$ is the real part of the effective spin mixing conductance.

The Pt layer acts as a spin-current detector and transforms the spin-polarized electron current injected due to the spin-pumping effect into an electrical charge current by means of the ISHE (see Fig. 1c) as $\mathbf{j}_c = \theta_{ISHE}\frac{2e}{\hbar}\mathbf{j}_s \times \sigma$ [2, 10, 13]. θ_{ISHE}, e and σ denote the spin Hall angle, the electron's elementary charge and the spin-polarization vector, respectively. Averaging the charge-current density over the Pt thickness yields

$$\bar{j}_c = \frac{1}{d_{Pt}}\int_0^{d_{Pt}} j_c(y)dy = \theta_{ISHE}\frac{\lambda}{d_{Pt}}\frac{2e}{\hbar}\tanh(\frac{d_{Pt}}{2\lambda})\, j_s^0. \tag{3}$$

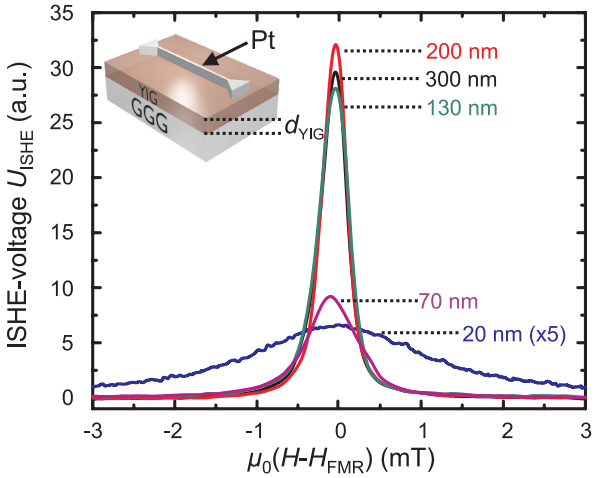

Fig. 3: [8] Typically measurements of the ISHE-induced voltage U_{ISHE} as a function of the magnetic field H for different YIG film thicknesses d_{YIG}. The ISHE-voltage for the 20 nm thick sample is multiplied by a factor of 5.

Taking into account the cross section A of the Pt layer, the ISHE-current can be calculated as $I_{ISHE} = A \cdot j_c$. Ohm's law connects I_{ISHE} with the ISHE-voltage via $U_{ISHE} = R \cdot I_{ISHE}$, where R is the electric resistance of the Pt layer.

Typical measurements of U_{ISHE} are shown in Fig. 3 for different YIG film thicknesses. The linewidth ΔH and the maximum value for U_{ISHE} can be obtained at the resonant field H_{FMR}. The general trend shows, that, for thinner samples, ΔH increases and the maximum values of U_{ISHE} decreases. This spin-pumping experiments were performed by sweeping the external field $\mathbf{H}$, while the magnetization precession of the YIG film was excited by the alternating microwave field $\mathbf{h}_{\sim}$ at a constant frequency of $f = 6.8\,\mathrm{GHz}$. The ISHE-voltage U_{ISHE} was detected at the edges of the Pt structure (see Fig. 1a) by means of a lock-in technique. For this purpose the amplitude of $\mathbf{h}_{\sim}$ was modulated at a frequency of 500 Hz. In order to avoid nonlinear multi-magnon scattering processes, a rather small exciting microwave power of 1 mW was used.

In contrast to VNA-FMR measurements of bare YIG films, in the spin-pumping experiments the magnetization precession loses spin angular momentum at the YIG/Pt interface due to the spin pumping effect. This results in an additional damping and, thus, in an enhancement of the FMR linewidth ΔH. Equation (1) still remains valid, if the intrinsic Gilbert damping α_0 is substituted by an effective Gilbert damping parameter α_{eff}. From Lorentzian fits to the data of the U_{ISHE} peaks (see Fig. 3) values for α_{eff} can be extracted. The results for α_{eff} are shown in Fig. 4a, in comparison to the values of α_0 from Fig. 2 they are larger up to a factor of 3.

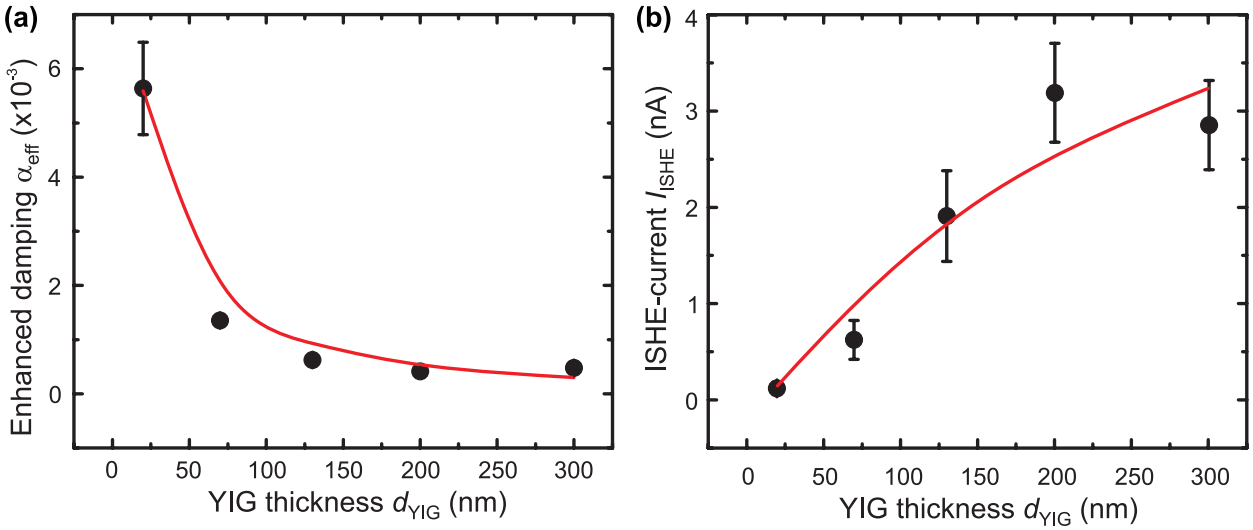

Fig. 4: [8] (a) Enhanced damping parameter α_{eff} of the YIG/Pt samples obtained by spin-pumping measurements at applied microwave powers of 1 mW. The solid curve shows a fit to Eq. (4) taking the FMR measured values for M_{s} and a constant value for $g_{\mathrm{eff}}^{\uparrow\downarrow}$ into account. The error bars for the measurement points at higher sample thicknesses are not visible on this scale. (b) Maximum ISHE-current I_{ISHE} at H_{FMR} as a function of the YIG film thickness d_{YIG}. The curve shows a fit to Eqs. (2) and (3) with the parameters $g_{\mathrm{eff}}^{\uparrow\downarrow} = (7.43 \pm 0.36) \cdot 10^{18}\,\mathrm{m}^{-2}$ and $\theta_{\mathrm{ISHE}} = 0.009 \pm 0.001$. The applied microwave power used is $P_{\mathrm{applied}} = 1\,\mathrm{mW}$.

α_{eff} increases clearly with decreasing YIG film thickness d_{YIG}. Its dependence on d_{YIG} can be described as [10]

$$\alpha_{\mathrm{eff}} = \alpha_0 + \Delta\alpha = \alpha_0 + \frac{g\mu_{\mathrm{B}}}{4\pi M_{\mathrm{s}} d_{\mathrm{YIG}}} g_{\mathrm{eff}}^{\uparrow\downarrow}, \tag{4}$$

where g is the g-factor and μ_{B} the Bohr magneton. The effective spin mixing conductance $g_{\mathrm{eff}}^{\uparrow\downarrow}$ is considered to be constant for all samples, since the Pt layer was grown onto all YIG films simultaneously. Using the saturation magnetization values M_{s} of the VNA-FMR measurements

(inset of Fig. 2), a fit to Eq. (4) yields $g_{\mathrm{eff}}^{\uparrow\downarrow} = (7.43 \pm 0.36) \cdot 10^{18}\,\mathrm{m}^{-2}$. The fit is depicted as a solid line in Fig. 4a.

Figure 4b shows the maxima of charge currents I_{ISHE} calculated via $U_{\mathrm{ISHE}} = R \cdot I_{\mathrm{ISHE}}$ from the measured U_{ISHE} values at resonance field H_{FMR} (see Fig. 3). The resistance R varies between $1450\,\Omega$ and $1850\,\Omega$ for the different samples. Evidently, I_{ISHE} increases up to a YIG film thickness of around 200 nm where it starts to saturate. The observed thickness dependent behavior is in agreement with the one reported for $Y_3Fe_5O_{12}$/Pt [4]. According to Eqs. (2), (3) and (4) it is $I_{\mathrm{ISHE}} \propto j_{\mathrm{s}}^0 \propto 1/\alpha_{\mathrm{eff}}^2 \propto (\alpha_0 + c/d_{\mathrm{YIG}})^{-2}$, where c is a constant. Therefore, the ISHE-current I_{ISHE} increases with increasing YIG film thickness and goes into saturation at a certain value of d_{YIG}. We determine the expected behavior of $I_{\mathrm{ISHE}} = A\,\bar{j}_{\mathrm{c}}$ (see also Eq. (3)) and compare it with our experimental data. In order to do so, the measured values for M_{s}, the original damping parameter α_0 determined by VNA-FMR measurements at 1 mW (see Fig. 2) and the enhanced damping parameter α_{eff} obtained by spin-pumping measurements at a microwave power of 1 mW (see Fig. 4a) are used. The Pt layer thickness is $d_{\mathrm{Pt}} = 8.5\,\mathrm{nm}$ and the microwave magnetic field is determined to be $h_{\sim} = 3.2\,\mathrm{A/m}$ for an applied microwave power of 1 mW using an analytical expression [14]. The spin-diffusion length in Pt is taken from literature as $\lambda = 10\,\mathrm{nm}$ [15] and the damping parameter is assumed to be constant as $\alpha_0 = 6.68 \cdot 10^{-4}$, which is the average of the measured values of α_0. The fit is shown as a solid line in Fig. 4b. We find a spin Hall angle of $\theta_{\mathrm{ISHE}} = 0.009 \pm 0.001$, which is in agreement with literature values [15]. Using the fit we estimate the saturation value of the generated current. Although we observe a transition to saturation at sample thicknesses of $200 - 300\,\mathrm{nm}$, we find that according to our fit, 90 % of the estimated saturation level of 5 nA (see Fig. 4b) is reached at a sample thickness of $1.2\,\mu\mathrm{m}$.

As a summary, the $Y_3Fe_5O_{12}$ thickness dependence of the spin-pumping effect detected by the ISHE has been investigated quantitatively. It is shown that the effective Gilbert damping parameter of the the YIG/Pt samples is enhanced for smaller YIG film thicknesses, which is attributed to an increase of the ratio between surface to volume. We observe a theoretically expected increase of the ISHE-voltage with increasing YIG film thickness tending to saturate above a certain thickness. The calculated spin mixing conductance and the spin Hall angle are in agreement with values reported in the literature.

Support by the Deutsche Forschungsgemeinschaft within the project CH 1037/1-1 is gratefully acknowledged.

References

[1] Y. Tserkovnyak, A. Brataas, G.E.W. Bauer, *Enhanced Gilbert damping in thin ferromagnetic films*, Phys. Rev. Lett. **88**, 117601 (2002).

[2] Y. Kajiwara, K. Harii, S. Takahashi, J. Ohe, K. Uchida, M. Mizuguchi, H. Umezawa, H. Kawai, K. Ando, K. Takanashi, S. Maekawa, E. Saitoh, *Transmission of electrical signals by spin-wave interconversion in a magnetic insulator*, Nature **464**, 262 (2010).

[3] J.E. Hirsch, *Spin Hall effect*, Phys. Rev. Lett. **83**, 1834 (1999).

[4] T. Tashiro, R. Takahashi Y. Kajiwara, K. Ando, H. Nakayama, T. Yoshino, D. Kikuchi, E. Saitoh, *Thickness dependence of spin pumping at YIG/Pt interface*, Proc. SPIE **8461**, 846106 (2012).

[5] V. Castel, N. Vlietstra, J. Ben Youssef, B.J. van Wees, *YIG thickness and frequency dependence of the spin-charge current conversion in YIG/Pt systems*, arXiv:1304.2190v1 (2013).

[6] S.O. Demokritov, *Spin Wave Confinement*, (Pan Stanford Publishing, Singapore 2008).

[7] M.B. Jungfleisch, V. Lauer, R. Neb, A.V. Chumak, B. Hillebrands, *Improvement of the yttrium iron garnet/platinum interface for spin pumping-based applications*, Appl. Phys. Lett. **103**, 022411 (2013).

[8] M.B. Jungfleisch, A.V. Chumak, A. Kehlberger, V. Lauer, D.H. Kim, M.C. Onbasli, C.A. Ross, M. Kläui, B. Hillebrands, *Thickness and power dependence of the spin-pumping effect in* $Y_3Fe_5O_{12}$*/Pt heterostructures measured by the inverse spin Hall effect*, arXiv:1308.3787v1 (2013).
[9] C. Kittel, *On the theory of ferromagnetic resonance absorption*, Phys. Rev. **73**, 155 (1948).
[10] H. Nakayama, K. Ando, K. Harii, T. Yoshino, R. Takahashi, Y. Kajiwara, K. Uchida, Y. Fujikawa, E. Saitoh, *Geometry dependence on inverse spin Hall effect induced by spin pumping in* $Ni_{81}Fe_{19}$*/Pt films*, Phys. Rev. B **85**, 144408 (2012).
[11] M. Sparks, *Ferromagnetic-relaxation theory*, (McGraw-Hill, New York, 1964).
[12] N. Kumar, D.S. Misra, N. Venkataramani,S. Prasad, R. Krishnan, *Magnetic properties of pulsed laser ablated YIG thin films on different substrates*, J. Magn. Magn. Mater. **272**, 899 (2004).
[13] K. Ando, S. Takahashi, J. Ieda, Y. Kajiwara, H. Nakayama, T. Yoshino, K. Harii, Y. Fujikawa, M. Matsuo, S. Maekawa, E. Saitoh, *Inverse spin-Hall effect induced by spin pumping in metallic system*, J. Appl. Phys. **109**, 103913 (2011).
[14] D. Chumakov, *Dissertation thesis* (2006).
[15] O. Mosendz, J.E. Pearson, F.Y. Fradin, G.E.W. Bauer, S.D. Bader, A. Hoffmann, *Quantifying spin Hall angles from spin pumping: Experiments and theory*, Phys. Rev. Lett. **104**, 046601 (2010).

4.6 Optimizing the spin-pumping induced inverse spin Hall voltage by growth conditions in Fe/Pt bilayers

E. Th. Papaioannou, P. Fuhrmann, M. B. Jungfleisch, T. Brächer, P. Pirro, V. Lauer, and B. Hillebrands

In collaboration with J. Lösch, Institut für Oberflächen- und Schichtanalytik (IFOS) and Landesforschungszentrum OPTIMAS, Trippstadter Str. 120, 67663 Kaiserslautern, Germany

Many aspects of magnetization dynamics in ferromagnetic (FM)/non magnetic (NM) bilayers have been investigated by means of spin pumping and the inverse spin Hall effect (ISHE) in various kinds of materials [1]. A prominent material combination is $Ni_{80}Fe_{20}$ (Py) and Pt bilayers [2, 3]. Recently, it has been shown that the spin-pumping mechanism is even applicable in insulating FM/NM bilayers like YIG/Pt (YIG:yttrium iron garnet) [5–8]. Although spin pumping is an interfacial effect, the manner in which it is affected by the structural parameters of the interface and therefore influences the ISHE signal strength, have so far not been investigated in detail. Lately, the role of the cleanliness of the YIG surface, [5] and the crystal perfection of YIG [9] in the YIG/Pt system proved the great importance of the interface properties. However in metallic systems the study of the influence of the growth mode is limited.

Here in this work, we adress the problem of structural and interfacial quality by using Fe/Pt bilayers epitaxially grown on MgO substrates [10]. We correlate the morphology of the interface and the presence of strong anisotropy to the spin-pumping efficiency, and therefore, on the ISHE signal strength.

Fe (12 nm)/Pt (10 nm) bilayers were grown on MgO (100) substrates (Fig. 1) by electron-beam evaporation in an ultrahigh vacuum (UHV) chamber with a base pressure of 3×10^{-11} mbar, at three different substrate temperatures: room temperature (RT), 150 °C and 300 °C. After the deposition of Fe/Pt, annealing at the corresponding growth temperature was performed. Fe (12 nm)/Al (2.5 nm) reference films were also fabricated at the same experimental conditions as the Fe/Pt samples. The Al layer was deposited as a capping layer in order to form naturally an Al_2O_3 oxide protective layer.

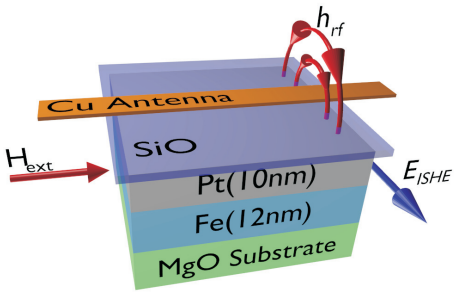

Fig. 1: Schematic diagram of the sample structure with the corresponding thicknesses. Ferromagnetic resonance is excited by a microwave magnetic field induced by a Cu microstrip antenna and a tunable magnetic external field (H_{ext}) while a silicon oxide plate isolates the Pt from the Cu antenna.

In Fig. 2 we present in-situ STM images for two samples grown at different temperatures: RT and 300 °C. The upper panel (left) shows the top surface of 12 nm Fe grown at RT on MgO substrate. The growth at RT results in the creation of small crystallites with a narrow size distribution that can be well fitted with a logarithmic - normal function (upper panel, right), giving an average grain

size of 5.9 ± 0.8 nm. The lower panel shows a Fe/Pt sample grown at 300 °C substrate temperature. The top surface of 12 nm Fe (left) and the surface after 10 nm of Pt growth on top of Fe (right) reveal crystallites with larger sizes and different shapes than the RT case. The Fe surfaces show a clear evolution with the growth temperature. As the growth temperature increases the average grain size become larger being 9.5 ± 0.7 nm for the sample grown at 150 °C and 14.6 ± 1.6 nm for the sample grown at 300 °C. The size distribution is broader, and not any more well fitted by a log-norm function. Simultaneously, the mean square roughness R^{rms} increases from $R^{rms}_{RT} = 0.13$ nm for the RT sample to $R^{rms}_{150°C} = 0.17$ nm and to $R^{rms}_{300°C} = 0.38$ nm for the other two samples. While the grains themselves are essentially flat, the grain boundaries are rough leading to height differences between individual grains. Indeed, one can observe a dramatic change in the islands' shape evolving from small spheres to almost square like crystallites for the 300 °C sample. The grain size is strongly dependent on the ratio of the melting temperature of the deposited material ($T^{element}_{melting}$) to the temperature of the substrate ($T_{substrate}$) [11]. For large values of the ratio one observes smaller grains with a narrower size distribution as for the RT grown sample, while for relatively smaller values of the ratio, a larger distribution of grain sizes with large grains as seen for the other two samples. The Pt evaporation on top of Fe seems to maintain the samples' surface characteristics and the differences between the samples. Slightly larger grain sizes are observed.

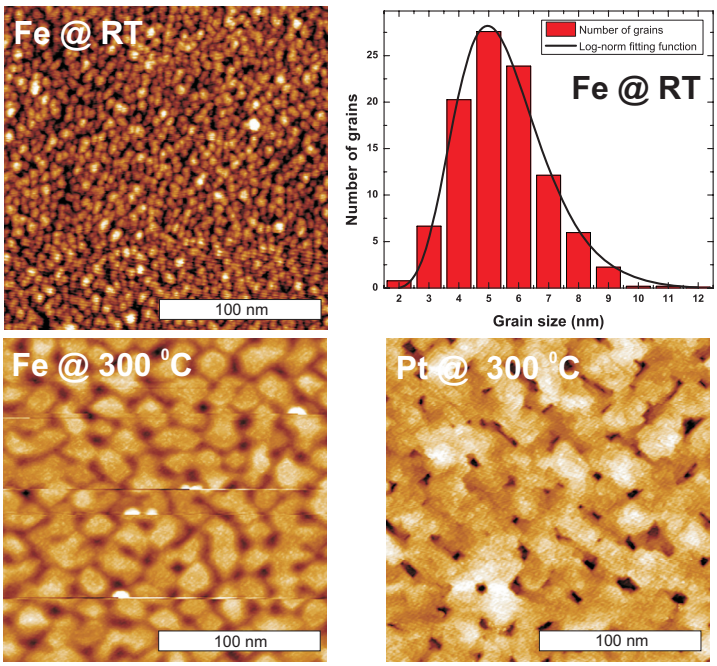

Fig. 2: (Upper panel) *in-situ* STM image of a Fe surface grown on MgO substrate at RT (left) and the corresponding grain size distribution fitted by a logarithmic-normal function giving an average grain size of 5.9 ± 0.8 nm (right). (Lower panel) *In situ* STM images of an Fe surface grown on MgO substrate at 300 °C (left) and of a Pt surface on top of Fe (right). A dramatic change in the islands' shape and size is observed with the deposition temperature.

In Fig. 3, XRD pole figures for two Fe/Pt samples are presented. The pole figures confirm for all samples the 45° in plane epitaxial relation (Fe[100] || MgO[110], Fe[110] || MgO[010]) between the substrate and the Fe for all growth temperatures. In contrast, the Pt layer on top of Fe exhibits different characteristics with the growth temperature. Well defined diffraction spots of Pt (220) arise for the sample grown at 300 °C (and at 150 °C, not shown). The complete coherency of Pt on Fe is shown by the fact that the 4 peaks of Pt (220) separated by 90° are rotated from the Fe (110) peaks by 45°. The epitaxial growth of the fcc Pt layer on bcc Fe along the [100] plane direction is of great interest. This kind of epitaxy can be correlated to the Bain epitaxial orientation [13] when the Pt cell is 45° rotated with respect to the Fe lattice. On the other side the Pt (220) diffraction spots in Fig. 3 for the sample grown at RT are very much scattered. Pt in this case exhibits a

preferred orientation of (111) oriented grains [10]. The pronounced differences in the growth modes of the different Fe/Pt bilayers lead to different magnetic behaviour of the samples, different spin-pumping efficiencies and ISHE strengths, as it is shown in the next paragraph.

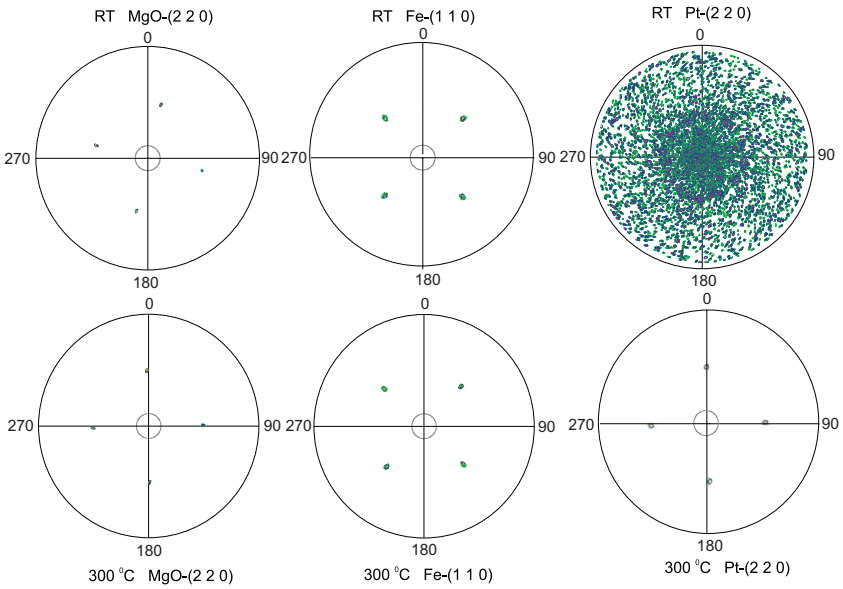

Fig. 3: XRD pole figures for two Fe/Pt samples: (top) grown at RT, and (bottom) grown at 300 °C. 45° in plane epitaxial relation between the substrate and the Fe is observed for all samples. Diffraction peaks of Pt (220) on Fe is observed for growth at 300 °C but not for the sample grown at RT which exhibits Pt (111) oriented crystallites.

FMR and ISHE experiments were performed with the external magnetic field parallel to the film plane, in two different directions: $\varphi = 0°$ (Fe [100] easy axis) and $\varphi = 45°$ (Fe [110] hard axis). In Fig. 4a the frequency dependence of the resonant field, measured at $\varphi = 45°$ and with two different setups (FMR, ISHE) is shown. The presented data refer to the sample grown at 300 °C. The form of FMR spectra along the hard axis is due to the presence of four- and two-fold anisotropy [10]. The peak positions of the FMR signal coincide with the ISHE data. The small discrepancy for low fields can be explained by imperfect azimuthal alignment since small variations of the in-plane angle from the hard axis can cause large shifts of the FMR peak position [12].

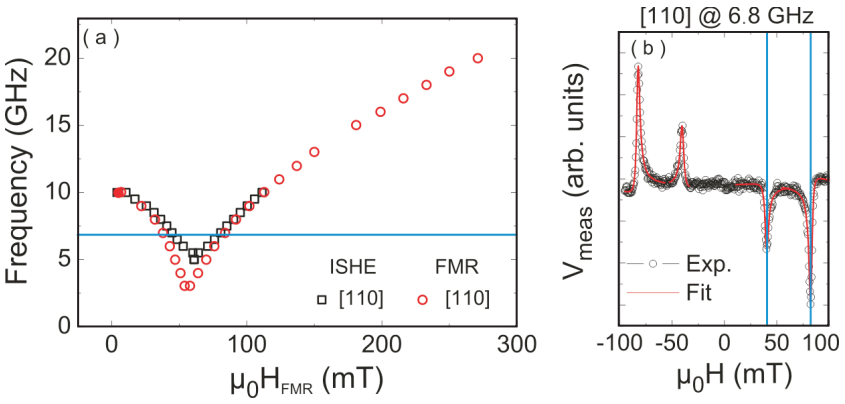

Fig. 4: a) Frequency dependence of the resonant external magnetic field along the Fe [110] hard axis direction. Two branches along [110] are observed due to pronounced anisotropy terms. b) Measured voltage at 6.8 GHz (horizontal line in 4a) along the [110] direction. The data refer to the sample grown at 300 °C.

In FMR condition a spin current is effectively pumped from the Fe layer into the Pt layer. The magnetization dynamics is excited by the microwave magnetic field of a 600 µm Cu microstrip antenna, and the external magnetic field is swept. We measure the spin-pumping induced ISHE-voltage [5, 10] that appears across the edges of the Pt layer perpendicular to the external magnetic

field (see Fig. 1, induced electromotive force E_{ISHE}). In Fig. 4b the measured voltage (V_{meas}) as a function of the external magnetic field applied in the [110] direction is presented, measured at 6.8 GHz. With the field reversal a sign reversal in V_{meas} signal is observed at the same absolute field values. The field values where the V_{meas} peaks are measured agree well with the FMR resonance positions at the measured frequency (denoted as horizontal line in Fig. 4a) and confirm spin pumping from the Fe layer to the Pt layer at the FMR frequencies. The reason for the appearance of two peaks is the alignment of the external field along the hard axis. In Fig. 4b the amplitude and the shape of V_{meas} reveal its dependence on the magnetic anisotropy of the films. However, as it has been previously discussed [3, 14], V_{meas} is the sum of three contributions: the spin pumping effect at the FMR frequency, the anisotropic magnetoresistance (AMR) effect at microwave fields, and the anomalous Hall effect (AHE). The possibility to distinguish between AMR and AHE contributions is given by the different dependencies of the effects with respect to the angle θ between the microwave antenna and the external magnetic field, $V_{\mathrm{AMR}} \propto \cos(2\theta)\cos(\theta)$, $V_{\mathrm{AHE}} \propto \cos(\theta)$ [15]. Due to limitations of our experimental setup to perform measurements with respect to θ another approach has been chosen to evaluate the data. This is based on the different signal forms of symmetric and antisymmetric components of V_{meas} as it is shown in Fig. 5a. The ISHE voltage (V_{ISHE}) at the FMR frequency obeys a Lorentz shape curve that can be decomposed into a symmetric and an antisymmetric part [4]. The physical origin of the symmetric part is the ISHE itself together with contributions from AMR and AHE, while the antisymmetric part has only contributions from the AMR and AHE. The $V_{\mathrm{meas}}(\mathrm{H})$ curve can be considered as a function that is formed by symmetric $V^{\mathrm{Sym}}(H)$ and antisymmetric $V^{\mathrm{ASym}}(H)$ parts, where $V^{\mathrm{Sym}}(H) = V_{\mathrm{ISHE}}(H) + V^{\mathrm{Sym}}_{\mathrm{AMR}}(H) + V^{\mathrm{Sym}}_{\mathrm{AHE}}(H)$ and $V^{\mathrm{ASym}}(H) = V^{\mathrm{ASym}}_{\mathrm{AMR}}(H) + V^{\mathrm{ASym}}_{\mathrm{AHE}}(H)$.

The lines in Fig. 4b and in Fig. 5a superimposed on the experimental black open circles data points are a result of a fit containing both symmetric and antisymmetric parts [16]. In order to separate the symmetric ISHE contribution from the overlapping symmetric AMR and AHE signals we have fabricated reference Fe/Al_2O_3samples. By measuring the reference samples, where no V_{ISHE} is expected, we could calculate the symmetric parameter ratio A^{ref} by fitting the spectra of the Fe reference samples with the symmetric and antisymmetric parts, Eq. (1):

$$A^{\mathrm{ref}} = (V^{\mathrm{Sym}}_{\mathrm{AMR}} + V^{\mathrm{Sym}}_{\mathrm{AHE}})/(V^{\mathrm{ASym}}_{\mathrm{AMR}} + V^{\mathrm{ASym}}_{\mathrm{AHE}}) \quad . \tag{1}$$

The antisymmetric contributions on V_{meas} of the Fe/Pt samples can be fitted to the measured curve Fig. 4b and separated from the symmetric contribution. Assuming that the asymmetric part of the reference samples is the same as that of the Fe/Pt samples, we can estimate V_{ISHE} with the help of Eq. (1) by subtracting the symmetric part from the reference samples:

$$V_{\mathrm{ISHE}} = V^{\mathrm{Sym}}_{\mathrm{Fe/Pt}} - (V^{\mathrm{Sym}}_{\mathrm{AMR}} + V^{\mathrm{Sym}}_{\mathrm{AHE}}) = V^{\mathrm{Sym}}_{\mathrm{Fe/Pt}} - A^{\mathrm{ref}} \cdot V^{\mathrm{ASym}}_{\mathrm{Fe/Pt}} \quad . \tag{2}$$

The ISHE current, $I_{\mathrm{ISHE}} = V_{\mathrm{ISHE}}/R$, increases linearly with deposition temperature. V_{ISHE} depends also on the absorbed microwave power at FMR frequency. To be able to compare the capability of different samples to convert an amount of absorbed energy via spin pumping into a DC current, we define the inverse spin Hall efficiency as: $\varepsilon = I_{\mathrm{ISHE}}/P_{\mathrm{Abs}}$, where P_{Abs} is the measured absorbed microwave power via the FMR mechanism. Figure 5b shows that the efficiency rises with deposition temperature that provides smoother and larger grains at the interface and better quality of epitaxial samples.

Furthermore, with the help of the reference samples, we have calculated the characteristic parameter of SP, the effective spin mixing conductance $g^{\uparrow\downarrow}$ [17] for the Fe/Pt samples. $g^{\uparrow\downarrow}$ is a quantifier

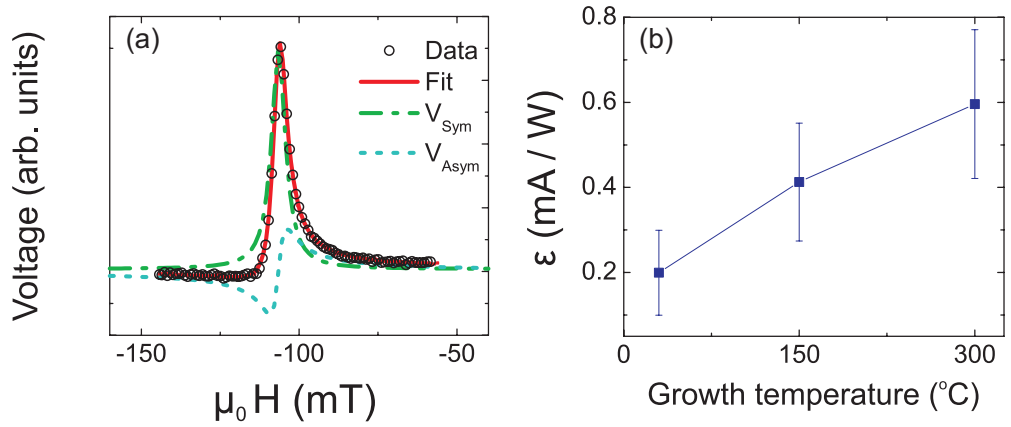

Fig. 5: a) Output measured voltage form. The points refer to measured data, the lines are fitting curves of $V_{\mathrm{meas}}(\mathrm{H})$, with the symmetric and antisymmetric components. b) ISHE efficiency with respect to the growth temperature of the Fe/Pt bilayers. The data were taken for an applied microwave power of 250 mW and refer to the V_{ISHE} peak that corresponds to the saturated state along the hard direction.

of the efficiency of spin pumping since it describes the transfer of angular momentum at the interface to Pt. $g^{\uparrow\downarrow}$ has been evaluated from FMR measurements from the linewidth ΔH of the FMR resonance that depends linearly on the microwave angular frequency, see Fig. 6a. From the linear fit we have calculated the corresponding Gilbert damping parameter α for both the reference Fe/Al_2O_3 and the Fe/Pt sample that we plot in Fig. 6b. $g^{\uparrow\downarrow}$ is then given by: [3, 5, 17]

$$g^{\uparrow\downarrow} = \frac{4\pi M_s^{\mathrm{Fe}} t_{\mathrm{Fe}}}{g\mu_B}\Delta\alpha \quad . \tag{3}$$

where $\Delta\alpha = \alpha_{\mathrm{Fe/Pt}} - \alpha_{\mathrm{Fe/Al_2O_3}}$ is the additional Gilbert damping constant due to the spin pumping. Equation 3 gives $g^{\uparrow\downarrow}$ values that are increasing with the growth temperature and the crystalline quality of the samples. In particular, $g^{\uparrow\downarrow}_{\mathrm{RT}} = (2.04 \pm 0.82)\cdot 10^{19}\ \mathrm{m}^{-2}$, $g^{\uparrow\downarrow}_{150^\circ\mathrm{C}} = (2.26 \pm 0.20)\cdot 10^{19}\ \mathrm{m}^{-2}$, and $g^{\uparrow\downarrow}_{300^\circ\mathrm{C}} = (2.99 \pm 1.01)\cdot 10^{19}\ \mathrm{m}^{-2}$ for the samples grown at RT, 150°C, and 300°C respectively. The obtained values are close to the ones observed in Py/Pt [3], $g^{\uparrow\downarrow} = (2.1 - 2.4)\cdot 10^{19}\mathrm{m}^{-2}$ and one order of magnitude higher than in a single crystalline YIG surface in the YIG/Pt system [9] (reported values for YIG/Pt system though strongly vary in literature between $10^{16}\ \mathrm{m}^{-2}$ and $10^{20}\ \mathrm{m}^{-2}$) [5].

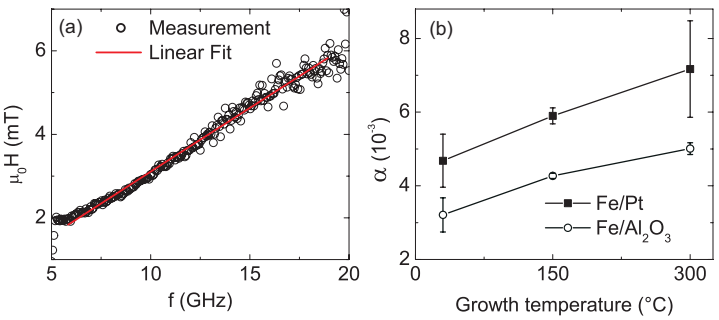

Fig. 6: a) Calculation of the damping from fitting the linewidth of the FMR measurements at different resonant frequencies. The presented data refer to the sample grown at 150°C. b) Gilbert damping constant α for Fe reference and Fe/Pt samples.

In summary, by controlling the epitaxial relationship and the interface morphology in Fe/Pt bilayers we were able to optimize the spin-pumping driven ISHE voltage. By increasing the growth

temperature we have achieved epitaxy of Pt on Fe that led to an increase of the ISHE current and the ISHE efficiency. The spin-pumping induced ISHE voltage shows two distinct ISHE-voltage peaks along the hard magnetization axis revealing its strong dependence on the magnetic anisotropies. The manipulation of the magnon-to-charge current conversion with the crystal symmetry paves the way for further developments of the ISHE and its applications.

This work has been recently published in Applied Physics Letters [10].

Financial support by Deutsche Forschungsgemeinschaft CH 1037/1-1 is gratefully acknowledged. T. Brächer is supported by a fellowship of the Graduate School Materials Science in Mainz (MAINZ) through DFG-funding of the Excellence Initiative (GSC 266).

References

[1] F.D. Czeschka, L. Dreher, M.S. Brandt, M. Weiler, M. Althammer, I.M. Imort, G. Reiss, A. Thomas, W. Schoch, W. Limmer, H. Huebl, R. Gross, S.T.B. Goennenwein, *Scaling behavior of the spin pumping effect in ferromagnet-platinum bilayers*, Phys. Rev. Lett. **107**, 046601 (2011).

[2] H. Nakayama, K. Ando, K. Harii, T. Yoshino, R. Takahashi, Y. Kajiwara, K. Uchida, Y. Fujikawa, E. Saitoh, *Geometry dependence on inverse spin Hall effect induced by spin pumping in $Ni_{81}Fe_{19}$/Pt films*, Phys. Rev. B **85**, 144408 (2012).

[3] O. Mosendz, V. Vlaminck, J.E. Pearson, F.Y. Fradin, G.E.W. Bauer, S.D. Bader, A. Hoffmann, *Detection and quantification of inverse spin Hall effect from spin pumping in permalloy/normal metal bilayers*, Phys. Rev. B **82**, 214403 (2010).

[4] T. Yoshino, K. Ando, K. Harii, *Universality of the spin pumping in metallic bilayer films*, Appl. Phys. Lett. **98**,132503 (2011).

[5] M.B. Jungfleisch, V. Lauer, R. Neb, A.V. Chumak, B. Hillebrands, *Improvement of the yttrium iron garnet/platinum interface for spin pumping-based applications*, Appl. Phys. Lett. **103**, 022411 (2013).

[6] Y. Kajiwara, K. Harii, S. Takahashi, J. Ohe, K. Uchida, M. Mizuguchi, H. Umezawa, H. Kawai, K. Ando, K. Takanashi, S. Maekawa, E. Saitoh, *Transmission of electrical signals by spin-wave interconversion in a magnetic insulator*, Nature **464**, 262 (2010).

[7] V. Castel, N. Vlietstra, J. Ben Youssef, B.J. van Wees, *Platinum thickness dependence of the inverse spin-Hall voltage from spin pumping in a hybrid yttrium iron garnet/platinum system*, Appl. Phys. Lett. **101**, 132414 (2012).

[8] A.V. Chumak, A.A. Serga, M.B. Jungfleisch, R. Neb, D.A. Bozhko, V.S. Tiberkevich, B. Hillebrands, *Direct detection of magnon spin transport by the inverse spin Hall effect*, Appl. Phys. Lett. **100**, 082405 (2012).

[9] Z. Qiu, K. Ando, K. Uchida, Y. Kajiwara, R. Takahashi, H. Nakayama, T. An, Y. Fujikawa, E. Saitoh, *Spin mixing conductance at a well-controlled platinum/yttrium iron garnet interface*, Appl. Phys. Lett. **103**, 092404 (2013).

[10] E.Th. Papaioannou, P. Fuhrmann, M.B. Jungfleisch, T. Brächer, P. Pirro, V. Lauer, J. Lösch, B. Hillebrands, *Optimizing the spin-pumping induced inverse spin Hall voltage by crystal growth in Fe/Pt bilayers*, Appl. Phys. Lett. **103**, 162401 (2013).

[11] V. Karoutsos, P. Papasotiriou, P. Poulopoulos, V. Kapaklis, C. Politis, M. Angelakeris, T. Kehagias, N.K. Flevaris, E.Th. Papaioannou, *Growth modes of nanocrystalline Ni/Pt multilayers with deposition temperature*, J. Appl. Phys. **102**, 043525 (2007).

[12] K. Zakeri, T. Kebe, J. Lindner, M. Farle, *Magnetic anisotropy of Fe/GaAs ultrathin films investigated by in situ ferromagnetic resonance*, J. Magn. Magn. Mater. **299**, L1 (2006).

[13] B. Daniels, W. Nix, B. Clemens, *Enhanced mechanical hardness in compositionally modulated Fe(001)Pt(001) and Fe(001)Cr(001) epitaxial thin films*, Thin Solid Films **253**, 218 (1994).

[14] E. Saitoh, M. Ueda, H. Miyajima, G. Tatara, *Conversion of spin current into charge current at room temperature: Inverse spin-Hall effect*, Appl. Phys. Lett. **88**, 182509 (2006).

[15] H.J. Juretschke, *Electromagnetic Theory of dc Effects in Ferromagnetic Resonance*, J. Appl. Phys. **31**, 1401 (1960).

[16] P. Fuhrmann, *Korrelation des Wachstumsmodus von dünnen Fe/Pt-Schichten zum inversen Spin-Hall-Effekt*, Diplomarbeit, Technische Universität Kaiserslautern (2013).

[17] Y. Tserkovnyak, A. Brataas, G.E.W. Bauer, *Spin pumping and magnetization dynamics in metallic multilayers*, Phys. Rev. B **66**, 224403 (2002).

4.7 Unidirectional spin-wave edge modes in perpendicularly magnetized permalloy structures

F. Ciubotaru, A. V. Chumak, V. I. Vasyuchka, A. A. Serga, and B. Hillebrands

Spin waves in micro- and nano-sized magnetic structures [1–8] have attracted growing attention due to their prospective application in magnon spintronic devices. For example, the use of spin waves as information carriers [9], for magnetic logic operations [10] and for signal processing [3] has been studied. The control of spin-wave excitation and the manipulation of their propagation characteristics over macroscopic distances is of crucial importance for the development of such devices. It is well known that the spin-wave dispersion for in-plane magnetized films strongly depends on the relative orientation of their wavevectors with respect to the magnetization direction. Therefore, to guide spin waves without changing their properties in complex structures involving bends and corners [7, 8, 11] is a challenging task. However, the spin wave dispersion in perpendicularly magnetized films is isotropic since the waves always propagate normal to the bias field. Consequently, this type of waves known as forward volume magnetostatic spin waves (FVMSWs) bears a high potential for information transport through bended waveguides.

In this work we performed systematic micromagnetic simulations [12] to characterize the spin-wave emission from a nano-sized antenna in perpendicularly magnetized permalloy (Py) microstructures. We show that depending on the excitation frequency the same antenna exhibits either a symmetric or an asymmetric spin-wave radiation. Furthermore, we found a uni-directional propagating spin-wave mode localized at the sample edge. We show that this mode can propagate without changing its properties even if the edge includes curves or 90° corners.

The simulated structure consists of a permalloy disc of 10 nm thickness with a diameter of 3 µm magnetized perpendicularly by a static bias field of $B_0 = 1.05\,\mathrm{T}$. Spin waves are excited by the alternating Oersted field associated with a microwave current flowing through a nano-sized antenna placed at the structure edge as defined in Fig. 1. The circularly shaped antenna has a diameter of 500 nm. The simulated area was discretized into $N_x \times N_y \times N_z = 300 \times 300 \times 1$ cells, each cell having a size of $10 \times 10 \times 10$ nm^3. The typical material parameters of Py were used: saturation magnetization $\mu_0 M_0 = 1\,\mathrm{T}$, exchange stiffness constant $A = 1.3 \times 10^{-11}\,\mathrm{J/m}$ and zero magnetocrystalline anisotropy. The damping parameter in the Landau-Lifshitz-Gilbert equation was $\alpha = 0.007$. In real structures the dipolar (demagnetizing) fields are not compensated for the spins located at the edges. Therefore, in the equilibrium position these spins will have different orientations with respect to the external field in order to minimize their energy. To remove this

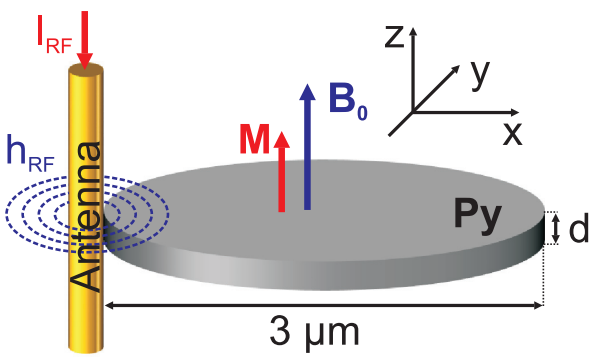

Fig. 1: Sketch of the simulated structure: a perpendicular magnetized permalloy disc with a diameter of 3 µm. Spin waves are excited by the dynamic Oersted field h_{RF} of a microwave current I_{RF} through a nano-sized antenna placed at the edge of the magnetic disc.

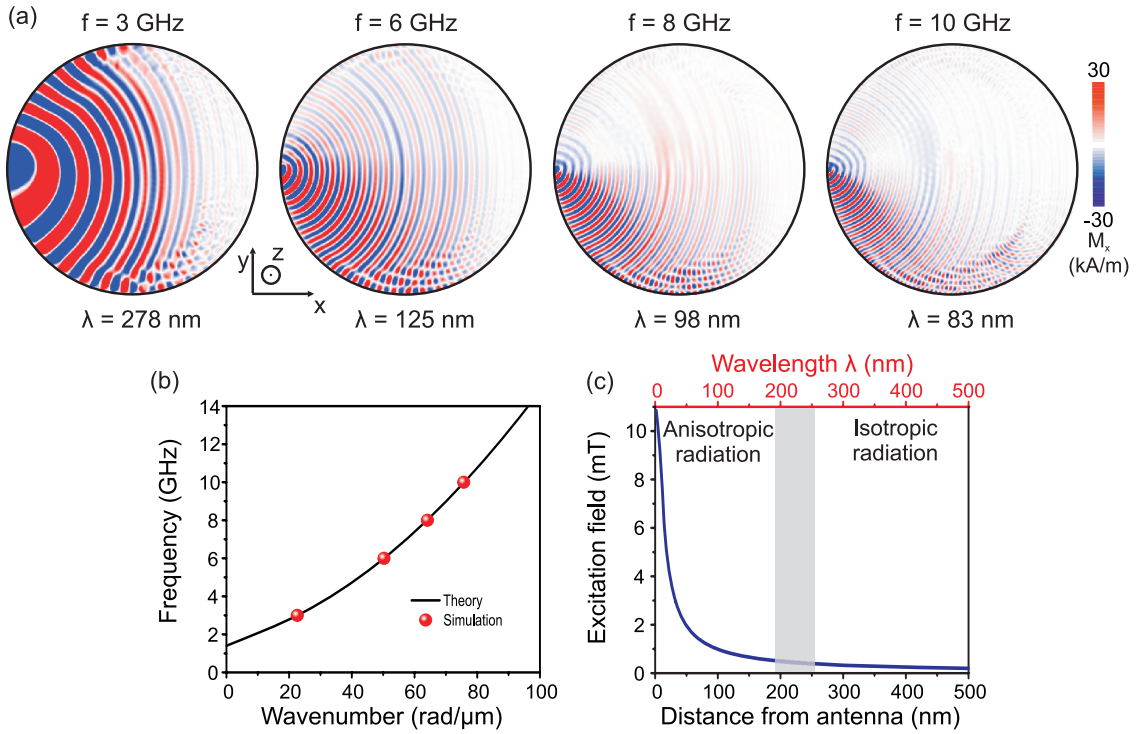

Fig. 2: a) Snapshot images of the magnetization oscillation pattern in a permalloy disc with the in-plane component M_x color coded. The distributions were recorded for different excitation frequencies: 3, 6, 8 and 10 GHz, respectively. b) Spin-wave dispersion relation calculated analytically for a 10 nm thick permalloy film. The red circles denote the wavenumbers extracted from the simulations. c) Spatial distribution of the excitation field. The shaded region marks the uncertainty between the isotropic - anisotropic spin-wave radiation, since the exact limit was not identified from the simulation.

effect and to have a uniform distribution of the internal field over the entire structure we artificially compensated the static demagnetizing field. Within this assumption, the simulated structure corresponds to the effective thickness of a real sample. The applied microwave power was considered sufficiently small to ensure a spin-wave radiation in the linear regime.

The analysis of the spin-wave emission from the antenna as a function of the excitation frequency is presented in Fig. 2. Due to symmetry reasons, forward volume waves are characterized by an isotropic radiation from the antenna. This fact can be clearly observed in Fig. 2a for an excitation frequency of 3 GHz. However, an unconventional behavior in the spin-wave radiation is observed for higher frequencies: An anisotropic spin-wave emission with respect to the excitation antenna. Furthermore, the asymmetric radiation pattern is getting more pronounced if the excitation frequency is increased. In order to understand the origin of the observed anisotropy in the spin-wave emission one might consider the following two mechanisms: 1) different types of waves are excited at higher frequencies; 2) effects caused by the spatio-temporal distribution of the excitation field in combination with the magnetization precession given by $-\mathbf{M} \times \mathbf{B}_{\mathbf{eff}}$, where $\mathbf{B}_{\mathbf{eff}}$ is the effective field. The very good agreement between the spin-wave wavenumbers extracted from simulations and those calculated analytically [13] (see Fig. 2b) evidence the fact that we are dealing only with volume waves in all cases, ruling out mechanism 1. Figure 2c shows the comparison between the spatial distribution of the microwave field and the spin-wave wavelengths extracted from simulations. One can easily observe that for low frequencies the excitation field is confined in a region much smaller than the wavelength of the spin waves. Thus, the excitation field acts as a point source from which the spin waves are isotropically radiated. At higher frequencies the

wavelengths of the spin waves become comparable to the spatial confinement of the microwave field. This means that the spin waves become sensitive to the relative magnitude and orientation of the x and y components of the excitation field. Both components of the microwave field act in phase for one half of the sample and out of phase for the other half. This fact in combination with the gyration motion of the magnetization leads to the observed asymmetry in the radiation pattern. This result is also supported by the fact that the spin-wave radiation asymmetry is mirrored by reversing the bias magnetic field.

The spin-wave radiation changes drastically for thick perpendicularly magnetized structures. For example, Fig. 3a shows a magnetization oscillation pattern obtained from the simulation of a 300 nm thick permalloy disc. The snapshot image was recorded at 1.3 ns after the start of spin-wave excitation. We identify two types of spin waves that are excited in this case: a non-reciprocal spin-wave mode with a relatively large wavelength, which propagates at the edge of the sample, and volume modes with a much shorter wavelength. Although the volume modes all have the same wavelength they derive from different sources. From Fig. 3a one can observe volume modes excited directly by the spin-wave antenna but also modes which are generated by the strong amplitude of the edge mode. The latter ones propagate from the edge towards the center of the disc. The snapshot image of the magnetization pattern recorded after 10 ns (displayed in Fig. 3b) shows clear evidence of the volume mode excited by the edge mode. From Fig. 3c one can notice that the wavenumbers of the volume waves extracted from the simulation match very well the analytical estimation.

The localization of the unidirectional spin-wave mode at the structure edge is a particular feature of this eigenmode and is not due to a potential well, which could be caused by an inhomogeneous internal field [14]. Note that we considered a uniform distribution of the internal field over the entire simulated area (due to compensation of the demagnetizing field). Up to now there is no theory to characterize this edge mode. To some extent one can consider the edge mode to be analogous to magnetostatic surface waves (MSSW) for in-plane magnetized films. In this approach the MSSW would propagate along the disk rim and the disk radius would play the role of the effective film thickness. We fitted the data extracted from the simulation using the conventional formula for the dispersion of the MSSWs [15] in which the film thickness (d) was considered as a free parameter. The values of the other parameters were kept the same as in the simulation. A good agreement between the simulation data and theory (see Fig. 3c) was obtained for $d = 50$ nm, which is much smaller than the disk radius of 1500 nm. Although the obtained value can be treated as an effective thickness, its physical origin should be understood.

Topological chiral edge modes protected against static perturbation were already predicted but for quite specific systems, e.g., systems with Dzyaloshinskii-Moriya interactions [16], or in a magnonic crystal [17]. In order to test the capability of the edge mode described in our work to follow a curved edge we simulated the magnetization dynamics in two structures: a disc with a notch and a bended waveguide, respectively. The parameters for the material and simulations were kept the same as in the previous cases. The snapshot images of the magnetization oscillation pattern for the two structures are displayed in Fig. 3c and 3d, respectively. One can clearly observe that the edge modes follow the structure boundaries without changing its properties in both cases. These observations are of high importance since they demonstrate the existence of spin-wave modes that can propagate inside twisted waveguides made from classical magnetic materials.

In summary, we have investigated spin-wave radiation in perpendicularly magnetized permalloy microstructures. We have found that an anisotropic spin-wave emission with respect to the excitation antenna can be achieved even for the volume waves. Furthermore, we show that the isotropic

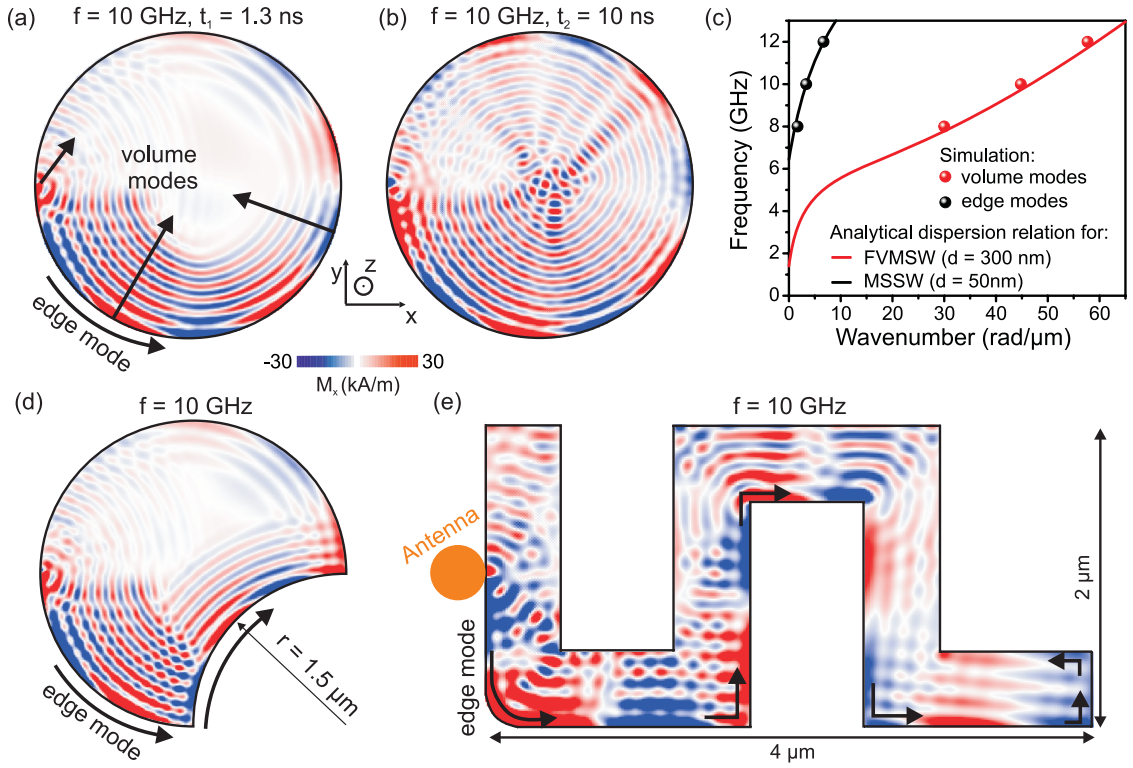

Fig. 3: Snapshot images of the magnetization oscillation pattern in a 300 nm thick permalloy disc recorder at 1.3 ns (a) and at 10 ns (b), respectively, after the start of the spin-wave excitation. c) Dispersion relations calculated analytically for two types of spin waves: magnetostatic forward volume waves (FWMSW) and magnetostatic surface waves (MSSW). The circles denote the wavenumbers extracted from the simulation. Snapshot images of the magnetization oscillation pattern for two permalloy structures: a disc with a notch (c) and a bended waveguide (d), respectively. Shown is the in-plane M_x component.

- anisotropic character of the spin-wave emission can be controlled by the excitation frequency. By increasing the thickness of the sample a unidirectional spin-wave mode localized at the sample edge can be excited. We demonstrate that this mode possesses remarkable characteristics, namely it can propagate following curved edges even if 90° corners are included. These results are important for the realization of magnonic circuits based on bended waveguides.

Financial support by the Deutsche Forschungsgemeinschaft grant SE-1771/1-2 is gratefully acknowledged.

References

[1] B. Lenk, H. Ulrichs, F. Garbs, M. Münzenberg, *The building blocks of magnonics*, Phys. Rep. **507**, 107 (2011).
[2] Y. Au, T. Davison, E. Ahmad, P.S. Keatley, R.J. Hicken, V.V. Kruglyak, *Excitation of propagating spin waves with global uniform microwave fields*, Appl. Phys. Lett. **98**, 122506 (2011).
[3] A.V. Chumak, P. Pirro, A.A. Serga, M.P. Kostylev, R.L. Stamps, H. Schultheiss, K. Vogt, S.J. Hermsdoerfer, B. Laegel, P.A. Beck, B. Hillebrands, *Spin-wave propagation in a microstructured magnonic crystal*, Appl. Phys. Lett. **95**, 262508 (2009).
[4] P. Pirro, T. Brächer, K. Vogt, B. Obry, H. Schultheiss, B. Leven, B. Hillebrands, *Interference of coherent spin waves in micron-sized ferromagnetic waveguides*, Phys. Stat. Sol. B **248**(10), 2404 (2011).
[5] H. Ulrichs, V.E. Demidov, S.O. Demokritov, S. Urazhdin, *Spin-torque nano-emitters for magnonic applications*, Appl. Phys. Lett. **100**, 162406 (2012).
[6] Y. Au, E. Ahmad, O. Dmytriiev, M. Dvornik, T. Davison, V.V. Kruglyak, *Resonant microwave-to-spin-wave transducer*, Appl. Phys. Lett. **100**, 182404 (2012).

[7] K. Vogt, H. Schultheiss, S. Jain, J.E. Pearson, A. Hoffmann, S.D. Bader, B. Hillebrands, *Spin waves turning a corner*, Appl. Phys. Lett. **101**, 042410 (2012).
[8] T. Brächer, P. Pirro, J. Westermann, T. Sebastian, B. Lägel, B. Van de Wiele, A. Vansteenkiste, B. Hillebrands, *Generation of propagating backward volume spin waves by phase-sensitive mode conversion in two-dimensional microstructures*, Appl. Phys. Lett. **102**, 132411 (2013).
[9] Y. Kajiwara, K. Harii, S. Takahashi, J. Ohe, K. Uchida, M. Mizuguchi, H. Umezawa, H. Kawai, K. Ando, K. Takanashi, S. Maekawa, E. Saitoh, *Transmission of electrical signals by spin-wave interconversion in a magnetic insulator*, Nature **464**, 262-266 (11 March 2010).
[10] K.-S. Lee, S.-K. Kim, *Conceptual design of spin wave logic gates based on a Mach-Zehnder-type spin wave interferometer for universal logic functions*, J. Appl. Phys. **104**, 053909 (2008).
[11] X. Xing, Y. Yu, S. Li, X. Huang, *How do spin waves pass through a bend?*, Sci. Rep. **3**, 2958 (2013).
[12] The simulations were performed using the OOMMF open code: M.J. Donahue, D.G. Porter, Report NISTIR 6376, NIST, Gaithersburg, MD, USA (1999)
[13] B.A. Kalinikos, A.N. Slavin, *Theory of dipole-exchange spin wave spectrum for ferromagnetic films with mixed exchange boundary conditions*, J. Phys. C: Solid State Phys. **19**, 7013 (1986).
[14] T. Sebastian, T. Brächer, P. Pirro, A.A. Serga, T. Kubota, H. Naganuma, M. Oogane, Y. Ando, B. Hillebrands, *Nonlinear emission of spin-wave caustics from an edge mode of a micro-structured $Co_2Mn_{0.6}Fe_{0.4}Si$ waveguide*, Phys. Rev. Lett. **110**, 067201 (2013).
[15] A.G. Gurevich, G.A. Melkov, *Magnetization Oscillations and Waves*, Boca Raton, FL: CRC (1996).
[16] L. Zhang, J. Ren, J.-S. Wang, B. Li, *Topological magnon insulator in insulating ferromagnet*, Phys. Rev. B **87**, 144101 (2013).
[17] R. Shindou, R. Matsumoto, S. Murakami, J. Ohe, *Topological chiral magnonic edge mode in a magnonic crystal*, Phys. Rev. B **87**, 174427 (2013).

4.8 Spin-wave propagation in a microstructured YIG/Pt bilayer waveguide

P. Pirro, T. Brächer, A. V. Chumak, B. Leven, and B. Hillebrands

In collaboration with C. Dubs, O. Surzhenko, P. Görnert, INNOVENT e.V., Prüssingstraße 27B, 07745 Jena, Germany

The field of magnon spintronics has received increased attention in the recent years due to the systematic exploration and utilization of the spin pumping effect and the (inverse) spin Hall effect. The combination of these two effects allows for an efficient transformation between conventional charge currents and magnonic currents. In this field, hetero-structures of yttrium iron garnet (YIG) covered with a thin layer of platinum (Pt) have developed into a model system to study the magnon to charge current conversion from an electrical insulator to a normal metal [1–4]. One of the reasons for the success of this combination is the outstanding low Gilbert damping of YIG which makes it also a very promising candidate for the pure magnonic part of magnon spintronics [5]. However, considering potential applications, the generally used large YIG structures with lateral dimensions in the millimeter range need to be miniaturized to enable the construction of on-chip magnonic logic circuits. An advanced type of these circuits could be made up from microstructured YIG waveguides with Pt thin film contact pads. These contact pads would serve on the one hand as an amplifier of the spin-wave propagation via the spin Hall and spin transfer torque effect [6] while on the other hand, they could be used as spin-wave detectors via the spin pumping and inverse spin Hall effect [1].

A big step forward in the development of microstructured YIG has been taken with the recent introduction of methods to produce high quality, low damping YIG films with thicknesses down to several tens of nm or below [7–9]. As up to now, only limited experiments have been performed with microstructured YIG, many questions and experimental challenges still need to be addressed in order to realize YIG/Pt hetero-structures on this scale. For instance, lateral structuring of a film into (sub-)micron wide waveguides requires ion etching which may affect the crystal properties (damping, exchange constant, saturation magnetization) of YIG and, thus, also the spin dynamics of the system. In addition, the influence of the Pt capping on the spin dynamics in YIG has not been fully explored yet.

In this Report, we present experimental results about the excitation of different spin-wave modes and their propagation in a 100 nm thick and 5 µm wide YIG waveguide covered with Pt. The YIG films have been grown by liquid phase epitaxy on a (111) gadolinium gallium garnet substrate (details see [10]). Then, a platinum film of 9 nm thickness has been deposited on top of several

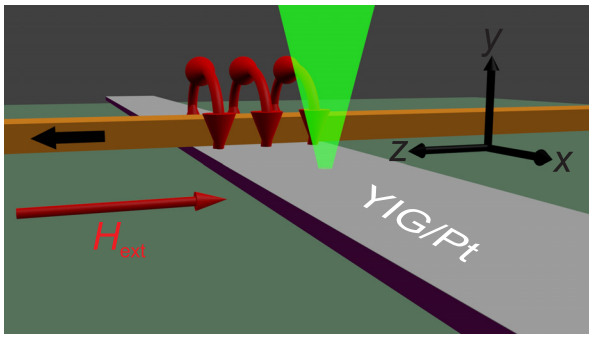

Fig. 1: Sample schematic: In a 5 µm wide waveguide patterned from a bilayer of YIG/Pt (100 nm/9 nm), spin waves are excited using the dynamic Oersted fields of a microwave current flowing in a copper antenna (width 3.5 µm). An external bias field $\mu_0 H_{ext}$ is applied along the short axis of the waveguide to achieve an efficient excitation of spin waves which propagate perpendicular to the static magnetization. The spin waves are detected using microfocus Brillouin light scattering.

cleaned YIG films using RF sputtering. The structuring of the waveguide was achieved afterwards using a protective resist mask and physical argon ion beam etching. As the last production step, a microwave antenna (width 3.5 µm, 520 nm thickness) made of a bilayer of titanium and copper has been deposited on top of the waveguide. Simultaneously, the saturation magnetization M_s and the Gilbert damping α of unstructured films from the same YIG wafer with and without Pt have been measured using ferromagnetic resonance (FMR) to check the influence of the Pt capping. A systematic measurement of the linewidth in the range of $2-14$ GHz enables us to separate the inhomogeneous linewidth ($\mu_0 \Delta H_0 = 0.16$ mT for the uncovered YIG film) from the frequency dependent broadening ($\mu_0 \Delta H$ increases up to 0.47 mT at 14 GHz for the uncovered YIG film) and thus to determine the Gilbert damping parameter α from a linear fit. As expected, the deposition of Pt increases α (from $0.28 \cdot 10^{-3}$ to $1.3 \cdot 10^{-3}$) due to spin interface effects, but M_s remains unchanged within the accuracy of the measurement ($M_s = 144 \pm 2$ kA/m).

To detect the spin-wave spectrum of the structure experimentally, we employ microfocus Brillouin light scattering as this method allows us to study the spin-wave intensity not only as a function of the magnetic field and the excitation frequency, but also space-resolved with a lateral resolution of about 250 nm. The spatial resolution of this technique is especially important as the detection of propagating spin waves via spin pumping and inverse spin Hall effect is a method which integrates the spin-wave intensity of all modes over the whole detection area and is, thus, unable to identify the different contributing spin-wave modes directly [1, 2].

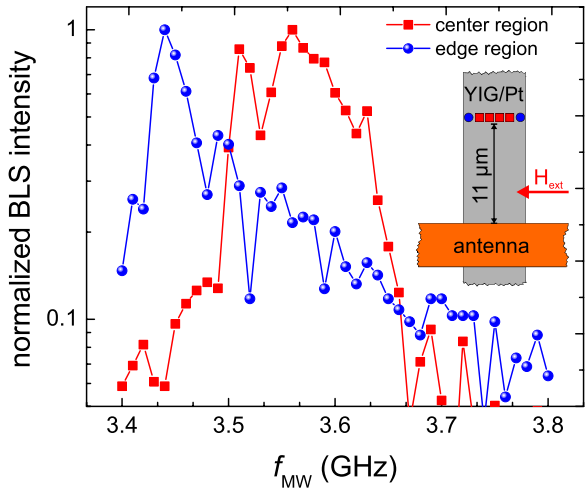

Fig. 2: Normalized Brillouin light scattering intensity as a function of the applied microwave frequency f_{MW}. The blue line with circular dots shows the spectrum measured at the edges of the waveguide (see inset). The red line with rectangular dots is an average of the different spectra from the center of the waveguide.

To achieve an efficient spin-wave excitation, we apply a static magnetic field of 70 mT perpendicular to the long axis of the waveguide. The dynamic Oersted field of a pulsed microwave current (pulse duration 3 µs, pulse repetition 5 µs) passing through the antenna exerts a torque on the static magnetization. This configuration results in an efficient excitation of Damon-Eshbach like spin waves which propagate perpendicular to the static magnetization. A microwave power of 0 dBm in the quasi-linear regime, where nonlinearity is not significantly influencing the spin-wave propagation, has been chosen. To obtain a first characterization of the excitation spectrum, microfocus Brillouin light scattering spectra as a function of the applied microwave frequency have been taken at different positions along the width of the waveguide at a distance of 11 µm from the antenna. Figure 2 shows the averaged spectrum of the edge regions and of the center of the waveguide. The main excitation in the center of the waveguide takes place at frequencies between $f_{MW} = 3.49 - 3.66$ GHz and we will refer to these spin-wave modes as the *waveguide modes*.

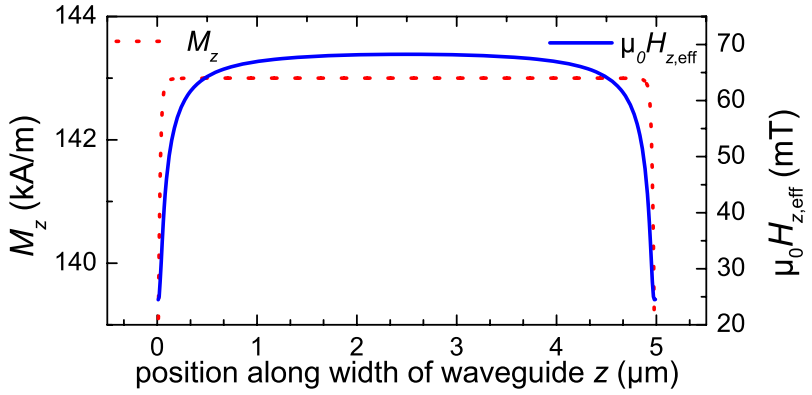

Fig. 3: Effective magnetic field $\mu_0 H_{z,\mathrm{eff}}$ and magnetization M_z along the external field for a YIG waveguide with homogenous saturation magnetization of $M_\mathrm{s} = 143\,\mathrm{kA/m}$, 100 nm thickness, 5 µm width, exchange constant $A = 3.5\,\mathrm{pA/m}$ and an external field of $\mu_0 H_\mathrm{ext} = 70\,\mathrm{mT}$ along the short axis (simulation using ref. [13]).

At the borders of the waveguide, *edge modes* around $f_\mathrm{MW} = 3.44\,\mathrm{GHz}$ show up. The reason for the appearance of these edge modes is the inhomogeneous distribution of the effective magnetic field H_eff and the z-component of the static magnetization M_z, a situation which has been analyzed experimentally and theoretically in detail for metallic systems [11, 12]. H_eff and M_z can be illustrated by calculating the ground state of the system in a micromagnetic simulation [13]. Figure 3 shows the two quantities under the assumption of a constant saturation magnetization M_s over the width of the waveguide (see caption for parameters). In the central region from $z = 1 - 4\,\mu\mathrm{m}$, field and magnetization are practically constant what leads to the appearance of waveguide modes in this area. In the region close to the edges, the effective field H_eff inside the waveguide is reduced by more than 50 % due to the demagnetizing fields emerging from the magnetic surface charges at the edges of the waveguide. This effective field well can be responsible for the localized edge modes with frequencies below the waveguide mode frequencies. In contrast, the magnetization in the direction of the external field drops only by about 2 % for this scenario and the effect of this reduction on the spin waves is negligible.

To get a better understanding of the nature of the involved spin-wave modes and to check the validity of the assumptions made in the micromagnetic simulation of Fig. 3, the spin-wave intensity as a function of the excitation frequency is measured at a distance of 5 µm from the antenna (see Fig. 4). The evolution of the modes can now be seen clearly: for frequencies below $f_\mathrm{MW} = 3.45\,\mathrm{GHz}$, the spin-wave intensity is completely confined to the edges of the waveguide. In the range $f_\mathrm{MW} = 3.45 - 3.50\,\mathrm{GHz}$, the maximum of the intensity is also located near the edges, but two additional local maxima closer to the center of the waveguide appear. For frequencies in the range of $3.50 - 3.57\,\mathrm{GHz}$, the mode which is commonly labeled as the third waveguide mode $n = 3$ (n denotes the number of intensity maxima across the width of the waveguide) is observed. For higher f_MW, the first waveguide mode $n = 1$ is predominantly detected.

We can compare the experimental results to theoretical considerations. For the waveguide modes, the thin film theory [14] with the appropriate effective field from micromagnetic simulations and a wave vector quantization over the waveguide's short axis provides an accurate description of the spin-wave mode dispersions [15–17] if the saturation magnetization and the effective field are homogeneous over the quantization width. Figure 5 shows the dispersion relations and the excitation efficiencies of the waveguide modes $n = 1, 3, 5$. Only odd waveguide modes can be efficiently excited [16, 18] (even modes have no net dynamic magnetic moment averaged over the width of the waveguide) using direct antenna excitation. The minimal frequencies of these three modes are also indicated for comparison in Fig. 4 as dashed lines. Considering the first and the third waveguide mode, we find a reasonable agreement between theory and experiment. The

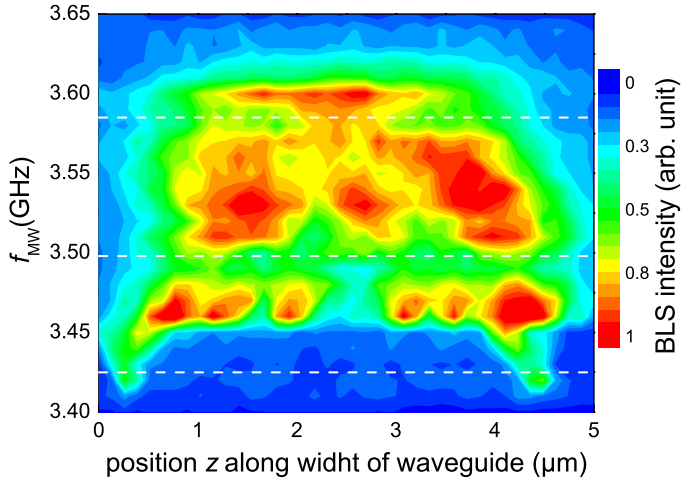

Fig. 4: Brillouin light scattering intensity as function of the position along the width of the waveguide (z-axis in Fig. 1) for different excitation frequencies f_{MW} for an external field of 70 mT. Frequencies below 3.45 GHz show strongly localized edge modes which start to extend into the center of the waveguide for frequencies between $3.45 - 3.50$ GHz. For higher f_{MW}, waveguide modes appear which have a local intensity maximum in the center of the waveguide. The dashed lines indicate the calculated minimal frequencies of the waveguide modes shown in Fig. 5.

fifth and higher waveguide modes are not visible in the experiment. As the excitation efficiency decreases approximately with $1/n^2$, this is due to a small precession amplitude of these modes. In fact, the experimental findings reveal that in the frequency range below 3.5 GHz, the edge modes are either excited more efficiently or have a lower spatial damping compared to the waveguide modes.

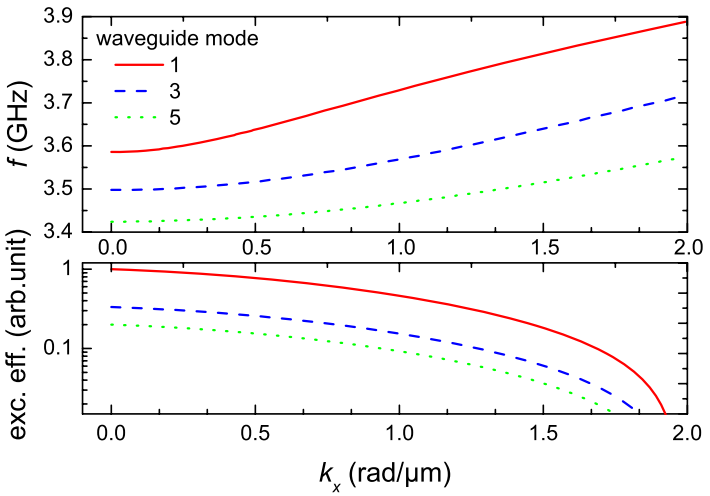

Fig. 5: Dispersion relations and excitation efficiencies for the first three odd waveguide modes of a transversally magnetized YIG waveguide calculated according to [14] with parameters from Fig. 3 ($\mu_0 H_{eff} = 68$ mT, effective width = 4.0 µm) for an antenna width of 3.5 µm.

As it is evident from the dispersion relations in Fig. 5, several spin-wave modes can coexist at one excitation frequency. This can lead to complex interference patterns which cannot be depicted completely by the mode profiles of Fig. 4, as they only display the spin-wave intensity at a fixed distance from the antenna. To visualize the interference of the different modes and their spatial decay, Fig. 6 shows 2D spin-wave intensity maps for different f_{MW}. Due to the different wavelengths and decay lengths, the mode profiles change drastically along the propagation direction (x). The waveguide modes which appear at $f > 3.59$ GHz have the highest overall propagation length, but for lower frequencies, edge modes can be identified as the ones with the largest decay length. A closer analysis of the spatial distribution of the edge modes and their frequencies has been performed using additional dynamic micromagnetic simulations, which show that the small frequency separation between edge and waveguide modes and the relatively high distance of the edge mode intensity maxima to the waveguide's edges (up to 1.5 µm) cannot be explained

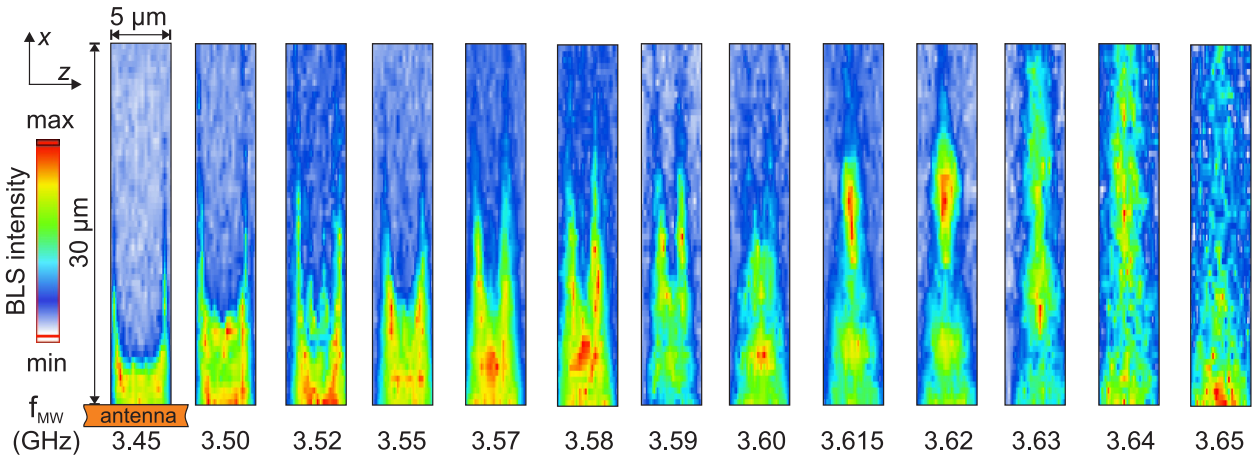

Fig. 6: Brillouin light scattering intensity maps at different excitation frequencies f_{MW} ($\mu_0 H_{\mathrm{ext}} = 70\,\mathrm{mT}$). Starting from $f_{\mathrm{MW}} = 3.45\,\mathrm{GHz}$, the spin-wave intensity maxima of the edge modes are shifted towards the middle of the waveguide with growing f_{MW} until pure waveguide modes with intensity maxima in the middle of the waveguide are excited for $f_{\mathrm{MW}} > 3.6\,\mathrm{GHz}$.

if a homogeneous saturation magnetization is assumed. Indeed, the simulations suggest that the continuous movement of the edge mode's intensity maxima towards the waveguide center with increasing spin-wave frequency can be understood using a saturation magnetization profile with a significant drop towards the edges of the waveguide. Another experimental observation supports the interpretation that the magnetic properties of the waveguide are inhomogeneous. Especially for $f_{\mathrm{MW}} > 3.60\,\mathrm{GHz}$, distinct Brillouin light scattering intensity maxima in the x-direction are observed which cannot be explained by the interference of different propagating spin-wave modes. Besides the effect of an additional interference of the propagating spin waves with the direct excitation by the out-of-plane field of the antenna, we identify microscopic inhomogeneities in the YIG crystal as being responsible for this effect. They can lead to scattering and reflection of spin waves and thus to the formation of quasi-standing spin-wave interference patterns. The inhomogeneities could be already present in the unstructured YIG films, but an influence of the ion beam patterning is likely as the material parameters of YIG are rather sensitive to distortions of the crystal lattice. Thus, the saturation magnetization, exchange constant and the damping could be affected due to the finite resolution of the ion beam etching process (caused by the angular distribution and the scattering of the incoming argon ions) which leads, especially at the edges of the waveguide, to a residual ion dose in YIG. In addition, patterning of a single crystal film can lead to additional stress in the remaining parts influencing the magnetic properties via magnetostriction.

An important parameter for magnon spintronics is the spin-wave decay length which might be deduced quantitatively from the 2D intensity maps in Fig. 6. But due to the complicated mode structure and the possible reflections mentioned above, the analysis of the decay length can only be performed for selected frequencies. Fitting spin-wave intensity (integrated over the width of the waveguide) along the propagation direction, we obtain an exponential decay length of the spin-wave amplitude of approximately $\delta_{Amp} = 31\,\mu\mathrm{m}$ (for $f_{\mathrm{MW}} = 3.60\,\mathrm{GHz}$) which is substantially larger than decay lengths reported for metallic microstructures [16, 19]. This value can be compared to the expected theoretical value $\delta_{\mathrm{Amp}} = v_g \tau$, where v_g is the group velocity and τ is the life time of the spin wave. The Gilbert damping of the (unpatterned) YIG/Pt bilayer ($\alpha = 1.3 \cdot 10^{-3}$) is equal to a life time $\tau \approx 28\,\mathrm{ns}$ for our experimental parameters which is large compared to metallic thin films (maximal $\tau_{metal} \approx 3\,\mathrm{ns}$). The group velocity v_g can be deduced from the dispersion relations in Fig. 5 or from dynamic micromagnetic simulations. Both methods yield a maximum

$v_{g,\max} \approx 1.0 - 1.1\,\mu\text{m/ns}$, so the theoretically estimated decay length is $\delta_{\text{Amp}} = 28 - 31\,\mu\text{m}$ for the maximum v_g. The agreement with our experimental findings is good if one considers that the plain film values of α and M_s, which might have been changed during the patterning process, have been used for the calculation. This indicates that the change of the material properties is concentrated to the edges of the waveguide and thus its influence on the decay length of the waveguide modes is not significant.

To conclude, we have presented experimental studies of spin-wave excitation and propagation in microstructured YIG/Pt bilayer waveguides. Depending on the chosen microwave frequency, different edge and waveguide modes have been excited. The patterning process seems to affect the mode structure most notably at the edges of the waveguide. As expected, the deposition of Pt leads to an enhanced Gilbert damping compared to the pure YIG case. However, the experiment shows that the life time of the spin waves in the microstructured YIG/Pt bilayer is still more than an order of magnitude higher than in the usually used metallic systems what leads to a high decay length of $\delta_{\text{Amp}} = 31\mu\text{m}$. Further studies based on our results could make use of the spin Hall and spin transfer torque effect to directly reduce the damping by applying a DC current to the Pt. Together with the detection of spin waves in microstructures via the spin pumping and the inverse spin Hall effect, low damping, insulator based micro magnonic circuits become feasible.

We acknowledge financial support by OPTIMAS Carl-Zeiss Doktoranden-Programm. T. Brächer is supported by a fellowship of the Graduate School Materials Science in Mainz (MAINZ) through DFG-funding of the Excellence Initiative (GSC 266).

References

[1] A.V. Chumak, A.A. Serga, M.B. Jungfleisch, R. Neb, D.A. Bozhko, V.S. Tiberkevich, B. Hillebrands, *Direct detection of magnon spin transport by the inverse spin Hall effect*, Appl. Phys. Lett. **100**, 082405 (2012).

[2] M.B. Jungfleisch, A.V. Chumak, V.I. Vasyuchka, A.A. Serga, B. Obry, H. Schultheiss, P.A. Beck, A.D. Karenowska, E. Saitoh, B. Hillebrands, *Temporal evolution of inverse spin Hall effect voltage in a magnetic insulator-nonmagnetic metal structure*, Appl. Phys. Lett. **99**, 182512 (2011).

[3] C.W. Sandweg, Y. Kajiwara, K. Ando, E. Saitoh, B. Hillebrands, *Enhancement of the spin pumping efficiency by spin wave mode selection*, Appl. Phys. Lett. **97**, 252504 (2010).

[4] C.W. Sandweg, Y. Kajiwara, A.V. Chumak, A.A. Serga, V.I. Vasyuchka, M.B. Jungfleisch, E. Saitoh, B. Hillebrands, *Spin pumping by parametrically excited exchange magnons*, Phys. Rev. Lett. **106** (21), 216601 (2011).

[5] A.A. Serga, A.V. Chumak, B. Hillebrands, *YIG magnonics*, J. Phys. D: Appl. Phys. **43**, 264002 (2010).

[6] H. Ulrichs, V.E. Demidov, S.O. Demokritov, W.L. Lim, J. Melander, N. Ebrahim-Zadeh, S. Urazhdin, *Optimization of Pt-based spin-Hall-effect spintronic devices*, Appl. Phys. Lett. **102**, 2402 (2013).

[7] O. d'Allivy Kelly, A. Anane, R. Bernard, J. Ben Youssef, C. Hahn, A.H. Molpeceres, C. Carrétéro, E. Jacquet, C. Deranlot, P. Bortolotti, R. Lebourgeois, J.C. Mage, G. de Loubens, O. Klein, V. Cros, A. Fert, *Inverse spin Hall effect in nanometer-thick yttrium iron garnet/Pt system*, Appl. Phys. Lett. **103**, 082408 (2013).

[8] N. Kumar, D.S. Misra, N. Venkataramani, S. Prasad, R. Krishnan, *Magnetic properties of pulsed laser ablated YIG thin films on different substrates*, J. Magn. Magn. Mater. **272**, E899 (2004).

[9] V. Castel, N. Vlietstra, J. Ben Youssef, B.J. van Wees, *YIG thickness and frequency dependence of the spin-charge current conversion in YIG/Pt systems*, arXiv: cond-mat.mtrl-sci, 1304.2190 (2013).

[10] YIG films were prepared form a PbO-B_2O_3-FeO_3 flux melt using standard isothermal dipping technique with a growth rate of $20\,\text{nm/s}$. The incorporation of Pb and Pt ions into the garnet lattice allows for a relative lattice mismatch lower than $9 \cdot 10^{-4}$.

[11] G. Gubbiotti, M. Conti, G. Carlotti, P. Candeloro, E.D. Fabrizio, K.Y. Guslienko, A. André, C. Bayer, A.N. Slavin, *Magnetic field dependence of quantized and localized spin wave modes in thin rectangular magnetic dots*, J. Phys.: Condens. Matter **16**, 7709 (2004).

[12] C. Bayer, J.P. Park, H. Wang, M. Yan, C.E. Campbell, P.A. Crowell, *Spin waves in an inhomogeneously magnetized stripe*, Phys. Rev. B **69**, 134401 (2004).

[13] M.J. Donahue, D.G. Porter, Interagency Report NISTIR **6376**, National Institute of Standards and Technology, Gaithersburg, MD (Sept 1999).

[14] B.A. Kalinikos, A.N. Slavin, *Theory of dipole-exchange spin wave spectrum for ferromagnetic films with mixed exchange boundary conditions*, Journal of Physics C: Solid State Physics, **19** pp. 7013, (1986).
[15] K. Vogt, H. Schultheiss, S.J. Hermsdoerfer, P. Pirro , A.A. Serga, B. Hillebrands, *All-optical detection of phase fronts of propagating spin waves in a $Ni_{81}Fe_{19}$ microstripe*, Appl. Phys. Lett. **95**, 182508 (2009).
[16] P. Pirro, T. Brächer, K. Vogt, B. Obry, H. Schultheiss, B. Leven, B. Hillebrands, *Interference of coherent spin waves in micron-sized ferromagnetic waveguides*, Phys. Stat. Sol. B **248**, No. 10, 2404-2408, (2011).
[17] T. Brächer, P. Pirro, B. Obry, B. Leven, A.A. Serga, B. Hillebrands, *Mode selective parametric excitation of spin waves in a $Ni_{81}Fe_{19}$ microstripe*, Appl. Phys. Lett. **99**, 162501 (2011).
[18] V.E. Demidov, M.P. Kostylev, K. Rott, P. Krzysteczko, G. Reiss, S.O. Demokritov, *Excitation of microwaveguide modes by a stripe antenna*, Appl. Phys. Lett. **95**, 112509 (2009).
[19] T. Sebastian, Y. Ohdaira, T. Kubota, P. Pirro, T. Brächer, K. Vogt, A.A. Serga, H. Naganuma, M. Oogane, Y. Ando, B. Hillebrands, *Low-damping spin-wave propagation in a micro-structured $Co_2Mn_{0.6}Fe_{0.4}Si$ Heusler waveguide*, Appl. Phys. Lett. **100**, 112402 (2012).

4.9 Realization of a micro-structured spin-wave multiplexer

K. Vogt, T. Sebastian, and B. Hillebrands

In collaboration with H. Schultheiss, F. Y. Fradin, J. E. Pearson, S. D. Bader, A. Hoffmann, Center for Nanoscale Materials, Argonne National Laboratory, Argonne, IL 60439, USA[1]

In this Report, we address fundamental issues associated with a novel magnonic approach for information transport and processing [1–7]. Magnons are the spin-wave excitation quanta of magnetic materials. They can be understood classically as the collective precession of the electrons' spins. The collective nature is mediated by the short-range quantum-mechanical exchange interaction, as well as the non-local magnetic dipole interaction. Spin waves carry spin angular momentum, as do electrons in spintronic applications [8,9], and enable the coherent transport of information encoded in its phase and amplitude. However, in contrast to spin-polarized electron-based spintronics, spin waves do not require dissipative charge transport. Spin waves also propagate over significantly larger distances compared to typical electron spin diffusion lengths in metals or semiconductors, even at room temperature. Furthermore, spin waves have the advantage that their frequencies increase faster for decreasing feature sizes in comparison to electromagnetic waves. Thus, even at $0.1 - 1\,\mathrm{THz}$, spin-wave wavelengths can be as short as only a few nanometers, which is orders of magnitudes smaller compared to electromagnetic waves. This facilitates higher integration density in spin-wave logic devices.

Spin waves exhibit a peculiarity that differentiates them from light or sound waves: their dispersion relation is highly anisotropic [10, 11]. This means that their energy significantly depends on the relative angle between their propagation direction and the magnetization orientation. As a result, if the magnetic material is exposed to a uniform external magnetic field, the spin waves will travel in the preferred direction with respect to the magnetization orientation. The need for such external magnetic fields has hampered the development of spin-wave devices that are based on combining spin waves in two dimensions.

Herein, we demonstrate a simple implementation of a micro-structured spin-wave multiplexer, which serves as an initial step toward the development of a viable spin-wave-based processor. In our approach, locally generated magnetic fields, rather than a uniform external field, alter the magnetization direction solely in designated regions of the spin-wave multiplexer. This enables us to tailor the dispersion relation in different parts of the structure to our advantage [12]. Thereby, we exploit the unique feature of the anisotropic dispersion relation of spin waves, and, thus, are able to switch spin-wave propagation directions.

Figure 1a shows an optical microscope image of the device. Using electron beam lithography and lift-off techniques, a 30 nm thick $Ni_{81}Fe_{19}$ (permalloy, Py) layer was patterned into a Y-shaped spin-wave waveguide having a constant width of 2 µm and an opening angle of 60°. In order to control the magnetization direction in the Y structure with local Oersted fields, a 50 nm thick and 3 µm wide Au conduit was fabricated below the spin-wave waveguide. Leads at the three ends of the Au conduit allow for connecting either its base and left arm (switch in Fig. 1a in position S1) or its base and right arm (switch in position S2) to an electric current source, respectively. In order to keep the electric current from flowing in the magnetic material, a 50 nm thick MgO layer serves

[1] Current affiliation of Helmut Schultheiss: Institut für Ionenstrahlphysik und Materialforschung, Helmholtz-Zentrum Dresden-Rossendorf, D-01328 Dresden, Germany

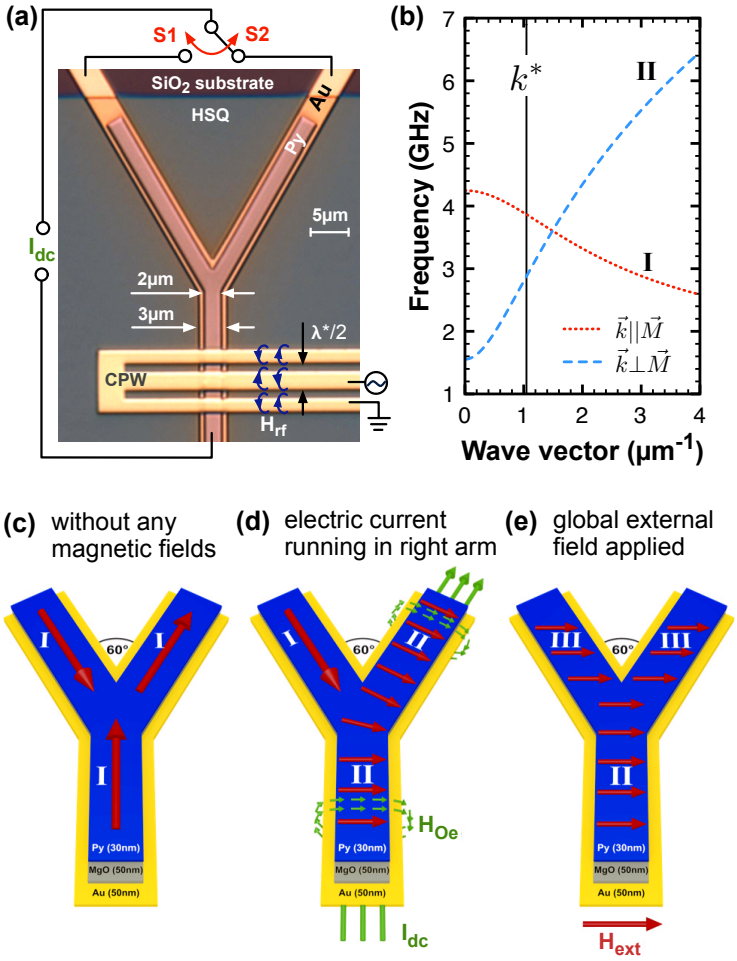

Fig. 1: (a) Microscope image showing the spin-wave multiplexer, the microwave antenna (CPW) and the leads for *dc* connections. (b) Dispersion relations for perpendicular (dashed line) and parallel (dotted line) alignment of the spin-wave wave vector **k** and the magnetization **M**, corresponding to regions I and II in the schematics of the magnetization distribution. (c)-(e) Magnetization configurations in remanence (d), with locally generated Oersted fields $\mathbf{H}_{\mathrm{Oe}}$ (d) and with an externally applied magnetic field $\mathbf{H}_{\mathrm{ext}}$ (d), respectively.

as an insulator from the gold conduit. A microwave current in the shorted coplanar waveguide (CPW) generates oscillating magnetic fields $\mathbf{H}_{\mathrm{rf}}$ that excite spin waves in the Py waveguide.

For in-plane magnetized films, the anisotropic dispersion relation favors propagation perpendicular to the magnetization direction **M**. As depicted by the dispersion relations [13, 14] in Fig. 1b, a perpendicular orientation between the spin-wave wave vector **k** and the magnetization direction **M** (dashed line, geometry II) results in a higher group velocity, which is given by the slope of the dispersion, compared to the case of parallel alignment (dotted line, geometry I). Thus, spin-wave transport perpendicular to **M** suffers less spatial decay. Without any applied magnetic field, however, the shape anisotropy of the micro-structured waveguide forces the magnetization to align along the spin-wave waveguide, as is depicted in Fig. 1c, since magnetic moments pointing transverse to the waveguide give rise to energetically unfavorable magnetic surface charges. In the absence of additional magnetic anisotropies, the energy that is required to maintain a transverse magnetization needs to be provided by an external magnetic field. In the spin-wave multiplexer presented here, local Oersted fields $\mathbf{H}_{\mathrm{Oe}}$ are induced by the electric current flowing in the gold conduit. As a consequence, the magnetization configuration inside the Y-shaped micro-structure can be controlled in several ways: Without any external magnetic field and any direct current in

the Au conduits, **M** is in remanence and aligns along the boundaries of the waveguide, as shown in Fig. 1c. If a direct current I_{dc} runs in the base and the right arm of the Y structure, as is the case in Fig. 1d, only the magnetic moments in this region will be forced to point transverse to the waveguide. Consequently, a spin wave that is excited in the base of the Y structure will propagate along the path that provides an undisturbed magnetization configuration, i.e., into the right arm. If a uniform external magnetic field $\mathbf{H}_{ext}$ is applied, the magnetic moments of the $Ni_{81}Fe_{19}$ will be aligned along the direction of this field, as illustrated in Fig. 1e. Consequently, the angle between **M** and the spin-wave wave vector **k** will change in the transition between the base and both arms, prohibiting spin-wave propagation beyond the junction of the Y structure, as we show below.

In order to evaluate the functionality of the proposed spin-wave multiplexer, we employed Brillouin light scattering (BLS) microscopy, a technique that utilizes the inelastic scattering of focused laser light on spin waves. Analysis of the scattered light with a high-resolution interferometer enables the direct mapping of the spin-wave intensity distribution with a spectral resolution of 100 MHz and a spatial resolution of 250 nm [15, 16].

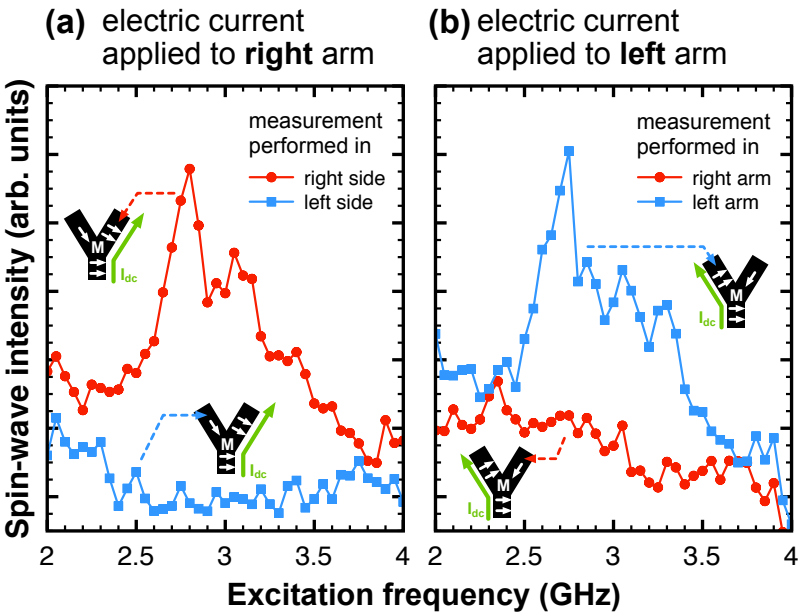

Fig. 2: Spin-wave intensities measured for excitation frequencies ranging from 2 – 4 GHz and an electric current of 100 mA flowing in the right (a) and left (b) arm of the Y structure. For both magnetization configurations, red circles denote the spin-wave intensity inside the right arm, whereas blue squares denote the intensity inside the left arm, both measured at 4.5 µm distance from the Y junction.

Measuring the BLS intensity for various excitation frequencies inside the arms of the Y-shaped multiplexer enables us to determine that the spin-wave propagation path can be switched. In Fig. 2a, 100 mA current pulses were applied to the right arm only. In order to avoid excessive heating, we applied current pulses with a duration of 150 ns and a repetition rate of 3 µs. The spin waves were excited by 100 ns microwave pulses synchronized to the *dc* pulses. For excitation frequencies ranging from 2 – 4 GHz, we then recorded the spin-wave intensity 4.5 µm behind the Y junction in the right (red circles) and left arm (blue squares). As can be seen, spin waves are solely detected inside the right arm where the magnetization is forced to the preferred propagation geometry II by the local Oersted fields (compare Fig. 1d). The measurement inside the left arm does not yield a spin-wave signal. The situation is reversed if the electric current is flowing in the left arm of the gold conduit, as is shown in Fig. 2b. Only the measurement in the left arm shows a spin-wave signal (blue squares). This confirms the functionality of the spin-wave multiplexer. Utilizing the electric current, we are able to switch the spin-wave propagation direction between the two arms of the Y-shaped waveguide.

A closer look at Fig. 2 reveals that only spin waves in the frequency range between $2.5-3.4\,\mathrm{GHz}$ propagate beyond the junction of the multiplexer. This is related to the spin-wave dispersion relation as well as the excitation efficiency of the antenna. The small blue arrows in Fig. 1a illustrate the oscillating magnetic fields $\mathbf{H}_{\mathrm{rf}}$ generated by the coplanar waveguide. Its periodicity imposes a wavelength of $\lambda^* = 6\,\mu\mathrm{m}$ and, thus, a wave vector of $k^* = 1.05\,\mathrm{rad}/\mu\mathrm{m}$ for which spin waves are excited most efficiently. As can be seen from the dashed dispersion relation in Fig. 1b, this wave vector corresponds to a frequency of 2.75 GHz, matching the frequency for which the spin-wave intensities detected in Fig. 2 reach their maxima. For lower and higher frequencies, the excitation efficiency of the antenna drops drastically. In addition, evaluating the slope of the dispersion relation shows that the group velocity is largest for the same spin-wave frequency of 2.75 GHz. Consequently, spin waves excited at this frequency propagate a longer distance before they attenuate and, thus, can be detected inside the arms.

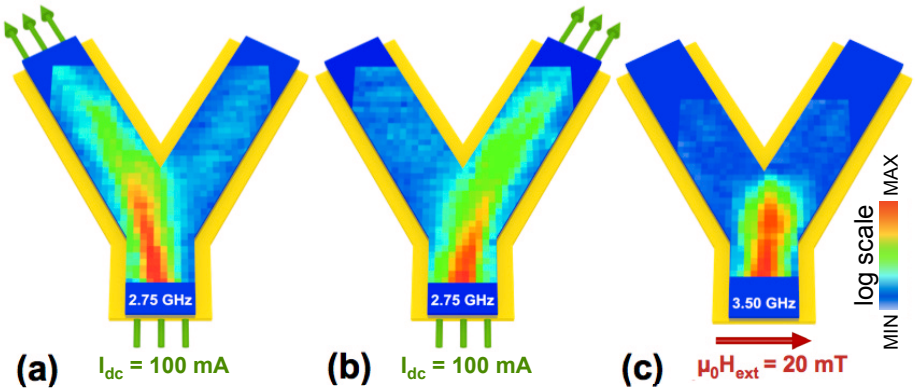

Fig. 3: Two-dimensional mapping of the spin-wave propagation path illustrating the switching: For a direct current of 100 mA applied to the left (a) and right (b) arm of the Y structure, respectively, the spin waves at 2.75 GHz are guided through the Y junction and only propagate in the same direction as the current flow. (c) Saturation with an external magnetic field $\mathbf{H}_{\mathrm{ext}}$ obscures any spin-wave transport beyond the junction.

Ultimate evidence for the functionality of the spin-wave multiplexer is obtained from the measured two-dimensional spin-wave intensity distributions. For the switching experiment, an excitation frequency of 2.75 GHz was chosen to match the maximum intensity that was previously determined inside the arms (see Fig. 2). Figure 3a illustrates the case for current pulses with 100 mA amplitude flowing in the left arm of the Au conduit. The spin-wave intensity scale is logarithmic and color coded where red (white) represents maximum (minimum) intensity. It is obvious that with the current flowing in the left pathway, the spin wave reaches the bifurcation and turns into the left arm only. Inside the right arm, no spin-wave intensity can be detected. When the 100 mA current pulses are applied to the right arm, as is the case in Fig. 3b, the spin wave only propagates into the right arm. This illustrates the possibility to switch the information channel in the proposed spin-wave multiplexer by means of locally generated Oersted fields. Surprisingly, Fig. 3c shows that spin-wave propagation is entirely prohibited behind the Y junction in case a uniform external magnetic field is applied. Spin waves are known to adiabatically adjust their wavelength in regions of inhomogeneous magnetic field strengths to compensate for magnetic field-induced shifts of the dispersion [17, 18]. But, apparently, spin-wave transport is prohibited if the relative orientation between the magnetization direction and the spin-wave wave vector changes. This provides new ways to manipulate spin-wave transport in magnetic micro-structures.

In conclusion, we have demonstrated how the spin-wave propagation path can be manipulated

in a prototype spin-wave multiplexer on the micrometer scale using locally generated magnetic fields. We want to emphasize that the dimensions of the devices discussed here were chosen to optimize the optical investigation of their operation. However, there are no physical limitations for miniaturizing them into the nanometer regime. Furthermore, the same approach can be adapted to ferromagnetic insulators, such as yttrium iron garnet, where the damping of the magnetization dynamics is greatly reduced and therefore the spin-wave propagation distance is significantly increased [19]. Lastly, while we use Oersted fields to readily vary local magnetic fields, it is also conceivable to use switchable stray fields or direct exchange coupling from adjacent magnetic elements [20], which would enable a low-power operation of the spin-wave multiplexer in more complex magnonic devices.

Financial support by the Carl-Zeiss-Stiftung is gratefully acknowledged. Work at Argonne and use of the Center for Nanoscale Materials was supported by the U.S. Department of Energy - Basic Energy Sciences under Contract No. DE-AC02-06CH11357. K. Vogt's secondment to Argonne was supported by the Graduate School *Materials Science in Mainz* (MAINZ) through DFG-funding of the Excellence Initiative (GSC 266).

References

[1] V.V. Kruglyak, R.J. Hicken, *Magnonics: Experiment to prove the concept*, J. Magn. Magn. Mater. **306**, 191 (2006).
[2] A. Khitun, M. Bao, K.L. Wang, *Spin wave magnetic nanofabric: A new approach to spin-based logic circuitry*, IEEE Trans. Magn. **44**, 9 (2008).
[3] S. Neusser, D. Grundler, *Magnonics: Spin waves on the nanoscale*, Adv. Mater. **21**, 2927 (2009).
[4] V.V. Kruglyak, S.O. Demokritov, D. Grundler, *Magnonics*, J. Phys. D **43**, 264001 (2010).
[5] A. Khitun, M. Bao, K.L. Wang, *Magnonic logic circuits*, J. Phys. D **43**, 264005 (2010).
[6] A. Khitun, K.L. Wang, *Non-volatile magnonic logic circuits engineering*, J. Appl. Phys. **110**, 034306 (2011).
[7] A. Khitun, *Multi-frequency magnonic logic circuits for parallel data processing*, J. Appl. Phys. **111**, 054307 (2012).
[8] S.A. Wolf, D.D. Awschalom, R.A. Buhrman, J.M. Daughton, S. von Molnar, M.L. Roukes, A.Y. Chtchelkanova, D.M. Treger, *Spintronics: A spin-based electronics vision for the future*, Science **294**, 1488 (2001).
[9] S.D. Bader, S.S.P. Parkin, *Spintronics*, Annu. Rev. Condens. Matter Phys. **1**, 71 (2010).
[10] R.W. Damon, J.R. Eshbach, *Magnetostatic modes of a ferromagnetic slab*, J. Phys. Chem. Solids **19**, 308 (1961).
[11] M.J. Hurben, C.E. Patton, *Theory of magnetostatic waves for in-plane magnetized isotropic films*, J. Magn. Magn. Mater. **139**, 263 (1995).
[12] K. Vogt, H. Schultheiss, S. Jain, J.E. Pearson, A. Hoffmann, S.D. Bader, B. Hillebrands, *Spin waves turning a corner*, Appl. Phys. Lett. **101**, 042410 (2012).
[13] K. Vogt, H. Schultheiss, S.J. Hermsdoerfer, P. Pirro, A.A. Serga, B. Hillebrands, *All-optical detection of phase fronts of propagating spin waves in a $Ni_{81}Fe_{19}$ microstripe*, Appl. Phys. Lett. **95**, 182508 (2009).
[14] Material parameters for $Ni_{81}Fe_{19}$ used for calculating the dispersion relations: saturation magnetization: $M_S = 800\,\mathrm{kA/m}$, gyromagnetic ratio: $\gamma/2\pi = 28\,\mathrm{GHz/T}$, and exchange stiffness constant: $A = 16\,\mathrm{pJ/m}$
[15] V.E. Demidov, S.O. Demokritov, B. Hillebrands, M. Laufenberg, P.P. Freitas, *Radiation of spin waves by a single micrometer-sized magnetic element*, Appl. Phys. Lett. **85**, 2866 (2004).
[16] H. Schultheiss, S. Schäfer, P. Candeloro, B. Leven, B. Hillebrands, A.N. Slavin, *Observation of coherence and partial decoherence of quantized spin waves in nanoscaled magnetic ring structures*, Phys. Rev. Lett. **100**, 047204 (2008).
[17] J. Jorzick, S.O. Demokritov, B. Hillebrands, M. Bailleul, C. Fermon, K.Y. Guslienko, A.N. Slavin, D.V. Berkov, N.L. Gorn, *Spin wave wells in nonellipsoidal micrometer size magnetic elements*, Phys. Rev. Lett. **88**, 047204 (2002).
[18] V.E. Demidov, M.P. Kostylev, K. Rott, J. Münchenberger, G. Reiss, S.O. Demokritov, *Excitation of short-wavelength spin waves in magnonic waveguides*, Appl. Phys. Lett. **99**, 082507 (2011).
[19] A.A. Serga, A.V. Chumak, B. Hillebrands, *YIG magnonics*, J. Phys. D **43**, 264002 (2010).
[20] L. O'Brien, D. Petit, E.R. Lewis, R.P. Cowburn, D.E. Read, J. Sampaio, H.T. Zeng, A.-V. Jausovec, *Tunable remote pinning of domain walls in magnetic nanowires*, Phys. Rev. Lett. **106**, 087204 (2011).

C. Magnonic Crystals

A magnonic crystal is a wave transmission medium which features an artificial lattice created by a wavelength-scale modulation in its material properties. Such systems belong to the class of metamaterials: synthetic media with properties derived from an engineered, mesoscopic structure. The wave transmission spectra of magnonic crystals typically include band gaps: frequency intervals over which propagation is prohibited.

In this Chapter we investigate spin-wave propagation in a micro-structured magnonic crystal fabricated by localized ion implantation (Report 4.10). The irradiation of the Permalloy waveguide with Cr^+ ions causes a periodic variation in the saturation magnetization along the waveguide. As a consequence, the spin-wave transmission spectrum exhibits a set of frequency bands, where spin-wave propagation is suppressed. We show that even a weak modification of the saturation magnetization by 7% is sufficient to decrease the spin-wave transmission in the band gaps by a factor of 10. Since the waveguide consisted of one single, topographically unchanged material, the generation of higher width modes is suppressed compared to earlier realizations of micro-scaled magnonic crystals. This drastically improves the operation characteristics of the crystal and makes it promising for future applications in magnon spintronic devices. Further, in Report 4.11, we compare the nonlinear spin-wave spectrum of this ion-implanted magnonic crystal waveguide with a similarly dimensioned reference waveguide. We observed four-magnon scattering processes of the originally excited spin waves into gap modes of the magnonic crystal located at the frequencies of the band gaps. Since this effect is absent in the reference waveguide, we might interpret it as an enhancement of nonlinear four-magnon scattering and show that it is possible to specifically pattern nonlinear spin-wave processes using artificial magnetic materials.

C. Magnonische Kristalle

Magnonische Kristalle sind Wellenleiterstrukturen, die eine künstlich erschaffene, periodische Modulation ihrer Materialeigenschaften aufweisen, wobei die Periodizitätslängen in der Größenordnung der Wellenlängen der propagierenden Wellen liegen. Solche Systeme gehören zur Klasse der sogenannten Metamaterialien: künstliche Materialien mit Eigenschaften, die durch eine gezielt entworfene mesoskopische Struktur hervorgerufen werden. Die Transmissionsspektren magnonischer Kristalle weisen typischerweise Bandlücken auf, also Frequenz-Bereiche, in denen die Wellenpropagation unterdrückt ist.

In diesem Abschnitt untersuchen wir die Spinwellenpropagation in einem mikrostrukturierten magnonischen Kristall, der durch lokalisierte Ionenimplantation hergestellt wurde (Bericht 4.10). Die Bestrahlung des Permalloy-Wellenleiters mit Cr^+-Ionen bewirkt eine periodische Veränderung der Sättigungsmagnetisierung entlang des Wellenleiters. In der Folge weist das Transmissionsspektrum eine Reihe von Frequenzbändern auf, in denen die Spinwellenpropagation unterdrückt ist. Wir zeigen, dass bereits eine leichte Modulation der Sättigungsmagnetisierung um 7% ausreicht um die Spinwellentransmission in den Bandlücken um einen Faktor 10 zu verringern. Im Vergleich zu früheren Realisierungen mikrostrukturierter magnonischer Kristalle ist hier die Erzeugung höherer Transversalmoden weniger ausgeprägt, da der Wellenleiter aus einem einzigen, topografisch unveränderten Material besteht. Dies wirkt sich enorm auf die Funktionseigenschaften des Kristalls aus und birgt ein großes Potential für zukünftige Anwendungen der Magnon-Spintronik. Des Weiteren vergleichen wir in Bericht 4.11 das nichtlineare Spinwellenspektrum dieses Wellenleiters auf Grundlage eines ionenimplantierten magnonischen Kristalls mit einem ähnlich dimen-

sionierten Referenzwellenleiter. Die Vier-Magnonen-Streuung von angeregten Spinwellen in Moden mit Frequenzen an den Bandlücken wurde beobachtet. Da dieser Effekt im Referenzwellenleiter nicht auftritt, interpretieren wir ihn als eine Verstärkung der nichtlinearen Vier-Magnonen-Streuung und zeigen, dass nichtlineare Spinwellenprozesse mithilfe magnonischer Kristalle gezielt kontrolliert werden können.

4.10 A micro-structured ion-implanted magnonic crystal

B. Obry, P. Pirro, T. Brächer, A. V. Chumak, F. Ciubotaru, E. Th. Papaioannou, A. A. Serga, and B. Hillebrands

In collaboration with J. Osten and J. Fassbender, Institut für Ionenstrahlphysik und Materialforschung, Helmholtz-Zentrum Dresden-Rossendorf, D-01328 Dresden, Germany, and Technische Universität Dresden, D-01062 Dresden, Germany

Magnonic crystals are artificially patterned magnetic media, which allow for a manipulation of the propagation properties of spin waves. The periodic modulation of their magnetic properties results in the formation of frequency bandgaps in the spin-wave transmission spectrum, where their propagation is suppressed [1, 2]. Owing to their potential for information processing and storage [3, 4] magnonic crystals are promising candidates for magnon spintronic devices [5]. The future use in a chip-based spin-logic architecture, however, requires high-quality microscopic magnonic crystals that are easy to produce.

A convenient method to pattern the magnetic properties of a sample without major modifiations to the sample topography is localized ion implantation [6–9]. Beside others, the implantation of ions in a $Ni_{81}Fe_{19}$ film leads to a reduction of its saturation magnetization [10–12]. Thus, localized ion implantation can be utilized to manipulate the spin-wave propagation by a pure magnetic patterning of a $Ni_{81}Fe_{19}$ film [13].

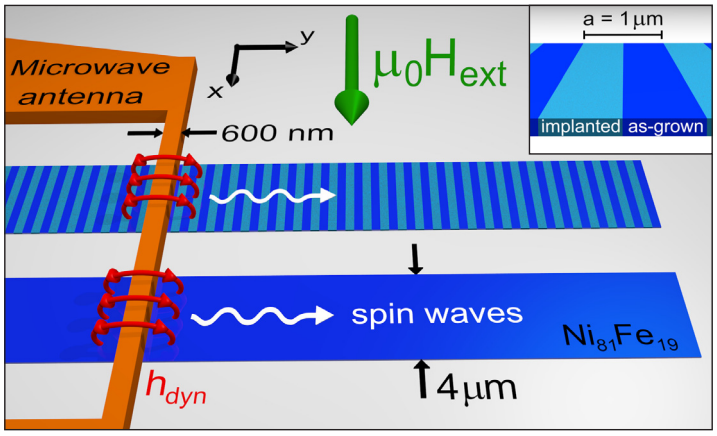

Fig. 1: Experimental sample setup. Spin waves are excited in two 4 µm wide $Ni_{81}Fe_{19}$ waveguides by the dynamic Oersted field h_{dyn} (indicated by the concentric double arrows) of a 400 nm thick and 600 nm wide Cu antenna. Along one of the waveguides the saturation magnetization has been modulated periodically by localized Cr^+ implantation with a lattice constant $a = 1\,\mu m$ (see inset). The other waveguide acts as a reference. An external in-plane magnetic field $\mu_0 H_{ext} = 30\,mT$ is applied perpendicularly to the spin-wave propagation direction in order to saturate the magnetization.

Here, we present a one-dimensional micro-structured magnonic crystal waveguide with a periodic modulation of the saturation magnetization obtained by localized ion implantation. While the magnetic patterning method has nearly no impact on the waveguide topography, the change in the spin-wave propagation in the waveguide is drastic. A set of pronounced frequency band gaps exists in the spin-wave transmission spectrum, corresponding to a rejection of spin waves by the magnonic crystal. A change in the waveguide's saturation magnetization of 7 % is sufficient for a suppression of spin-wave propagation by an order of magnitude [14].

The experiments were performed on two $Ni_{81}Fe_{19}$ waveguides (Fig. 1) with a width of $w = 4\,\mu m$

and a nominal thickness of $t = 20\,\text{nm}$, which were fabricated by means of conventional lift-off techniques and molecular beam evaporation. While one of the waveguides served as a reference waveguide, a periodic modulation in the saturation magnetization M_s was imposed on the second waveguide by localized ion implantation. For this, a polymethyl methacrylate (PMMA) mask was patterned on top of the sample by e-beam lithography containing a set of 4 µm wide and 500 nm long windows with a periodicity of 1 µm (inset of Fig. 1). The subsequent irradiation of the sample by a broad beam of Cr^+ ions with a kinetic energy of 30 keV and a fluence of $4.4 \times 10^{15}\,\text{ions/cm}^2$ resulted in a decrease of M_s in the unshielded regions to $93 \pm 6\,\%$ of its original value, as determined from polar magneto-optic Kerr effect measurements [15] on equally treated reference samples. Finally, a 200 nm thick and 600 nm wide Cu antenna was produced on top of the waveguides (Fig. 1). Applying a microwave current to the antenna, spin waves were excited in the $Ni_{81}Fe_{19}$ waveguides by the dynamic Oersted field h_{dyn} of the antenna, and they propagated perpendicularly to an external in-plane magnetic field $\mu_0 H_{ext} = 30\,\text{mT}$ (Damon-Eshbach geometry). The spin-wave intensity was detected using Brillouin light scattering (BLS) microscopy, which provides a high dynamic spectral range and a spatial resolution of 250 nm [16].

The magnonic crystal character of the modulated waveguide becomes apparent in the measurement of the spin-wave transmission spectra (Fig. 2a). Here, the detected spin-wave intensity measured at a propagation distance of a few micrometers from the antenna has been plotted as a function of the microwave excitation frequency. For a better comparison, the spectra were normalized in intensity. With respect to the reference waveguide, the transmission spectrum of the magnonic crystal waveguide reveals two pronounced band gaps for spin-wave frequencies at 5.9 GHz and at about 7.0 GHz, where the spin-wave intensity drops by a factor of 10. These frequency regions constitute the rejection bands of the magnonic crystal.

Figure 2b displays the Damon-Eshbach type spin-wave dispersion relation, which was calculated according to Ref. [17] for a magnetic field of $\mu_0 H_{int} = 27.3\,\text{mT}$ and a saturation magnetization of $M_s = 675\,\text{kA/m}$ [18]. The latter value was determined from polar magneto-optic Kerr effect measurements on non-irradiated $Ni_{81}Fe_{19}$ reference films, while the magnetic field value takes into account the demagnetizing fields originating at the waveguide edges [19]. The dispersion relation reflects the characteristic features of the reference transmission spectrum. While the strong onset of spin-wave transmission at lower frequencies corresponds to the ferromagnetic resonance (FMR) frequency $f_{FMR} = 4.3\,\text{GHz}$, the gradual decrease in the detected spin-wave intensity towards higher frequencies can be understood by taking into account the finite size of the microwave antenna [20]. For the given antenna width of 600 nm an efficient excitation of spin waves is restricted to spin waves up to a maximum wave vector of $k_{max} \approx 10\,\text{rad/µm}$. According to Fig. 2b, this results in an upper limit for the spin-wave frequency of $f_{max} = 8.2\,\text{GHz}$, which perfectly agrees with the observed values in the transmission spectrum of the reference waveguide (Fig. 2a).

Furthermore, for the transmission spectrum of the magnonic crystal waveguide, the positions of the frequency band gaps coincide with the first two resonance conditions for Bragg scattering from the periodic magnonic crystal pattern. The latter are indicated by the dotted lines in Fig. 2 and were calculated using the Bragg condition $k = n\pi/a$, which connects the spin-wave wave vector k with the lattice constant $a = 1\,\mu\text{m}$ of the artificial lattice, where n is an integer number. It has to be noted that the waveguide thickness t was used as a fitting parameter in the calculation of the spin-wave dispersion relation (Fig. 2b). While the thickness has basically no impact on the position of the FMR frequency, it strongly influences the frequency values for Bragg reflection. The resulting thickness value of $t = 19\,\text{nm}$ reproduces the nominal thickness quite well. Since no capping layer was used on top of the $Ni_{81}Fe_{19}$, the oxidation of the waveguide surface and thus a reduction of

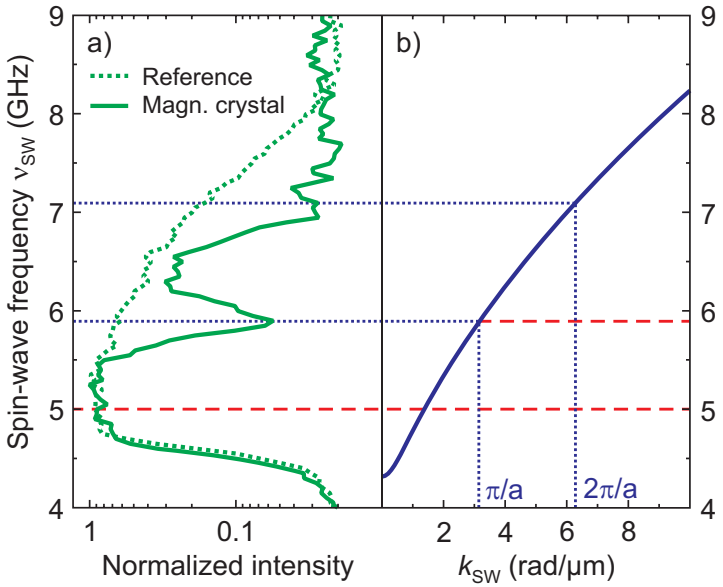

Fig. 2: a) Normalized spin-wave transmission spectra of the magnonic crystal waveguide (solid line) and the reference waveguide (dotted line). The spectra were recorded for an external magnetic field of $\mu_0 H_{ext} = 30\,\mathrm{mT}$. b) Calculated spin-wave dispersion relation for the same field and a waveguide width of 4 µm. The first two band gap positions are indicated by the dotted lines. Dashed lines mark spin-wave frequencies studied in Fig. 3.

the effective thickness is most likely.

A more detailed analysis of the spin-wave propagation in the magnonic crystal waveguide was achieved by space-resolved BLS microscopy measurements (Fig. 3). Here, spatial maps of the spin-wave intensity distribution within the waveguides were taken for an excitation frequency in the transmission and rejection band, respectively. The investigated frequencies are indicated by the dashed lines in Fig. 2. Spin waves were excited by the antenna at $x = 0\,\mu\mathrm{m}$ and detected locally by scanning the BLS laser focus across the waveguide. The detected spin-wave intensity is color-coded with bright (dark) color representing high (low) intensity. In both cases the propagation in the magnonic crystal waveguide was compared to the propagation in the conventional reference waveguide.

For the excitation of spin waves in the transmission band with a frequency of $f_{exc} = 5.0\,\mathrm{GHz}$ a weak difference between both intensity maps was observed (Fig. 3a). While in the reference waveguide the spin waves decay homogeneously with increasing distance from the antenna, a faster decay as well as a small overlaid oscillation in the intensity occurs in the magnonic crystal waveguide. Apparently, this is due to the implementation of the irradiated regions with a reduced M_s and an increased Gilbert damping [11] allowing for spin-wave reflection at the transitions between the irradiated and non-irradiated areas. A more quantitative analysis of the spin-wave decay along the waveguide is given in Fig. 3c. Here, the total transmitted spin-wave intensity is shown as a function of the distance from the antenna, obtained by integrating the detected spin-wave signal over the x position in Fig. 3a. In the case of the reference waveguide the slope of this curve yields information about the spin-wave damping. However, for the magnonic crystal waveguide this is not trivial, since multiple reflections from the irradiated regions as well as the periodically modified saturation magnetization and damping have to be taken into account. In order to simplify the analysis, an effective decay length d was used to quantify the transmission through the waveguide, i.e., to account for both damping and reflection losses. Fitting an exponential decay of the spin-wave intensity I according to $I(y) = I(y=0) \times \exp(-y/d)$ to the experimental data yielded values of $d = 3.2\,\mu\mathrm{m}$ for the reference waveguide and $d = 2.6\,\mu\mathrm{m}$ for the magnonic crystal waveguide (Fig. 3c). A small increase in d by a factor of 1.2 due to the irradiation was determined.

In contrast, the excitation of spin waves with a frequency of $f_{exc} = 5.9\,\mathrm{GHz}$, i.e., inside the band gap, has a notable impact on their propagation in the magnonic crystal waveguide. The intensity

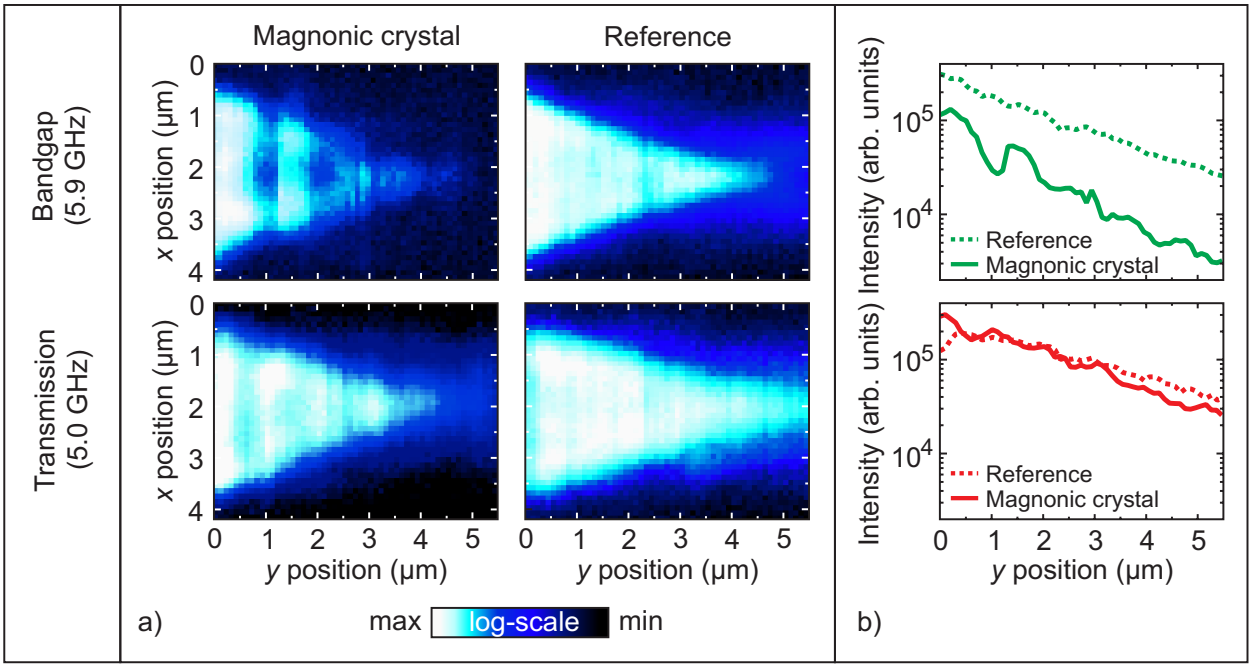

Fig. 3: Investigation of the spatial spin-wave intensity distribution with a frequency in the transmission band (lower panel) and in the rejection band (upper panel). The lateral spin-wave intensity distribution was mapped by Brillouin light scattering microscopy for the magnonic crystal waveguide (upper panel in a)) and the reference waveguide (lower panel in a)). For a comparison of the spatial decay along the waveguides the integral intensity distribution along the waveguide is plotted. The microwave antenna is located at $y = 0\,\mu\text{m}$.

maps in Fig. 3b reveal a pronounced overlaid oscillation in the magnonic crystal waveguide being a sign of a standing spin-wave pattern due to the Bragg reflections from the artificial lattice. In addition, the decay of the transmitted intensity (Fig. 3d) in the magnonic crystal waveguide ($d = 1.2\,\mu\text{m}$) was increased with respect to the reference waveguide ($d = 2.1\,\mu\text{m}$) by a factor of 1.8. Beside the increased effective damping, the offset in intensity between both curves in Fig. 3d suggests that the excitation of spin waves in the magnonic crystal waveguide within the band gap has a lower efficiency. These observations give rise to the assumption that the suppression of spin waves by a factor of 10 in the rejection band is caused by two different effects: Partly, the effective spin-wave damping is increased due to Bragg scattering from the artificial crystal, but additionally the location of the antenna inside the magnonic crystal leads to a decreased excitation efficiency inside the rejection band.

In conclusion, localized ion implantation is a convenient method to fabricate high-performance magnonic crystal waveguides on the microscopic scale. A relatively weak, periodic change in the waveguide's saturation magnetization of 7 % is sufficient for the formation of pronounced band gaps, where spin-wave propagation is efficiently suppressed. Since the waveguide consisted of one single, topographically unchanged material, spin waves with frequencies in the transmission bands were nearly unaffected. Hence, this class of magnonic crystal waveguides bears a high potential for future application in magnon spintronic devices.

The authors would like to thank the Nano Structuring Center (NSC) of the TU Kaiserslautern for support with the sample preparation. Financial support by the DFG (SE-1771/1-2) is gratefully acknowledged. T. Brächer is supported by a fellowship of the Graduate School Materials Science in Mainz (MAINZ) through DFG-funding of the Excellence Initiative (GSC 266).

This work has been recently published in Applied Physics Letters [14].

References

[1] C.G. Sykes. J.D. Adam, J.H. Collins, *Magnetostatic wave propagation in a periodic structure*, Appl. Phys. Lett. **29**, 388 (1976).

[2] S.A. Nikitov, Ph. Tailhades, C.S. Tsai, *Spin waves in periodic magnetic structures – magnonic crystals*, J. Magn. Magn. Mater. **236**, 320 (2001).

[3] A.V. Chumak, A.N. Slavin, V.S. Tiberkevich, A.D. Karenowska, A.A. Serga, J.F. Gregg, B. Hillebrands, *All-linear time reversal by a dynamic artificial crystal*, Nature Commun. **1**, 141 (2010).

[4] A.V. Chumak, V.I. Vasyuchka, A.A. Serga, M.P. Kostylev, V.S. Tiberkevich, B. Hillebrands, *Storage-recovery phenomenon in magnonic crystal*, Phys. Rev. Lett. **108**, 257207 (2012).

[5] V.V. Kruglyak, S.O. Demokritov, D. Grundler, *Magnonics*, J. Phys. D **43**, 264001 (2010).

[6] G. Volluet, P. Hartemann, *Reflection of magnetostatic forward volume waves by ion implanted gratings*, Proc. IEEE Ultrasonics Symp., 394 (1981).

[7] R.L. Carter, J.M. Owens, C.V. Smith, K.W. Reed, *Ion-implanted magnetostatic wave reflective array filters*, J. Appl. Phys. **53**, 2655 (1982).

[8] W.M. Kaminsky, G.A.C. Jones, N.K. Patel, W.E. Booij, M.G. Blamire, S.M. Gardiner, Y.B. Xu, J.A.C. Bland, *Patterning ferromagnetism in $Ni_{80}Fe_{20}$ films via Ga^+ ion irradiation*, Appl. Phys. Lett. **78**, 1589 (2001).

[9] I. Barsukov, F.M. Römer, R. Meckenstock, K. Lenz, J. Lindner, S. Hemken to Krax, A. Banholzer, M. Körner, J. Grebing, J. Fassbender, M. Farle, *Frequency dependence of spin relaxation in periodic systems*, Phys. Rev. B **84**, 140410(R) (2011).

[10] L. Folks, R.E. Fontana, B.A. Gurney, J.R. Childress, S. Maat, J. A. Katine, J.E.E. Baglin, A.J. Kellock, *Localized magnetic modification of permalloy using Cr^+ ion implantation*, J. Phys. D **36**, 2601 (2003).

[11] J. Fassbender, J. von Borany, A. Mücklich, K. Potzger, W. Möller, J. McCord, L. Schultz, R. Mattheis, *Structural and magnetic modifications of Cr-implanted Permalloy*, Phys. Rev. B **73**, 184410 (2006).

[12] J. Fassbender, J. McCord, *Control of saturation magnetization, anisotropy, and damping due to Ni implantation in thin $Ni_{81}Fe_{19}$ layers*, Appl. Phys. Lett. **88**, 252501 (2006).

[13] B. Obry, T. Meyer, P. Pirro, T. Brächer, B. Lägel, J. Osten, T. Strache, J. Fassbender, B. Hillebrands, *Microscopic magnetic structuring of a spin-wave waveguide by ion implantation in a $Ni_{81}Fe_{19}$layer*, Appl. Phys. Lett. **102**, 022409 (2013).

[14] B. Obry, P. Pirro, T. Brächer, A.V. Chumak, J. Osten, F. Ciubotaru, A.A. Serga, J. Fassbender, B. Hillebrands, *A micro-structured ion-implanted magnonic crystal*, Appl. Phys. Lett. **102**, 202403 (2013).

[15] D. Markó, T. Strache, K. Lenz, J. Fassbender, R. Kaltofen, *Determination of the saturation magnetization of ion irradiated Py/Ta samples using polar magneto-optical Kerr effect and ferromagnetic resonance*, Appl. Phys. Lett. **96**, 022503 (2010).

[16] V.E. Demidov, S.O. Demokritov, B. Hillebrands, M. Laufenberg, P.P. Freitas, *Radiation of spin waves by a single micrometer-sized magnetic element*, Appl. Phys. Lett. **85**, 2866 (2004).

[17] B.A. Kalinikos, A.N. Slavin, *Theory of dipole-exchange spin wave spectrum for ferromagnetic films with mixed exchange boundary conditions*, J. Phys. C: Solid State Phys. **19**, 7013 (1986).

[18] Further assuming a $Ni_{81}Fe_{19}$ waveguide with thickness $t = 19\,\text{nm}$ and width $w = 4\,\mu\text{m}$, a gyromagnetic ratio $\gamma = 28\,\text{GHz/T}$, and an exchange stiffness constant $A = 1.6 \cdot 10^{-11}\,\text{J/m}$.

[19] S.O. Demokritov, V.E. Demidov, in *Spin Wave Confinement*, edited by S.O. Demokritov (Pan Stanford Publishing Pte. Ltd., Singapore, 2009), Chap. 1.

[20] V.E. Demidov, M.P. Kostylev, K. Rott, P. Krzysteczko, G. Reiss, S.O. Demokritov, *Excitation of microwaveguide modes by a stripe antenna*, Appl. Phys. Lett. **95**, 112509 (2009).

4.11 Non-linear spin-wave scattering into the gap modes of a magnonic crystal

B. Obry, P. Pirro, T. Brächer, A. V. Chumak, F. Ciubotaru, E. Th. Papaioannou, A. A. Serga, and B. Hillebrands

In collaboration with J. Osten and J. Fassbender, Institut für Ionenstrahlphysik und Materialforschung, Helmholtz-Zentrum Dresden-Rossendorf, D-01328 Dresden, Germany, and Technische Universität Dresden, D-01062 Dresden, Germany

Nonlinear magnon-magnon scattering processes represent the mutual interactions of spin waves at high precession angles. The huge variety of possible scattering channels has motivated a number of investigations of nonlinear processes over the last decades and has led, among others, to the discovery of Bose-Einstein condensation of magnons at room temperature [1]. Furthermore, nonlinear magnon-magnon scattering provides plenty of applications for magnon spintronics due to their potential to manipulate the spin-wave frequency. In the case of macroscopic systems made from $Y_3Fe_5O_{12}$ (YIG) nonlinear effects have been utilized to prototype several spin-wave logic functional elements, e.g. a spin-wave transistor [2] and a spin-wave memory [3]. Nonlinear spin-wave processes also play an important role in microscopic structures as has been shown in several investigations [4–8]. These processes should be especially intensive in a micro-structured magnonic crystal, which can accumulate and spatially concentrate spin-wave energy. Since magnonic crystals are essential elements of a magnon spintronic architecture, insight into nonlinear effects of spin waves propagating in a magnonic crystal waveguide is of crucial importance.

In this Report, we compare the nonlinear spin-wave spectrum of an ion-implanted, micro-structured magnonic crystal waveguide with a similarly dimensioned reference waveguide. Based on the analysis of four-magnon scattering processes, a predominant scattering into gap modes, i.e., spin waves with frequencies in the magnonic band gaps, is determined. From space-resolved measurements of the spin-wave intensity distribution in the waveguide a change in the effective damping of these gap modes can be identified.

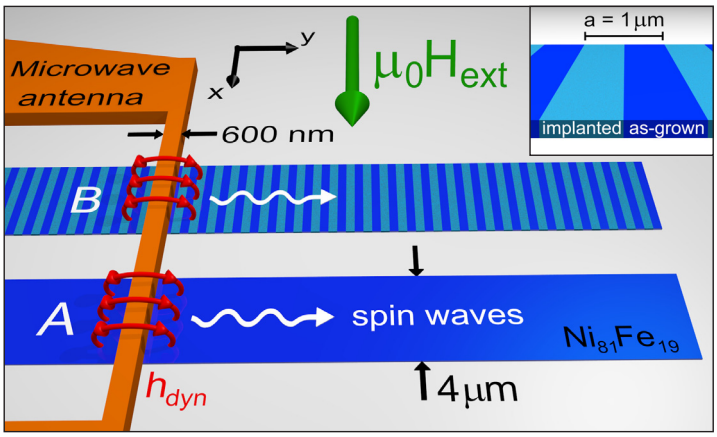

Fig. 1: Experimental sample setup. Spin waves are excited in two 4 µm wide $Ni_{81}Fe_{19}$ waveguides by the dynamic Oersted field h_{dyn} of a 400 nm thick and 600 nm wide Cu antenna. While waveguide A acts as a reference waveguide, the saturation magnetization has been modulated periodically along waveguide B by localized Cr^+ implantation with a lattice constant $a = 1\,\mu m$ (see inset). The waveguides' magnetization is aligned perpendicular to the spin-wave propagation direction by an external in-plane magnetic field $\mu_0 H_{ext} = 30\,mT$.

The nonlinear spin-wave spectra were recorded on two $Ni_{81}Fe_{19}$ waveguides (Fig. 1) which were fabricated by lift-off processes and molecular beam epitaxy. Both waveguides have a thickness

of $t = 20\,\text{nm}$ and a width of $w = 4\,\mu\text{m}$. While waveguide A served as a reference waveguide, the saturation magnetization along waveguide B was modulated by means of localized implantation of Cr^+ ions (30 keV, $4.4 \times 10^{15}\,\text{ions/cm}^2$) to obtain a magnonic crystal waveguide with a lattice constant of $a = 1\,\mu\text{m}$ (see inset of Fig. 1) as discussed in Section 4.10. For this, a modulation of the saturation magnetization of $M_s/M_s^0 = 93\,\%$ was chosen, where M_s^0 denotes the magnetization value in the non-irradiated regions. At last, a 600 nm wide Cu antenna was fabricated on top of the waveguides (Fig. 1), which allowed for an excitation of spin waves propagating along the waveguides and perpendicular to an externally applied magnetic field of $\mu_0 H_{\text{ext}} = 30\,\text{mT}$ in the plane of the sample. For the investigation of nonlinear spin-wave processes an exciting microwave current with a power of $P_{\text{MW}} = 2.5\,\text{mW}$ and varying excitation frequency f_{MW} was applied to the antenna. The detection of the spin waves was done using Brillouin light scattering microscopy with a spatial resolution of 250 nm [9].

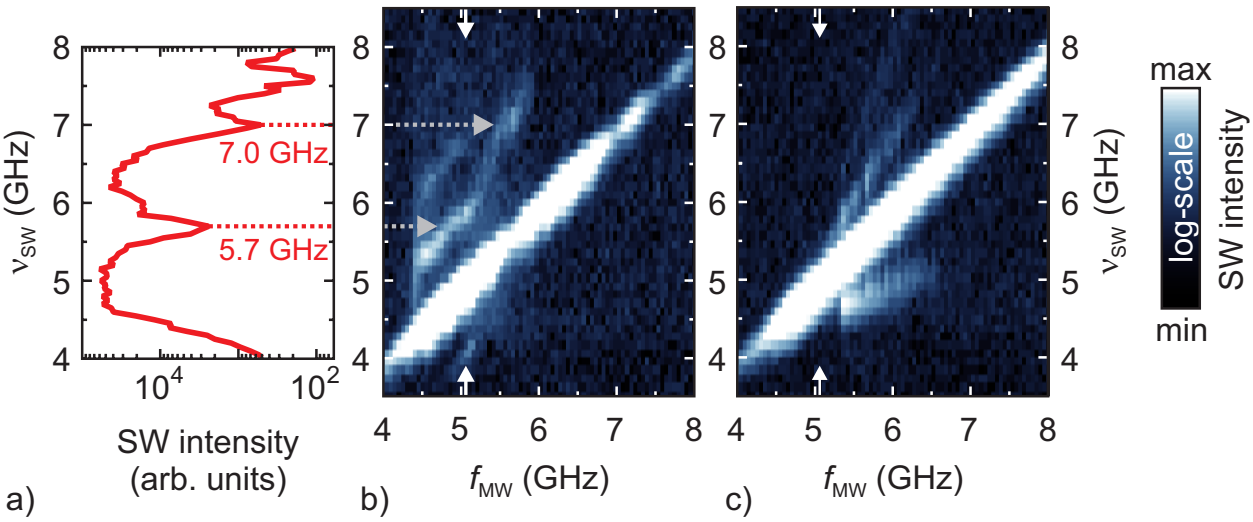

Fig. 2: a) Transmission of directly excited spin waves by the magnonic crystal waveguide for a strongly nonlinear excitation. The positions of the first two band gaps are indicated by dotted lines. b) Nonlinear spin-wave spectrum of the magnonic crystal waveguide containing the spin-wave intensity as a function of the spin-wave frequency ν_{SW} and the excitation frequency f_{MW}. White (black) color represents a high (low) spin-wave intensity. The nonlinearly scattered modes are indicated by horizontal arrows. c) Nonlinear spin-wave spectrum of the reference waveguide. The vertical arrows indicate the selected excitation frequency f_{MW} for the measurements in Fig. 3 and 4.

For a first characterization of the nonlinear spin-wave processes in a micro-structured magnonic crystal the spin-wave excitation spectra of both waveguides are compared. Figure 2 displays the results containing the measured spin-wave intensities (color-coded) as a function of the excitation frequency f_{MW} and the detected spin-wave frequency ν_{SW}. A high (low) spin-wave intensity is represented by bright (dark) color. Thus, the intense signal along the diagonal of both graphs ($f_{MW} = \nu_{SW}$) is caused by the directly excited spin waves. Any other signal represents a spin-wave mode originating from nonlinear spin-wave processes. Since energy is conserved in magnon-magnon scattering processes, the observed nonlinear modes cannot be caused by three-magnon processes but are rather mediated by four-magnon scattering. In the present considerations, the scattering of two incoming magnons with the same frequency ν into two outcoming magnons with frequencies ν^- and ν^+ is assumed. In the case of the reference waveguide (Fig. 2c) nonlinear spin-wave processes are observed for excitation frequencies $f_{MW} \geq 5.3\,\text{GHz}$ and show parallels to recent

observations from Pirro *et al.* in Heusler materials [10]. The frequency of the nonlinearly scattered modes as well as their frequency difference to the directly excited mode increase linearly with increasing excitation frequency. In comparison, the nonlinear spectrum of the magnonic crystal waveguide (Fig. 2c) exhibits significant qualitative differences, i.e., the scattered modes appear at different spin-wave frequencies with a discontinuous change in ν_{SW} at about $f_{MW} \approx 5.3\,\mathrm{GHz}$. Additionally, they can be observed for excitation frequencies below 5.3 GHz, which is in contrast to the reference waveguide.

In order to emphasize the influence of the magnonic lattice on the nonlinear scattering processes, the single spin-wave spectra for an excitation frequency of $f_{MW} = 5.05\,\mathrm{GHz}$ for both waveguides are contrasted in Fig. 3. These spectra represent the data from a single column in Figs. 2b and c marked by the vertical arrows. Next to the directly excited spin-wave signal at $\nu = 5.05\,\mathrm{GHz}$, which appears in both spectra, the magnonic crystal waveguides yields three additional peaks (ν^-, ν^+, and ν^{++}) originating from nonlinear four-magnon scattering processes. These peaks are absent in the reference spectrum, leading to the conclusion that in a magnonic crystal waveguide nonlinear effects can be enhanced for a given excitation spectrum.

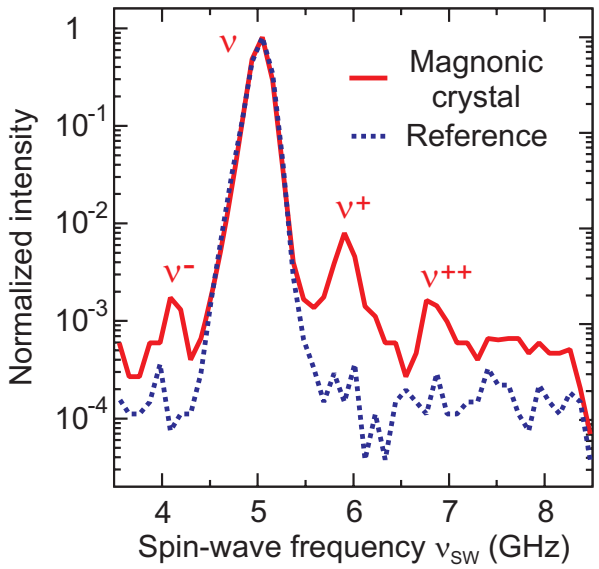

Fig. 3: Comparison of the BLS spectra for a nonlinear excitation of spin waves in the magnonic crystal waveguide (solid line) and the reference waveguide (dotted line) for an excitation frequency of $f_{MW} = 5.05\,\mathrm{GHz}$. The spectrum of the magnonic crystal waveguide exhibits three additional spin-wave signals ν^-, ν^+, and ν^{++} originating from four-magnon scattering processes.

This modification of nonlinear spin-wave processes in a magnonic crystal can be understood by considering the transmission spectrum of the magnonic crystal waveguide (Fig. 2a). It exhibits distinct band gaps, i.e., frequency intervals in which the transmission of spin waves through the waveguide is suppressed. The generation of magnonic band gaps can be interpreted as the Bragg reflection of spin waves from the periodic magnonic lattice, if the Bragg condition $k = n\pi/a$ is fulfilled. The latter connects the spin-wave wave vector k with the lattice constant a of the magnonic crystal, where the integer number n indicates the scattering order. Thus, the frequency positions of the magnonic band gaps inside the transmission spectrum are given by the periodicity of the magnonic lattice. When comparing the transmission spectrum of the magnonic crystal waveguide with its nonlinear spin-wave spectrum, a good agreement of the frequency positions of the first two band gaps (dotted lines in Fig. 2a) with the frequencies of the nonlinear spin-wave modes (horizontal arrows in Fig. 2b) becomes obvious. This indicates that the frequency positions of the nonlinear modes are governed by the magnonic lattice so that the directly excited spin waves predominantly scatter into modes at the magnonic band gaps, hence justifying to term them “gap modes”.

The predominant scattering of spin waves into gap modes in the magnonic crystal requires either a change in the nonlinear coupling between the respective modes of the waveguide or a modification in their damping. Since the reduction in saturation magnetization due to the ion irradiation is rather small and cannot account for a drastic variation of the nonlinear coupling parameters, the further investigations concentrate on the damping of the individual modes of the nonlinear spin-wave spectrum. For this, spatial maps of the spin-wave intensity distribution along the magnonic crystal waveguide were recorded (Fig. 4a). The resulting intensity maps of the directly excited spin waves (ν) as well as the two nonlinearly excited modes ν^- and ν^+ are given in Fig. 4b, where spin waves were excited by the antenna at $y = 0\,\mu\text{m}$. The intensity pattern of the directly excited spin waves with $\nu = 5.05\,\text{GHz}$ reproduces the propagation of the spin waves in the transmission band of the magnonic crystal waveguide (see Section 4.10), yielding a homogeneous decay of the detected spin-wave intensity with increasing distance to the antenna. As this frequency is not inside any band gap, the spin-wave propagation is unaffected by the magnonic lattice. In contrast, the gap modes ν^- and ν^+ are concentrated to the region close to the antenna and exhibit a rapid decay for higher values of y. This reflects in their decay length which can be quantified from Fig. 4c, where the total transmitted spin-wave intensity of the waveguide is plotted as a function of the distance to the antenna (y position). The decay length of the spin-wave intensity can be extracted from the slope of the graphs in a logarithmic representation, assuming an exponential decay of the total spin-wave intensity along the waveguide. Here, any background noise was subtracted from the measurements. From the data a decay constant of $\delta = 2.0\,\mu\text{m}$ can be determined for the directly excited spin-wave mode, while the gap modes both yield a value of $\delta = 0.6\,\mu\text{m}$. This significant difference in the spatial intensity distribution between the directly excited and the nonlinearly scattered modes can be attributed to the fact that the frequency of the nonlinear mode ν^+ is located inside the first band gap at 5.9 GHz. Thus, the propagation of those spin waves along the waveguide is suppressed due to the Bragg reflection from the magnonic lattice.

From another point of view, the reduction of the decay constant in the case of the gap modes indicates a decrease in the effective damping in the regions close to the antenna. According to the argumentation from Ref. [11, 12] the propagation of spin waves away from the antenna region can be interpreted as an additional contribution to the local damping at the position of the antenna. This damping contribution is absent for spin waves inside the band gap, as the Bragg scattering from the periodic lattice suppresses their propagation. Hence, the nonlinear mode ν^+ experiences a lower effective damping in the regions close to the antenna, which has to be included in the considerations of the nonlinear scattering. Due to the decreased damping the population of the modes inside the band gap increases rapidly so that the inefficient coupling between the directly excited spin-wave modes and the gap modes can be overcompensated. Consequently, in a magnonic crystal waveguide the dominating modes being favoured for nonlinear scattering processes are given by the modes with a frequency inside the band gaps, i.e., the gap modes. In this respect, the appearance of the three nonlinearly scattered peaks in Fig. 3 is triggered by the gap mode ν^+. Energy conservation in the four-magnon scattering process then accounts for the observation of the signal at ν^-, while the peak at ν^{++} can be understood as a secondary four-magnon scattering process, where the scattering of two incoming magnons with the frequency ν^+ results in two scattered magnons with frequencies ν and ν^{++}. Thus, the nonlinear spectrum of a magnonic crystal is determined by the reduced effective damping of spin waves in the regions close to the antenna. The localization of the nonlinear scattering to the excitation region results in the spatial intensity maps observed in Fig. 4b.

In conclusion, the artificial periodic lattice of magnonic crystals drastically modifies the nonlinear spin-wave spectrum of a waveguide. The investigation of the spin-wave excitation and propagation

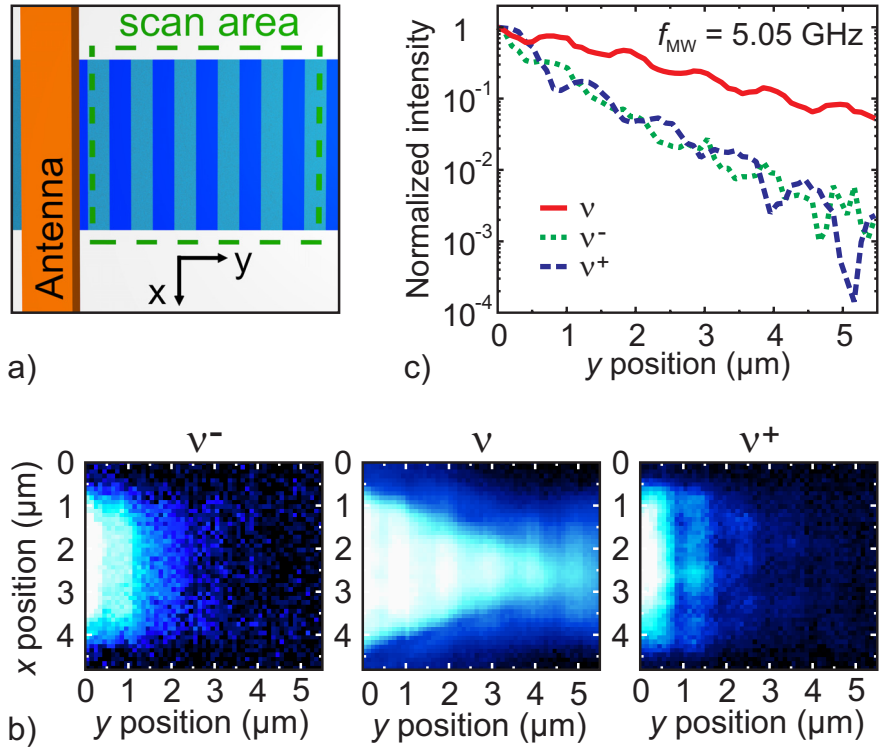

Fig. 4: Spatial spin-wave intensity distribution along the magnonic crystal waveguide for a nonlinear excitation of spin waves. a) The scan area contains the full waveguide width and spreads over several periods of the magnonic lattice. b) Spatial maps of the spin-wave intensity distribution for the directly excited spin-wave mode (ν) and the modes populated by four-magnon scattering (ν^-, ν^+). Bright (dark) color indicates a high (low) signal intensity. The antenna is located at $y = 0\,\mu$m. c) Normalized decay of the total spin-wave intensity along the magnonic crystal waveguide, extracted from b) by integrating the measured spin-wave intensity over the waveguide width.

in a micro-structured magnonic crystal waveguide compared to a reference waveguide revealed a qualitative change and - in some frequency intervals - an enhancement of nonlinear four-magnon scattering processes. In the magnonic crystal waveguide a scattering into gap modes was observed, which are located at the frequencies of the magnonic band gaps. For these modes, a local decrease in the spin-wave damping due to the Bragg scattering from the magnonic lattice could be experimentally verified. Hence, since magnonic crystals are artificially patterned systems, it is possible to specifically pattern nonlinear spin-wave processes in a localized region of a spin-wave waveguide by adjusting the magnonic lattice constant. The presented findings bear the potential to launch a series of further developments like, e.g. microscopic frequency converters, transistors, and storage elements, for various applications in the field of magnon spintronics.

The authors would like to thank the Nano Structuring Center (NSC) of the TU Kaiserslautern for support with the sample preparation. Financial support by the DFG (SE-1771/1-2) is gratefully acknowledged. T. Brächer is supported by a fellowship of the Graduate School Materials Science in Mainz (MAINZ) through DFG-funding of the Excellence Initiative (GSC 266).

References

[1] S.O. Demokritov, V.E. Demidov, O. Dzyapko, G.A. Melkov, A.A. Serga, B. Hillebrands, A.N. Slavin, *Bose-Einstein condensation of quasi-equilibrium magnons at room temperature under pumping*, Nature **443**, 430 (2006).

[2] A.V. Chumak, A.A. Serga, B. Hillebrands, *Magnon transistors for all-magnon data processing*, submitted to: Science.
[3] A.V. Chumak, V.I. Vasyuchka, A.A. Serga, M.P. Kostylev, V.S. Tiberkevich, B. Hillebrands, *Storage-recovery phenomenon in magnonic crystal*, Phys. Rev. Lett. **108**, 257207 (2012).
[4] H. Schultheiss, X. Janssens, M. van Kampen, F. Ciubotaru, S.J. Hermsdoerfer, B. Obry, A. Laraoui, A.A. Serga, L. Lagae, A.N. Slavin, B. Leven, B. Hillebrands, *Direct current control of three magnon scattering processes in spin-valve nanocontacts*, Phys. Rev. Lett. **103**, 157202 (2009).
[5] V.E. Demidov, J. Jersch, K. Rott, P. Krzysteczko, G. Reiss, S.O. Demokritov, *Nonlinear propagation of spin waves in microscopic magnetic stripes*, Phys. Rev. Lett. **102**, 177207 (2009).
[6] T. Sebastian, T. Brächer, P. Pirro, A.A. Serga, B. Hillebrands, T. Kubota, H. Naganuma, M. Oogane, Y. Ando, *Nonlinear emission of spin-wave caustics from an edge mode of a microstructured $Co_2Mn_{0.6}Fe_{0.4}Si$ waveguide*, Phys. Rev. Lett. **110**, 067201 (2013).
[7] V.E. Demidov, M. Buchmeier, K. Rott, P. Krzysteczko, J. Münchenberger, G. Reiss, S.O. Demokritov, *Nonlinear hybridization of the fundamental eigenmodes of microscopic ferromagnetic ellipses*, Phys. Rev. Lett. **104**, 217203 (2010).
[8] H. Schultheiss, K. Vogt, B. Hillebrands, *Direct observation of nonlinear four-magnon scattering in spin-wave microconduits*, Phys. Rev. B **86**, 054414 (2012).
[9] V.E. Demidov, S.O. Demokritov, B. Hillebrands, M. Laufenberg, P.P. Freitas, *Radiation of spin waves by a single micrometer-sized magnetic element*, Appl. Phys. Lett. **85**, 2866 (2004).
[10] P. Pirro, T. Sebastian, T. Brächer, A.A. Serga, B. Hillebrands, *Nonlinear magnon instability in Heusler waveguides*, Annual Report of the AG Magnetismus, TU Kaiserslautern, Kaiserslautern, Germany (2012).
[11] A.N. Slavin, V. Tiberkevich, *Spin wave mode excited by spin-polarized current in a magnetic nanocontact is a standing self-localized wave bullet*, Phys. Rev. Lett. **95**, 237201 (2005).
[12] V.E. Demidov, S. Urazhdin, H. Ulrichs, V. Tiberkevich, A.N. Slavin, D. Baither, G. Schmitz, S.O. Demokritov, *Magnetic nano-oscillator driven by pure spin current*, Nature Mat. **11**, 1028 (2012).

D. Spin Caloric Transport

Spin Caloric Transport is a dynamically growing field of research, which investigates the interplay between spin- and heat-based transport phenomena. The observation of the spin Seebeck effect (SSE) in a magnetic insulator demonstrates the crucial role of collective magnetization excitations, i.e. spin waves and their quanta, magnons, in spin caloric transport processes, and illustrates the conceptual distinction between this phenomenon and conventional thermoelectric generation. Most interesting and important is the conversion of a heat flow into magnon currents and vice versa in a magnetic insulator. On a long time scale this may lead to the utilization of heat currents to support the transfer and processing of spin information.

Report 4.12 presents the first measurements of the time evolution of the longitudinal spin Seebeck effect in yttrium iron garnet/platinum (YIG/Pt) bilayers performed by laser heating experiments. Our findings reveal that the rise time of the SSE is sub-microsecond fast though the temperature in the system establishes in milliseconds. This confirms that the temporal evolution of the SSE depends on the thermal gradient in the YIG/Pt. The comparison of the experiments with the developed model show that the longitudinal SSE effect is caused by the thermally driven magnons and depends on the thermal magnon diffusion in a magnetic material.

In Report 4.13 the magnon-phonon energy transfer is investigated in the process of the reflection for both backward volume and surface spin waves using infrared thermography, Brillouin light scattering spectroscopy, and micromagnetic simulations. We have found that the volume waves are elastically scattered from the end of the waveguide whereas the magnetostatic surface waves undergo a chiral reflection in combination with the formation of both width and thickness standing modes. The interaction of the standing modes with the lattice leads to the formation of thermal gradients with increasing temperature towards the end of the sample.

D. Spin-kalorischer Transport

Der spin-kalorische Transport ist ein rasant wachsendes Forschungsfeld, welches das Zusammenspiel zwischen Spin-basierten und Wärme-basierten Transportphänomenen untersucht. Die Untersuchungen des Spin-Seebeck-Effekts (SSE) in magnetischen Isolatoren zeigen dabei die wichtige Rolle auf, welche die kollektiven Anregungen des magnetischen Systems - also Spinwellen - in spin-kalorischen Transportprozessen spielen. Weiterhin verdeutlichen diese Beobachtungen die konzeptuelle Unterscheidung zwischen diesen Phänomenen auf der einen sowie konventionellen thermoelektrischen Effekten auf der anderen Seite. Von größtem Interesse und von größter Wichtigkeit in diesem Forschungsgebiet ist die Untersuchung der Umwandlung von Wärmeflüssen in reine Spinströme in Isolatoren. Perspektivisch kann das Verständnis dieser Prozesse zur Nutzung von Wärmeströmen für den Transport sowie die Verarbeitung von Spin-Information beitragen.

In Bericht 4.12 wird die erstmalige Messung der Zeitentwicklung des longitudinalen Spin-Seebeck-Effekts vorgestellt, die in Yttrium-Eisen-Granat/Platin-Doppellagen mittels laserinduziertem Heizen durchgeführt wurde. Die Ergebnisse lassen einen zeitlichen Anstieg des SSE-Signals unterhalb einer Mikrosekunde erkennen, obwohl der Temperaturanstieg des Systems in der Größenordnung von Millisekunden abläuft. Dies bestätigt, dass die Zeitentwicklung des Spin-Seebeck-Effekts vielmehr von der Größe des Temperaturgradienten im YIG/Pt abhängt. Ein Vergleich der Experimente mit einem theoretischen Modell lässt den Schluss zu, dass der longitudinale

SSE durch thermisch erzeugte Magnonen verursacht wird und von der thermischen Diffusion der Magnonen im magnetischen Material abhängt.

Bericht 4.13 diskutiert Untersuchungen zum gegenseitigen Energieübertrag zwischen Magnonen und Phononen, welcher im Zuge der Reflexion von Rückwärts-Volumenspinwellen sowie Oberflächen-Spinwellen auftritt. Dieser Effekt wird aus Messungen mithilfe der Infrarot-Thermografie, Brillouin-Lichtstreuspektroskopie sowie in mikromagnetischen Simulationen deutlich. Während Rückwärts-Volumenspinwellen am Ende des Wellenleiters elastisch gestreut werden, erfahren Oberflächen-Spinwellen eine chirale Reflexion, die zusammen mit der Ausbildung von stehenden Wellen entlang der Dicke und der Breite des Wellenleiters einhergeht. Die Wechselwirkung der stehenden Wellen mit dem Kristallgitter führt dabei zur Ausbildung thermischer Gradienten, sodass die Temperatur zum Ende des Wellenleiters hin ansteigt.

4.12 Temporal evolution of the spin Seebeck effect

M. Agrawal, V. I. Vasyuchka, A. A. Serga, A. Kirihara, P. Pirro, T. Langner, M. B. Jungfleisch, A. V. Chumak, E. Th. Papaioannou, and B. Hillebrands[1]

The spin Seebeck effect (SSE) [1–3] is one of the most fascinating phenomena in the contemporary era of spin-caloritronics [4]. Although there have been numerous experimental and theoretical studies about this effect, the underlying physics is yet not well understood. The most accepted theory predicts that the SSE is driven by the difference in the local temperatures of magnon-, phonon-, and electron baths [5, 6] of the system. However, no clear evidences of such differences have been observed experimentally [7]. So, the origin of this effect is still under discussion. Moreover, the question whether the SSE is an interface or bulk effect, is still open.

To shed light on this controversial physics, we developed an entirely new experimental approach where we studied the temporal evolution of the SSE in YIG|Pt bilayer structures. The observations were realized in the longitudinal configuration of the SSE [3]. In the longitudinal spin Seebeck effect (LSSE), a thermal gradient is created perpendicular to the film plane, and the spin current generated by thermal excitations of magnetization (thermal magnons) is measured along the thermal gradient.

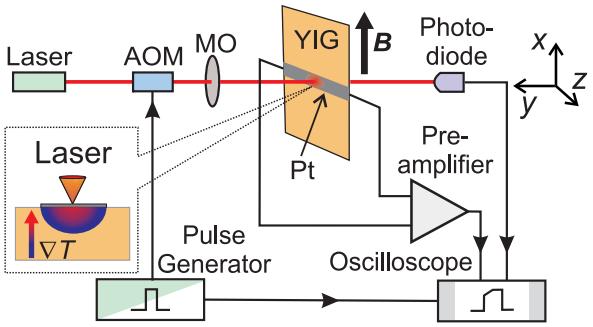

Fig. 1: Sketch of the experimental setup. A continuous laser beam (wavelength 655 nm), modulated by an acousto-optical modulator (AOM), was focused down on a 10 nm thick Pt strip, deposited on a 6.7 µm thick YIG film, by a microscope objective (MO). The laser intensity profile was monitored by an ultrafast photo-diode. An in-plane magnetic field $B = 20$ mT was applied to the YIG film. The heated Pt strip created a thermal gradient perpendicular to the YIG|Pt interface (see the inset). The generated voltage across the Pt strip due to ISHE was amplified and measured by an oscilloscope.

The LSSE measurements were performed on a bilayer of a magnetic insulator, Yttrium Iron Garnet (YIG), and normal metal, Pt. A 6.7 µm thick YIG sample of dimensions 14 mm×3 mm was grown by liquid phase epitaxy on a 500 µm thick Gallium Gadolinium Garnet (GGG) substrate. To achieve a good YIG|Pt interface quality, a detailed cleaning process as discussed in Ref. [8] was followed before the deposition of Pt. A strip (3 mm×100 µm) of 10 nm thick Pt was deposited on the cleaned YIG surface by MBE at a pressure of 5×10^{-11} mbar with a growth rate of 0.05 nm/s. In Fig. 1, a schematic diagram of the experimental setup is shown. A laser heating technique [9, 10] was implemented to heat the Pt strip from the top surface to create a vertical thermal gradient along the y direction perpendicular to the bilayer interface (See Fig. 1). For this purpose, a continuous laser beam (wavelength 655 nm) was modulated by an acousto-optical modulator (AOM), and focused down at the middle of the Pt strip using a microscopic objective. To study the temporal profile of the laser beam in parallel, the transmitted laser beam through the YIG sample was monitored by an ultrafast photo-diode. A rise time (10%-90%) of 200 ns was observed for the laser pulses (solid

[1] A. Kirihara is affiliated with Smart Energy Research Laboratories, NEC Corporation, Tsukuba 305-8501, Japan

line in Fig. 2 a). The sample structure was mounted on a copper block to provide a thermal heat sink.

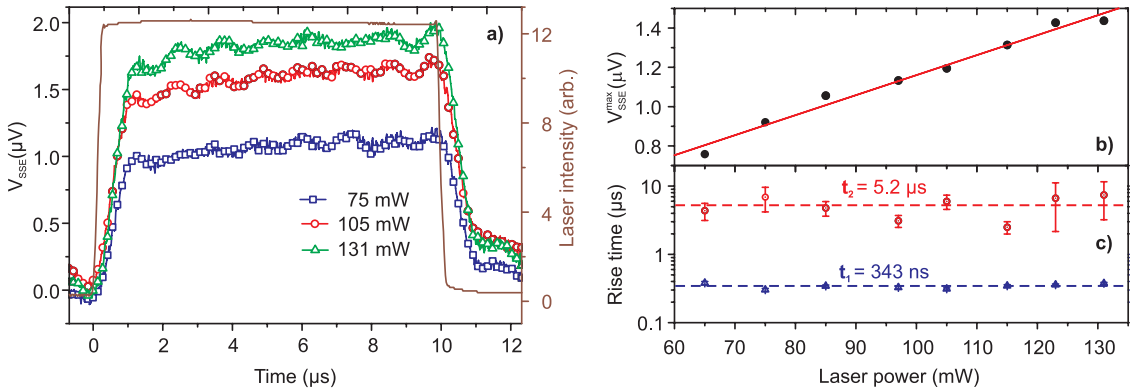

Fig. 2: a) The time profiles of the laser intensity (solid line), and the SSE voltage (V_{SSE}) at various laser powers of 75 mW(open circle), 105 mW (open square), and 131 mW (open triangle). b) Measured $V_{\mathrm{SSE}}^{\mathrm{max}}$, with linear fitting, and c) the rise times t_1 and t_2 as a function of laser power. The rise times are practically unchanged with the laser power.

The time-resolved measurements of LSSE were carried out using a 10 µs long laser pulse with a repetition rate of 10 kHz. An in-plane magnetic field B = 20 mT was applied to saturate the YIG film magnetization along the x direction. As a result of the LSSE, a spin current flowed along the y direction. By the inverse spin Hall effect, this spin current converts into an electric field along the z direction in Pt. The electric field was detected as a potential difference V_{SSE} between the two short edges of the Pt strip (shown in Fig. 1). The SSE voltage V_{SSE} was amplified by a high input impedance preamplifier and monitored on an oscilloscope. The measurements were performed for both $\pm x$ directions of the magnetic field. The SSE voltage changes its polarity by reversing the direction of magnetic field [3]; an absolute average value of V_{SSE} was evaluated to eliminate a thermal emf offset.

In Fig. 2a, the temporal profile of the laser light intensity and V_{SSE} for different laser heating powers are plotted. The SSE signal rises sharply for the first 1 µs and then gradually attains a saturation level $V_{\mathrm{SSE}}^{\mathrm{max}}$. With increasing laser power, $V_{\mathrm{SSE}}^{\mathrm{max}}$ increases linearly (Fig. 2b). This linear behavior indicates that the laser heating is in the linear regime, and no nonlinear phenomena are involved in this process. A comparison of the rising edges of the laser intensity and the SSE signal provides a clear signature that the SSE has no direct correlation with the laser intensity profile.

To understand the ongoing mechanism, we first analyzed the rise times of V_{SSE} for different laser powers. We fitted the spin Seebeck signal V_{SSE} with a saturating double exponential function $1 - A\exp(-t/t_1) - B\exp(-t/t_2)$ which essentially correlates with the heat dynamics of a system owing to heat losses. In Fig. 2c, the rise times, t_1 and t_2, show that, within the limits of experimental error, they are independent of the laser power. Average values of $t_1 = 343$ ns and $t_2 = 5.2$ µs were obtained by using data shown in Fig. 2c. These rise times are different from the rise time of the laser intensity (10%-90% rise time $\approx$ 200 ns).

Our first hunch to interpret these rise times was to study the temperature evolution in the YIG|Pt system. Fortunately, the Pt strip grown over the YIG film can be utilized as a perfect resistance-temperature-detector to measure the temperature at the surface of the YIG film. We performed the resistance measurements of the Pt strip to calculate the variation of the temperature in the YIG|Pt

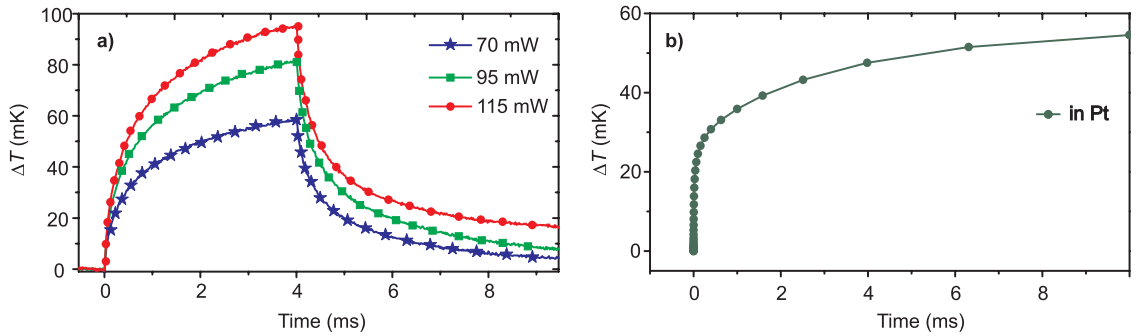

Fig. 3: a) Experimentally observed time profile of the variation of temperature in Pt on heating with a 4 ms long laser pulse with various powers. b) Numerically calculated time profile of the temperature in Pt using COMSOL simulations.

system by the laser heating. To do so, a constant current $I_c = 0.5\,\mathrm{mA}$ was passed through the Pt strip (room temperature resistance $R_{Pt} \approx 508\,\Omega$), and the potential drop ($\Delta V_{Pt} = \Delta R_{Pt} I_c$) due to the heating of Pt was measured with the same experiment setup used for the V_{SSE} measurements. A much longer laser pulse of 4 ms was used to heat the Pt strip. Note that the thermal emf (few microvolts) has negligible influence on these measurements as the potential drop (ΔV_{Pt}) is very large ($\approx 0.25\,\mathrm{V}$). With the help of auxiliary measurements of static resistance versus temperature performed on the same Pt strip, ΔV_{Pt} can be expressed in terms of temperature (T). In Fig. 3a, the variation in the temperature of the Pt strip (ΔT) is plotted for different laser powers. A rise time of 2 ms, obtained by fitting the data with a single saturating exponential function, is three orders of magnitude longer than the rise time of the SSE signal. The saturating exponential behavior of the temperature illustrates that the heat losses in the system dominantly control the heat dynamics of Pt. Further, our measurements evident that, likewise the SSE signal, the rise time of the temperature is also independent of the laser power.

Clearly, from the measurement of the Pt resistance, it can be concluded that the temperature of the system has no direct correlation with the fast time-scale of the SSE. To dig out the cause attributing to the fast rising of the SSE, we propose a model where we consider the thermally-induced motion of magnons in a system of normal metal|magnetic material (e.g., Pt|YIG) subject to a thermal gradient. In such a system, the spin current flowing in/out of the normal metal depends upon the temperature difference of the magnon- and the phonon baths at the interface [5, 6] and the magnon accumulation close to the interface in the magnetic material [11]. On the application of a temperature gradient, thermal magnons having higher population at hotter regions—in equilibrium their population is proportional to the phonon temperature—propagate towards colder regions with less magnon population. The propagation of magnons creates a magnon density gradient in the system along with the phonon thermal gradient. This implies that the spatial distribution of the magnon density depends on the magnon population (phonon temperature) and their propagation lengths. Therefore, the spin Seebeck voltage can be considered as a combination of an interface effect and a bulk contribution from the magnon motions and, eventually, can be expressed as

$$V_{SSE} \propto \alpha(T_N - T_M) + \beta \int_y \nabla T_y \exp(-y/L)\,\mathrm{d}y \quad , \tag{1}$$

where T_N is the phonon temperature (= electron temperature) in the normal metal, T_M the magnon temperature at the interface, ∇T_y the phonon thermal gradient perpendicular to the interface, and L

the effective magnon diffusion length. The parameter α defines the coupling between the electron bath in the normal metal and the magnon bath in the magnetic material. The coupling parameter β specifies the magnon-magnon coupling within the magnetic material. The second term of Eq. (1) is an integration along the phonon thermal gradient over the thickness of the magnetic material.

In order to determine the phonon thermal gradient ∇T_y , we numerically solved the 2D phonon heat conduction equation for the YIG|Pt bilayer using the COMSOL Multiphysics simulation package [12]. In the simulation model, a 10 nm thick and 10 µm wide Pt rectangular film was placed on a 6.7 µm thick and 300 µm wide YIG film. The entire structure was mounted on a GGG substrate (50 µm×300 µm). The simulation parameters are indicated in Table 1. The YIG|Pt interfacial thermal resistance [13] was implemented in the simulations. However, this consideration made no remarkable difference in the outcome of the simulations. As boundary conditions, the temperatures along the short edges of the YIG and GGG layers (see the inset in Fig. 4a) were kept fixed to 293.15 K. These boundaries resembled the heat sink in the experimental set-up. A 2 µm wide area at the middle of the Pt block was considered as a heat source which replicated the laser heating in the experimental set-up.

Table 1: Material parameters used for COMSOL simulations.

Material	Density (kg/m^3)	Thermal conductivity (W/m K)	Heat capacity (J/kg K)
Pt	21450 [14]	20 [15]	130 [14]
YIG	5170 [17]	6.0 [16]	570 [18]
GGG	7080 [16]	7.94 [16]	405 [16]

In Fig. 3b, the simulated temporal evolution of the average temperature in Pt is shown. The temperature dynamics in Pt ($\approx$ 3 ms) was obtained as slow as it was observed in the Pt-resistance-measurement experiment. From simulations, we find that a gradual increase in the average temperature is due to the large heat capacity and volume of the system. On the other hand, the thermal gradient close to interface shows fast dynamics. We evaluated the average thermal gradient ∇T_{avg} along lines parallel to interface for various distances d from the interface in the YIG film (see the inset in Fig. 4a). These parallel lines essentially represent the parallel planes (xz) in the experimental geometry. In Fig 4a, the average thermal gradient for different distances d from the interface are shown. Contrary to the temperature in Pt, the average thermal gradient rises very rapidly and saturates within microseconds. As d, i.e., the depth of the reference line (a plane in a 3D model) from the interface, increases, the rise time of the temperature gradient raises due to the slow-down of the heat flow caused by a finite thermal conductivity and the increasing thermal capacity ($\propto$ volume). Note that even after the first 10 µm, the heat was not fully distributed up to the ends of the Pt block, therefore the dimensions of the model were not affecting the temporal profile of thermal gradients. Furthermore, the simulations show that the lateral heat flow in the YIG film and the heat transport within the Pt strip have minor influences on the average thermal gradients.

The fast rise of the thermal gradient ($\approx$ 50 ns) at the interface of the YIG|Pt bilayer ($d = 0$ nm), shown in Fig. 4a, leads to the conclusion that the time-scale of the SSE cannot be explained by examining only the time evolution of the thermal gradient at the interface. The time scale of the SSE must be influenced by a rather slower process. On the basis of this argument, the first term of Eq. (1), which is proportional to the phonon thermal gradient at the interface [5, 13], can be considered static over the time-scale of our interest ($>$ 50 ns). Using the phonon thermal gradient data, obtained from the COMSOL simulations, we calculated the integral term of Eq. (1) for different magnon propagation lengths. The integral was computed from the interface up to the

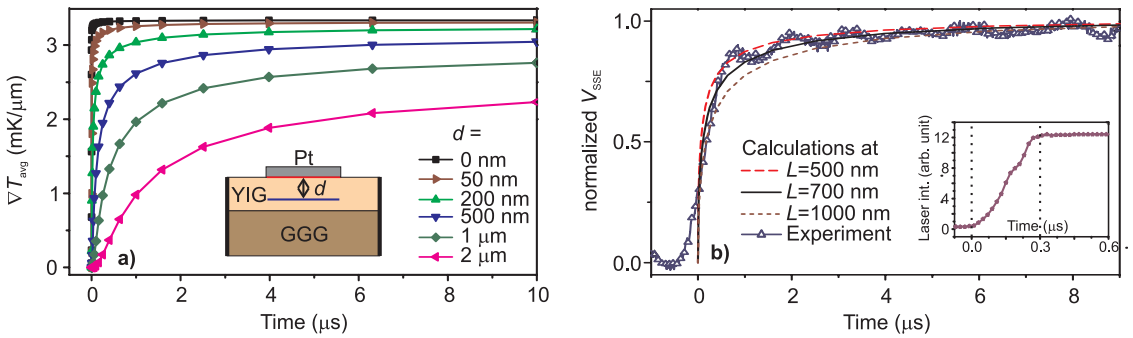

Fig. 4: a) Numerically calculated time profile of the thermal gradients, ∇T_{avg}, in YIG at $d = 0\,\mathrm{nm}$ (interface), 50 nm, 200 nm, 500 nm, 1 μm, and 2 μm distances away form the YIG|Pt interface.The inset shows the model geometry of the COMSOL simulations. The thick vertical lines represent the constant temperature boundaries (293.15 K). b) Comparison of normalized values of spin Seebeck voltage V_{SSE}, measured experimentally, with the numerical calculations for different effective magnon diffusion lengths $L = 500\,\mathrm{nm}$, 700 nm, 1000 nm. The inset shows the switching time (0%-100%, $\approx 0.25\,\mu\mathrm{s}$) of the laser intensity.

thickness of the YIG film. In Fig. 4, the normalized value of the experimentally and numerically calculated V_{SSE} for $L = 500\,\mathrm{nm}$, 700 nm, and 1000 nm are plotted as a function of time. Clearly, our model replicates the experimentally observed time scales of the SSE. On comparing the calculated values of V_{SSE} with the experimental results, we estimate the effective magnon diffusion length to be equal to $\approx 700\,\mathrm{nm}$. Note that the very first slow increase in the normalized V_{SSE} values (for time $\leq 0\,\mu\mathrm{s}$) originates from the switching time of the laser ($\approx 0.25\,\mu\mathrm{s}$), shown in the inset to Fig 4. The effective magnon diffusion length exhibits the depth inside YIG over which the thermal gradient is crucial for the SSE.

Our model indicates that the temporal evolution of the SSE depends on the thermal gradient in the vicinity of the YIG|Pt interface. It is important to notice that the magnon diffusion times are neglected in our model because their group velocities are much higher than the group velocities of phonons. Further, thermal magnons up to a depth of a few hundreds of nanometer in YIG are effectively contributing to the SSE. The typical effective magnon diffusion length of 700 nm agrees with recent theoretical calculations [19, 20]. These findings rule out the possibilities of parasitic interface effects [21] involved in the SSE.

In conclusion, we have presented time-resolved measurements of the spin Seebeck effect in YIG|Pt bilayers performed by the laser heating experiments. Our findings reveal that the rise time of the SSE is sub-microsecond fast, and the SSE signal attains its maximum within a few microseconds though the temperature in the system establishes in milliseconds. The time scale of the SSE is independent of the strength of the heating source. From our model of the magnon diffusion in thermal gradients, we find that the SSE is governed by the diffusion of the thermal magnons from the interface toward the bulk. Moreover, the establishment of the thermal gradient in the YIG film close to the interface determines the time-scales of the SSE. Our model estimates a typical diffusion length for thermal magnons to be around 700 nm in the YIG|Pt system. Our results shed light on the underlying physics of the spin Seebeck effect.

The authors thank F. Heussner for the computational support, V. Lauer for sample-fabrication support, and T. Brächer, T. Meyer, and G. A. Melkov for valuable discussions. We acknowledge financial support by Deutsche Forschungsgemeinschaft (SE 1771/4-1) within Priority Program 1538 “Spin Caloric Transport”, and the technical support from the Nano Structuring Center, TU Kaiserslautern.

References

[1] *Spin Caloritronics*, edited by G.E.W. Bauer, A.H. MacDonald, S. Maekawa, special issue of Solid State Commun. **150**, 459 (2010).

[2] K. Uchida, S. Takahashi, K. Harii, J. Ieda, W. Koshibae, K. Ando, S. Maekawa, E. Saitoh, *Observation of the spin Seebeck effect*, Nature (London) **455**, 778 (2008).

[3] K. Uchida, H. Adachi, T. Ota, H. Nakayama, S. Maekawa, E. Saitoh, *Observation of longitudinal spin-Seebeck effect in magnetic insulators*, Appl. Phys. Lett. **97**, 172505 (2010).

[4] G.E.W. Bauer, E. Saitoh, B.J. van Wees, *Spin caloritronics*, Nat. Mater. **11**, 391 (2012).

[5] J. Xiao, G.E.W. Bauer, K. Uchida, E. Saitoh, S. Maekawa, *Theory of magnon-driven spin Seebeck effect*, Phys. Rev. B **81**, 214418 (2010).

[6] J.I. Ohe, H. Adachi, S. Takahashi, S. Maekawa, *Numerical study on the spin Seebeck effect*, Phys. Rev. B **83**, 115118 (2011).

[7] M. Agrawal, V.I. Vasyuchka, A.A. Serga, A.D. Karenowska, G.A. Melkov, B. Hillebrands, *Direct measurement of magnon temperature: new insight into magnon-phonon coupling in magnetic insulators*, Phys. Rev. Lett. **111** 107204 (2013).

[8] M.B. Jungfleisch, V. Lauer, R. Neb, A.V. Chumak, B. Hillebrands, *Improvement of the yttrium iron garnet/platinum interface for spin pumping-based applications*, Appl. Phys. Lett. **103**, 022411 (2013).

[9] M. Walter, J. Walwoski, V. Zbarsky, M. Münzenberg, M. Schäfers, D. Ebke, G. Reiss, A. Thomas, P. Peretzki, M. Seibt, J.S. Moodera, M. Czerner, M. Bachmann, C. Heiliger, *Seebeck effect in magnetic tunnel junctions*, Nat. Mater. **10**, 742 (2011).

[10] A. Boehnke, M. Walter, N. Roschewsky, T. Eggebrecht, V. Drewello, K. Rott, M. Münzenberg, A. Thomas, G. Reiss, *Time-resolved measurement of the tunnel magneto-Seebeck effect in a single magnetic tunnel junction*, Rev. Sci. Instrum. **84**, 063905 (2013).

[11] A. Kehlberger, R. Röser, G. Jakob, M. Kläui, *Determination of the origin of the spin Seebeck effect-bulk vs. interface effects*, *arxiv.org/abs/1306.0784*.

[12] COMSOL Multiphysics with Heat Transfer Module.

[13] M. Schreier, A. Kamra, M. Weiler, J. Xiao, G.E.W. Bauer, R. Gross, S.T.B. Goennenwein, *Magnon, phonon, and electron temperature profiles and the spin Seebeck effect in magnetic insulator/normal metal hybrid structures*, Phys. Rev. B **88**, 094410 (2013).

[14] D. Lide. *CRC Handbook of Chemistry and Physics, 89th Edition* (Taylor & Francis, 2008).

[15] Q.G. Zhang, B.Y. Cao, X. Zhang, M. Fujii, K. Takahashi, *Size effects on the thermal conductivity of polycrystalline platinum nanofilms*, J. Phys.: Condens. Matter **18** 7937 (2006).

[16] A.M. Hofmeister, *Thermal diffusivity of garnets at high temperature*, Phys. Chem. Miner. **33** 45 (2006).

[17] A.E. Clark, R.E. Stranka, *Elastic constants of single crystal YIG*, J. Appl. Phys. **32** 1172 (1961).

[18] M. Guillot, F. Tchéou, A. Marchand, P. Feldmann, R. Lagnier, *Specific heat in erbium and yttrium iron garnet crystals*, Z. Phys. B **44** 53 (1981).

[19] A.A. Kovalev, Y. Tserkovnyak, *Thermomagnonic spin transfer and Peltier effects in insulating magnets*, Europhys. Lett. **97** 67002 (2012).

[20] S. Hoffman, K. Sato, Y. Tserkovnyak, *Landau-Lifshitz theory of the longitudinal spin Seebeck effect*, Phys. Rev. B **88**, 064408 (2013).

[21] S.Y. Huang, X. Fan, D. Qu, Y.P. Chen, W.G. Wang, J. Wu, T.Y. Chen, J.Q. Xiao, C.L. Chien, *Transport magnetic proximity effects in platinum*, Phys. Rev. Lett. **109**, 107204 (2012).

4.13 Spin wave reflection and magnon-phonon energy transfer

F. Ciubotaru, V. I. Vasyuchka, A. V. Chumak, T. Langner, A. A. Serga, and B. Hillebrands

The interaction between the phonon and magnon subsystems of a magnetic medium constitutes a hot topic of research of the modern spincaloritronics [1–7]. The complexity of magnon spectra, their dependence on the orientation of a bias magnetic field, and the existence of both bulk and surface magnon modes make this task very complicated and intriguing. For example, a unidirectional spin-wave heat conveyer [8] caused by a non-reciprocal surface spin wave has been recently demonstrated. Here we report on local heat deposition by surface spin waves reflected at the end of a spin-wave waveguide. We show that this phenomenon is associated with the *intrinsic* properties of the reflection process: The magnetic energy is transferred to the phonon bath through non-propagating bulk magnon modes, which are excited to compensate a spin-wave symmetry breaking at the edge of a magnetic medium.

The spin-wave waveguide investigated in this work is carved from a single-crystalline yttrium iron garnet film (YIG, $Y_3Fe_5O_{12}$) of 16 µm thickness grown on a 500 µm thick gadolinium gallium garnet (GGG) substrate. The waveguide is 1.2 mm wide and 20 mm long. One end of this YIG stripe is cut sharp under a right angle (90°) to produce a perfect spin-wave mirror while the other end is tapered under a 30° angle to avoid the backscattered waves. The spin-waves are excited by a microwave driven stripline antenna of 50 µm width placed across the waveguide 5 mm apart from its right-angled end. In our experiments the YIG stripe was tangentially magnetized by a bias field $H = 1750$ Oe either along or across its long axis. The first case corresponds to the excitation and propagation of a reciprocal backward volume magnetostatic spin wave (BVMSW) and the second one to a non-reciprocal magnetostatic surface spin wave (MSSW) [9–11]. Figure 1 schematically illustrates the sample geometry and the experimental techniques employed in this work. The temperature distribution caused by the energy transfer from spin waves to the phonon system is mapped by an infrared camera (FLIR SC655) with a thermal sensitivity of 0.05 K, a spatial resolution of 50 µm, and a time resolution of 5 ms. The dynamics of the traveling spin waves is measured by means of space- and time-resolved Brillouin light scattering spectroscopy (BLS).

The first experiments were aimed to determine the spin-wave transmission characteristics by use of an additional microstrip antenna placed closer to the tapered end of the YIG waveguide. It was found that the BVMSW transmission is highest at 6.9 GHz and vanishes at 6.7 GHz due to the increase of the BVMSW wavenumber and corresponding decrease of its excitation efficiency

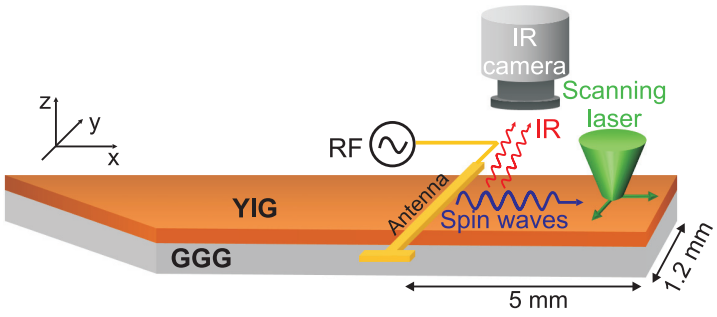

Fig. 1: Sketch of the experimental setup. Spin waves are excited in a single-crystalline YIG waveguide of 16 µm thickness by a 50 µm wide microwave stripline antenna. The temperature distribution associated with the heat induced by propagating spin-waves is measured using an infrared camera. The spin-wave intensity is probed by Brillouin light scattering spectroscopy.

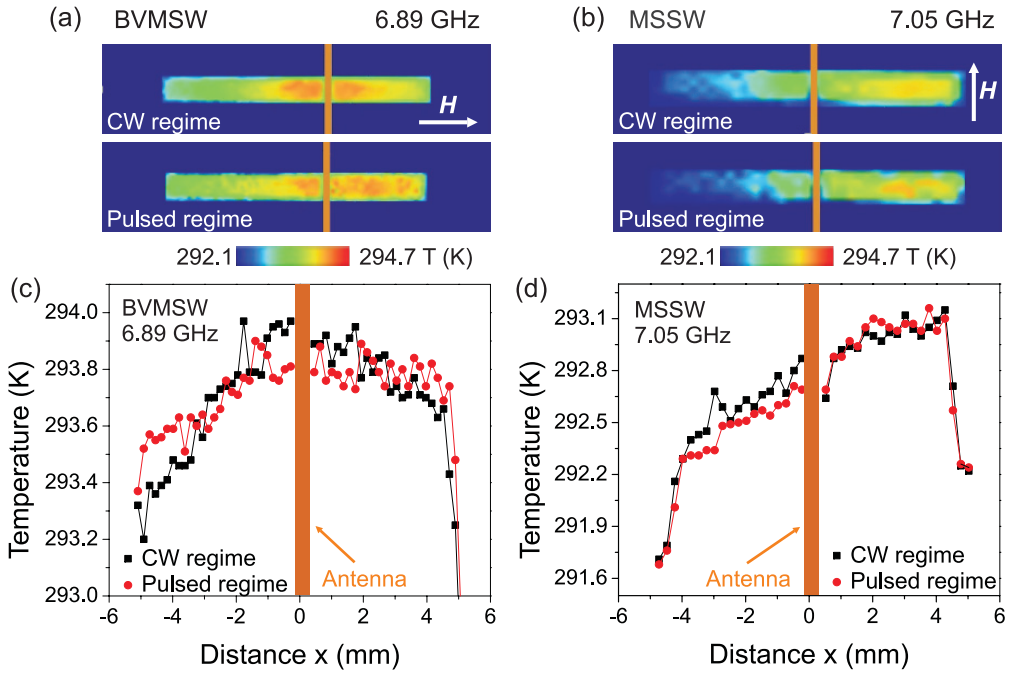

Fig. 2: Temperature distribution images in the case of BVMSWs (a) and MSSWs (b), respectively. The top images correspond to a continuous microwave excitation (CW) at an applied power of 80 mW for BVMSW and of 8 mW for MSSW, respectively. The bottom images correspond to a spin-wave excitation in the pulsed regime (20 ns-long microwave pulse and 800 ns repetition rate). The applied power was 630 mW for BVMSW and 100 mW for MSSW. (c) and (d) Temperature profiles as a function of the distance from the antenna extracted in the center of the waveguide for the two cases presented in (a) and (b).

and group velocity. The propagation of the magnetostatic surface waves is detected in a frequency band from 6.93 GHz to 7.2 GHz.

Figure 2 shows the temperature distributions in the YIG stripe which is heated either by BVMSW (at 6.89 GHz) or by MSSW (at 7.05 GHz). In the BVMSV case the spin-wave heat is symmetrically allocated relative to the temperature maximum at the excitation antenna (see the top panel in Fig 2a). This symmetry can be easily understood by taking into account the excitation and propagation reciprocity of BVMSWs. The temperature decrease towards the ends of the YIG strip is associated with the decay of the wave in course of its propagation. The slight asymmetry visible in Fig. 2c appears due to the additional heating of the YIG film by the wave reflected from the right edge of the waveguide. Similar temperature maps are observed in the entire BVMSW passband. Furthermore, the symmetry of temperature distribution for the backward volume waves is nearly independent on the applied microwave power. Only an increase of the absolute value of temperature upon increasing the microwave power was observed.

A drastically different temperature distribution is observed in the passband of the magnetostatic surface waves: The temperature maximum is shifted from the antenna to the right-angled end of the sample (see Fig. 2b).

In order to understand this unconventional behavior we have to take into account the non-reciprocal character of the magnetostatic surface waves. It is well known that these waves are excited by a microstrip antenna in a direction given by the product: $\mathbf{M} \times \mathbf{n}$, where $\mathbf{M}$ denotes the saturation magnetization vector and $\mathbf{n}$ is the normal vector of the surface. Within this consideration an unidirectional spin-wave heat conveyer [8] is expected to be realized, and obviously, our measurements

confirm this phenomenon. However, the unidirectional excitation of the surface wave can explain the different temperatures to the left and to the right sides of the antenna but not the temperature maximum at the sample end. Indeed, in Ref. [8] the temperature maximum caused by the spin-wave heat conveyer is localized close to the excitation antenna. The small temperature grow shown in Ref. [8] at the tip of the tapered spin-wave waveguide appears due to the concentration of the spin-wave energy into a very small sample area. This geometrically dependent mechanism is completely unapplicable to our experimental situation as we use a regular spin-wave waveguide. Thus, the physical nature of the enhanced magnon-phonon conversion at the spin-wave mirror must be clarified.

First of all, in order to verify our findings and to exclude the influence of the interference between the incident and reflected spin-waves on the observed temperature dependencies we have redone our observations in a pulsed regime. Microwave pulses of 20 ns duration at the same carrier frequencies as the frequencies of the corresponding continuous waves were applied to the antenna. A repetition rate of 800 ns ensured that the consecutive pulses did not overlap. In addition, the applied microwave power was increased from 8 to 100 mW to be able to observe small thermal effects caused by the short spin-wave packets. The recorded temperature distributions displayed in the bottom panels in Figs. 2a and b show no appreciable difference between the two excitation regimes.

In a next step, the spin-wave dynamics of the reflection process was investigated by means of time- and spatially resolved BLS spectroscopy. The MSSW and BVMSW packets were exited with the same parameters as for the pulsed infrared measurements. The BLS data are presented in Fig 3. The panels show two-dimensional intensity distribution maps of a single traveling spin-wave packet at successive moments of time. No qualitative difference in the behavior of the BVMSW and MSSW pulses is visible on the way from the antenna to the end of the sample. The BVMSW packet moves slightly faster ($v_{gr}^{\mathrm{BVMSW}} = 2.5\,\mathrm{cm}/\mu\mathrm{s}$) than the MSSW one ($v_{gr}^{\mathrm{MSSW}} = 1.5\,\mathrm{cm}/\mu\mathrm{s}$) and therefore is somewhat shorter.

At the same time, one can immediately notice that the reflected wave packets evolve completely differently for the two spin-wave species. The BVMSW pulse is reflected nearly in the same shape as just before the incidence. The intensity oscillations near the end of the waveguide are consistent with the carrier wavelength of the BVMSW packet, and thus are caused by the interference of the incident and the reflected waves. Therefore, the end of the structure acts as a good spin-wave mirror from which the BVMSW magnons scatter nearly elastically. It is obvious, that no elastic scattering of magnons at the end of the structure can be assumed for the MSSW case: A strong packet distortion and broadening is clearly visible. In addition, the intensity oscillations at the end of the waveguide are not anymore consistent with the expected interference pattern of a traveling spin wave.

These facts allow us to suppose that the MSSW dynamics near the end of the waveguide is influenced by excitation of additional spin-wave modes. Indeed, the intrinsically non-reciprocal character of MSSW means that this wave cannot be reflected at the end of the sample without symmetry breaking: The spin-wave intensity maximum must be shifted from the top to the bottom surface of the magnetic film. The spatially non-uniform spin-wave modes compensate this symmetry breaking and ensure the electromagnetic boundary conditions at the edges of a magnetic medium. Moreover, as such modes exist only at the sample end they can deposit an excessive heat to this region of the sample because of their non-propagating character.

In order to gain deeper insight into the physical mechanisms involved in the process of the spin-wave reflection we performed micromagnetic simulations [12] of our experimental situation. Since

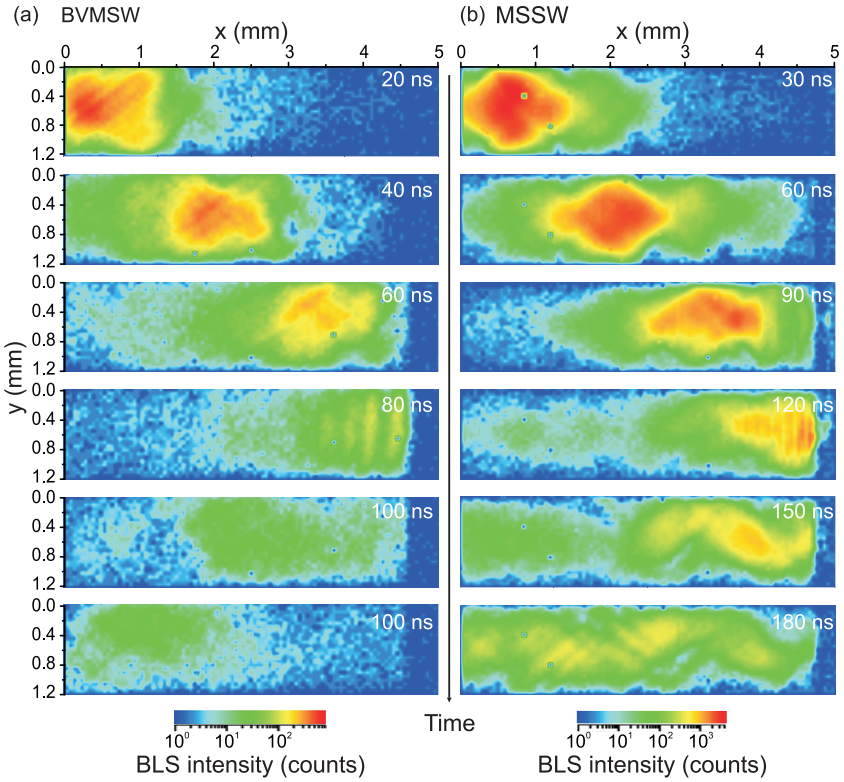

Fig. 3: Spatial maps of the intensity of spin-wave packets of 20 ns duration measured by space- and time-resolved Brillouin light scattering spectroscopy at successive moments of time. The panels correspond to the excitation of backward volume waves (a) and of the magnetostatic surface waves (b), respectively. The zero position marks the position of the excitation antenna.

the simulation of the entire YIG sample is not suitable due to extremely long computational times we decreased the size of the model sample: It is a 16 µm thick YIG waveguide with the lateral dimensions of 4 mm × 1 mm. The simulated area is divided into 400 × 100 × 8 cells, each cell has a size of 10 µm × 10 µm × 2 µm. The spin-waves are excited by an alternating microwave field induced by a wire antenna of 50 µm in diameter. The wire antenna is placed across the waveguide at 2.5 mm from its right end, which plays the role of the spin-wave mirror. In order to avoid spin-wave reflection from the left end of the sample damping boundary conditions are used there.

The simulations performed for the backward volume waves at different frequencies in both pulsed and continuous regimes of excitation show the same behavior as it was observed in the BLS experiments: i) the incident and the reflected pulses have nearly the same shape; and ii) the spatial distribution of oscillation in the spin-wave intensity at the end of the waveguide is consistent with the wavelength of the excited spin waves. These results confirm the assumption of an elastic scattering process of the volume waves by the end of the structure.

In the next paragraphs we address the simulation of propagation and reflection of magnetostatic surface waves. As a starting point we simulated MSSW in a pulsed regime. The excitation frequency was set to $f_e = 7.165$ GHz. The intensity of spin waves in the center of the waveguide at 1.25 mm distance from its right end is shown as a function of time in Fig. 4a. As it was expected, the intensity of the incident wave packet is higher on the top surface while the intensity of the reflected packet is higher on the bottom surface of the film.

By integrating the spin-wave intensity over the width, thickness and the entire simulated time for different positions along the waveguide we are able to calculate the spin-wave energy that flows through each section of the waveguide (see Fig. 4b). This energy is proportional to the total heat deposited by the relaxing spin waves (both incident and reflected) in the corresponding points of the sample. The initial decrease of the transferred energy, which is caused by the relaxation of the MSSW in course of its propagation, gives place to the energy increase near the end of the

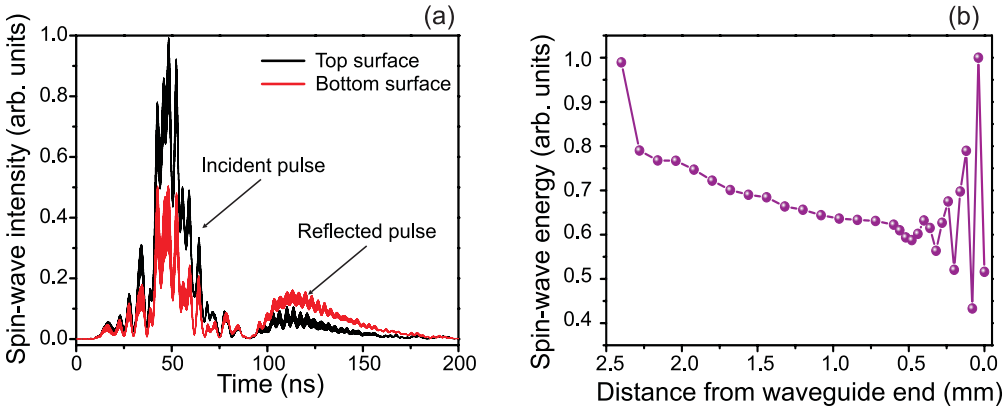

Fig. 4: a) Intensity of the surface spin waves excited in a pulsed regime as a function of time. The spin waves are excited with a frequency of 7.165 GHz by a pulse of 15 ns duration. The data was extracted in two points on the top and on the bottom surface located in the center of the waveguide at 1.25 mm from its right end. b) Energy carried by spin waves (same regime as in (a)) as a function of the distance from the end of the waveguide. The energy was calculated by integrating the spin-wave intensity over the thickness, the width and over the entire simulated time.

structure. This increase agrees well with our hypothesis about the role of the localized spin-wave modes. However, at this point it is hard to determine the contribution of the modes because of a strong oscillation pattern caused by the interference of the incident and reflected waves: The spatial periodicity of the observed oscillations is half of the MSSW wavelength ($\lambda = 250\,\mu$m).

It is worth to mention that the MSSW intensity profile over the film thickness is proportional to $\exp(-2\pi z/\lambda)$, where z is the coordinate perpendicular to the waveguide surface. It means that the overlap between the incident and reflected waves, and thus the intensity of the interference pattern can be significantly reduced by using MSSWs with a shorter wavelength. We performed an additional simulation considering an excitation frequency of 7.285 GHz and, consequently, a spin-wave wavelength of $\sim 70\,\mu$m. To exclude spurious effects which may arise due to the dispersion broadening of the MSSW pulse at this spectral point we used a continuous spin-wave excitation. From Fig. 5a one can clearly see that the oscillations of the spin-wave energy are strongly reduced in this case. Nevertheless, comparing the extracted profile of the transferred energy with the conventional exponential spin-wave decay (red curve in Fig. 5a) one can still notice the pronounced energy increase near the end of the waveguide.

Moreover, our simulations directly evidence the previously assumed conversion of the surface wave to higher spin-wave modes at the reflecting edge. At 1 mm distance from the waveguide end the distribution of the spin-wave intensity across the thickness of the YIG film (shown in Fig. 5b) has an exponential profile with near zero value at the bottom surface. The same distribution extracted at 50 µm distance from the end has a drastically different character (see Fig. 5b). A few oscillations are clearly visible and their appearance is an important indicative for the presence of standing waves across the waveguide thickness. Furthermore, the MSSW intensity distributions extracted across the width at the top and the bottom film surfaces at 50 µm from the waveguide end (marked with black circles in Fig. 5c and d) also show pronounced oscillations. This fact underlays the presence of standing modes across the waveguide width as well. In contrast, the distribution of intensities extracted at 1 mm from the end (red circles in Fig. 5c and d) has a bell-like shape. Altogether, these observations evidence clearly the fact that standing waves are formed on both the thickness and the width in the proximity of the end of the waveguide.

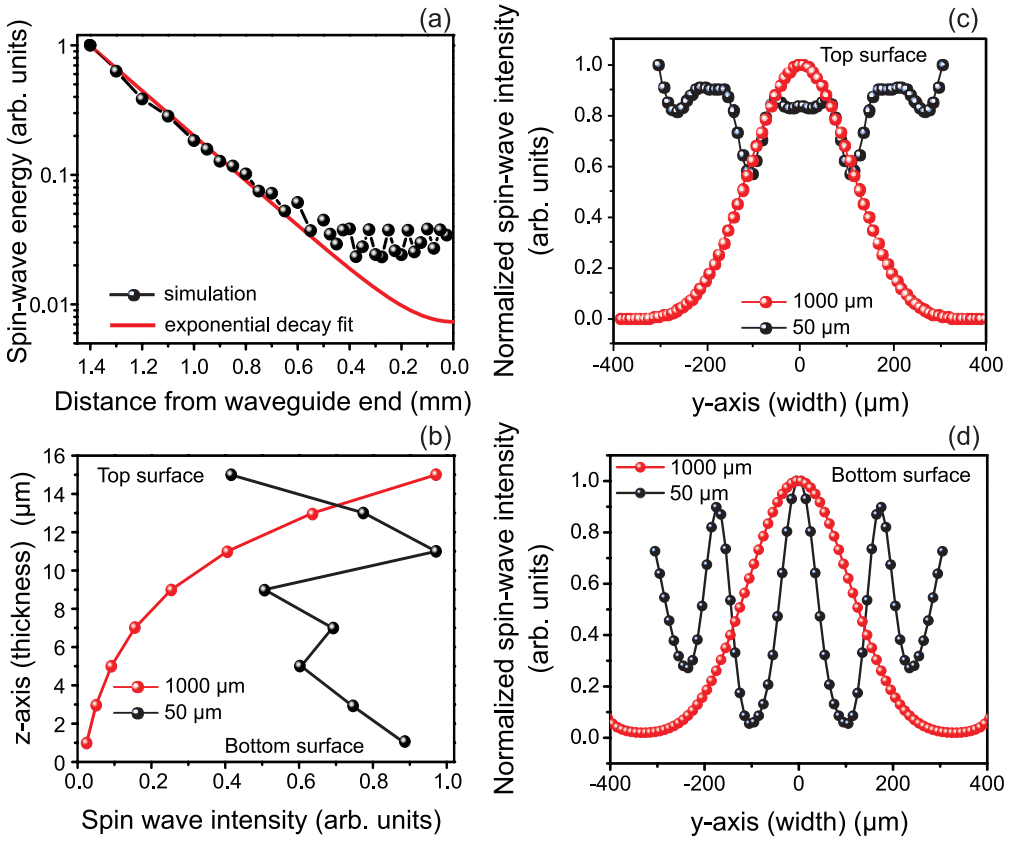

Fig. 5: (a) Energy carried by spin waves as a function of the distance from the end of the waveguide. (b) Distributions of the MSSW intensity across the thickness of the waveguide extracted at 1 mm and at 50 µm from its end. The zero position denotes the top surface. Distribution of the MSSW intensity across the waveguide width at the top surface (c) and at the bottom surface (d) extracted at 50 µm and at 1 mm from the waveguide end, respectively. Each distribution was normalized to its maximum. The spin waves are excited continuously with a frequency of 7.285 GHz.

In summary, we have investigated the reflection of both the magnetostatic backward volume and the surface spin waves at the end of the spin-wave waveguide by means of infrared thermography, Brillouin light scattering spectroscopy, and micromagnetic simulations. We have found that the edge of a magnetic medium acts as a perfect mirror which reflects the volume waves nearly elastically. On the contrary, the magnetostatic surface waves suffer a complex reflection mechanism due to their non-reciprocal character: The formation of both width and thickness standing spin-wave modes at the end of the waveguide is revealed. The spatially localized generation and consequent relaxation of these spin-wave modes lead to a local heat deposition at the reflecting end of the magnetic medium.

We acknowledge financial support by Deutsche Forschungsgemeinschaft within Priority Program 1538 “Spin Caloric Transport”.

References

[1] H. Adachi, K. Uchida, E. Saitoh, J. Ohe, S. Takahashi, S. Maekawa, *Gigantic enhancement of spin Seebeck effect by phonon drag*, Appl. Phys. Lett. **97**, 252506 (2010).

[2] C.M. Jaworski, J. Yang, S. Mack, D.D. Awschalom, R.C. Myers, J.P. Heremans, *Spin-Seebeck effect: A phonon driven spin distribution*, Phys. Rev. Lett. **106**, 186601 (2011).

[3] K. Uchida, H. Adachi, T. An, T. Ota, M. Toda, B. Hillebrands, S. Maekawa, E. Saitoh, *Long-range spin Seebeck effect and acoustic spin pumping*, Nat. Mater. **10**, 737-741 (2011).
[4] M. Agrawal, V.I. Vasyuchka, A.A. Serga, A.D. Karenowska, G.A. Melkov, B. Hillebrands, *Direct measurement of magnon temperature: New insight into magnon-phonon coupling in magnetic insulators*, Phys. Rev. Lett. **111**, 107204 (2013).
[5] D.R. Birt, K. An, A. Weathers, L. Shi, M. Tsoi, X. Li, *Brillouin light scattering spectra as local temperature sensors for thermal magnons and acoustic phonons*, Appl. Phys. Lett. **102**, 082401 (2013).
[6] M. Schreier, A. Kamra, M. Weiler, J. Xiao, G.E.W. Bauer, R. Gross, S.T.B. Goennenwein, *Magnon, phonon, and electron temperature profiles and the spin Seebeck effect in magnetic insulator/normal metal hybrid structures*, Phys. Rev. B **88**, 094410 (2013).
[7] T.T. Heikkilä, M. Hatami, G.E.W. Bauer, *Spin heat accumulation and its relaxation in spin valves*, Phys. Rev. B **81**, 100408 (2010).
[8] T. An, V.I. Vasyuchka, K. Uchida, A.V. Chumak, K. Yamaguchi, K. Harii, J. Ohe, M.B. Jungfleisch, Y. Kajiwara, H. Adachi, B. Hillebrands, S. Maekawa, E. Saitoh, *Unidirectional spin-wave heat conveyer*, Nature Mater. **12**, 549-553 (2013).
[9] T. Schneider, A.A. Serga, T. Neumann, B. Hillebrands, *Phase reciprocity of spin-wave excitation by a microstrip antenna*, Phys. Rev. B **77**, 214411 (2008).
[10] M.P. Kostylev, *Non-reciprocity of dipole-exchange spin waves in thin ferromagnetic films*, J. Appl. Phys. **113**, 053907 (2013).
[11] A.A. Serga, A.V. Chumak, B. Hillebrands, *YIG magnonics*, J. Phys. D: Appl. Phys. **43**, 264002 (2010).
[12] The simulations were performed using the OOMMF open code: M.J. Donahue, D.G. Porter, Report NISTIR 6376, NIST, Gaithersburg, MD, USA (1999).

E. New Materials and Heusler Compounds

The material class of Heusler compounds contains several promising candidates regarding their utilization in the field of *spintronics* and in particular *magnon spintronics*. The major reasons for the interest in Heusler compounds are their high Curie temperature, their high spin polarization, and their low magnetic Gilbert damping.

Spintronics can be regarded as an extension of conventional electronics by using the electrons' spin as an additional degree of freedom for applications in data storage and sensing. Spintronic devices mainly rely on magneto-resistive effects such as the giant magneto resistance or tunneling magneto resistance. For the optimization of these effects, it is crucial to find materials with a high spin polarization like the Heusler compounds. The field of magnon spintronics can mainly benefit from the low Gilbert damping in some of the Heusler compounds. The major motivation behind magnon spintronics is an energy-efficient information transport and processing that is purely based on magnons, which are the fundamental excitations in a magnetic material. A major challenge in magnon spintronics is the identification and development of suitable low-damping materials for the realization of magnon conduits on the microscale. This challenge can be addressed by the utilization of Heusler compounds.

Heusler compounds have the general composition X_2YZ, where X and Y are transition metals, and Z is an element from the main groups III-V. One of the most promising classes of Heusler materials is given by the cobalt-based compounds with the composition Co_2YZ. The reason for both, the high spin polarization as well as the low Gilbert damping, is the half-metallic character of Heusler compounds. Half metallicity describes the different features in the band structure of minority and majority electrons close to the Fermi energy. For the minority electrons, a band gap can be found at the Fermi energy. In contrast to this, the majority spin channel exhibits a finite density of states at the Fermi level and, thus, metallic character.

Our group is part of the joint Japanese-German research unit *Advanced Spintronic Materials and Transport Phenomena* (ASPIMATT), which addresses the development, the characterization, and the optimization of Heusler materials for the utilization in spintronics and magnon spintronics. The working package addressed in our group covers *Nonlinear spin-wave dynamics and radiation properties of small Heusler devices* in the field of magnon spintronics.

Recent experiments with the compound $Co_{40}Fe_{20}B_{20}$ revealed a great potential for future spintronic and magnon spintronic applications. One reason for the interest in $Co_{40}Fe_{20}B_{20}$ is its low damping that was observed even in polycrystalline samples. In Report 4.14, we present an extensive study of the material parameters, and in particular the Gilbert damping, depending on the annealing temperature using magneto-optical methods and microwave techniques.

In Report 4.15, the investigation of the Gilbert damping in individual microstructures made of the Heusler compound $Co_2Mn_{0.6}Fe_{0.4}Si$ will be discussed. These investigation are based on time-resolved Brillouin light scattering microscopy and parametric amplification of spin dynamics. It is shown, that the low Gilbert damping observed in $Co_2Mn_{0.6}Fe_{0.4}Si$ thin films is preserved in the patterning process and, therefore, it is available for the design of microscopic magnon conduits.

E. Neue Materialien und Heusler-Legierungen

In der Materialklasse der Heusler-Verbindungen finden sich zahlreiche viel versprechende Kandidaten hinsichtlich der Verwendung in den Feldern der *Spintronik* und der *Magnonspintronik*. Die

Hauptgründe für das Interesse an den Heusler-Materialien sind ihre hohe Curie-Temperatur, ihre hohe Spinpolarisation und ihre niedrige magnetische Gilbert-Dämpfung.

Die Spintronik stellt eine Erweiterung konventioneller Elektronik dar, die durch die Nutzung des Elektronenspins als zusätzlichem Freiheitsgrad zur Datenspeicherung und in der Sensorik realisiert wird. Spintronische Bauelemente stützen sich hauptsächlich auf Effekte wie den Riesenmagnetowiderstand oder den Tunnelmagnetowiderstand. Die Optimierung dieser Effekte setzt Materialien mit einer hohen Spinpolarisation, wie die Heusler-Verbindungen, voraus. Das Feld der Magnonspintronik kann wiederum hauptsächlich von der niedrigen Gilbert-Dämpfung in Heusler-Materialien profitieren. Die Motivation hinter der Magnonspintronik ist eine energieeffiziente Datenverarbeitung auf Basis von Magnonen, welche die fundamentalen Anregungen eines magnetischen Festkörpers sind. Eine der großen Herausforderungen der Magnonspintronik ist die Identifizierung und die Entwicklung von geeigneten Materialen für die Realisierung von magnonischen Wellenleitern auf der Mikrometerskala. Diese Herausforderung kann durch die Verwendung von Heusler Materialien angegangen werden.

Heusler-Materialien zeigen eine generelle Zusammensetzung der Form X_2YZ. Hierbei sind X und Y Übergangsmetalle, während Z eine Elemet aus den Hauptgruppe III-V ist. Eine der interessantesten Untergruppen von möglichen Heusler-Verbindungen ist die Gruppe der Kobalt basierten Materialien der Form Co_2YZ.

Der Grund für die hohe Spinpolarisation sowie auch die geringe Gilbert-Dämpfung liegt in der halbmetallischen Natur der Heusler-Verbindungen. Dieser halbmetallische Charakter beschreibt die Unterschiede in der Bandstruktur der Majoritäts- und Minoritätsladungsträger insbesondere nahe der Fermi-Energie. Für die Minoritätselektronen lässt sich eine Bandlücke an der Fermi-Kante beobachten, während die Bandstruktur der Majoritätselektronen eine endliche Zustandsdichte, und damit metallischen Charakter, aufweist.

Unsere Gruppe ist Teil der japanisch-deutschen Forschergruppe *Advanced Spintronic Materials and Transport Phenomena* (ASPIMATT), welche die Entwicklung, Charakterisierung und Optimierung von Heusler-Materialien für die Verwendung in Spintronik und Magnonspintronik zum Ziel hat. Das Arbeitspaket, das in unserer Gruppe bearbeitet wird, trägt den Titel *Nonlinear spin-wave dynamics and radiation properties of small Heusler devices* und befasst sich mit dem Gebiet der Magnonspintronik.

Kürzlich durchgeführte Experimente zeigen das große Potential der Legierung $Co_{40}Fe_{20}B_{20}$ bezüglich zukünftiger Anwendungen in Spintronik oder Magnonspintronik. Ein Grund für das wachsende Interesse an $Co_{40}Fe_{20}B_{20}$ ist die geringe Gilbert Dämfpung, die sogar in polykristallinen Proben beobachtet werden konnte. In Bericht 4.14 präsentieren wir eine ausführliche Studie über die Materialeigenschaften von $Co_{40}Fe_{20}B_{20}$, und insbesondere der Dämpfung, in Abhängigkeit von der Annealing-Temperatur. Die Studie stützt sich auf magnetooptische Methoden und Mikrowellentechnik.

In Bericht 4.15 wird die Untersuchung der Gilbert-Dämpfung in individuellen Mikrostrukturen aus dem Heusler Material $Co_2Mn_{0.6}Fe_{0.4}Si$ diskutiert. Diese Untersuchungen wurden mittels zeitaufgelöster Brillouin-Lichtstreumikroskopie und der parametrischen Verstärkung von Spinwellen durchgeführt. Es wird gezeigt, dass die niedrige Dämpfung, die in $Co_2Mn_{0.6}Fe_{0.4}Si$-Filmen beobachtet wurde, im Prozess der Mikrostrukturierung erhalten bleibt, und somit auch für das Design von mikroskopischen Spinwellen-Wellenleitern zur Verfügung steht.

4.14 Annealing influence on the Gilbert damping parameter and the exchange constant of $Co_{40}Fe_{40}B_{20}$ thin films

A. Conca, E. Th. Papaioannou, S. Klingler, J. Greser, T. Sebastian, B. Leven, and B. Hillebrands

The search for materials with low damping properties is very active due to their importance for many fields such as spin-wave propagation and manipulation experiments and spin−torque nano-oscillators in magnon spintronics. In this sense, CoFeB is a very promising material for which low damping values have been reported [1–3]. CoFeB is commonly used in the fabrication of magnetic tunneling junctions, providing high TMR ratios in combination with MgO barriers. It is known that an annealing step is required to induce a crystallization of the as-deposited amorphous CoFeB thin films and thus achieve large magnetoresistance values. However, the influence of the annealing temperature on the damping or other magnetic properties has not been systematically studied. Furthermore, some apparent contradictions can be found in the literature. Bilzer *et al.* [1] reported an increase of the Gilbert damping parameter α from 0.006 for as-deposited films to 0.032 for $Co_{72}Fe_{18}B_{10}$ films annealed at 280 °C. On the contrary, values as low as $\alpha = 0.004$ are reported for $Co_{40}Fe_{40}B_{20}$ films annealed at 310 °C [3], which may indicate that the annealing does not influence much the damping properties. It has to be pointed out, that the different composition of the films in these two works makes a direct comparison difficult. To add more confusion, a value of $\alpha = 0.013$ has been also reported for as-deposited $Co_{40}Fe_{40}B_{20}$ films [4].

Recently, our group reported on measurements on the damping parameter and the exchange constant of as-deposited $Co_{40}Fe_{40}B_{20}$ thin films [2]. A low damping value of $\alpha = 0.0042$ and an exchange constant of $A = 1.5 \cdot 10^{-11}$ J/m was measured. Now, we report on the influence of the annealing temperature on these and other film properties.

Films with a thickness of $d = 78$ nm were deposited by magnetron rf sputtering on SiO_2 substrates in a chamber with a base pressure of $5 \cdot 10^{-7}$ mbar and capped with a 7 nm thick MgO layer. The Ar pressure during deposition was $4.7 \cdot 10^{-3}$ mbar with a gas flow of 10 sccm. The films were annealed at several temperatures during 30 min in a different chamber with a base pressure of $5 \cdot 10^{-10}$ mbar. The dynamic properties and material parameters were studied by measuring the ferromagnetic resonance using a strip−line vector network analyzer (VNA-FMR). A magneto-optical Kerr (MOKE) effect setup in longitudinal geometry with a spatial resolution of about 200 µm, and a laser wavelength of 635 nm was used to characterize the optical properties.

Figure 1a shows the Kerr rotation dependence on the annealing temperature T_{ANN}. Due to the limited penetration depth of light in metallic systems, only the top $10-20$ nm of the films are probed. The large increase of the Kerr signal, which almost doubles itself, is quite remarkable. It hints to a strong modification of the film surface starting from $T_{ANN} = 300$ °C. Differently to the steady increase of the Kerr signal, the coercive field (Fig. 1b) remains almost unchanged up to $T_{ANN} = 383$ °C and then a sharp jump is observed. This apparent contradiction may indicate that the surface is first affected by the annealing in comparison to the bulk of the film.

The study of the dependence of the frequency of the ferromagnetic resonance (FMR) peak and of the perpendicular standing spin−wave (PSSW) modes on the applied magnetic field provides information about the saturation magnetization M_s and the exchange constant A of the material. Figure 2 shows exemplarily this dependence for a $Co_{40}Fe_{40}B_{20}$ film annealed at 200 °C. A sample spectrum for $\mu_0 H = 52.6$ mT is also shown in the inset. Due to the limited sensitivity of the exper-

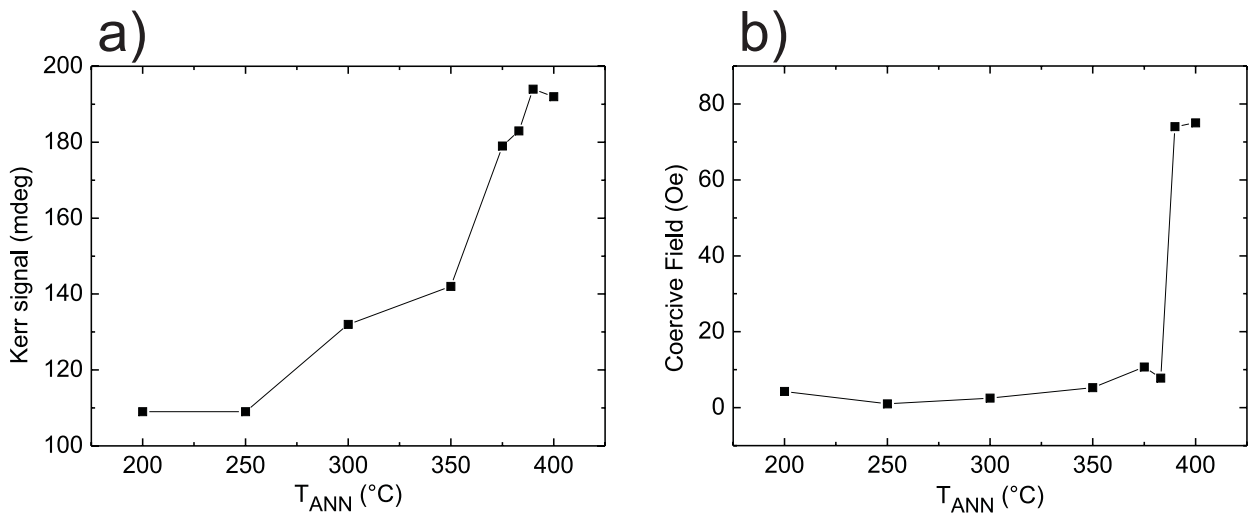

Fig. 1: Dependence of the Kerr signal (a) and coercive field (b) on the annealing temperature for 78 nm thick $Co_{40}Fe_{40}B_{20}$ films.

imental setup, only the first PSSW mode is visible. For the extraction of M_s the FMR frequencies were fitted (grey line) using Kittel's formula [5]:

$$f_{FMR} = \frac{|\gamma|\,\mu_0}{2\pi}\sqrt{(H_{ext}+H_{ani})(H_{ext}+H_{ani}+M_S)} \quad , \tag{1}$$

where H_{ext}, H_{ani} are the applied and anisotropy magnetic field, respectively, and γ is the gyromagnetic ratio of the free electron. The frequency of the PSSW modes can be calculated following the expression [6]

$$f_{\mathrm{PSSW}} = \frac{|\gamma|\,\mu_0}{2\pi}\left[\left(H_{\mathrm{ext}}+\frac{2A}{M_{\mathrm{S}}}\left(\frac{p\pi}{d}\right)^2\right)\times\left(H_{\mathrm{ext}}+\frac{2A}{M_{\mathrm{S}}}\left(\frac{p\pi}{d}\right)^2+4\pi M_{\mathrm{S}}\right)\right]^{1/2} \quad , \tag{2}$$

where p is the order of the PSSW mode, A is the exchange constant and d is the thickness of the film. The fit to the formula is also plotted in Fig. 2 (black line).

Figure 3a shows the obtained values for M_s for different annealing temperatures. The saturation magnetization is slighty varying around a mean value over the temperature range with a small decrease starting at $T_{ANN} = 375\,^{\circ}C$. The values for M_s cannot be measured for values $T_{ANN} \geq 390\,^{\circ}C$, i.e. for the temperature range where the large increase of the coercive field is observed. The reason for that is an extreme broadening of the FMR peak, which does not allow for frequency measurements. The same is also true for the PSSW peak.

The dependence of the exchange constant A is plotted in Fig. 3b. It shows a steady increase of the values similar to the one observed for the Kerr signal but smaller in magnitude. The largest obtained value for $Co_{40}Fe_{40}B_{20}$ is $A = (1.89 \pm 0.15) \cdot 10^{-11}\,J/m$ for $T_{ANN} = 383\,^{\circ}C$. This value is still much smaller than the one reported for the related alloy $Co_{72}Fe_{18}B_{10}$, ($2.84 \cdot 10^{-11}\,J/m$ [1]) or for CoFe alloys ($3.84 - 2.61 \cdot 10^{-11}\,J/m$ for different compositions [1, 7]). The most probable reason is the largest B content in our case.

The Gilbert damping parameter α dependence on the annealing temperature is shown in Fig. 3c. The details about the estimation of α are reported elsewhere [2,8]. The α parameter remains almost unchanged up to a sharp increase starting at $T_{ANN} = 383\,^{\circ}C$. For temperatures above 390 °C the

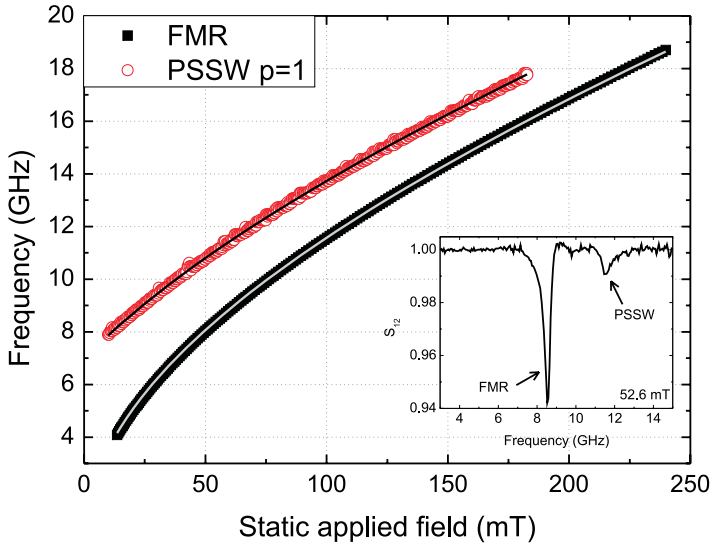

Fig. 2: Dependence of the FMR frequency and the first PSSW mode on the external applied magnetic field. Lines represent fits to the experimental data using Eqs. 1 and 2 from which M_s and A are extracted.

extreme broadening of the FMR peaks indicates a large increase of damping although the final value cannot be estimated. This fact is marked as a dashed line in Fig. 3c.

In summary, there are two parameters, the Kerr signal and the exchange constant A, which show a steady change with T_{ANN}. Two other parameters, coercive field and α show sharp changes starting from $T_{ANN} = 383\,^{\circ}C$. The changes in M_S are in any case small. It is noteworthy that the parameters that show a steady change are the ones which may be affected by surface changes. For the Kerr signal, the reason is the already commented limited probing depth of light (ca. 20 nm). For the exchange constant the reason is less straightforward. The parameter d in Eq. 2 must be interpreted as an *effective* film thickness and not as the physical film thickness. For instance, a magnetic film may have a top dead layer due to oxidation or surface degradation. A strong surface roughness may also lead to an effective thickness different from the nominal one. In our case, it is already known that the crystallization process of CoFeB films is marked by the formation of CoFe crystallites and the segregation of B atoms. Furthermore, B easily diffuses in MgO and the crystallization process is depth-dependent [9, 10]. We believe, that these facts are responsible for the steadier changes of A in comparison to α, M_s or the coercive field.

Financial support by the state of Rhineland-Palatinate (MBWWK and MWKEL) and by the European Regional Development Fund (ERDF) in the frame of the Spintronic Technology Platform (STeP) is acknowledged. The authors wish to thank the Nano Structuring Center (NSC) in Kaiserslautern and T. Brächer for their support in thin film preparation.

References

[1] C. Bilzer, T. Devolder, J.-V. Kim, G. Counil, C. Chappert, S. Cardoso, P.P. Freitas, *Study of the dynamic properties of soft CoFeB films*, J. Appl. Phys. **100**, 053903 (2006).
[2] A. Conca, J. Greser, T. Sebastian, S. Klingler, B. Obry, B. Leven, B. Hillebrands, *Low spin-wave damping in amorphous $Co_{40}Fe_{40}B_{20}$ thin films*, J. Appl. Phys. **113**, 213909 (2013).
[3] X. Liu, W. Zhang, M.J. Carter, G. Xiao, *Ferromagnetic resonance and damping properties of CoFeB thin films as free layers in MgO-based magnetic tunnel junctions*, J. Appl. Phys. **110**, 033910 (2011).
[4] F. Xu, Q. Huang, Z. Liao, S. Li, C.K. Ong, *Tuning of magnetization dynamics in sputtered CoFeB thin film by gas pressure*, J. Appl. Phys. **111**, 07A304 (2012).
[5] C. Kittel, *On the Theory of Ferromagnetic Resonance Absorption*, Phys. Rev. **73**, 155 (1948).
[6] S.O. Demokritov, B. Hillebrands, *Spin Dynamics in Confined Magnetic Structures I*, Springer, Berlin, (2002).

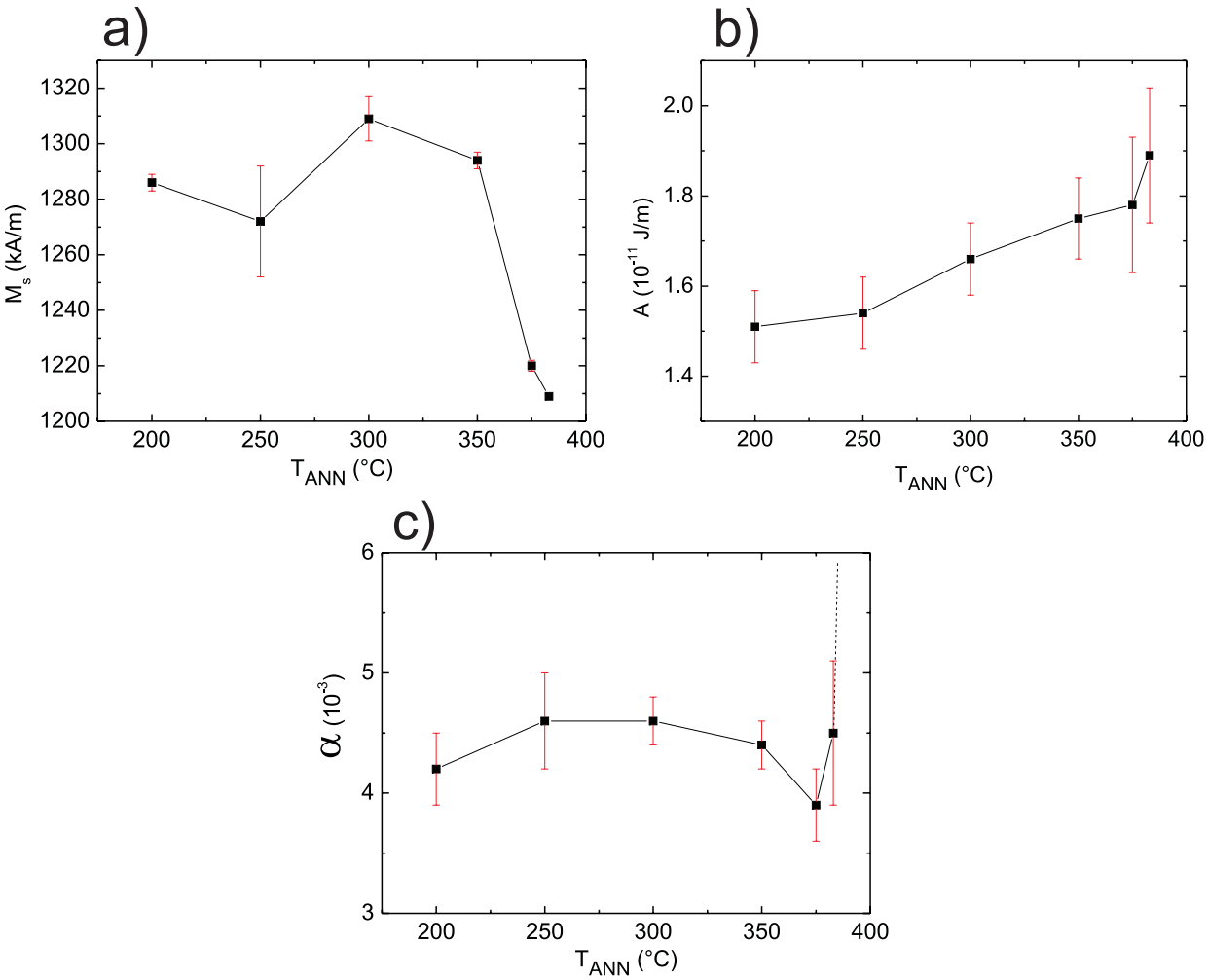

Fig. 3: Dependence of the saturation magnetization M_s (a), the exchange constant A (b) and the Gilbert damping parameter α (c) on the annealing temperature for 78 nm thick $Co_{40}Fe_{40}B_{20}$ films.

[7] X. Liu, R. Sooryakumar, C.J. Gutierrez, G.A. Prinz, *Exchange stiffness and magnetic anisotropies in bcc $Fe_{1-x}Co_x$ alloys*, J. Appl. Phys. , **75**, 7021 (1994).

[8] A. Conca, J. Greser, T.Sebastian, B. Hillebrands, *FMR and MOKE characterization of $Co_{40}Fe_{40}B_{20}$ thin films*, AG Magnetismus Annual Report 2012.

[9] Y. Lu, B. Lépine, G. Jézéquel, S. Ababou, M. Alnot, J. Lambert, A. Renard, M. Mullet, C. Deranlot, H. Jaffrès, F. Petroff, J.-M. George, *Depth analysis of boron diffusion in MgO/CoFeB bilayer by x-ray photoelectron spectroscopy*, J. Appl. Phys. , **108**,043703 2010.

[10] C.Y. You, T. Ohkubo, Y.K. Takahashi, K. Hono, *Boron segregation in crystallized MgO/amorphous-Co40Fe40B20 thin films*, J. Appl. Phys. , **104**, 033517 (2008).

4.15 A study of the Gilbert damping in individual Heusler microstructures via time-resolved parametric amplification

T. Sebastian, T. Brächer, P. Pirro, A. A. Serga, and B. Hillebrands

In collaboration with Y. Kawada, H. Naganuma, M. Oogane, and Y. Ando, Department of Applied Physics, Graduate School of Engineering, Tohoku University, Aoba-yama 6-6-05, Sendai 980-8579, Japan

The class of cobalt-based Heusler compounds contains several promising candidates for the research field of spin dynamics. The anticipated advantages of Heusler compounds are mainly given by a smaller Gilbert damping with respect to most conventional 3d-ferromagnets. Our previous results on the increased propagation distance as well as the occurrence of the nonlinear emission of higher spin-wave harmonics in microstructured $Co_2Mn_{0.6}Fe_{0.4}Si$ (CMFS) waveguides show how *magnon spintronics* can benefit from the utilization of CMFS compared to the commonly used $Ni_{81}Fe_{19}$ with a substantially larger damping [1, 2]. In addition, these results indicate a low Gilbert damping even in CMFS microstructures. However, a quantitative analysis of the damping in microstructures has not been presented so far.

Therefore, this Report is devoted to the evaluation of the Gilbert damping parameter in an individual microstructure patterned from a CMFS Heusler thin film. The Gilbert damping in Heusler materials - among all other material parameters - strongly depends on the crystallographic order of the thin film [3, 4]. The lowest Gilbert damping is usually reported for the highest order, the $L2_1$ state. While the analysis of the crystallographic order and the Gilbert damping by x-ray diffraction (XRD) and ferromagnetic resonance (FMR) are standard techniques for homogeneous thin films [5], the measurement turns out to be more complicated on the microscale. At the same time, it is not self-evident that the crystallographic order and, therefore, the low Gilbert damping are preserved in the patterning process due to possible mechanical stress, border roughness, or heating effects.

In this Report, an approach for the measurement of the Gilbert damping in individual microstructures will be introduced and applied to an elliptical CMFS element [6]. The underlying physical principle of this method is the parallel parametric amplification of spin dynamics from the thermal level.

A sketch of the sample structure is shown in Fig. 1a. A 10 nm thick elliptical CMFS microstructure with a major axis of 3 µm and a minor axis of 2 µm was placed on top of an Ag antenna with a width of 8 µm. Details about the fabrication of the thin film as well as the patterning process can be found in [1, 2, 5].

For the amplification of spin dynamics, the alternating *pumping field* $\mathbf{h_P}$ was applied to the sample via microwave currents running through the antenna structure. The connection of the antenna structure to external microwave circuitry was realized via a picoprobe. This pumping field as well as a static magnetic bias field with an amplitude of $\mu_0 H_{\mathrm{ext}} = 48.5\,\mathrm{mT}$ were applied parallel to each other in the short-axis direction of the CMFS ellipse.

Because of this geometry with $\mathbf{H_{ext}} \parallel \mathbf{M_0} \parallel \mathbf{h_P}$, the pumping field $\mathbf{h_P}$ cannot exert a torque $\mathbf{h_P} \times \mathbf{M_0}$ on the static magnetization $\mathbf{M_0}$, since $|\mathbf{M_0} \times \mathbf{h_P}| = |\mathbf{M_0}||\mathbf{h_P}| \sin(0°) = 0$. Therefore, the usual torque-based excitation mechanism cannot be used to excite spin dynamics in this case. In contrast,

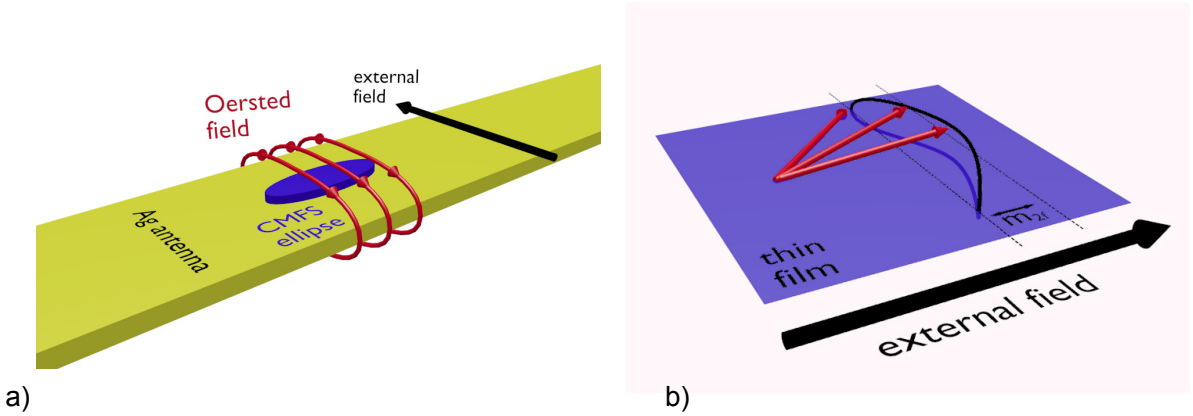

Fig. 1: a) Sample layout for the observation of the parametric amplification in CMFS microstructures. An elliptical CMFS element with a major axis of 3 µm and a minor axis of 2 µm was placed on a 8 µm wide Ag antenna. The oscillating Oersted fields $\mathbf{h_P}$ created by microwave currents in this antenna structure are parallel to the direction of the external magnetic field $\mathbf{H_{ext}}$ with an amplitude of $\mu_0 H_{\mathrm{ext}} = 48.5\,\mathrm{mT}$. b) Illustration of the elliptic precession of a magnetic moment in a magnetic thin film with the dynamic magnetization component $\mathbf{m_{2f}}$ parallel to the external field.

the pumping field couples to a dynamic magnetization component $\mathbf{m_{2f}}$ with $\mathbf{m_{2f}} \parallel \mathbf{H_{ext}}$ via the Zeeman energy $\propto \mathbf{h_P} \cdot \mathbf{m_{2f}}$ and, thus, can parametrically amplify an existing precession [7–10].

This dynamic magnetization component $\mathbf{m_{2f}}$ is a result of the elliptical magnetization precession in magnetic thin films. A finite film thickness gives rise to demagnetizing fields caused by magnetization components normal to the surface of this film. Therefore, the precession of a magnetic moment will immediately cause dynamic demagnetizing fields, whenever the magnetic moment points out of the thin film during its precessional motion. Due to these demagnetizing fields, and to minimize the energy of the system, the circular trajectory will change to an elliptical one. This situation is illustrated in Fig. 1b.

As can be seen, the ellipticity of the precessional motion results in the dynamic magnetization component $\mathbf{m_{2f}}$ parallel to the pumping as well as the bias field. In addition, the component $\mathbf{m_{2f}}$ oscillates with twice the frequency as the overall precession of the magnetic moment. Thus, to couple to $\mathbf{m_{2f}}$ and, therefore, to amplify the overall precession most efficiently, the pumping field has to be driven at twice the frequency of the overall precession, too.

In all experiments presented below, the frequency of the pumping field was fixed at $f_{\mathrm{P}} = 15\,\mathrm{GHz}$. Therefore, as discussed above, the frequency of the overall precession of the amplified and detected spin-wave mode was $f_{\mathrm{SW}} = 7.5\,\mathrm{GHz}$. The amplitude of the pumping field was controlled via the applied microwave power P: $|\mathbf{h_P}| \propto \sqrt{P}$.

Parallel parametric amplification can be regarded as an opposed process to the damping in the magnetic system. While the damping reduces the precession amplitude until the magnetic moment is aligned with the effective field in its equilibrium position, parametric amplification increases the amplitude. Therefore, parallel parametric amplification is a threshold process: Only if the pumping field is strong enough to overcome the damping, the intensity of the involved spin-wave modes will rise above the thermal level. Because of this relation between the pumping field and the damping, parametric amplification can be used to evaluate the Gilbert damping parameter.

The relation of the pumping field $\mathbf{h_P}$ and the Gilbert damping parameter α during the process of parametric amplification for the actual sample layout can be written as follows [6–8]:

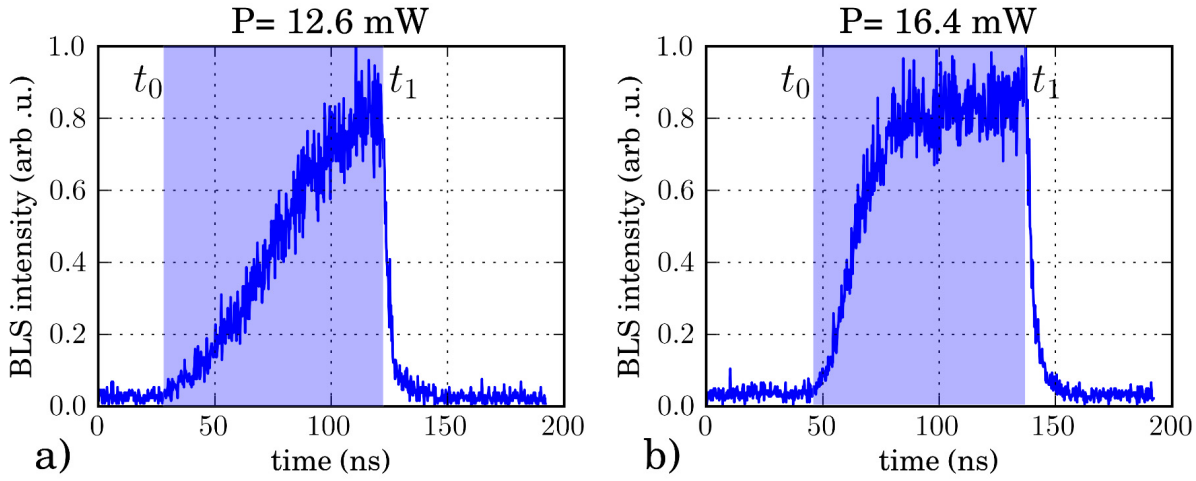

Fig. 2: Time-resolved BLS measurement on a CMFS ellipse with a major axis of 3 µm and a minor axis of 2 µm. The BLS intensity at $f = 7.5$ GHz increases exponentially from the thermal level after application of microwave powers of a) $P = 12.6$ mW and b) $P = 16.4$ mW, respectively. At time t_0 the pumping field is applied and switched off again at time t_1. The amplification is marked by the shaded area in the graphs.

$$I_{\mathrm{SW}}(t) = I_0 \exp\left[-(2\pi f_{\mathrm{SW}}\alpha - V\sqrt{P})t\right] \quad , \tag{1}$$

where $I_{\mathrm{SW}}(t)$ and I_0 are the time-dependent spin-wave intensity as well as the intensity level of thermally activated spin waves, respectively. The amplitude as well as the coupling of the pumping field to the magnetization precession are expressed via the square root of the microwave power $\sqrt{P}$ and a proportionality constant V, respectively. Among other parameters, V depends on the ellipticity of the precession, the proportionality factor between $\sqrt{P}$ and $|\mathbf{h_P}|$, and the relative orientation and phase of magnetization and pumping field. However, V is not important for the further evaluation and is, therefore not discussed in detail. A detailed discussion of the above relations can be found in [7, 8].

To evaluate the Gilbert damping experimentally on the basis of Eq. 1, we performed time-resolved Brillouin light scattering (BLS) microscopy. BLS is the inelastic scattering of photons and magnons. The detected intensity of the inelastically scattered light is proportional to the intensity of the investigated spin-wave modes. Detailed discussions about BLS in general as well as the experimental realization of a BLS microscope with time resolution in particular can be found in Refs. [11–13]. The instrument that was used for the following experiments has a space resolution of around 250 nm and a time resolution of 250 ps.

Figure 2 shows the time-resolved BLS intensity obtained at a probing position in the center of the CMFS element for different microwave powers of $P = 12.6$ mW and $P = 16.4$ mW. For both measurements, the procedure and the overall trend are the same: the detected BLS intensity starts at the thermal level. At time t_0 the pumping field is switched on and the BLS intensity rises due to the parametric amplification until a saturation level is reached. Therefore, we can conclude, that in both measurements the amplitudes of the pumping fields were above the threshold for parametric amplification. The saturation of the spin-wave intensity is a well-known phenomenon that can be attributed to dephasing processes between the pumping field $\mathbf{h_P}$ and the dynamic magnetization $\mathbf{m_{2f}}$. Since these processes and the saturation level itself are not of further importance for the following evaluation of the data, the reader is referred to the discussion of these effects in [8]. After the pumping field is switched off at time t_1, the intensity drops to the thermal level again due

to the Gilbert damping.

In principle, the time constant of the spin-wave decay after t_1 can be also used to evaluate the damping constant directly. However, this decay is too fast to allow for a reliable detection given the limited time resolution of the BLS microscope. Therefore, the evaluation of the Gilbert damping from the time dependence of the rising flank will be discussed in the following.

The time dependence of the rising flanks in Fig. 2 can be described by the exponential relation:

$$I_{\mathrm{BLS}}(t) = I_0 \exp\left(-\frac{t-t_0}{\tau}\right) \quad , \tag{2}$$

where τ is the time constant of the amplification. As can be seen by comparing the data for different microwave powers in Fig. 2a and Fig. 2b , the characteristic timescale τ for the amplification of spin dynamics strongly depends on the amplitude of the pumping field $|\mathbf{h_P}| \propto \sqrt{P}$. Therefore, the time constant $\tau = \tau(P)$, that can be extracted from the experimental data, is a function of the applied microwave power.

As already mentioned above, τ is not only a function of the power P but also of the damping in the magnetic system. The combination of Eqs. (1) and (2) allows to draw the following connection between the time constant $\tau(P)$, that is determined in the measurement, and the Gilbert damping parameter α :

$$\frac{1}{\tau} = V\sqrt{P} - 2\pi f_{\mathrm{SW}}\alpha \quad . \tag{3}$$

Equation (3) describes the linear dependence of $1/\tau$ on the square root of the microwave power $\sqrt{P}$, where the axis interception is given by the damping parameter α. By measuring $1/\tau$ as a function of $\sqrt{P}$, it is therefore possible to estimate the Gilbert damping α via a linear least-square fit according to Eq. (3).

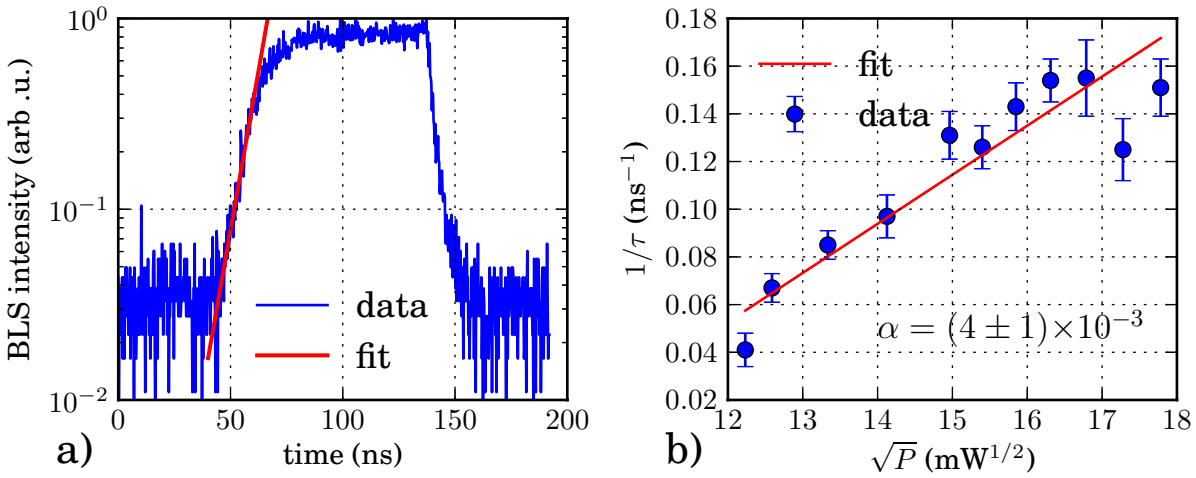

Fig. 3: a) Time-resolved BLS intensity on a CMFS ellipse with a major axis of 3 µm and a minor axis of 2 µm for an applied microwave power of $P = 16.4$ mW and a microwave frequency of $f = 15$ GHz. On a logarithmic scale the rising flank shows a linear dependence on the time. This observation is in accordance with the assumption of an exponential increase of the BLS intensity given in Eq. (2). A fit to the data yields the parameter $1/\tau$. b) Time constant $1/\tau$ in dependence on the square root of the applied microwave power $\sqrt{P}$. The data is presented together with a least-square fit according to Eq. (3).

The time-resolved measurement already presented in Fig. 2b is shown in Fig. 3a together with a fit according to Eq. (2) to estimate $1/\tau$. In agreement with the assumption of an exponential increase of the BLS intensity, the rising flank of the BLS intensity shows a linear dependence on the time in a logarithmic presentation of the data.

Figure 3b summarizes the results of several measurements for different microwave powers. A least-square fit according to Eq. (3) yields a Gilbert damping parameter of $\alpha = (4 \pm 1) \times 10^{-3}$. This value is in agreement with the Gilbert damping obtained for homogeneous CMFS thin films with dominating $L2_1$ order via a standard FMR technique ($\alpha = 3 \times 10^{-3}$ in [5]).

As already indicated by our previous results about an increased propagation distance as well as the nonlinear of emission of spin-wave caustics observed in a microstructured CMFS waveguide, the presented quantitative evaluation confirms low values of the Gilbert damping in the investigated CMFS microstructure.

While the effect of this low damping was already illustrated for the spin-wave propagation in CMFS waveguides, it also reveals a big potential for other fields of spin dynamics. In particular, all direct-current based schemes for the excitation of spin dynamics or the switching of magnetic layers directly depend on a low Gilbert damping [14–18]. Therefore, the results above strongly suggest the utilization of CMFS in all related experiments.

In summary, we presented an approach for the evaluation of the Gilbert damping in microstructures via time-resolved BLS measurements of the parametric amplification of spin dynamics. Our results show that the low Gilbert damping observed in CMFS thin films via FMR can be preserved in the patterning process.

We gratefully acknowledge financial support by the DFG Research Unit 1464 and the Strategic Japanese-German Joint Research Program from JST: ASPIMATT. T. Brächer is supported by a fellowship of the Graduate School Materials Science in Mainz (MAINZ) through DFG funding of the Excellence Initiative (GSC 266). We thank our colleagues from the Nanostructuring-Center of the TU Kaiserslautern for their assistance in sample preparation.

References

[1] T. Sebastian, Y. Ohdaira, T. Kubota, P. Pirro, T. Brächer, K. Vogt, A.A. Serga, H. Naganuma, M. Oogane, Y. Ando, B. Hillebrands, *Low-damping spin-wave propagation in a microstructured $Co_2Mn_{0.6}Fe_{0.4}Si$ Heusler waveguide*, Appl. Phys. Lett. **100**, 112402 (2012).

[2] T. Sebastian, P. Pirro, T. Brächer, T. Kubota, A.A. Serga, H. Naganuma, M. Oogane, Y. Ando, B. Hillebrands, *Nonlinear emission of spin-wave caustics from an edge mode of a microstructured $Co_2Mn_{0.6}Fe_{0.4}Si$ waveguide*, Phys. Rev. Lett. **110**, 067201 (2013).

[3] Y. Miura, K. Nagao, M. Shirai, *Atomic disorder effects on half-metallicity of the full-Heusler alloys $Co_2Cr_{1-x}Fe_xAl$: A first-principles study*, Phys. Rev. B **69**, 144413 (2004).

[4] S. Picozzi, A. Continenza, A. Freeman, *Role of structural defects on the half-metallic character of Co_2MnGe and Co_2MnSi Heusler alloys*, Phys. Rev. B **69**, 094423 (2004).

[5] T. Kubota, S. Tsunegi, M. Oogane, S. Mizukami, T. Miyazaki, H. Naganuma, Y. Ando, *Half-metallicity and Gilbert damping constant in $Co_2Fe_xMn_{1-x}Si$ Heusler alloys depending on the film composition*, Appl. Phys. Lett. **94**, 122504 (2009).

[6] H. Ulrichs, V.E. Demidov, S.O. Demokritov, S. Urazhdin, *Parametric excitation of eigenmodes in microscopic magnetic dots*, Phys. Rev. B **84**, 094401 (2011).

[7] D. Chartoryzhskii, B. Kalinikos, O. Vendik, *Parallel pump spin wave instability in thin ferromagnetic films*, Solid State Commun. **20**, 985 (1976).

[8] V.S. L'vov, *Wave turbulence under parametric excitation*, Band 2, Springer, Berlin (1994).

[9] A.G. Gurevich, G.A. Melkov, *Magnetization oscillations and waves*, CRC Press (1996).

[10] T. Brächer, P. Pirro, A.A. Serga, B. Hillebrands, *Localized parametric generation of spin waves in a longitudionally magnetized $Ni_{81}Fe_{19}$ waveguide*, Appl. Phys. Lett. **103**, 142415 (2013).
[11] J. Cochran, *Brillouin light scattering intensities for patterned magnetic thin films*, J. Magn. Magn. Mater. **212**, 40 (2000).
[12] V.E. Demidov, S.O. Demokritov, B. Hillebrands, M. Laufenberg, P.P. Freitas, *Radiation of spin waves by a single micrometer-sized magnetic element*, Appl. Phys. Lett. **85**, 2866 (2004).
[13] H. Schultheiss, C.W. Sandweg, B. Obry, S.J. Hermsdoerfer, S. Schäfer, B. Leven, B. Hillebrands, *Dissipation characteristics of quantized spin waves in nano-scaled magnetic ring structures*, J. Phys. D **41**, 164017 (2008).
[14] V.E. Demidov, S. Urazhdin, S.O. Demokritov, *Direct observation and mapping of spin waves emitted by spin-torque nano-oscillators*, Nat. Mater. **9**, 984 (2010).
[15] M. Madami, S. Bonetti, G. Consolo, S. Tacchi, G. Carlotti, G. Gubbiotti, F.B. Mancoff, M.A. Yar, J. Åkerman, *Direct observation of a propagating spin waves induced by spin-transfer torque*, Nat. Nanotechnol. **6**, 635 (2011).
[16] Y. Sakuraba, K. Izumi, T. Iwase, S. Bosu, K. Saito, K. Takanashi, Y. Miura, K. Futatsukawa, K. Abe, M. Shirai, *Mechanism of large magnetoresistance in $Co_2MnSi/Ag/Co_2MnSi$ devices with current perpendicular to the plane*, Phys. Rev. B **82**, 094444 (2010).
[17] Y. Sakuraba, M. Ueda, Y. Miura, K. Sato, S. Bosu, K. Saito, M. Shirai, T. Konno, K. Takanashi, *Extensive study of giant magnetoresistance properties in half-metallic Co_2(Fe, Mn)Si-based devices*, Appl. Phys. Lett. **101**, 252408 (2012).
[18] V.E. Demidov, S. Urazhdin, H. Ulrichs, V. Tiberkevich, A.N. Slavin, D. Baither, G. Schmitz, S.O. Demokritov, *Magnetic nano-oscillator driven by pure spin current*, Nat. Mater. **11**, 1 (2012).

F. Applied Spintronics

A substantial part of our research is devoted to fields that have a close relation to applications. Our group is aiming to intensify the communication flow between the academic and the industrial world in order to promote the necessary transfer of technology and *know-how*. Since beginning of the year 2012 we are taking part in the industrial collaboration project STeP (Spintronic Technology Platform) funded by the Ministerium für Bildung, Wissenschaft, Weiterbildung und Kultur in Rhineland-Palatinate in the frame of the European EFRE-Program. The Platform is built jointly with the industrial partner Sensitec, Mainz, and the Johannes Gutenberg University Mainz. Among its main goals, one can cite the generation of new capabilities in the field of spintronics, the construction of a R&D infrastructure directed to small and medium enterprises in Rhineland-Palatinate together with the innovation in GMR and TMR technologies with a strong emphasis on the use of industrial production lines for the creation and testing of new sensor concepts. In this project we contribute to the design and testing of new sensor concepts, the material characterization, especially of Heusler thin films and in other subjects.

Also in 2012 the Greater Region Magnetism Network (GRMN) has been established in the framework of the University of the Greater Region. Here, the universities of Lorraine, Saarrebruck and Kaiserslautern joined their forces to explore magnetic phenomena and their novel application potential. As main aim of the GRMN the synergy of expertise and activities to develop concerted teaching strategies as well as highly innovative technology transfer concepts has been identified. One prominent example hereof is presented in Report 4.19.

In Report 4.16 the optimization of the growth of thin $Ni_{81}Fe_{19}$ and CoFeB films towards the magnetic properties required for all-optical measurements is discussed. Parameters such as surface roughness, controlled magnetic anisotropy and magnetic softness are in the focus of interest.

In Report 4.17 lifetime measurements of CoFeB/MgO/CoFeB tunneling junctions are presented. This characterization follows industrial requirements and is part of the STeP project.

In Report 4.18 a study of the material parameters in YIG employing ferromagnetic resonance spectroscopy is presented.

In Report 4.19 the success story of an example for technology transfer of magnetic sensors in daily life is presented. In cooperation with ELGO Electronics GmbH the Taipei 101 skyscraper has been rebuilt to demonstrate magnetic sensor application in elevator positioning systems for the presentation at various public relations activities.

F. Angewandte Spindynamik

Ein Teil unserer Aktivitäten ist auf anwendungsorientierte Forschung gerichtet. Unsere Gruppe versucht Brücken zwischen der akademischen und der industriellen Welt zu bauen, um den Technologietransfer und den Ideenaustausch zu fördern. Seit Anfang 2012 nehmen wir an der Spintronik-Technologie-Plattform (STeP) teil, finanziert vom Ministerium für Bildung, Wissenschaft, Weiterbildung und Kultur in Rheinland-Pfalz im Rahmen des europäischen EFRE-Programms. Dieses Projekt ist eine Zusammenarbeit zwischen der TU Kaiserslautern, der Universität Mainz und dem Industriepartner Sensitec, der große Erfahrung in der Sensorik und in den praktischen Anwendungen der Spintronik gesammelt hat. Als Hauptziele der Plattform kann man unter anderem folgende erwähnen: den Aufbau neuer Kompetenzen auf dem Gebiet der Spintronik, die Bereitstellung der Forschungsinfrastruktur und des anwendungsorientiertem universitären *Know-How* besonders für

kleine und mittlere Unternehmen (KMU) in Rheinland-Pfalz und die Förderung von Innovation im Bereich der GMR und TMR-Technologien. Unsere Aufgabe besteht unter anderen darin, das Design neuer Sensoren mit mikromagnetischen Simulationen zu unterstützen und die Charakterisierung von Heusler-Dünnschichtsystemen vorzunehmen.

Als weitere prominente Initiative auf dem Gebiet der anwendungsorientierten Forschung wurde ebenfalls im Jahre 2012 das Magnetismusnetzwerk der Großregion (GRMN) im Rahmen der Universität der Großregion etabliert. Hier bündeln die Universitäten von Lothringen, Saarbrücken und Kaiserslautern ihr *know-how* und ihre *Netzwerkstrukturen*, um magnetische Phänomene und ihr Anwendungspotential auszuloten. Ein Hauptziel dieser Initiative ist es, die Synergie der Expertisen und Aktivitäten zu nutzen um ein konzertiertes Lehrkonzept auf dem Gebiet des Magnetismus und innovative *Technologietransfer-Konzepte* zu entwickeln.

Im Bericht 4.16 wird die Untersuchung des Wachstums dünner $Ni_{81}Fe_{19}$ und CoFeB-Schichten diskutiert. Ziel ist es, die für magneto-optische Messungen relevanten Schichteigenschaften, wie z.B. Oberflächenrauhigkeit, die die magnetischen Eigenschaften besonders auch in Mikrostrukturen beeinflussen, zu optimieren.

Im Bericht 4.17 werden Untersuchungen zu Lebenszeiten von CoFeB/MgO/CoFeB Tunnelstrukturen nach industriellem Maßstab vorgestellt, die im Rahmen des STeP-Projektes durchgeführt wurden.

Im Bericht 4.18 werden Untersuchungen der Materialkonstanten von YIG mittels Ferromagnetischer Resonanz-Messungen vorgestellt.

Im Bericht 4.19 ist ein erfolgreiches Beispiel des Technologietransfers magnetischer Sensoren in das tägliche Leben in enger Kooperation mit der Industrie vorgestellt. In Zusammenarbeit mit ELGO Electronics GmbH wurde ein Modell des Wolkenkratzers Taipei 101 nachgebaut, um den Einsatz magnetischer Sensoren in der Positionstechnologie von Aufzügen auf Ausstellungen zu demonstrieren.

4.16 Optimization of the growth of $Ni_{81}Fe_{19}$ and $Co_{40}Fe_{40}B_{20}$ thin films for an all-optical characterization of micron-sized elliptical elements

A. Ruiz-Calaforra, T. Brächer, T. Fischer, A. Conca, B. Leven, and B. Hillebrands

In the present years, the application of newly-discovered magnetic effects such as the tunneling magneto resistance (TMR) effect [1] or the spin transfer torque (STT) effect [2, 3] have led to large advances [4, 5] in the development of magnetic sensors and magnetic memories. These two effects, which utilize the electron spin in addition to its charge, are strongly dependent on the combination of the used materials. A key issue is the proper choice of the magnetic layers, as their magnetic properties, such as the damping or the spin polarization, have a large impact on the operation efficiency [6]. Two of the materials which are commonly used for this purpose are the ferromagnetic alloys NiFe and CoFeB [7, 8]. Experiments have demonstrated that these soft magnetic materials present a low damping parameter [9–11] and a relative high spin polarization [12–15].

The main aim of the work presented here is an all-optical study of the magnetic properties of micron-sized NiFe and CoFeB elliptical elements by employing magneto-optical Kerr effect (MOKE) magnetometry. For this, an optimization of the growth of the metallic stacks which will compose the elements is needed. Hereby, we will focus on achieving a smooth topography, a controlled magnetic anisotropy and magnetic softness and a large magneto-optical signal (i.e. large Kerr rotation).

Thin films of $Ni_{81}Fe_{19}$ and $Co_{40}Fe_{40}B_{20}$ (NiFe and CoFeB hereafter) with thicknesses of 5 ± 1 nm and 6 ± 1 nm, respectively, were deposited by magnetron rf sputtering on SiO_2 substrates in a chamber with a base pressure of around $5 \cdot 10^{-7}$ mbar. The Ar pressure during deposition was $4.8 \cdot 10^{-3}$ mbar with a power of 200 W and a gas flow of 10 sccm. For these parameters, the sputtering rate of NiFe is about 1.8 nm/cycle and about 1.9 nm/cycle in the case of CoFeB. Here, a cycle means one sweep of the substrate plate into and out of the sputter target scope while the Ar plasma is burning constantly. This is used to achieve a reproducible thin film thickness for relatively large sputtering rates which themselves have been determined to lead to optimal material parameters for thick film growth. In the frame of this work, it is necessary to define the uniaxial anisotropy parallel to one of the sample edges. In order to achieve this, the sample is positioned between two plane magnets with opposite poles facing each other. At the same time, during the deposition the substrate plate is rotated at 20 rpm to avoid shadowing effects during one cycle and any influence on the magnetocrystalline anisotropy by the residual magnetic fields present in the deposition chamber.

For the magnetic characterization of the films a longitudinal MOKE magnetometer with an incidence angle of 45° was employed. A diode laser with a wavelength of 635 nm is focused down to a spatial resolution of about 200 µm. A rotational stage allows for magnetization reversal measurements for all in-plane orientations of the sample with respect to the applied field. Figure 1 shows the measured angular dependence of the coercive field H_C for an exemplary NiFe film (Fig. 1a) and an exemplary CoFeB film (Fig. 1b) deposited on a SiO_2 substrate. Both films present a weak uniaxial anisotropy with their easy axis in the direction of the position of the magnets (at 0° and 180°). The value of $\mu_0 H_C$ along this direction is of 0.038 mT for NiFe and 0.5 mT for CoFeB.

For the study of the dynamic properties, the elliptical elements will be placed on top of Cu coplanar waveguides (CPW) with a transparent BCB insulating layer in between [16]. For this reason,

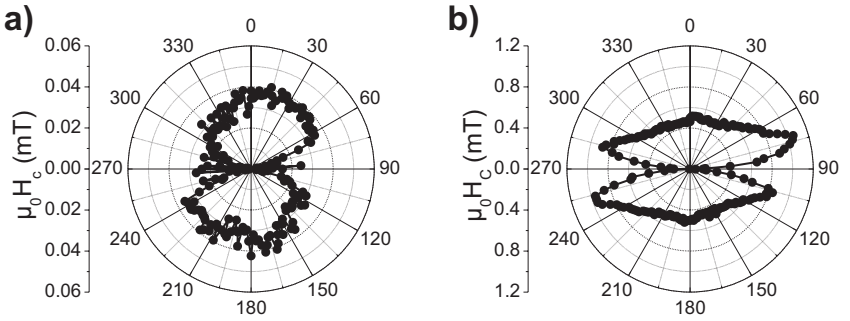

Fig. 1: Angular dependence of the in-plane coercive field H_C of a) a 5 ± 1 nm $Ni_{81}Fe_{19}$ thin film and b) a 6 ± 1 nm $Co_{40}Fe_{40}B_{20}$ thin film deposited on a SiO_2 substrate.

the optical contrast of the elements on the Cu CPWs, which is a prerequisite for the optical measurements, is very poor. In order to enhance this contrast a thick metallic buffer layer is needed under the ferromagnetic material. A good candidate for this purpose is the non-magnetic metal Ru. This material offers a very slow growing speed (approx. 1.5 nm/min), optimum for a precise thickness growth leading to a very smooth surface. A 5 nm thick NiFe film grown on top of 15 nm Ru presents a root-mean-square roughness of $Sq = 0.4$ nm. However, such films exhibit a very low magneto-optical signal. Figure 2a shows a comparison of the hysteresis loops obtained during magnetization reversal measurements for a 5 nm NiFe thin film grown directly on a SiO_2 substrate, with a 7.5 nm Ru underlayer, and with a 15 nm Ru underlayer. With the presence of Ru, the amplitude of the magneto-optical signal decreases with increasing Ru thickness and, at the same time, H_C increases. A similar behavior has been observed for CoFeB films deposited with and without Ru.

The introduction of the Ru underlayer can have various effects on the magnetic properties of the ferromagnetic layer on top. For instance, as the surface of the Ru differs from the SiO_2 surface, the growth of the ferromagnet might differ and an existing magnetic dead layer can vary [17–19]. Furthermore, when using Ru, we cannot exclude spin diffusion from the ferromagnet into the Ru, as observed in [20, 21] which may influence the damping properties. To prevent this, a MgO interlayer is grown between the Ru and the ferromagnet. Samples with a combination of different MgO and Ru thicknesses as underlayer of a 5 nm thick NiFe film have been grown. Figure 2b shows a summary of the results for the magneto-optical signal (i.e. amplitude of the Kerr rotation) and H_C for all films. It can be observed that the introduction of the MgO interlayer has no major impact on the change of H_C which is still increased with respect to a growth without a Ru underlayer and which still increases with increasing Ru thickness. This indicates, that the change in H_C is mainly due to the different surface morphology of Ru which is not drastically changed by the thin MgO interlayer. On the contrary, the introduction of the MgO interlayer strongly enhances the magneto-optical signal which increases with increasing MgO thickness for a fixed Ru thickness. As the magneto-optical signal depends on a large number of material parameters of the ferromagnetic layer, such as the spin-orbit coupling, the exchange constant, and the final and the initial state of the optic transition, as well as on the reflectivity of the layer system, it is very difficult to identify the reason for this increase.

As mentioned above, a thick metallic underlayer is beneficial due to its increase of the optical contrast. On the other hand, a low magneto-optical signal is a large disadvantage for the MOKE measurements. Furthermore, a large H_C of the magnetic film might be undesired as it could increase the needed current density to switch the magnetization orientation of the elements in a MTJ cell. Therefore, to have a compromise between all requisites, the final buffer layer used is the bilayer Ru (7.5 nm) / MgO (5 nm).

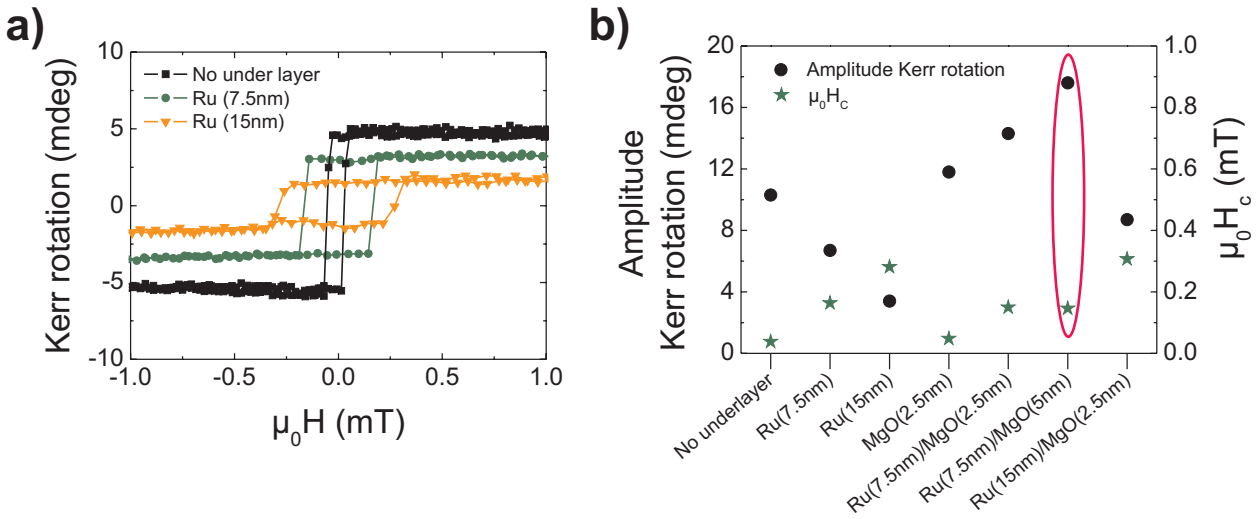

Fig. 2: a) Magnetization reversal measurements along the easy axis of a 5 ± 1 nm $Ni_{81}Fe_{19}$ thin film deposited on different thicknesses of Ru underlayer. b) Results of the amplitude of the Kerr rotation and H_C for a 5 ± 1 nm $Ni_{81}Fe_{19}$ thin film grown on different underlayers. The highlighted set of data indicates the optimum underlayer.

Exemplary results on the angular dependence of the in-plane H_C for NiFe and CoFeB thin films with Ru (7.5 nm) / MgO (5 nm) buffer layer deposited on a SiO_2 substrate are shown in Fig. 3a and b, respectively. The resulting magnetic anisotropy is similar to the ones obtained before for both materials. The coercive field is higher in both cases as a consequence of introducing Ru as an underlayer. In the case of NiFe $\mu_0 H_C = 0.12$ mT along the easy axis direction and in the case of CoFeB $\mu_0 H_C = 0.85$ mT. The figures below each polar plot in Fig. 3 show exemplarily hysteresis loops of each material along the easy (0°) and hard (90°) axes.

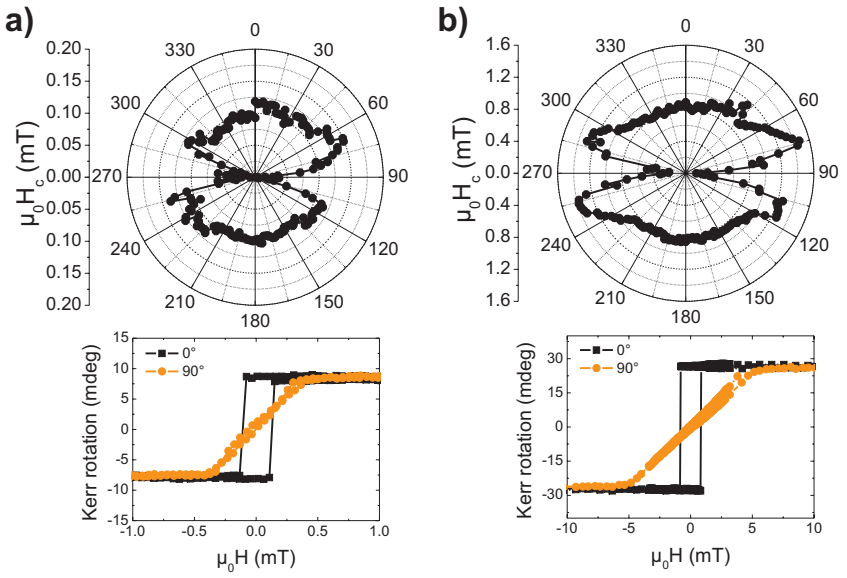

Fig. 3: Angular dependence of the in-plane coercive field H_C of a) a 5 ± 1 nm $Ni_{81}Fe_{19}$ thin film and a b) 6 ± 1 nm $Co_{40}Fe_{40}B_{20}$ thin film deposited on a SiO_2 substrate with a Ru (7.5 nm) / MgO (5 nm) buffer layer. Below each polar plot exemplary hysteresis loops of each material along the easy (0°) and hard (90°) axes.

The magnetic anisotropy of the film can be influenced by the alignment of the magnets with respect to the sample during deposition. If the magnets are aligned parallel to one edge of the sample, so is the magnetic anisotropy (see Fig. 4a (black)). If the magnets are tilted with respect to the sample, this results in a rotation of the magnetic anisotropy, as shown in Fig. 4a (gray) for a tilt of 30°.

From both films micron-sized elliptical elements with different dimensions have been structured by ion beam etching where the long axis of all ellipses is aligned parallel to an edge of the sample (i.e. at 0°). The magnetic anisotropy of these microstructured elements has been studied employing a microfocused magneto-optical Kerr microscope [22]. Figures 4b and c show the comparison of the magnetic anisotropy for ellipses of the same dimensions (6 µm×3 µm and 6 µm×1.5 µm, respectively). In the first case (Fig. 4b), the anisotropy of the elements is defined by the anisotropy of the film, as the shape anisotropy is rather small. On the other hand, if the aspect ratio between the long axis and the short axis of the elements is increased the shape anisotropy increases as well. If the shape anisotropy becomes larger than the magnetic anisotropy induced during growth, the overall magnetic anisotropy follows the geometry of the ellipse, as can be seen in Fig. 4c. This results give a hint on the importance of the control of the orientation of the magnetic field during the deposition for a well defined orientation of the magnetic anisotropy of the MTJ elements.

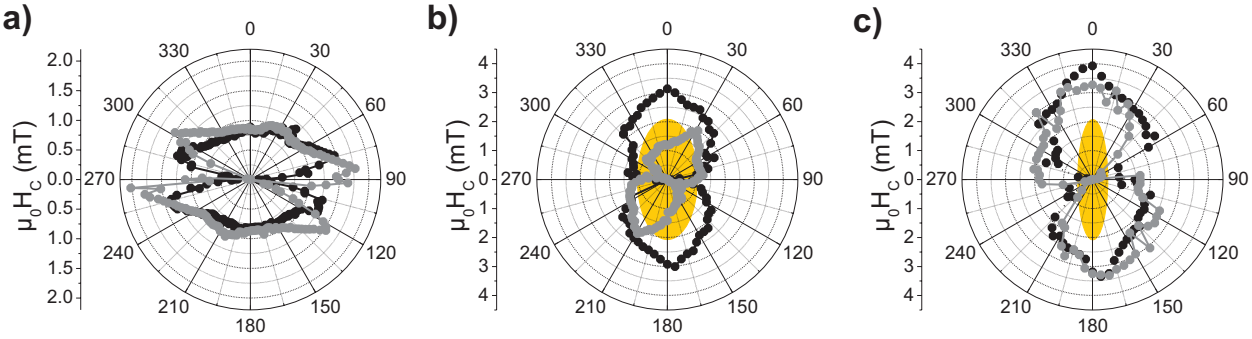

Fig. 4: Angular dependence of the in-plane coercive field H_C of: a) 6 ± 1 nm thick $Co_{40}Fe_{40}B_{20}$ thin film deposited with the magnetic field parallel to the edges (black) and with the magnetic field rotated 30° (gray) (see text), b) 6 ± 1 nm thick $Co_{40}Fe_{40}B_{20}$ elliptical elements with dimensions 6 µm×3 µm patterned from the film with parallel alignment of the magnetic field (black) and with rotated alignment of the magnetic field (gray) c) 6 ± 1 nm thick $Co_{40}Fe_{40}B_{20}$ elliptical elements with dimensions 6 µm×1.5 µm patterned from the film with parallel alignment of the magnetic field (black) and rotated alignment (gray). The shaded area represents the orientation of the ellipses

In conclusion, the growth of $Ni_{81}Fe_{19}$ and $Co_{40}Fe_{40}B_{20}$ thin films was optimized with respect to a large MOKE signal and the optical contrast needed for the measurement on micron-sized elements by the introduction of a Ru (7.5 nm) / MgO (5 nm) underlayer. An analysis of the magnetization reversal curves reveals that a Ru underlayer increases the coercive field H_C of the ferromagnetic material with a Ru thickness dependency. At the same time, the magneto-optical signal decreases with increasing Ru thickness. The introduction of an MgO interlayer greatly benefits the magneto-optical signal and this effect is enhanced with increasing MgO thicknesses. Furthermore, a desired alignment of the magnetic anisotropy could be achieved by the application of a magnetic field during growth. Elliptical elements have been structured out of films with different magnetic anisotropies. We demonstrated that the aspect ratio determines whether the shape anisotropy or the magnetic anisotropy of the film defines the easy axis direction of the element.

The authors would like to thank Björn Heinz and Moritz Geilen, as well as the Nano Structuring Center of the TU Kaiserslautern for assistance in sample preparation. Financial support by the state Rhineland-Palatinate (MBWWK and MWKEL) and by the European Regional Development Fund (ERDF) in the frame of the Spintronic Technology Platform (STeP) is gratefully acknowledged. T. Brächer is supported by a fellowship of the Graduate School Materials Science in Mainz (MAINZ) through DFG-funding of the Excellence Initiative (GSC 266).

References

[1] M. Jullière, *Tunneling between ferromagnetic films*, Phys. Lett. **54A**, 225 (1975).

[2] J.C. Slonczewski, *Current-driven excitation of magnetic multilayers*, J. Magn. Magn. Mater. **159**, L1-L7 (1996).

[3] L. Berger, *Emission of spin waves by a magnetic multilayer traversed by a current*, Phys. Rev. B **54**, 9353 (1996).

[4] M. Hosomi, H. Yamagishi, T. Yamamoto, K. Bessho, Y. Higo, K. Yamane, H. Yamada, M. Shoji, H. Hachino, C. Fukumoto, H. Nagao, H. Kano, *A novel nonvolative memory with spin torque transfer magnetization switching: Spin-RAM*, Electron Devices Meeting (IEDM), 459 (IEEE, 2005).

[5] K. Tsuchida, T. Inaba, K. Fujita, Y. Ueda, T. Shimizu, Y. Asao, T. Kajiyama, M. Iwayama, K. Sugiura, S. Ikegawa, T. Kai, M. Amano, N. Shimomura, H. Yoda, Y. Watanae, *A 64Mb MRAM with clamped-reference and adequate-reference schemes*, 2010 IEEE International Solid-State Circuits Conference, 258 (2010).

[6] A. Brataas, A.D. Kent, H. Ohno, *Current-induced torques in magnetic materials*, Nature Materials **11**, 372 (2012).

[7] J. Miyazaki, T. Yaoi, S. Ishio, *Large magnetoresistance effect in 82Ni–Fe/Al-Al$_2$O$_3$/Co magnetic tunneling junction*, J. Magn. Magn. Mater. **98**, L7-L9 (1991).

[8] D.D. Djayaprawira, K. Tsunekawa, M. Nagai, H. Machara, S. Yamagata, N. Watanabe, S. Yuasa, Y. Suzuki, K. Ando, *230% room-temperature magnetoresistance in CoFeB/MgO/CoFeB magnetic tunnel junctions*, Appl. Phys. Lett. **86**, 092502 (2005).

[9] M. Oogane, T. Wakitani, S. Yakata, R. Yilgin, Y. Ando, A. Sakuma, T. Miyazaki, *Magnetic damping in ferromagnetic thin films*, Jpn. J. Appl. Phys. **45**, 3889 (2006).

[10] F. Xu, Q. Huang, Z. Liao, S. Li, C.K. Ong, *Tuning of magnetization dynamics in sputtered CoFeB thin film by gas pressure*, J. Appl. Phys. **111**, 07A304 (2012).

[11] A. Conca, J. Greser, T. Sebastian, S. Klingler, B. Obry, B. Leven, B. Hillebrands, *Low spin-wave damping in amorphous Co$_{40}$Fe$_{40}$B$_{20}$ thin films*, J. Appl. Phys. **113**, 213909 (2013).

[12] J.S. Moodera, G. Mathon, *Spin polarized tunneling in ferromagnetic junctions*, J. Magn. Magn. Mater. **200**, 248 (1999).

[13] D.J. Monsma, S.S.P. Parkin, *Spin polarization of tunneling current from ferromagnet/Al$_2$O$_3$ interfaces using copper-doped aluminum superconducting films*, Appl. Phys. Lett. **77**, 720 (2000).

[14] D. Wang, C. Nordman, J.M. Daughton, Z. Qian, J. Fink, *70% TMR at room temperature for SDT sandwich junctions with CoFeB as free and reference layers*, IEEE Trans. Magn. **40**, 2269 (2004).

[15] T. Kubota, T. Daibou, M. Oogane, Y. Ando, T. Miyazaki, *Tunneling spin polarization and magnetic properties of Co–Fe–B alloys and their dependence on boron content*, Jpn. J. Appl. Phys. **46**, L250 (2007).

[16] P. Martín Pimentel, S.J. Hermsdoerfer, H.T. Nembach, B. Leven, S. Trellenkamp, S. Wolff, B. Hillebrands, *A crossed coplanar waveguide design for ultrafast magnetization switching utilizing polymer insulation layers*, Appl. Phys. Lett. **88**, 122510 (2006).

[17] C.-Y. Hung, M. Mao, S. Funada, T. Schneider, L. Miloslavsky, M. Miller, C. Qian, H.C. Tong, *Magnetic properties of ultrathin NiFe and CoFe films*, J. Appl. Phys. **87**, 6618 (2000).

[18] Y.-H. Wang, W.-C. Chen, S.Y. Yang, K.-H. Shen, C. Park, M.-J. Kao, M.-J. Tsai, *Interfacial and annealing effects on magnetic properties of CoFeB thin films*, J. Appl. Phys. **99**, 08M307 (2006).

[19] K. Oguz, P. Jivrajka, M. Venkatesan, G. Feng, J. M. D. Coey, *Magnetic dead layers in sputtered Co$_{40}$Fe$_{40}$B$_{20}$ films*, J. Appl. Phys. **103**, 07B526 (2008).

[20] H. Lee, L. Wen, M. Pathak, P. Janssen, P. LeClair, C. Alexander, C.K.A. Mewes, T. Mewes, *Spin pumping in Co$_{56}$Fe$_{24}$B$_{20}$ multilayer systems*, J. Phys. D : Appl. Phys. **41**, 215001 (2008).

[21] S. Chen, M. Tang, Z. Zhang, B. Ma, S.T. Lou, Q.Y. Jin, *Interfacial effect on the ferromagnetic damping of CoFeB thin films with different under-layer*, Appl. Phys. Lett. **103**, 032402 (2013).

[22] T. Sebastian, A. Conca, G. Wolf, H. Schultheiß, B. Leven, B. Hillebrands, *Magneto-optical investigation of the shape anisotropy of individual micron-sized magnetic elements*, J. Appl. Phys. **110**, 083909 (2011).

4.17 Lifetime measurements for CoFeB/MgO/CoFeB magnetic tunneling junctions in the frame of the Spin Technology Platform

A. Conca, B. Leven, and B. Hillebrands

In collaboration with J. Paul, R. Lehndorff, Sensitec GmbH, Mainz, Germany, F. Casper, Institute of Inorg. Chemistry and Anal. Chemistry, Johannes Gutenberg Universität, Mainz, Germany and Prof. Dr. Claudia Felser, Max-Planck-Institut für Chemische Physik fester Stoffe, Dresden.

The Spintronic Technology Platform (STeP) in Rhineland-Palatinate is conceived as a tool for technology transfer between university and industry for magnetic materials and their applications. The main focus is on thin film technology, including also multilayered systems.

STeP is a collaboration between the University of Kaiserslautern and the Johannes Gutenberg University of Mainz together with the industrial partner Sensitec GmbH [1], a market leader in the field of magnetic sensors. By using the clean room facilities and technological know-how of Sensitec, university researchers aim to develop new device designs, deposition techniques for new materials and new measurement and testing procedures. All this activities are directed to the creation of a research infrastructure in Rhineland-Palatinate available for SMEs and to the promotion of innovation in the field of spintronics, concretely, of magnetoresistive effects.

The main application field of magnetoresistive effects is in the production of magnetic field sensors for angle, rotation speed or position measurement in the automotive branche, in industrial machinery or in robotics and cybernetics [1] .

One of the main technological aims of STeP is the implementation and optimization of MgO as a barrier material for magnetic tunneling junctions (MTJ) in an industrial environment. The basic working unit for a MTJ is formed by two metallic ferromagnetic thin films acting as electrodes separated by a very thin ($1-3\,\mathrm{nm}$) insulating layer or barrier (MgO or Al_2O_3). The magnetoresistive effect behind is the TMR (tunnelling magnetoresistance) effect based on a spin-dependent tunneling probability of the electrons through the barrier. Although the deposition of high quality MgO tunneling barriers is more complicated than for Al_2O_3, MgO has a very important advantage: the presence of the *spin filtering* effect. Due to the required symmetry match between the electronic bands in the electrodes and in the barrier, some of the bands allow for a preferential tunneling (lower decay rate in the barrier and larger tunneling probability). For this reason, the degree of spin polarization of the tunneling current is highly increased contributing to a very large magnetoresistive effect.

The presence of a very thin insulating layer is also the weakest point of a TMR-based device. Electrostatic discharges are able to completely destroy a working device. This problem can be solved by the on-chip implementation of security diodes or by the adequate preparation of mounting workers. However, there is a more insidious effect resulting from the working principle of tunneling junctions. Since the electrodes are metallic and the current is flowing perpendicular to the layers, the voltage drop is occurring over a distance of only a few nanometers at the barrier. The result is a high electric field of the order of $10^7\,\mathrm{V/m}$. This electric field represents a stress

[1] The production of read heads for hard discs, which is in any case a type of magnetic sensor, is also a very important area. It has very special requirements for design and performance which differs strongly from the other types.

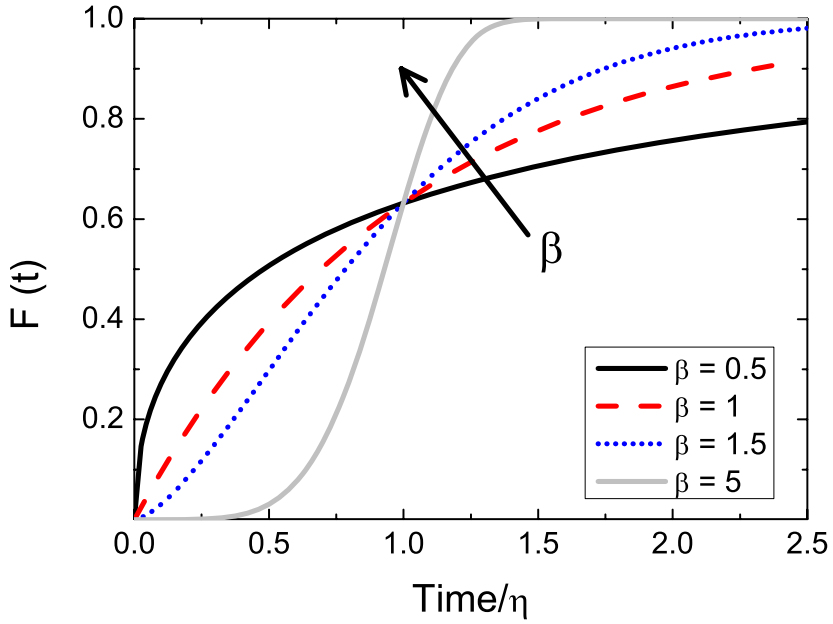

Fig. 1: Weibull cumulative function $F(t)$, describing the total fraction of broken elements after a time t, calculated for different values of the shape parameter β. Time is given in units of the characteristic lifetime η.

agent which is able, after a certain time, to produce a dielectric breakdown of the barrier. For a single TMR device, this event cannot be predicted since it is a stochastic event similar to metal failure under mechanical stress. However, it is of capital importance to quantitatively estimate the failure rate of a device or sensor after a certain working time. One of the activities of STeP is the development and establishment of an actual measurement procedure to study this effect.

A study of the breakdown processes in MTJs can only be done in a statistical way. From the investigation on SiO_2 thin layers, it was first known that the dielectric breakdown can be described using the Weibull statistics [2]. This was later confirmed for MTJs with Al_2O_3 [3,4] and MgO [5] barriers. The Weibull probability function $f(t)$ describes the fraction of broken elements per time unit:

$$f(t) = \frac{\beta}{\eta}\left(\frac{t}{\eta}\right)^{\beta-1} \exp\left(-\left[\frac{t}{\eta}\right]^{\beta}\right) \quad . \tag{1}$$

Here, η is the characteristic lifetime of the junction population and β is the shape parameter. A more convenient quantity is the total fraction F of broken elements after a certain time t:

$$F(t) = 1 - \exp\left(-\left[\frac{t}{\eta}\right]^{\beta}\right) \quad . \tag{2}$$

$F(t)$ is also known as the Weibull cumulative function. Here, it is straightforward to see that after a time $t = \eta$, 63.2% of the junctions are broken. In order to understand the role of the shape parameter β, $F(t)$ in plotted in Fig. 1 for several β values. One can distinguish three cases. For $\beta < 1$ (black line) a large *infant mortality* is present, i.e. a significant fraction of the elements break fast just after applying the stress. The opposite happens for $\beta > 1$ (dotted data and grey line) where few elements break at the beginning and the failure rate increases with time (aging). The limit case $\beta = 1$ implies a constant failure rate indicating a random external agent.

The characterization of the breakdown processes was applied for circular CoFeB/MgO/CoFeB junctions (TMR= 74%, RA=1.2 MΩ · µm) with a diameter of 10 µm. Figure 2a shows the measured

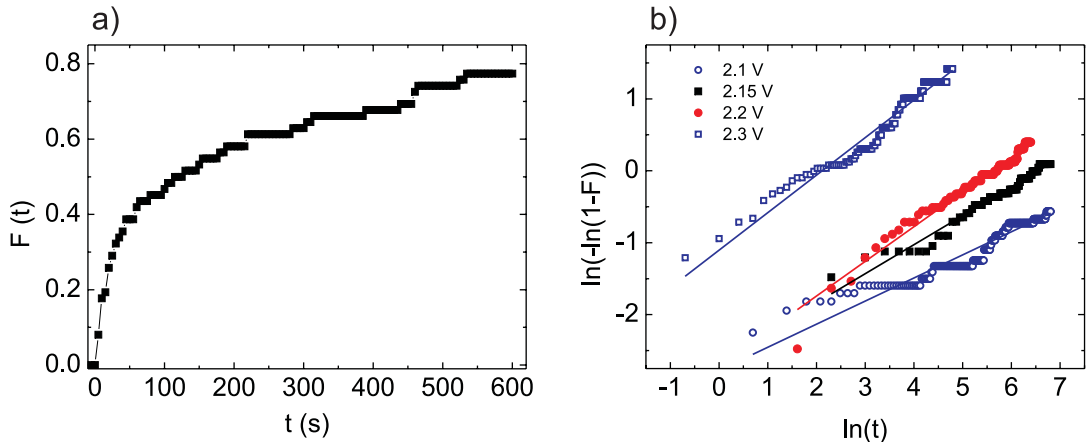

Fig. 2: a) Measured fraction $F(t)$ of broken CoFeB/MgO/CoFeB magnetic tunneling junctions with an applied stress voltage of 2.1 V. b) Weibull plots for different stress voltages.

$F(t)$ function under a stress voltage of 2.1 V. It is clear that the the actual case is one with a large infant mortality. A fit to the data provides a value of 0.52 for β. For better comparison between different data sets, the use of Weibull plots is recommendable. The Weibull plots are the result of applying the logarithmic function to Eq. (2) resulting in:

$$\ln\left[-\ln(1-F(t))\right] = \beta \cdot \ln(t) - \beta \cdot \ln(\eta) \quad . \tag{3}$$

Figure 2b shows Weibull plots for different voltages. In the Weibull plots the slope is directly connected to β. That means that if this parameter is voltage independent, the Weibull plots for different voltages should be parallel. This is approximately the case for our junctions. The averaged β value is 0.43. This value is similar to the one obtained by IBM for MgO barriers [5].

The scaling of the lifetime with the applied voltage is immediately recognized in the Weibull plots by a shift of the data sets for different values. A constant lifetime will result in an overlapping of the data. In most of the cases, this will point to an external agent such as spurious voltage peaks from measurement devices or insufficient electrostatic protection. This would be also the case for $\beta = 1$.

Typical working conditions voltages for MTJs are much lower than the voltages used here (below 0.5 V). However, the lifetimes in the low voltage region can reach values well over 10^6 years. It is impossible then to get enough statistics with a reasonable measurement time. For this reason, the stress processes are accelerated by measuring at larger voltages. The open question now is the relation between the measured lifetimes at large voltages and the expected lifetimes at working conditions. In the literature several models are chosen, going from an inverse power law model to a more or less complicated exponential law [3,4,6,7]. In our case, we choose a simple exponential dependence, which has been proved for Al_2O_3 [3,4,6] and MgO [8] tunneling barriers:

$$\eta = A \, \exp(-BV) \quad . \tag{4}$$

Figure 3 shows the measured dependence of η on the applied voltage. The line represents a fit to an exponential law, which is able to describe the dependence. The same dependence has been confirmed for other junction sets with different deposition conditions. Now it is possible to extrapolate and estimate the lifetime for the low voltage regime (0.4 V). It is clear that the obtained

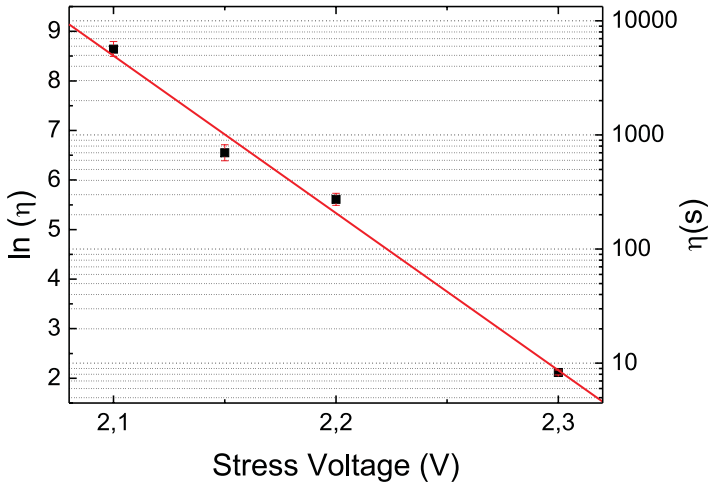

Fig. 3: Dependence of the characteristic lifetime η of the tunneling junctions and $\ln(\eta)$ on the stress voltage. The line is a fit to Eq. (4) to estimate the lifetime in the low voltage regime.

value will be accompanied by a certain error bar. Since we are interested in the minimum lifetime that it is possible to guarantee, a conservative approach recommends the use of the lowest possible value compatible with our measurement uncertainty (worst case scenario). This is, for this set $\eta(0.4V) = 3.1 \cdot 10^{18}$ years. This large value is an indication of the high quality of the tunneling barrier but it lacks of practical meaning.

Once η is estimated it is more convenient to express the result in a different way: the fraction of elements which will be broken after a working time of 10 years (i.e. $F(10y)$) or any time span of interest for a certain purpose. For this case we obtain $F(10y) = 0.03 \cdot 10^{-6} = 0.03$ ppm. This value is of capital importance, when using TMR based sensors in real conditions, to calculate rentability or appropriate guarantee conditions or just design convenient redundant mechanisms to almost rule failing out.

For the engineering of real devices, the use of several junctions electrically connected in series is common. This approach narrows the properties distribution of the different elements of the wafer by averaging the signal of several junctions and it increases the total output signal. This represents also a strategy to reduce device failures. First, the breakdown of a single junction may have only minor relevance in the overall signal, second, the voltage drop in each single junction can be tune as small as desired. For a given required maximum device failure rate, the measured η value and Eq. (4) can thus be used to define the adequate number of junctions.

In summary, a measurement procedure to determine the failure rates and lifetimes of magnetic tunneling junctions have been established. First results confirmed the high quality of the MgO junctions produced at the Sensitec facilities in Mainz although a significant infant mortality has been observed. Currently, measurements are performed to understand lifetime dependence on different deposition conditions and parameters such as barrier thickness, annealing temperature, etc.

Financial support by the state of Rhineland-Palatinate (MBWWK and MWKEL) and by the European Regional Development Fund (ERDF) in the frame of the Spintronic Technology Platform (STeP) is acknowledged. The authors wish as well to thank Stefan Eilers and Matthias Bürkle for their technical support at Sensitec.

References

[1] www.sensitec.com

[2] Kin P. Cheung, *Plasma charging damage*, Springer Verlag, p. 14 (2000).
[3] J. Das, R. Degraeve, P. Roussel, G. Groeseneken, G. Borghs, J. De Boeck, *Area scaling and voltage dependence of time-to-breakdown in magnetic tunnel junctions*, J. Appl. Phys. **91**, 7712 (2002).
[4] H. Kim, J. Sok, B.K. Cho, J.R. Rhee, W. Parkand, T. Kim, *Dielectric characteristics of magnetic tunnel junctions using amorphous CoNbZr layers*, J. of the Korean Physical Society, **46**, No. 6,1425 (2005).
[5] T. Min, Q. Chen, R. Beach, G. Jan, C. Horng, W. Kula, T. Torng, R. Tong, T. Zhong, D. Tang, P. Wang, M. Chen, J.Z. Sun, J.K. Debrosse, D.C. Worledge, T.M. Maffitt, W.J. Gallagher, *A study of write margin of spin torque transfer magnetic random access memory technology*, IEEE Trans. Magn. **46**, 2322 (2010).
[6] M. Gibbons, K. Sin, S. Funada X. Shi, *Lifetime of magnetic tunnel junction under voltage stress*, Proc. of INTERMAG Europe 2002.
[7] H. Yamazaki, H. Hirabayashi, N. Oyama M. Sakai, *Characteristics of TMR angle sensors*, Proc. SENSOR+TEST Conferences 2011.
[8] C. Yoshida, M. Kurasawa, Y. Min Lee, K. Tsunoda, M. Aoki Y. Sugiyama, *A study of dielectric breakdown mechanism in CoFeB/MgO/CoFeB magnetic tunnel junction*, Proc. Reliability Physics Symposium (IRPS), 2009 IEEE International Conferences.

4.18 Study of material parameters of YIG films with ferromagnetic resonance techniques

S. Klingler, A. Conca, A. V. Chumak, and B. Hillebrands

In collaboration with T. Mewes and B. Khodadadi, Center for Materials for Information Technology, University of Alabama, Tuscaloosa, Alabama, USA, and C. Dubs, O. Surzhenko, and P. Görnert, INNOVENT e.V. Technologieentwicklung, Jena

This report is based on a stay of the first author in Tuscaloosa, Alabama, at the Center for Materials for Information Technology (MINT) at the University of Alabama. Every year the MINT-Center offers the opportunity for interested students to gain experience in the study of magnetic films with microwave techniques in an international research team, and the first author took part in this program.

One of the most important technologies to replace the electron charge as information carrier is the development of spintronics. In this new emerging field the electron spin is used as information carrier which can be manipulated without current and therefore without the limitations of electronics through heating processes. Spin is transported not only by electrons but also by magnons, the quanta of dynamic excitations of the magnetic system. With Yttrium Iron Garnet (YIG) a material system was found with an ultra low damping of smaller than $\alpha = 10^{-4} - 10^{-5}$ and a propagating distance of spin waves in the centimeter regime [1]. The expectation of fruitful research and technological progress led to a huge interest and improvement in spintronic applications and spin wave physics. In this connection the material parameters of YIG are of crucial importance for the application of this material in magnonics and spintronics.

In this report we present measurements of the saturation magnetization M_s and the exchange constant A of liquid phase expitaxy (LPE) grown YIG films. The sample films were grown on horizontally rotated (111) Gadolinium Gallium Garnet (GGG) substrates and have a thickness of $0.91, 1.6$ and $2.6\,\mu$m and a size of 3×3 mm. The YIG samples were investigated with a waveguide ferromagnetic resonance (FMR) setup in a frequency range from 5 to 40 GHz in in-plane and out-of-plane configuration. The exchange constant and saturation magnetization were determined using the first perpendicular standing spin wave modes (PSSW) and the method of Schreiber and Frait [2]. The results for both configurations are compared and thereby an angular dependence was detected.

In an external magnetic field $\mathbf{H}$ a torque forces the magnetization $\mathbf{M}$ of a sample to precess around the direction of the field so that its motion can be described by the Landau-Lifshitz and Gilbert equation

$$\frac{\partial \mathbf{M}}{\partial t} = -|\gamma| \mathbf{M} \times \mathbf{H} - \frac{\alpha}{M_s} \mathbf{M} \times \frac{\partial \mathbf{M}}{\partial t}, \tag{1}$$

where M_s is the saturation magnetization, $\gamma < 0$ the gyromagnetic ratio and α the Gilbert damping parameter [4]. The first term on the right hand side of the equation describes the free motion of the magnetization around the direction of the effective applied field. The second term on the right hand side introduces a damping of this movement to the equation which forces the magnetization to become parallel to the effective field.

The field $\mathbf{H}$ in Eq. 1 must be understood as an effective value including all possible contributions (e.g. anisotropy fields and demagnetization fields):

$$\mathbf{H}_{\text{eff}} = \mathbf{H}_{\text{appl}} + \mathbf{H}(t) + \mathbf{H}_{\text{ex}} + \mathbf{H}_{\text{ani}} + \mathbf{H}_{\text{demag}} + \ldots \tag{2}$$

For this work the exchange interaction plays a major role which can be described as an exchange field with the form [5]

$$\mathbf{H}_{\mathrm{ex}} = -\frac{2A}{M_{\mathrm{s}}^2}\nabla^2\mathbf{M}. \tag{3}$$

Here, A is the exchange constant. The interpretation of the exchange field is easier in the energy space. For two adjacent spins the overlap of the spin wave functions influences the energy of the system due to Pauli's exclusion principle. In the case of ferromagnets the energy contribution of the exchange field becomes negative for parallel spins so that the system is in its favorable energy state. For any other direction of the spins, energy is needed in comparison to the ground state. This energy contribution can be described by an exchange field which forces the spins to be parallel again. The exchange interaction is a short range interaction, so that mainly adjacent spins interact with each other.

If now a microwave field is applied to the system it will induce a precession of the magnetization due to the torque created by the microwave field. The resonance condition for the microwave field in dependence of the field direction relative to the sample surface can be described by Kittel's formula [3]. For the in-plane configuration the applied field is parallel to the sample surface and the resonance condition is given by

$$\left(\frac{\omega}{|\gamma|}\right)_{\mathrm{ip}} = \sqrt{\left(H_{\mathrm{appl}} + \frac{2A}{M_{\mathrm{s}}}k^2\right)\left(H_{\mathrm{appl}} + \frac{2A}{M_{\mathrm{s}}}k^2 + 4\pi M_{\mathrm{eff}}\right)}. \tag{4}$$

In the out-of-plane configuration the applied field is perpendicular to the sample surface and the resonance condition is described by

$$\left(\frac{\omega}{|\gamma|}\right)_{\mathrm{oop}} = H_{\mathrm{appl}} + \frac{2A}{M_{\mathrm{s}}}k^2 - 4\pi M_{\mathrm{eff}}. \tag{5}$$

In both cases $k = n\pi/d$ is the wave vector of the n-th excited perpendicular standing spin wave which is quantized over the thickness d of the sample and $\frac{2A}{M_{\mathrm{s}}}k^2$ is the exchange field. For the mode with $n = 0$ the classical case of ferromagnetic resonance is given. For $n \neq 0$ a perpendicular standing spin wave is excited.

For measuring the material constants a waveguide FMR setup was used. It contains an electromagnet to apply the external field in the range of 0 to 16.5 kOe. For this experiment a microwave power of 10 dBm was used to excite the spin waves. Furthermore the waveguide was rotated so that the angle between field and sample surface could be varied from 0 to 360°. The absorption signal was amplified by a lock-in amplifier. The scan of a Lorenzian absorption peak with the lock-in field results in an output voltage which has the form of the derivative of the original signal. For analyzing the spectra (e.g. Fig. 1a) a LabView progam is used for fitting the resonances. The parameters of the fit function take absorption and dispersion into account, so that the program delivers directly the resonance positions and the peak-to-peak linewidths without foregone data reduction.

For the out-of-plane configuration, where magnetization and external field are perpendicular to the sample surface, Eq. (5) is used for the estimation of the saturation magnetization and the exchange constant. In a plot where the position of the resonances over the square of the mode number n^2 is drawn, the resonance field is defined by Eq. 5:

$$H_{\mathrm{appl}}^{\mathrm{res}} = -\frac{2A}{M_{\mathrm{s}}}\frac{\pi^2}{d^2}n^2 + \left(\frac{\omega}{|\gamma|}\right)_{\mathrm{oop}} + 4\pi M_{\mathrm{eff}}. \tag{6}$$

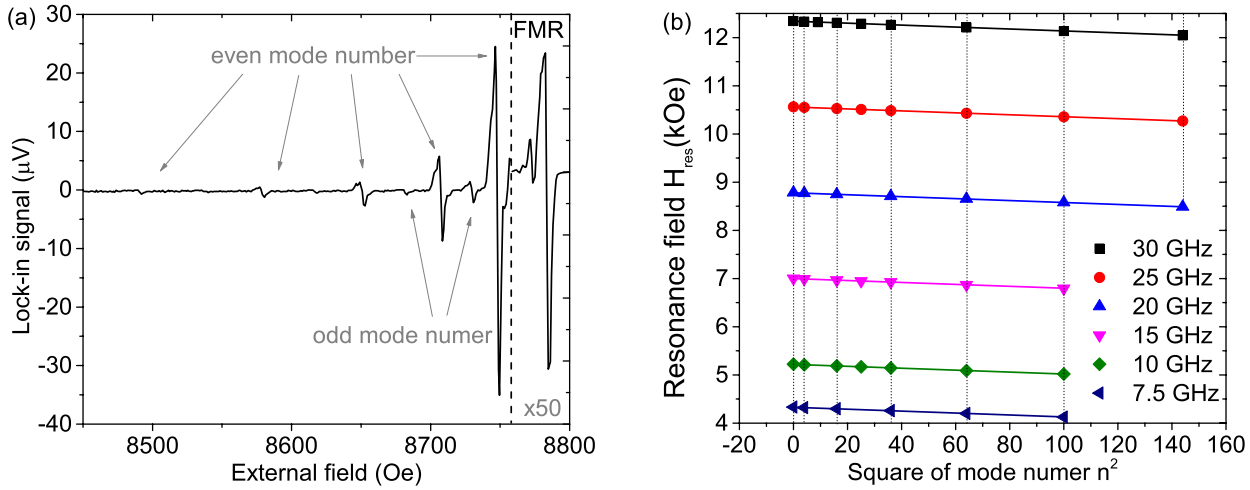

Fig. 1: (a) Example spectrum for the YIG sample with $d = 1.6\,\mu\text{m}$ in out-of-plane configuration at 20 GHz. The even mode numbers have a odd number of anti-nodes as explained in the text. The scale for the FMR peak is streched by a factor of 50 right to the dashed line. (b) Line positions found in the spectrum of YIG with $d = 1.6\,\mu\text{m}$ in out-of-plane configuration. It is obvious that the line positions follow a linear function in dependence of n^2. Since A, M_s and γ are shared fitting parameters, they are the same for every frequency. The dashed lines show the positions of the resonances with even mode numbers.

Thus the slope of the linear function corresponds to $\frac{2A}{M_s}\frac{\pi^2}{d^2}$ and the effective magnetization is defined by the y-intercept of the graph minus the given values for frequency over the gyromagnetic ratio. This method was recommended by Schreiber and Frait in 1996 [2]. For both configurations it was assumed that the films had no significant perpendicular anisotropy, i.e. $M_s = M_{\text{eff}}$.

Slope and y-intercept are obtained by a so called global fit. This means that the line positions of all measured frequencies are plotted over the square of the mode number and the exchange constant, gyromagnetic ratio and saturation magnetization are shared fit parameters. With this, the best results for all measurements are found at the same time. The graph of the global fit for $d = 1.6\,\mu\text{m}$ is shown in Fig. 1b.

In the spectra mainly the resonances with an even mode number were observed. The absorption of modes with an odd mode number was about ten times smaller in average than for the modes with even mode numbers. This effect can be understood assuming a model of "perfect pinning" [6]: since the magnetization on the surface of the sample is pinned, the excited spin waves propagate in phase on the sample surface. The results are standing spin waves which consist of $(n+1)$ anti-nodes. For spin waves with an even number of anti-nodes the contribution of each anti-node to the absorption summarizes in the ideal case to zero. In contrast to that, a spin wave with an odd number of anti-nodes has a non-vanishing contribution to the absorption. The measured resonances with an even number of anti-nodes can be interpreted with small field inhomogeneities which contradict the boundary conditions for perfect pinning. The smaller amplitude of this waves and the fact that there is a continuous mode numbering seen in the spectra confirm this "perfect pinning" assumption.

The results of the measurements are shown in Tab. 1. The exchange constant of YIG was extracted to be $A = 3.48 \cdot 10^{-7}\,\frac{\text{erg}}{\text{cm}}$, where the saturation magnetization is $4\pi M_s = 1651.6\,\text{G}$ and the gyromagnetic ratio is $\gamma = 2.807\,\frac{\text{MHz}}{\text{Oe}}$. The values of the exchange constant of all three samples match very well within the error bars and do not change with the thickness of the sample, which speaks for the high quality of the films.

For the in-plane configuration the spectrum looks different as it can be seen in Fig. 2a. The FMR

configuration	d (µm)	$4\pi M_s$ (G)	$A10^{-7}$erg/cm	γ(MHz/Oe)
out of plane	0.91	1651.0 ± 1.6	3.49 ± 0.01	2.809 ± 0.001
	1.6	1660.6 ± 2.3	3.48 ± 0.01	2.809 ± 0.001
	2.6	1643.1 ± 3.7	3.44 ± 0.08	2.802 ± 0.002
in-plane	0.91	1733.2 ± 3.8	3.71 ± 0.01	2.810 ± 0.001
	1.6	1790.0 ± 5.8	3.81 ± 0.01	2.809 ± 0.001
	2.6	1805.3 ± 2.7	3.82 ± 0.04	2.809 ± 0.001

Table 1: Results for the YIG samples with different thicknesses

resonance and the PSSW resonances overlap and the resonance fields are moved to lower fields due to demagnetization effects. With Kittel's formula Eqn. (4) the dependence of the resonance frequency on the external field can be described. The evaluation is also different since there is no linear behavior over the square of the mode number.

In a first step the effective magnetization of the sample is extracted by setting the exchange field for the FMR mode with $n = 0$ manually to be zero. Kittel's expression for the FMR mode provides then the effective magnetization.

In a second step, for every resonance in the spectra, the exchange field can be found again with Kittel's expression, where the effective magnetization from the first step is used. The evaluation is equal to step one, but we do not observe the FMR mode but the higher order modes. We obtain an exchange field which depends on an unknown mode number.

Third, the exchange field of the modes is varied over the presumed mode number. As a first hint the mode amplitude in the spectrum is again useful to decide whether the mode is an even or an odd mode. If the exchange field follows a linear function over the square of the mode number the exchange constant is given by the slope of this function as presented in Fig. 2b. Again, mainly resonances with even mode numbers were observed.

For all three samples the exchange constant, saturation magnetization and the gyromagnetic ratio could be estimated as shown in Tab. 1. The exchange constant for all three samples is approximately constant, as in the experiments in out-of-plane configuration. The same results are obtained for the saturation magnetization which stays constant over the film thickness; only the sample with $d = 0.91\,\mu\text{m}$ shows a smaller value for M_s.

As final values for the saturation magnetization, the average of both configurations is used: $4\pi M_{s,oop} = 1651\,\text{G}$ and $4\pi M_{s,ip} = 1776\,\text{G}$. The total error for these measurements can be estimated to be at least 7 G, so that the values of the saturation magnetization do not fit together within the error bars. Even with a larger error, the difference of 125 G cannot be explained. In comparison, as a typical saturation magnetization of YIG $4\pi M_s = 1750\,\text{G}$ is used [1].

As final values for the exchange constant an average of both configurations is used: $A_{oop} = 3.47 \cdot 10^{-7}\,\frac{\text{erg}}{\text{cm}}$ and $A_{ip} = 3.78 \cdot 10^{-7}\,\frac{\text{erg}}{\text{cm}}$. A comparison chart for the exchange constant of YIG was published by Anderson 1964 [8], where the value for A varys between $1.18 \cdot 10^{-7}$ and $6.1 \cdot 10^{-7}\,\frac{\text{erg}}{\text{cm}}$, so that our results fit into the field of exchange constants obtained by other groups.

The exchange constants vary as the saturation magnetization does. Indeed both fit parameters are antagonists, as can be seen in Kittel's expressions Eq. (5) and (4). To obtain, e.g., the same slope in Fig. 2b one can choose different values for both parameters as long as the proportion of both is similar. Since for the out-of-plane configuration a smaller saturation magnetization was obtained, the exchange constant has to be smaller, too. For the proportion between $2A$ and M_s

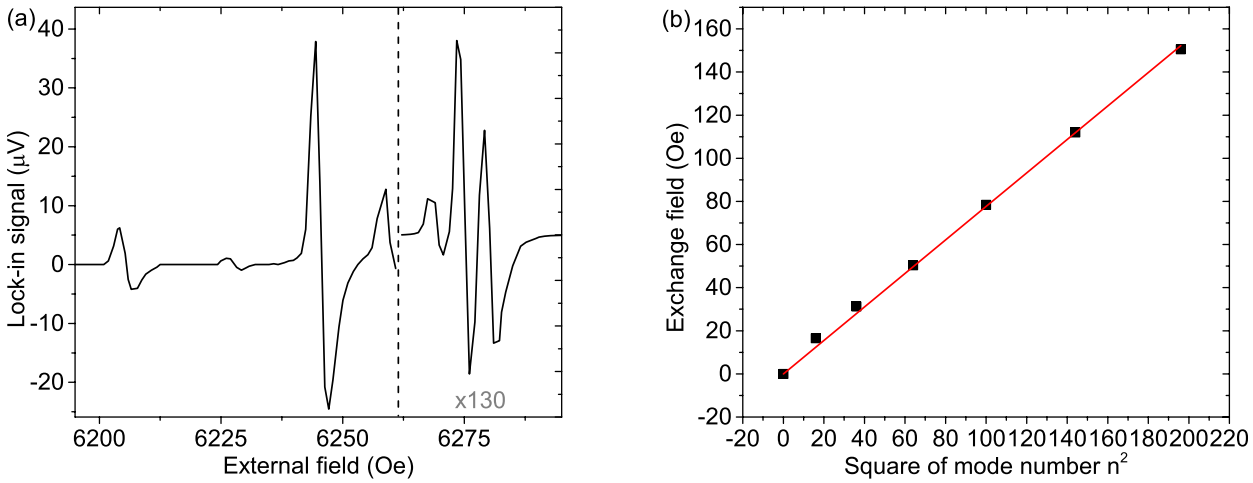

Fig. 2: (a) Example spectrum for the YIG sample with $d = 1.6\,\mu\text{m}$ in in-plane configuration at 20 GHz. The derivations of the first two resonances overlap in such a way that a multiple resonance fit had to be used to extract the linewidth and position of both resonances. The scale for the FMR peak streched by the factor of 130. (b) The exchange fields of the sample with $d = 2.6\,\mu\text{m}$ follow a linear function of the square of the mode number. The slope of the function is proportional to the exchange constant. Each point in the graph stands for the exchange field of one resonance.

we obtain $4.20 \cdot 10^{-10}\,\frac{\text{erg}}{\text{cm}\cdot\text{G}}$ in the out-of-plane configuration and $4.25 \cdot 10^{-10}\,\frac{\text{erg}}{\text{cm}\cdot\text{G}}$ in the in-plane configuration. The difference between the measured exchange constants can now be ascribed to the errors of the saturation magnetization. The reason for this angular dependence for the same samples can be a magnetic anisotropy, which affects different by the determination of A and M_s for in-plane and out-of-plane measurements, as shown in [9]. Another reason might be a mechanical-stress-induced anisotropy of A due to the lattice mismatch between YIG and GGG or a deviation to the perfect pinning assumption. A further discussion is necessary to find the origin of the angular dependence.

We thank the group from the University of Alabama for their support and supervision and the *Nano Structuring Center* in Kaiserslautern for technical support. Part of this work was supported by NSF-CAREER Grant #0952929.

References

[1] A.A. Serga, A.V. Chumak, B. Hillebrands, *YIG magnonics*, J. Phys. D : Applied Physics **43**, 264002 (2010).
[2] F. Schreiber, Z. Frait, *Spin-wave resonance in high-conductivity films: The Fe-Co alloy system*, Phys. Rev. B **54**, 6473-6480 (1996).
[3] C. Kittel, *On the theory of ferromagnetic resonance absorption*, Phys. Rev. **73**, 155 161 (1948).
[4] T.L. Gilbert, *Classics in magnetics: a phenomenological theory of damping in ferromagnetic materials*, IEEE Trans. Magn. **40**, 3443-3449 (2004).
[5] H. Schultheiß, *Kohärenz und Dämpfungsverhalten von Spinwellen in magnetischen Mikrostrukturen*, Dissertation (2010).
[6] C. Kittel, *excitation of spin waves in a ferromagnet by a uniform rf field*, Phys. Rev. **110**, 1295-1297 (1958).
[7] M.J. Hurben, C.E. Patton, *Theory of two magnon scattering microwave relaxation and ferromagnetic resonance linewidth in magnetic thin films*, J. Appl. Phys. **83**, 4344-4365 (1998).
[8] E.E. Anderson, *Molecular field model and the magnetization of YIG*, Phys. Rev. **134**, A1581-A1585 (1964).
[9] V.B. Bobkov, I.V. Zavuslyak, V.F, Romanyuk, *Microwave spectroscopy of magnetostatic waves in epitaxial ferrite films*, Journal of Communications Technology & Electronics **48**, 196-206 (2003).

4.19 Success story of technology transfer of magnetic sensor applications

B. Leven, E. Th. Papaioannou, A. Conca, P. Clausen, D. Weller, and B. Hillebrands

In 2012 the Greater Region Magnetism Network (GRMN) was established in the framework of the University of the Greater Region. Within this GRMN initiative the universities of Lorraine, Sarrebruck and Kaiserslautern combine their know-how and workforce not only to explore new magnetic phenomena but also their potential for application and strategies for technology transfer. A further aim is to develop new strategies towards pupil and student education as well as teacher training seminars in magnetism related phenomena. One main goal is to translate the technology and application to everyday's life. To do so, the group in Kaiserslautern focused on the development of pedagogical demonstrators of magnetic sensor applications to be presented at faires, open days at universities and other public relation activities. In this Report we will give one prominent example how to rise curiosity and awareness of people who are not dealing with science at all.

Using the industrial magnetism platform INNOMAG e.V. (http://www.innomag.org) we established a collaboration with the company ELGO Electronic, a German company known for high precision measurement, positioning and control systems mainly based on magnetic sensor technology.

Since ELGO magnetic sensors are established in skyscrapers for highly precise elevator positioning, as prominent example the Taipei 101 tower (Taiwan) was identified to be a good demonstrator model. It was built true to scale with a height of 1.30 m including an elevator with ELGO positioning system. The Taipei 101 tower was realized using transparent acrylic glas to allow for a detailed insight into the working principle of the magnetic positioning sensor, which is moving contactless in 1 mm distance to a magnetic tape line. To rise the observers curiosity the tower walls were equipped with green diodes illuminating the whole tower. A large digit display in the electronic

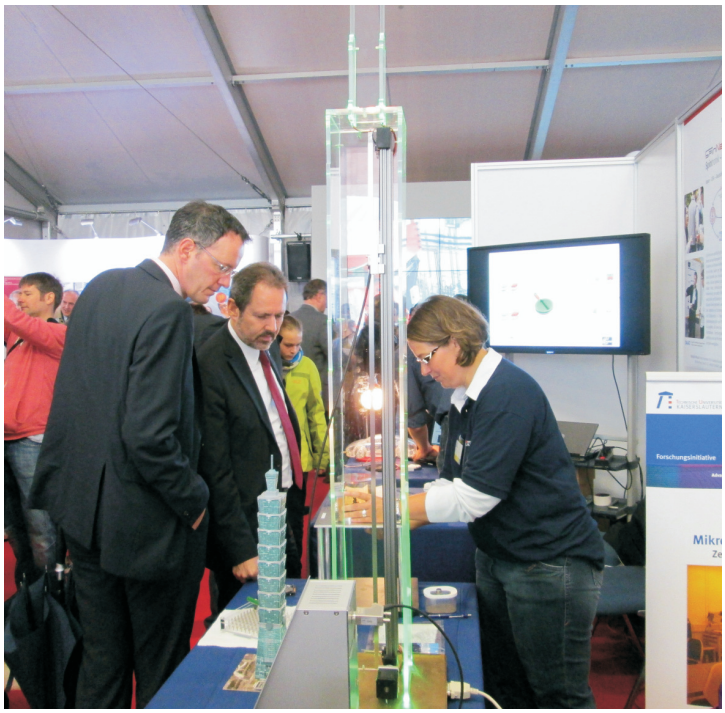

Fig. 1: The successful Taipei 101 Tower demonstrator presented at the *Wissenschaftsmarkt 2013* in Mainz. The Lord Mayor of Mainz, Michael Ebling (on the left), was caught by the design and amazed by realizing how magnetic application is involved in daily life.

unit moving the elevator shows the floor corresponding to the elevator position. Figure 1 shows the Taipei 101 demonstrator.

On the Fair *Wissenschaftsmarkt in Mainz 2013* in September 2013 the Taipei 101 demonstrator was presented for the first time. As eye-catcher on the exhibition stand for magnetism technology transfer in collaboration with the Graduate School of Excellence *Material Science in Mainz (MAINZ)* and the *Spintronic Technology Transfer Platform STeP* the Taipei 101 tower rose an immense interest of people. The size and illumination gathered the attention of the visitors, the design caused recognition effects - and finally curiosity on what is the demonstrator about. Here, we could successfully convince visitors on how magnetism is deeply involved in everyday's life, even hidden but highly effective. Visitors were amazed on the magnetic tape line, tested the magnetic digit using a magnetic contrast sheet, and let the elevator move up- and downwards observing the contactless sensing magnetic sensor at work. Intense discussion with the visitors and the presentation of a magnetic playground strongly increased the awareness of our visitors on where and how magnetic sensors and magnetism at all influence our daily life.

Financial support by the European Commission within the GRMN project and the state Rhineland-Palatinate is gratefully acknowledged.

Chapter 5: Publications

Most publications can be downloaded from http://www.physik.uni-kl.de/hillebrands.

5.1 submitted

1. *Sub-microsecond fast temporal evolution of the spin Seebeck effect*
   M. Agrawal, V.I. Vasyuchka, A.A. Serga, A. Kirihara, P. Pirro, T. Langner, M.B. Jungfleisch, A.V. Chumak, E.Th. Papaioannou, B. Hillebrands
   submitted to Phys. Rev. Lett.

2. *Thickness and power dependence of the spin-pumping effect in $Y_3Fe_5O_{12}$/Pt heterostructures measured by the inverse spin Hall effect*
   M.B. Jungfleisch, A.V. Chumak, A. Kehlberger, V. Lauer, D.H. Kim, M.C. Onbasli, C.A. Ross, M. Kläui, B. Hillebrands
   submitted to Phys. Rev. B

5.2 published

1. *The dynamic magnonic crystal: new horizons in artificial crystal based signal processing*
   A.V. Chumak, A.D. Karenowska, A.A. Serga, B. Hillebrands
   in "*Magnonics: From fundamentals to applications*", Topics in Applied Physics, Vol. 125
   S.O. Demokritov, A.N. Slavin editors, Springer-Verlag, Berlin (2013)

2. *Explosive electromagnetic radiation by the relaxation of a multi-mode magnon system*
   V.I. Vasyuchka, A.A. Serga, C.W. Sandweg, D.V. Slobodianiuk, G.A. Melkov, B. Hillebrands
   Phys. Rev. Lett. **111**, 187206 (2013)

3. *Magneto-optical characterization of singlecrystalline $Co_2FeAl_{0.4}Si_{0.6}$ thin films on MgO(100) substrates with Cr and MgO seed layers*
   A. Ruiz-Calaforra, A. Conca, T. Graf, F. Casper, B. Leven, C. Felser, B. Hillebrands
   J. Phys. D: Appl. Phys. **46**, 475001 (2013)

4. *Optimizing the spin-pumping induced inverse spin Hall voltage by crystal growth in Fe/Pt bilayers*
   E.Th. Papaioannou, P. Fuhrmann, M.B. Jungfleisch, T. Brächer, P. Pirro, V. Lauer, J. Lösch, B. Hillebrands
   Appl. Phys. Lett. **103**, 162401 (2013)

5. *Magnonic band gaps in waveguides with a periodic variation of the saturation magnetization*
   F. Ciubotaru, A.V. Chumak, B. Obry, A.A. Serga, B. Hillebrands
   Phys. Rev. B **88**, 134406 (2013)

6. *Localized parametric generation of spin waves in a longitudinally magnetized $Ni_{81}Fe_{19}$ waveguide*
   T. Brächer, P. Pirro, A.A. Serga, B. Hillebrands
   Appl. Phys. Lett. **103**, 142415 (2013)

7. *Direct measurement of magnon temperature: New insight into magnon-phonon coupling in magnetic insulators*
   M. Agrawal, V.I. Vasyuchka, A.A. Serga, A.D. Karenowska, G.A. Melkov, B. Hillebrands
   Phys. Rev. Lett. **111**, 107204 (2013)

8. *Improvement of the yttrium iron garnet / platinum interface for spin pumping-based applications*
   M.B. Jungfleisch, V. Lauer, R. Neb, A.V. Chumak, B. Hillebrands
   Appl. Phys. Lett. **103**, 022411 (2013)

9. *Low spin-wave damping in amorphous $Co_{40}Fe_{40}B_{20}$ thin films*
   A. Conca, J. Greser, T. Sebastian, S. Klingler, B. Obry, B. Leven, B. Hillebrands
   J. Appl. Phys. **113**, 213909 (2013)

10. *A micro-structured ion-implanted magnonic crystal*
    B. Obry, P. Pirro, T. Brächer, A.V. Chumak, J. Osten, F. Ciubotaru, A.A. Serga, J. Fassbender, B. Hillebrands
    Appl. Phys. Lett. **102**, 202403 (2013)

11. *Unidirectional spin-wave heat conveyer*
    T. An, V.I. Vasyuchka, K. Uchida, A.V. Chumak, K. Yamaguchi, K. Harii, J. Ohe, M.B. Jungfleisch, Y. Kajiwara, H. Adachi, B. Hillebrands, S. Maekawa, E. Saitoh
    Nature Materials, **12**, 549-553 (2013)

12. *Generation of propagating backward volume spin waves by phase-sensitive mode conversion in two-dimensional microstructures*
    T. Brächer, P. Pirro, J. Westermann, T. Sebastian, B. Lägel, B. van de Wiele, A. Vansteenkiste, B. Hillebrands
    Appl. Phys. Lett. **102**, 132411 (2013)

13. *Heat-induced damping modification in yttrium iron garnet / platinum hetero-structures*
    M.B. Jungfleisch, T. An, K. Ando, Y. Kajiwara, K. Uchida, V.I. Vasyuchka, A.V. Chumak, A.A. Serga, E. Saitoh, B. Hillebrands
    Appl. Phys. Lett. **102**, 062417 (2013)

14. *Nonlinear emission of spin-wave caustics from an edge mode of a micro-structured $Co_2Mn_{0.6}Fe_{0.4}Si$ waveguide*
    T. Sebastian, T. Brächer, P. Pirro, A.A. Serga, T. Kubota, H. Naganuma, M. Oogane, Y. Ando, B. Hillebrands
    Phys. Rev. Lett. **110**, 067201 (2013)

15. *Microscopic magnetic structuring of a spin-wave waveguide by ion implantation in a $Ni_{81}Fe_{19}$ layer*
    B. Obry, T. Meyer, P. Pirro, T. Brächer, B. Lägel, J. Osten, T. Strache, J. Fassbender, B. Hillebrands
    Appl. Phys. Lett. **102**, 022409 (2013)

16. *Atom probe tomography of ion-irradiated ultra-thin Fe/Cr/Fe trilayers with sub-nm spatial resolution*
H. Gnaser, R. Schiller, M. Wahl, B. Reuscher, A. Zeuner, M. Kopnarski, R. Neb, B. Hillebrands
J. Phys. D: Appl. Phys. **45**, 50503 (2012)

17. *Spin-wave propagation and transformation in a thermal gradient*
B. Obry, V.I. Vasyuchka, A.V. Chumak, A.A. Serga, B. Hillebrands
Appl. Phys. Lett. **101**, 192406 (2012)

5.3 Ph.D. theses

1. *Linear and nonlinear spin dynamics in $Co_2Mn_{0.6}Fe_{0.4}Si$ Heusler microstructures*
Thomas Sebastian, TU Kaiserslautern, October 2013

2. *Spin pumping and inverse spin Hall effect in yttrium iron garnet/ platinum heterostructures*
Matthias Benjamin Jungfleisch, TU Kaiserslautern, October 2013

3. *Design der Spinwellenpropagation durch eine magnetische Strukturierung ein- und zweidimensionaler Systeme*
Björn Obry, TU Kaiserslautern, October 2013

4. *Spinwellentransport in zweidimensionalen Mikrostrukturen*
Katrin Schultheiß, TU Kaiserslautern, September 2013

5.4 Diploma theses

1. *Korrelation des Wachstumsmodus von dünnen Fe/Pt-Schichten zum inversen Spin-Hall-Effekt*
Philipp Fuhrmann, TU Kaiserslautern, September 2013

2. *Herstellungsoptimierung von YIG/Pt-Doppelschichten zur Steigerung des Spinpump-Prozesses*
Viktor Lauer, TU Kaiserslautern, December 2012

5.5 Master theses (Master of education)

1. *Aufbau eines Demonstrations- und Praktikumsversuchs zum spinkalorischen Transport von Spinwellen*
Stefan Weirich, TU Kaiserslautern, March 2013

Chapter 6: Conferences, Workshops, Schools, Seminars

(shown in chronological order; if not indicated otherwise the contributions were presented by the first author)

6.1 Conferences

6.1.1 Invited talks

B. Hillebrands:
New materials for magnon-spintronic applications
Material Science Week 2012: MSW 2012, Sendai, Japan, November 2012

B. Hillebrands:
Spin Caloritronics
Tutorial, 12th Joint MMM/Intermag Conference, Chicago, USA, January 2013

B. Hillebrands:
Magnonic Transport Phenomena
Plenary Talk, DPG Frühjahrstagung, Regensburg, March 2013

A.V. Chumak:
From magnon flow to spin current and back
DPG Frühjahrstagung, Regensburg, March 2013

B. Hillebrands:
TeMoRy: A robust storage cell based on TMR
12. MR-Symposium "Magnetoresistive Sensors and Magnetic Systems", Wetzlar, Germany, March 2013

A.V. Chumak:
Phonon-mediated Bose-Einstein magnon condensation
NewSpin 3 Conference "Spin-phenomena: From Model Systems to Complex Matter", Mainz, Germany, April 2013

B. Hillebrands:
Heat control of and by magnons
OSU Materials Week, Columbus, USA, May 2013

B. Hillebrands:
Magnon Caloritronics
Spin Caloritronics V, Columbus, USA, May 2013

A.A. Serga:
Magnon spintronics using Heusler compounds
JSPS York-Tohoku Research Symposium on "Magnetic Materials and Spintronics", York, United Kingdom, June 2013

B. Hillebrands:
Magnon gases
International Symposium on Spin Waves 2013, St. Petersburg, Russia, June 2013

A.V. Chumak:
Nanostructured magnetic metamaterials - magnonic crystals
Collaborative Conference on Materials Research (CCMR 2013), Jeju Island, South Korea, June 2013

B. Hillebrands:
Heat control of and by magnons
Magnonics 2013, Varberg, Sweden, August 2013

A.V. Chumak:
Magnon transistor and data buffering element
Magnonics 2013, Varberg, Sweden, August 2013

B. Hillebrands:
Magnon-Caloritronics
Gordon Research Conference "Spin Dynamics in Nanostructures", Hong Kong, China, August 2013

B. Hillebrands:
Magnon-Caloritronics
SPIE Optics + Photonics 2013, San Diego, USA, August 2013

B. Hillebrands:
Smart Magnon Spintronics
Half Plenary Talk, Donostia International Conference on Nanoscaled Magnetism and Applications (DICNMA 2013), Donostia-San Sebastián, Spain, September 2013

V.I. Vasyuchka:
Magnon caloritronic effects in a magnetic insulator
Donostia International Conference on Nanoscaled Magnetism and Applications (DICNMA 2013), Donostia-San Sebastián, Spain, September 2013

A.V. Chumak:
Spin pumping by magnons
Donostia International Conference on Nanoscaled Magnetism and Applications (DICNMA 2013), Donostia-San Sebastián, Spain, September 2013

A.V. Chumak:
Spin pumping by magnons
V Euro-Asian Symposium "Trends in MAGnetism" (EASTMAG-2013), Vladivostok, Russia, September 2013

A.A. Serga:
Magnon gases and condensates: Ultrahot Bose-Einstein magnon condensate in a phase space
V Euro-Asian Symposium "Trends in MAGnetism" (EASTMAG-2013), Vladivostok, Russia, September 2013

A.A. Serga:

Magnon transistor and signal processing with magnonic crystals
International Conference "Functional Materials" (ICFM-2013), Haspra, Ukraine, September-October 2013

6.1.2 Contributed talks and posters

K. Vogt, H. Schultheiss, S. Jain, J.E. Pearson, A. Hoffmann, S.D. Bader, B. Hillebrands:

Spin waves turning a corner
12th Joint MMM/Intermag Conference, Chicago, USA, January 2013

G.N. Kakazei, G.R. Aranda, S.A. Bunyaev, V.O. Golub, E.V. Tartakovskaya, A.V. Chumak, A.A. Serga, B. Hillebrands, K.Y. Guslienko:

Probing dynamical magnetization pinning in circular dot as a function of the external magnetic field orientation
12th Joint MMM/Intermag Conference, Chicago, USA, January 2013

M.B. Jungfleisch, T. An, K. Ando, Y. Kajiwara, K. Uchida, V.I. Vasyuchka, A.V. Chumak, A.A. Serga, B. Hillebrands, E. Saitoh:

Heat-induced spin-transfer torque in YIG/Pt structures
12th Joint MMM/Intermag Conference, Chicago, USA, January 2013

A.A. Serga, D.A. Bozhko, P. Clausen, A.V. Chumak, G.A. Melkov, B. Hillebrands:

A phonon-mediated Bose-Einstein magnon condensation
12th Joint MMM/Intermag Conference, Chicago, USA, January 2013

K. Vogt, B. Hillebrands, H. Schultheiss, J.E. Pearson, F.Y. Fradin, S.D. Bader, A. Hoffmann:

Controlling Spin-wave propagation with Oersted fields
APS March Meeting, Baltimore, USA, March 2013

A.V. Chumak, A.D. Karenowska, V.S. Tiberkevich, A.A. Serga, J. Gregg, A. Slavin, B. Hillebrands:

Frequency conversion and time reversal via a dynamic metamaterial
META'13, the 4th International Conference on Metamaterials, Photonic Crystals and Plasmonics, Sharjah, United Arab Emirates, March 2013

A.A. Serga, A.V. Chumak, V.I. Vasyuchka, M.P. Kostylev, V.S. Tiberkevich, B. Hillebrands:

Storage-recovery phenomenon in a magnetic artificial crystal
META'13, the 4th International Conference on Metamaterials, Photonic Crystals and Plasmonics, Sharjah, United Arab Emirates, March 2013

T. Brächer, P. Pirro, B. Obry, A.A. Serga, B. Hillebrands:

Localized parametric generation in a longitudinally magnetized microstrip
NewSpin 3 Conference "Spin-phenomena: From Model Systems to Complex Matter", Mainz, Germany, April 2013

T. Sebastian, P. Pirro, T. Brächer, A.A. Serga, B. Hillebrands, T. Kubota, H. Naganuma, M. Oogane, Y. Ando:

Nonlinear emission of spin-wave caustics from an edge mode of a microstructured $Co_2Mn_{0.6}Fe_{0.4}Si$ waveguide

NewSpin 3 Conference "Spin-phenomena: From Model Systems to Complex Matter", Mainz, Germany, April 2013

A.A. Serga, D.A. Bozhko, P. Clausen, V.I. Vasyuchka, G.A. Melkov, B. Hillebrands:

Hot Bose-Einstein magnon condensate in the wavevector-space

NewSpin 3 Conference "Spin-phenomena: From Model Systems to Complex Matter", Mainz, Germany, April 2013

M. Agrawal, V.I. Vasyuchka, A.A. Serga, A.D. Karenowska, G.A. Melkov, B. Hillebrands:

Magnon temperature measurement: New insights into Spin Seebeck effect

NewSpin 3 Conference "Spin-phenomena: From Model Systems to Complex Matter", Mainz, Germany, April 2013

V.I. Vasyuchka, A.A. Serga, A.V. Chumak, B. Hillebrands:

Spin wave mediated heating in a magnetic insulator

NewSpin 3 Conference "Spin-phenomena: From Model Systems to Complex Matter", Mainz, Germany, April 2013

T. Langner, M. Vogel, V.I. Vasyuchka, A.V. Chumak, A.A. Serga, G. von Freymann, B. Hillebrands:

Thermally induced magnonic crystals

NewSpin 3 Conference "Spin-phenomena: From Model Systems to Complex Matter", Mainz, Germany, April 2013

P. Clausen, D.A. Bozhko, V.I. Vasyuchka, A.V. Chumak, A.A. Serga, G.A. Melkov, B. Hillebrands:

Influence of laser power on phase transition in a magnon gas

NewSpin 3 Conference "Spin-phenomena: From Model Systems to Complex Matter", Mainz, Germany, April 2013

T. Meyer, B. Obry, B. Hillebrands:

Brillouin light scattering investigations of perpendicular standing spin waves at Au and Ag nanoparticles on top of a $Ni_{81}Fe_{19}$ film

NewSpin 3 Conference "Spin-phenomena: From Model Systems to Complex Matter", Mainz, Germany, April 2013

M.B. Jungfleisch, V. Lauer, R. Neb, A.V. Chumak, B. Hillebrands:

Optimization of YIG/Pt interface for spin-pumping-based applications

NewSpin 3 Conference "Spin-phenomena: From Model Systems to Complex Matter", Mainz, Germany, April 2013

A. Kehlberger, R. Röser, G. Jakob, U. Ritzmann, D. Hinzke, U. Nowak, M. Onbasli, D. Hun Kim, C. Ross, M.B. Jungfleisch, B. Hillebrands, M. Kläui:

Genuine spin Seebeck effect probed by thickness dependence in YIG films

NewSpin 3 Conference "Spin-phenomena: From Model Systems to Complex Matter", Mainz, Germany, April 2013

T. Langner, M. Vogel, V.I. Vasyuchka, A.V. Chumak, A.A. Serga, G. von Freymann, B. Hillebrands:
Thermally induced magnonic crystals
Spin Caloritronics V, Columbus, USA, May 2013

B. Obry, T. Brächer, P. Pirro, A.V. Chumak, F. Ciubotaru, A.A. Serga, J. Osten, J. Fassbender, B. Hillebrands:
Spin waves in a microstructured metallic magnonic crystal with periodic variation of the saturation magnetization
Yamada Conference LXVII: The 8th International Symposium on Metallic Multilayers (MML 2013), Kyoto, Japan, May 2013

A.V. Chumak, M.B. Jungfleisch, V. Lauer, R. Neb, B. Hillebrands:
Optimization of YIG/Pt interface for spin-pumping based applications
Yamada Conference LXVII: The 8th International Symposium on Metallic Multilayers (MML 2013), Kyoto, Japan, May 2013

T. Koyama, P. Pirro, T. Brächer, T. Sebastian, I. Ikhtiar, Y. Ohdaira, T. Kubota, H. Naganuma, M. Oogane, Y. Ando, B. Hillebrands:
Investigation of interaction between domain structure/domain wall and spin waves in $Co_2Mn_{0.6}Fe_{0.4}Si$ Heusler alloy
Yamada Conference LXVII: The 8th International Symposium on Metallic Multilayers (MML 2013), Kyoto, Japan, May 2013

A. Conca, J. Greser, T. Sebastian, S. Klingler, E.Th. Papaioannou, B. Leven, B. Hillebrands:
Dynamic characterization of $Co_{40}Fe_{40}B_{20}$ thin films by ferromagnetic resonance: Influence of the annealing temperature
Yamada Conference LXVII: The 8th International Symposium on Metallic Multilayers (MML 2013), Kyoto, Japan, May 2013

T. Brächer, P. Pirro, A.A. Serga, B. Hillebrands:
Parametric spin-wave generation in a longitudinally magnetized magnonic waveguide on the micrometer scale
International Symposium on Spin Waves 2013, St. Petersburg, Russia, June 2013

A.V. Chumak, B. Obry, T. Brächer, P. Pirro, F. Ciubotaru, A.A. Serga, J. Osten, J. Fassbender, B. Hillebrands:
Spin waves in a microstructured ion-implanted magnonic crystal
International Symposium on Spin Waves 2013, St. Petersburg, Russia, June 2013

P. Pirro, T. Sebastian, T. Brächer, A.A. Serga, T. Kubota, H. Naganuma, M. Oogane, Y. Ando, B. Hillebrands:
Spin-wave instabilities in micro-structured $Co_2Mn_{0.6}Fe_{0.4}Si$ waveguide
International Symposium on Spin Waves 2013, St. Petersburg, Russia, June 2013

T. Meyer, B. Obry, T. Brächer, P. Pirro, A.V. Chumak, F. Ciubotaru, A.A. Serga, J. Osten, J. Fassbender, B. Hillebrands:
Spin waves in a microstructured ion-implanted magnonic crystal
Magnonics 2013, Varberg, Sweden, August 2013

A.A. Serga, P. Clausen, D.A. Bozhko, V.I. Vasyuchka, A.V. Chumak, G.A. Melkov, B. Hillebrands:
Laser light influence on Bose-Einstein magnon condensate
Magnonics 2013, Varberg, Sweden, August 2013

M. Agrawal, V.I. Vasyuchka, A.A. Serga, A.D. Karenowska, G.A. Melkov, B. Hillebrands:
Study of magnon-phonon coupling and magnon temperature: New insights into spin Seebeck effect
Magnonics 2013, Varberg, Sweden, August 2013

V.I. Vasyuchka, A.A. Serga, A.V. Chumak, B. Hillebrands:
Spin wave mediated heating in a magnetic insulator
Magnonics 2013, Varberg, Sweden, August 2013

P. Fuhrmann, E.Th. Papaioannou, J. Greser, B. Hillebrands:
Manipulating spin pumping and Inverse Spin Hall effect with crystal structure in Fe/Pt bilayers
Magnonics 2013, Varberg, Sweden, August 2013

V.I. Vasyuchka, F. Ciubotaru, A.A. Serga, A.V. Chumak, B. Hillebrands:
Thermal transport by reciprocal and non-reciprocal magnons
Gordon Research Conference "Spin Dynamics in Nanostructures", Hong Kong, China, August 2013

A.A. Serga:
Ultrahot Bose-Einstein magnon condensate in a phase space
Joint European Magnetic Symposia (JEMS 2013), Rhodes, Greece, August 2013

V.I. Vasyuchka, F. Ciubotaru, A.A. Serga, A.V. Chumak, B. Hillebrands:
Thermal transport by reciprocal and non-reciprocal magnons
Joint European Magnetic Symposia (JEMS 2013), Rhodes, Greece, August 2013

M. Agrawal, H. Idzuchi, Y. Fukuma, A.A. Serga, Y. Otani, B. Hillebrands:
Investigation of spin-dynamics in non-local spin valves
International Conference on Nanoscale Magnetism (ICNM-2013), Istanbul, Turkey, September 2013

6.1.3 Contributions to the DPG Frühjahrstagung

19 contributions: DPG Frühjahrstagung, Regensburg, March 2013

6.2 Workshops and Schools

6.2.1 Invited lectures

B. Hillebrands:
Heat control of and by magnons
510. WE-Heraeus seminar "Nonmagnetic control of spin", Bad Honnef, Germany, January 2013

B. Hillebrands:
Magnon Spintronics + Spincaloritronics
NewSpin 3 Summer School, Mainz, Germany, April 2013

A.A. Serga:
Thermal transport by reciprocal and non-reciprocal magnons
DFG-Kolloquium in SPP 1538 "Spin Caloric Transport", Bad Honnef, Germany, April 2013

V.I. Vasyuchka:
Heat conveyer in magnetic insulators
DFG-Kolloquium in SPP 1538 "Spin Caloric Transport", Bad Honnef, Germany, April 2013

A.A. Serga:
Nonlinear spin-wave dynamics and radiation properties of small Heusler devices
Annual meeting of ASPIMATT JST-DFG Research Unit, Dresden, Germany, July 2013

A.V. Chumak:
Spin pumping by magnons
Annual meeting of ASPIMATT JST-DFG Research Unit, Dresden, Germany, July 2013

A.A. Serga:
Bose-condensation of mixed phonon-magnon states
7th Annual Retreat of the SFB/TR 49, Bensheim, Germany, September 2013

V.I. Vasyuchka:
Magnon caloritronics
Workshop Spin caloritronics in insulators, Mainz, Germany, October 2013

6.2.2 Contributed talks and posters

T. Langner, B. Obry, P. Pirro, T. Brächer, K. Vogt, A.A. Serga, B. Leven, B. Hillebrands:
Spin-wave resonance in $Ni_{81}Fe_{19}$ microstripes containing a mechanical gap
510. WE-Heraeus seminar "Nonmagnetic control of spin", Bad Honnef, Germany, January 2013

A.A. Serga, M. Agrawal, V.I. Vasyuchka, A.D. Karenowska, G.A. Melkov, B. Hillebrands:
Magnon temperature measurement: New insights into spin Seebeck effect
510. WE-Heraeus seminar "Nonmagnetic control of spin", Bad Honnef, Germany, January 2013

V.I. Vasyuchka, A.A. Serga, A.V. Chumak, B. Hillebrands:
Control of magnon mediated heating in a magnetic insulator
510. WE-Heraeus seminar "Nonmagnetic control of spin", Bad Honnef, Germany, January 2013

T. Langner, M. Vogel, V.I. Vasyuchka, A.V. Chumak, A.A. Serga, G. von Freymann, B. Hillebrands:
Thermally induced magnonic crystals
DFG-Kolloquium in SPP 1538 "Spin Caloric Transport", Bad Honnef, Germany, April 2013

M. Agrawal, V.I. Vasyuchka, A.A. Serga, A.D. Karenowska, G.A. Melkov, B. Hillebrands:
Magnon temperature measurement: New insight into spin Seebeck effect
DFG-Kolloquium in SPP 1538 "Spin Caloric Transport", Bad Honnef, Germany, April 2013

T. Meyer, B. Obry, B. Hillebrands:
Brillouin light scattering investigations of perpendicular standing spin waves at Au and Ag nanoparticles on top of a $Ni_{81}Fe_{19}$ film
The 6th IEEE Magnetics Society Summer School, Assisi, Italy, June 2013

T. Langner, V.I. Vasyuchka, M.B. Jungfleisch, A.V. Chumak, A.A. Serga, B. Hillebrands:
Dynamical heating of ferrimagnetic structures in a wide range of magnetic fields
The 6th IEEE Magnetics Society Summer School, Assisi, Italy, June 2013

T. Sebastian, P. Pirro, T. Brächer, T. Kubota, A.A. Serga, H. Naganuma, M. Oogane, Y. Ando, B. Hillebrands:
Nonlinear emission of spin-wave caustics from an edge mode of a microstructured $Co_2Mn_{0.6}Fe_{0.4}Si$ waveguide
Annual meeting of ASPIMATT JST-DFG Research Unit, Dresden, Germany, July 2013

T. Brächer, P. Pirro, A.A. Serga, B. Hillebrands:
Parallel parametric amplification of spin waves in ferromagnetic microstructures
4th MAINZ Student Seminar, Stockholm, Sweden, August 2013

M. Agrawal, V.I. Vasyuchka, A.A. Serga, B. Hillebrands:
Magnon temperature: New insight into spin Seebeck effect
4th MAINZ Student Seminar, Stockholm, Sweden, August 2013

T. Brächer, P. Pirro, A.A. Serga, B. Hillebrands:
Parallel parametric amplification of spin waves in ferromagnetic microstructures
1st COS Pine Summer school in Physics 2013 "Topological Insulators and Spintronics", Taipei, Taiwan, September 2013

V.I. Vasyuchka:
Magnon caloritronics
GRMN Workshop on Magnetism, Nancy, France, September 2013

B. Leven:
Magnon Spintronics
GRMN Workshop on Magnetism, Nancy, France, September 2013

B. Hillebrands:
Magnon-SHE and magnonic crystals
GRMN Workshop on Magnetism, Nancy, France, September 2013

B. Obry, P. Pirro, T. Brächer, A.V. Chumak, T. Meyer, J. Osten, T. Strache, F. Ciubotaru, A.A. Serga, J. Fassbender, B. Hillebrands:
Novel patterning techniques for magnon transport
GRMN Workshop on Magnetism, Nancy, France, September 2013

V. Lauer, M.B. Jungfleisch, R. Neb, A.V. Chumak, B. Hillebrands:
Improvement of YIG/Pt interface for spin pumping-based applications
GRMN Workshop on Magnetism, Nancy, France, September 2013

P. Clausen, D.A. Bozhko, A.V. Chumak, V.I. Vasyuchka, A.A. Serga, B. Hillebrands:
Ultrahot Bose-Einstein magnon condensate in a phase space
GRMN Workshop on Magnetism, Nancy, France, September 2013

T. Sebastian:
Nonlinear emission of spin-wave caustics from an edge mode of a microstructured $Co_2Mn_{0.6}Fe_{0.4}Si$ *waveguide*
GRMN Workshop on Magnetism, Nancy, France, September 2013

A. Conca Parra, B. Leven, B. Hillebrands:
The Spintronic Technology Platform (STeP) and the Service Center for New Materials (TT-DINEMA): Technology transfer in Rhineland-Palatinate
GRMN Workshop on Magnetism, Nancy, France, September 2013

D.A. Bozhko, P. Clausen, A.A. Serga, V.I. Vasyuchka, A.V. Chumak, G.A. Melkov, B. Hillebrands:
Bose condensation of mixed phonon-magnon states
7th Annual Retreat of the SFB/TR 49, Bensheim, Germany, September 2013

P. Clausen, D.A. Bozhko, A.A. Serga, V.I. Vasyuchka, G.A. Melkov, B. Hillebrands:
Bose-Einstein condensation of exchange magnons
7th Annual Retreat of the SFB/TR 49, Bensheim, Germany, September 2013

T. Langner, V.I. Vasyuchka, B. Obry, A.V. Chumak, A.A. Serga, B. Hillebrands:
Magnon mediated heat and spin transport in a magnetic insulator
Workshop Spin caloritronics in insulators, Mainz, Germany, October 2013

M. Agrawal, V.I. Vasyuchka, A.A. Serga, A.D. Karenowska, G.A. Melkov, B. Hillebrands:
Magnon temperature measurement: New insight into spin Seebeck effect
Workshop Spin caloritronics in insulators, Mainz, Germany, October 2013

M. Agrawal, A.A. Serga, B. Hillebrands:
Temporal evolution of spin Seebeck effect
3rd SpinCaT PhD Workshop, Dresden, Germany, October 2013

T. Langner, M. Vogel, V.I. Vasyuchka, A.V. Chumak, A.A. Serga, G. von Freymann, B. Hillebrands:
Thermally induced magnonic crystals
3rd SpinCaT PhD Workshop, Dresden, Germany, October 2013

6.3 Invited seminar talks and colloquia

M.B. Jungfleisch, V. Lauer, R. Neb, D.A. Bozhko, V.S. Tiberkevich, A.V. Chumak, A.A. Serga, B. Hillebrands:
Spin pumping and inverse spin Hall effect in yttrium iron garnet/platinum heterostructures
Argonne National Lab, Argonne, USA, January 2013

A.V. Chumak:
Magnons as an alternative to a charge current
University of Groningen, Groningen, Netherlands, April 2013

B. Hillebrands:
Magnon Caloritronics, Lecture on occasion of the 70th birthday of Gernot Güntherodt
Physikalisches Kolloquium, RWTH Aachen, Aachen, Germany, April 2013

B. Hillebrands:
Magnonic Metamaterials
Birthday Colloquium Gernot Güntherodt, May 2013

6.4 Seminars

P. Clausen, D.A. Bozhko, A.V. Chumak, A.A. Serga, G.A. Melkov, B. Hillebrands:
Phonon mediated Bose-Einstein magnon condensation
SFB/TR 49 Student Seminar Summer Term 2013, Dannenfels, Germany, April 2013

6.5 Annual group retreat

In 2013 our group organized a three-day retreat at the Kurhaus am Trifels, Annweiler. We had two days of intense scientific discussion and 14 presentations by our group members. Dr. Klaus Kremb, former principal of Gymnasium Winnweiler, gave a fascinating evening talk on *"Mit den nothwendigsten Werkzeugen zum Vortrage der Physik versehen"- Die "Physikalisch-ökonomische Gesellschaft zu Lautern"und ihre "Kameral-Hohe-Schule"(1768/74-1784).* On the first day, the group members participated in a soft skill seminar on "Intercultural communication" held by Dr. phil. Kundri Böhmer-Bauer.

6.6 Other meetings and trade fairs

B. Hillebrands:
Presentation of GRMN
Innomag-Treffen, Dresden, Germany, March 2013

A. Conca Parra, B. Leven, B. Hillebrands:
Presentation of the Spintronic Technology Platform
Hannover Messe 2013, Hannover, Germany, April 2013

A. A. Serga, V. I. Vasyuchka, E. Th. Papaioannou, T. Meyer:
Seminar about Tandem-FPI alignment with Dr. J. Sandercock
JRS Scientific Instruments/The Table Stable Ltd, Mettmenstetten, Switzerland, April 2013

B. Hillebrands:
Magnonen für den Computer von übermorgen
Dresdener Nacht der Wissenschaften, Dresden, Germany, July 2013

B. Leven, A. Conca, E. Th. Papaioannou, V. Lauer, S. Klingler:
Presentation of GRMN
Wissenschaftsmarkt, Mainz, Germany, September 2013

6.7 Awards and Fellowships

T. Sebastian, P. Pirro, T. Brächer, T. Kubota, A.A. Serga, H. Naganuma, M. Oogane, Y. Ando, B. Hillebrands:
Poster award for "Nonlinear emission of spin-wave caustics from an edge mode of a microstructured $Co_2Mn_{0.6}Fe_{0.4}Si$ waveguide"
Annual meeting of ASPIMATT JST-DFG Research Unit, Dresden, Germany, July 2013

Appendix: Impressions from 2013

PH.D. defense Dr. Katrin Schultheiß

PH.D. defense Dr. Björn Obry

PH.D. defense Dr. Benjamin Jungfleisch

PH.D. defense Dr. Thomas Sebastian

Wissenschaftsmarkt in Mainz

Group excursion

TECHNISCHE UNIVERSITÄT
KAISERSLAUTERN

Prof. Dr. Burkard Hillebrands
Fachbereich Physik
Landesforschungszentrum OPTIMAS
Technische Universität Kaiserslautern, Germany
P.O. Box 3049
67653 Kaiserslautern
Phone: +49 631 205-4228
Fax: +49 631 205-4095
E-mail: hilleb@physik.uni-kl.de
Internet: http://www.physik.uni-kl.de/hillebrands/